

Processing and Characterization of Multi-walled Carbon Nanotube Reinforced Aluminium Metal Matrix Composite

By

Tao Peng

A thesis submitted for the degree of

DOCTOR OF PHILOSOPHY

School of Metallurgy and Materials
University of Birmingham

UNIVERSITY OF
BIRMINGHAM

University of Birmingham Research Archive

e-theses repository

This unpublished thesis/dissertation is copyright of the author and/or third parties. The intellectual property rights of the author or third parties in respect of this work are as defined by The Copyright Designs and Patents Act 1988 or as modified by any successor legislation.

Any use made of information contained in this thesis/dissertation must be in accordance with that legislation and must be properly acknowledged. Further distribution or reproduction in any format is prohibited without the permission of the copyright holder.

Synopsis

Carbon nanotube attracts the global attention due to its nano size, high specific strength, extreme tensile strength and Young's modulus, and excellent thermal and electrical conductivity. These properties, coupled the lightness of carbon nanotubes, gives them great potential as reinforcement in aluminium matrix to fabricate strong and light-weight composites for demanding applications, such as aerospace and automobile. Therefore, a study has been made to incorporate multi-walled carbon nanotube (MWNT) into aluminium using powder metallurgical route to manufacture bulk Al-MWNT composite.

In this research, 0-2.0 wt. % MWNT has been ball milled with aluminium powders for 0-20 h to yield "as-milled" composite powders, which were compacted and sintered to produce bulk Al-MWNT composites. The evolution of "as-milled" powders was studied by a combination of scanning electron microscopy (SEM), particle size analysis, and apparent and tapped density. The densities of the green compact and sintered specimens were determined according to Archimedes' method. The sintered specimens were subjected to standard Vickers hardness test and MPIF standard tensile test to measure their mechanical properties. The cross-section microstructure of the "as-milled" powders and sintered specimens were characterized by a combination of optical microscopy and scanning electron microscopy (SEM). The phases and the crystal structure in the "as-milled" powders and the sintered specimens were identified by X-ray diffraction (XRD). The evolution and dispersion of MWNT in the "as-milled" Al-MWNT composite powders and sintered

Al-MWNT composite matrix were studied by SEM and Raman spectroscopy.

It is found that without the aid of process control agent (PCA), the "as-milled" powders were welded together and formed granules of around 2 mm in size. Two kinds of PCA (e.g. ethanol and stearic acid) were used in this study. The powders ball-milled with 1. 0 wt. % ethanol is found to yield smaller particles (i.e. 2.43 μm, milling for 10 h) and excessive defects (i.e. I_D/I_G: 1.11, milling for 10 h) are introduced into the structure of MWNT, as compare to 1. 0 wt. % of stearic acid (i.e. particle size: 59.78 μm, I_D/I_G: 0.99, milling for 10 h). Since the structure of MWNT is very essential in the enhancement of the composites, stearic acid was then chosen as the process control agent in the subsequent experiments.

Ball milling of elemental aluminium powders resulted in the increase of particle size to 73.86 ± 4.29 μm after 10 h of milling before decreasing to 63.78 ± 3.43 μm after milling for 20 h. The hardness of the "as-milled" elemental powders steadily increased with the increasing of milling time due to the accumulation of strain and grain refinement during ball milling process. The increased hardness reduced the compactability of the "as-milled" elemental aluminium powders and lowered the green density. The thickness of alumina on the surface of the "as-milled" Al powders increased with the increasing of milling time and impeded the diffusion and densification process during sintering. The ultimate tensile strength of the sintered aluminium materials was enhanced by grain refinement. However, the ductility of the sintered aluminium materials was reduced by the increasing of porosity and the amount of nano-sized Al_2O_3 at the boundaries.

The addition of 1.0 wt. % MWNT into elemental aluminium powders reduced the particle size of the “as-milled” powders by hindering the contact and welding of aluminium particles. However, the structure of MWNT was damaged by the violent impact and collision of milling balls. The damage of MWNT led to the formation of amorphous carbon which reacted with aluminium to form Al_3C_4. The effect of increased amount of porosity, Al_3C_4 and Al_2O_3 in the composite matrix led to a reduction of the ductility of the sintered Al-1.0 wt. % MWNT composite. The hardness and ultimate tensile strength of the sintered Al-1.0 wt. % MWNT specimens, fabricated using 15 h ball-milled Al-1.0 wt. % MWNT composite powders, were 32.24 % and 15.88 % higher than those of sintered specimen produced from the 15 h ball-milled aluminium powders without MWNT addition. This is due to the grain refinement in the ball milling and the load transfer strengthening of MWNT in aluminium metal matrix composite.

Increasing the MWNT concentration (i.e. 2.0 wt. %) led to further reduction of particle size. A higher content of MWNT resulted in more damaged MWNT during the ball milling process and more Al_3C_4 was formed during the sintering process. Moreover, MWNT agglomerates were observed in the Al-2.0 wt. % MWNT composite which hindered the densification process and lowered the density of the sintered composite.

Preface

The work described in the current thesis was carried out by the author in the School of Metallurgy and Materials at the University of Birmingham from October 2011 to September 2014, under the supervision of Dr. I. T. H. Chang.

The data and analysis presented in this thesis is original except where otherwise noted. None of this research has been submitted for any degree at any university.

Part of the current work was published and presented in international conferences as follows:

[1] T. Peng, I. Chang, Uniformly dispersion of carbon nanotube in aluminum powders by wet shake-mixing approach, Powder Technol, 284 (2015) 32-39.

[2] T. Peng, I. Chang, Mechanical alloying of multi-walled carbon nanotubes reinforced aluminum composite powder, Powder Technol, 266 (2014) 7-15.

[3] T. Peng, I. Chang, A Novel Method to Homogenously Disperse Carbon Nanotubes in Aluminum Powders, in: Euro Powder Metallurgy 2014 Congress & Exhibition, Salzburg, Austria, 2014.

[4] D. Uzunsoy, T. Peng, I. Chang, I. Istif, Investigation of Wear Behavior of Aluminum Alloy Reinforced with Carbon Nanotubes, SAE International Journal of Materials and Manufacturing, 7 (2014) 596-601.

[5] I. Istif, O. Isın, D. Uzunsoy, T. Peng, I. Chang, Prediction of Wear Behavior of Aluminum Alloy Reinforced with Carbon Nanotubes Using Nonlinear Identification, in, SAE Technical Paper, 2014.

[6] T. Peng, I. Chang, Mechanical Alloying of Multi-wall Carbon Nanotube and Aluminium Composite Powder, in: National Student Conference in Metallic Materials Manchester, UK, 2012.

Acknowledgement

I would like to express my deepest gratitude towards my supervisor Dr. Isaac Chang for his excellent supervision, smart guidance and constant patient. His valuable experience and precious advices led me into the real world of materials as well as made me realize the amazing magic of materials.

Appreciation also shown to: Dr. Constantin Lucian Falticeanu, Dr. Andy Ward, Dr. Nicolas Harrison, Dr Su Sei and all the staff in the School of Metallurgy and Materials. Thanks to their continued support, inspirational encouragement and priceless friendship.

Especially, I would like to thank Professor Paul Bowen, Head of the School of Metallurgy and Materials, for the provision of the materials processing and characterization facilities. Also I acknowledge the financial support provided by China Scholarship Council.

Finally, I would like to thank my parents for their unconditional support, unlimited love and understanding all along my life.

Contents

Chapter 1. Introduction ***1***

Chapter 2. Literature Review ***6***

2. 1. Introduction 6

2. 2. Aluminium 7

2. 2. 1. The abundance of aluminium 7
2. 2. 2. The properties of aluminium 7
2. 2. 3. The application of aluminium and its alloy 8
2. 2. 4. The challenges of aluminium 9

2. 3. Carbon nanotube 10

2. 3. 1. The structure of carbon nanotube 11
2. 3. 1. 1. Single-walled and multi-walled carbon nanotube 13
2. 3. 1. 2. The morphology of carbon nanotube 14
2. 3. 2. The synthesis of carbon nanotube 15
2. 3. 2. 1. Arc discharges 15
2. 3. 2. 2. Laser ablation 16
2. 3. 2. 3. Chemical vapour deposition (CVD) 17
2. 3. 3. The properties of carbon nanotube 19
2. 3. 3. 1. Mechanical properties 19
2. 3. 3. 2. Electrical properties 20
2. 3. 3. 3. Thermal properties 21
2. 3. 4. The application of carbon nanotube 21
2. 3. 5. The characterization of carbon nanotube 23

2. 4. Carbon nanotube reinforced aluminium metal matrix 24

2. 4. 1. Composite material 24
2. 4. 2. Carbon nanotube reinforced composites 25
2. 4. 2. 1. CNT reinforced polymer composites 25
2. 4. 2. 2. CNT reinforced ceramic composites 27
2. 4. 2. 3. CNT reinforced metal matrix composites 28
2. 4. 3. Strengthening mechanism 54
2. 4. 3. 1. Grain refinement strengthening 54
2. 4. 3. 2. Dislocation strengthening 55
2. 4. 3. 3. Thermal mismatch strengthening 56
2. 4. 3. 4. Orowan loop strengthening 57
2. 4. 3. 5. Load transfer strengthening 58
2. 4. 4. Challenges 61
2. 4. 4. 1. Agglomeration and dispersion of carbon nanotube in matrix 61
2. 4. 4. 2. Interfacial bonding between matrix and carbon nanotube 64
2. 4. 4. 3. The structure of carbon nanotube in Al-CNT composite 65

2. 5. Powder metallurgy 68

2. 5. 1. The advantages of powder metallurgy 69
2. 5. 2. The powder metallurgy process 70
2. 5. 2. 1. Powder production 71
2. 5. 2. 2. Blending and mixing 73
2. 5. 2. 3. Shaping and pressing 74
2. 5. 2. 4. Consolidation 74
2. 5. 2. 5. Finishing operations 75

Chapter 3. Experiment and characterization 76

3. 1. Introduction 76

3. 2. Pristine materials 77

3. 2. 1 Aluminium 77
3. 2. 2 Carbon nanotube 79

3. 3. Materials processing 81

3. 2. 3 Powder mixing 81
3. 2. 4 Pressing of powder 83
3. 2. 5 Sintering of powder 85

3. 4. Characterization 86

3. 4. 1 Sample grinding and mounting 86
3. 4. 2 Etching 87
3. 4. 3 Optical microscopy 88
3. 4. 4 Scanning electron microscopy (SEM) 88
3. 4. 5 Vickers micro-hardness test 89
3. 4. 6 Tensile test 90
3. 4. 7 Apparent density and tapped density 91
3. 4. 8 Green density, sintered density and relative density 93
3. 4. 9 X-ray diffraction (XRD) 94
3. 4. 10 Differential scanning calorimetry (DSC) 95
3. 4. 11 Raman spectroscopy 96
3. 4. 12 Particle size analysis 96

3. 5. Preparation of powder and bulk specimen 97

Chapter 4. The effect of process control agent on the Al-1.0 wt. % MWNT composite powders 101

4. 1. Introduction 101

4. 2. Results 101

4. 2. 1 The morphology of the ball-milled Al-1.0 wt. % MWNT composite powders 101

4. 2. 1. 1. No PCA.....101
4. 2. 1. 2. 1.0 wt. % Stearic acid.....102
4. 2. 1. 3. 1.0 wt. % Ethanol.....104
4. 2. 2 The particle size distribution of the ball-milled Al-1.0 wt. % MWNT composite powders.....106
4. 2. 2. 1. 1.0 wt. % Stearic acid.....106
4. 2. 2. 2. 1.0 wt. % Ethanol.....107
4. 2. 2. 3. The comparison of median particle size (D_{50}) between different process control agent.....108
4. 2. 3 The Raman spectra of the MWNT in the ball-milled Al-1.0 wt. % MWNT composite powders.....110
4. 2. 3. 1. 1.0 wt. % Stearic acid.....111
4. 2. 3. 2. 1.0 wt. % Ethanol.....112
4. 2. 3. 3. The comparison of I_D/I_G of MWNT between different process control agent.....113

4. 3. Discussion.....115

4. 3. 1 The effect of process control agent on the Al-1.0 wt. % MWNT composite powders.....115
4. 3. 2 The effect of different process control agent on the Al-1.0 wt. % MWNT composite powders.....116
4. 3. 3 The effect of different process control agent on the structure of MWNT.118

4. 4. Summary.....119

***Chapter 5. The effect of ball milling on the microstructure and mechanical properties of aluminium materials*.....121**

5. 1. Introduction.....121

5. 2. The effect of ball milling on aluminium powders.....122

5. 2. 1 Results.....122
5. 2. 1. 1. Morphology.....122
5. 2. 1. 2. Cross-section.....124
5. 2. 1. 3. Particle size distribution.....128
5. 2. 1. 4. X-ray diffraction.....131
5. 2. 1. 5. Differential scanning calorimetry.....132
5. 2. 1. 6. Vickers micro-hardness.....133
5. 2. 2 Discussion.....134
5. 2. 2. 1. The effect of ball milling on the structure of aluminium powders.....134
5. 2. 2. 2. The effect of ball milling on the hardness of aluminium powders.....137
5. 2. 3 Summary.....139

5. 3. The effect of ball milling on the sintered aluminium materials.....140

5. 3. 1 Results 140
5. 3. 1. 1. Cross-section 140
5. 3. 1. 2. Sintered density 145
5. 3. 1. 3. X-ray diffraction 146
5. 3. 1. 4. Vickers micro-hardness 148
5. 3. 1. 5. Tensile properties 148
5. 3. 2 Discussion 150
5. 3. 1. 1. The formation of Al_2O_3 in the sintered aluminium materials 150
5. 3. 1. 2. The strengthening mechanism of the sintered aluminium materials 153
5. 3. 3 Summary 155

Chapter 6. The effect of ball milling on the microstructure and mechanical properties of multi-walled carbon nanotube reinforced aluminium composite 156

6. 1. Introduction 156

6. 2. The effect of ball milling on the Al-1.0 wt. % MWNT composite powders 158

6. 2. 1 Results 158
6. 2. 1. 1. Morphology 158
6. 2. 1. 2. Cross section 161
6. 2. 1. 3. Particle size distribution 165
6. 2. 1. 4. X-ray diffraction 166
6. 2. 1. 5. Raman spectroscopy 167
6. 2. 1. 6. Vickers micro-hardness 169
6. 2. 2 Discussion 170
6. 2. 2. 1. The evolution and distribution of MWNT in the ball-milled Al-1.0 wt. % composite powders 170
6. 2. 2. 2. The structure evolution of MWNT in the ball-milled Al-1.0 wt. % composite powders 173
6. 2. 2. 3. The effect of MWNT on the ball-milled aluminium powders 175
6. 2. 3 Summary 176

6. 3. The effect of ball milling on the sintered Al-1.0 wt. % MWNT composite material 177

6. 3. 1 Results 177
6. 3. 1. 1. Cross-section 177
6. 3. 1. 2. The dispersion of MWNT in the sintered Al-1.0 wt. % MWNT composite 180
6. 3. 1. 3. Sintered density 181
6. 3. 1. 4. X-ray diffraction 182
6. 3. 1. 5. Raman spectroscopy 186
6. 3. 1. 6. Vickers micro-hardness 187
6. 3. 1. 7. Tensile properties 188
6. 3. 1. 8. Fracture surface 190

6. 3. 2 Discussion 193
6. 3. 2. 1. The evolution and dispersion of MWNT in the sintered Al-1.0 wt. % MWNT composite 193
6. 3. 2. 2. The strengthening of the sintered Al-1.0 wt. % MWNT composite 195
6. 3. 3 Summary 199
Chapter 7. The effect of multi-walled carbon nanotube concentration on the microstructure and mechanical properties of Al-MWNT composite materials 200
7. 1. Introduction 200
7. 2. The effect of multi-walled carbon nanotube concentration on the Al-MWNT composite powders 201
7. 2. 1 Results 201
7. 2. 1. 1. Morphology 201
7. 2. 1. 2. The dispersion of multi-walled carbon nanotube 203
7. 2. 1. 3. Cross section 205
7. 2. 1. 4. Particle size distribution 207
7. 2. 1. 5. X-ray diffraction 209
7. 2. 1. 6. Raman spectroscopy 210
7. 2. 1. 7. Vickers micro-hardness 212
7. 2. 2 Discussion 213
7. 2. 2. 1. The dispersion of MWNT in the ball-milled Al-MWNT composite powders 213
7. 2. 2. 2. The evolution of MWNT in the ball-milled Al-MWNT composite powders 214
7. 2. 2. 3. The effect of MWNT concentration on the ball-milled Al-MWNT composite powders 215
7. 2. 3 Summary 215
7. 3. The effect of multi-walled carbon nanotube concentration on the sintered Al-MWNT composite materials 217
7. 3. 1 Results 217
7. 3. 1. 1. Cross section microstructure 217
7. 3. 1. 2. Sintered density 218
7. 3. 1. 3. X-ray diffraction 219
7. 3. 1. 4. Tensile strength 221
7. 3. 2 Discussion 222
7. 3. 2. 1. The strengthening mechanism of the sintered Al-MWNT composite materials 222
7. 3. 3 Summary 227
Chapter 8. Conclusion and future work 229
8. 1. Conclusion 229

8. 2. Future work 231

Reference ***..... 233***

Chapter 1. Introduction

Aluminium (Al) and its alloy are widely used in the packaging, transportation, electrical and modern machinery sections because of their low density (only 35% of steel), high specific strength (Aluminium 7075-T6, 323 % of stainless steel), good ductility and malleability, excellent corrosion resistance, impressive electrical (3.8×10^7 S/m, just behind silver, copper and gold) [7] and thermal conductivity (205 W/(mK)). Furthermore, they are attractive engineering materials because of its abundance in ores (the most abundant metal element) [8], relatively low production price and recyclability. However, relatively low tensile strength of aluminium (90 MPa, 11.84 % of ASTM A514 steel [9]) and its alloy (Aluminium 7075-T6: 572 MPa, 75 % of ASTM A514 steel [9]) restricts the application of this material in the high loading environment.

To solve this problem, reinforcements like ceramic particles (i.e. SiC [10-13], Al_2O_3 [14, 15], B_4C [16, 17] and Si_3N_4 [18]) and nano fibres (i.e. Al_2O_3 [19]) have been added into aluminium by spraying [10], infiltrating molten [10, 20], mechanical alloying [12-17] and stir-casting [11, 18]. Among all the potential reinforcements, carbon nanotube (CNT) stands out and attracts the most attention due to its superior aspect ratio, incomparable tensile strength (multi-walled carbon nanotube (MWNT), 63 GPa [21]) and elastic modulus (MWNT, up to 5 TPa [21]), exceptional electrical (current density: 4×10^9 A/cm^2 [22]) and thermal conductivity (2980 W/m/K [23], 3500 W/m/K [24]). It is assumed that carbon nanotube can not only strengthen but also introduce various distinctive characteristics into the aluminium

matrix to improve its overall properties and performances.

Therefore, the main aims of the current research are to fabricate MWNT reinforced aluminium composite with homogeneous dispersion of MWNT in the composite matrix and obtain enhanced mechanical properties. The significance of this research is to study the effect of multi-walled carbon nanotube (MWNT) addition on the microstructure and properties of the sintered Al-MWNT composite. Several challenges are expected to be addressed. Firstly, it is necessary to find the appropriate process control agent (PCA) to prevent the excessive welding of aluminium while introduce less defects into the structure of MWNT in the ball milling process. Secondly, it is critical to demonstrate the feasibility of employing ball milling to de−agglomerate and disperse MWNT into aluminium matrix. Thirdly, it is significant to find the favourable milling time and the concentration of MWNT to optimise the mechanical properties of the Al-MWNT composite.

The detailed objectives are to:

1. Incorporate carbon nanotube into aluminium powders and fabricate homogenous dispersed carbon nanotube reinforced aluminium composite materials by ball milling method.
2. Produce ball-milled Al-MWNT composite powders and sintered Al-MWNT composite materials with different process control agent, varied milling time and different MWNT concentration.
3. Characterize and investigate the microstructure and the characteristics of the

as-produced Al-MWNT and optimize the processing parameters.

This research programme is concerned with Al-MWNT composite fabricated by ball milling followed by press and sintering routes. The current thesis is divided into eight chapters.

In chapter 2, a literature review is provided, regarding the fabrication and properties of carbon nanotube reinforced aluminium metal matrix composite including the characteristics of aluminium and carbon nanotube, the approaches of manufacturing and the mechanical properties of the as-produced Al-CNT composite. The ball milling technique is described in detail as it is the main method employed in the current research to disperse MWNT into aluminium powders.

In chapter 3, the characteristics of the raw materials, the production process of Al-MWNT composite and the techniques of characterisation are introduced.

In chapter 4, the effect of the process control agent (PCA) on the ball milling of elemental aluminium and Al-MWNT composite powders is introduced. 1.0 wt. % of process control agent, either ethanol or stearic acid were added into elemental aluminium powders and Al – 1.0 wt. % MWNT composite powders separately and ball milled for 0 – 20 h. The control group without any PCA was ball milled for the same period of time. The particle size of the "as-milled" elemental aluminium powders was measured by particle size analyser. The structure of MWNT in the "as-milled" powders was characterized by Raman spectroscopy.

In chapter 5, the effect of ball milling on the elemental aluminium powders and the sintered aluminium materials is presented. Elemental aluminium powders with 1.0 wt. % stearic acid were ball milled in argon for 5 – 20 h at a speed of 250 rpm. Subsequently, the "as-milled" elemental aluminium powders were compacted and sintered. The evolution of aluminium particles was studied by scanning electron microscopy (SEM)**.** The microstructure of the "as-milled" elemental aluminium powders and as-sintered elemental aluminium materials are revealed by SEM and X-ray diffraction (XRD). The hardness and tensile strength of the as-sintered aluminium materials were also measured.

In chapter 6, the effect of ball milling on the Al-1.0 wt. % MWNT composite powders and the sintered Al-1.0 wt. % MWNT composite material is described. 1. 0 wt. % MWNT and 1.0 wt. % stearic acid were ball milled with aluminium powders in argon for 5 – 20 h at 250 rpm. The bulk Al-1.0 wt. % MWNT composite specimens were produced by pressing and sintering of "as-milled" composite powders. The microstructure of the ball-milled composite powders and sintered composite materials, and the distribution and structure of MWNT were studied by a combination of XRD, SEM and Raman spectroscopy. The mechanical properties of the composite materials were determined using Vickers hardness and tensile test methods. The thermal stability of the "as-milled" Al-MWNT composite powders was studied by DSC.

In chapter 7, the effect of various MWNT concentration on the ball milled composite

powders and the as-sintered bulk composite materials is described. 0.5 – 2.0 wt. % MWNT and 1.0 wt. % stearic acid were ball milled with aluminium powders in argon for 15 h at 250 rpm. The phases and crystal structure of "as-milled" Al-MWNT composite powders and sintered Al-MWNT composite are characterized by XRD. The structure and dispersion of MWNT were studied by a combination of Raman spectroscopy and SEM. The mechanical properties of the sintered Al-MWNT composite materials were determined using Vickers hardness and tensile test methods in order to understand the strengthening mechanism.

In chapter 8, the findings of the project are summarized and the suggestions for future work are presented.

Chapter 2. Literature Review

2. 1. Introduction

Since the discovery by Iijima [25] in 1991, carbon nanotube (CNT) emerged as ideal reinforcements in metal matrix composites to enhance stiffness and strength as well as weight saving. This is due to the high Young's modulus (up to 5.0TPa reported for single-walled CNT [26]), excellent tensile strength and other superb physical properties. Although multi-walled CNT shows a lower Young's modulus (up to 1.0TPa [26]), they are more widely employed because of their relatively lower price comparing to that of single-walled CNT [27]. With the declining of global oil and depletion of the ozone layer in the atmosphere, using light-weight and strong reinforcements like CNT to increase the fuel efficiency of engine while providing high strength and stiffness has become highly desirable.

In the last decade, numerous research efforts have been made in developing CNT for metal matrix composites (MMCs) [28-36]. However, several critical issues have to be addressed before achieving the full potentials of CNT as reinforcements. High volume fraction and homogeneous distribution of CNT in MMCs are the main obstacles because the static electricity and strong van der Waals forces of attraction between the long and thin tubes make CNT extremely vulnerable to agglomeration. The other technical problem is the poor interfacial bonding of CNT and metal which is essential to the overall mechanical performances. Also, the preservation of the cylindrical structure of CNT after various processing is vital to the final overall property of the composite material.

2. 2. Aluminium

2. 2. 1. The abundance of aluminium

Aluminium is the most abundant metal element and the third most abundant element (8.1 %) just after oxygen (47 %) and silicon (28 %) in the Earth's crust [8] which is illustrated in Fig. 2. 1. Two hundred years ago, the existence of aluminium is known by few people despite the rich reserves of aluminium in the nature environment. This is because aluminium is too reactive to exist in its pure form and extraction techniques from ores have not yet been developed in the old days. Surprisingly, aluminium is used everywhere in our daily life nowadays: cutleries, plates, cooking pots, window frames, even vehicle bodies and fuels for rocket, etc.

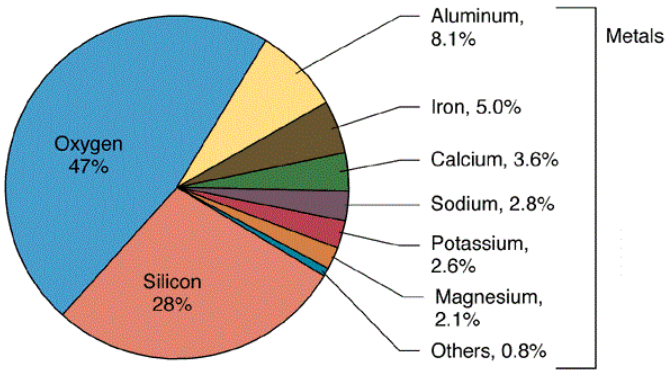


Fig. 2. 1 The content of the elements in the earth crusts [37].

2. 2. 2. The properties of aluminium

Aluminium is one of the most versatile elements. It has impressive mechanical properties,

strong corrosion resistance, and remarkable thermal and electrical conductivity. Among all the superb characteristics, the low density and light weight are the most prominent features that make aluminium stand out from the other metals. Its specific weight (2.7 g/cm^3) is only one third of that of copper (8.9 g/cm^3) and less than half of that of iron (7.8 g/cm^3) which is significant for automobile, aviation, aerospace and defence industries as it helps to lower the weight of component, improve the fuel efficiency and reduce the greenhouse gas emission.

2. 2. 3. The application of aluminium and its alloy

Aluminium, based on its abundance, impressive characteristics and the advances of modern technology, finds its positions in diverse creative applications and meets different demanding challenges. Since the 1950s, the primary aluminium production worldwide kept a steady and sustained growing trend and aluminium is widely utilized in construction, packing and transportation sectors. Fig. 2. 2 shows the global aluminium consumption of different application sectors in 2010.

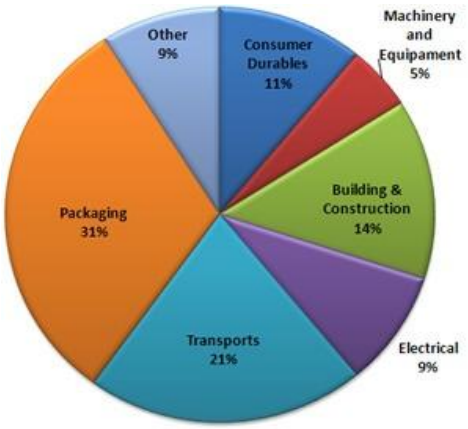


Fig. 2. 2 The consumption segments of aluminium in 2010 [38].

2. 2. 4. The challenges of aluminium

Although aluminium has enormous outstanding properties and wide spectrum of applications in diverse industries, the downside and disadvantages of its characteristic are not neglectable.

Firstly, the low hardness and low strength of pure aluminium are hard to satisfy various modern requirements for relatively high stiffness, strong strength and good wear and abrasion resistance. Although some alloying elements were incorporated into aluminium matrix to increase the mechanical properties, the strongest aluminium alloy is around 517 MPa tensile strength which is only one third of that of the heat-treated steel (1.7 GPa tensile strength).

Secondly, the capital cost of smelting and extraction of aluminium is much higher than steel, which restrict the wider adoption of aluminium in industrial production and manufacturing as profit is the top priority in commercial business. In theory, aluminium can be 100% recycled from scrap and do not lose its quality. What's more important is that recycle the same amount of aluminium consume less than 20 % (5 % for beverage can recycle) of the energy required for smelting process. Today, only one third of the global aluminium consumption is from recycling while the rest two thirds are from primary production. There is a huge driving force to increase the amount of Al for recycling because of the need to (1) lower the material cost, (2) reduce the pollution of mining and metallurgy and (3) save the valuable energy and resource on the earth.

2. 3. Carbon nanotube

Carbon, the most versatile nature element, is widely involved in scientific research and commercial applications due to its diverse properties depending on the different arrangement and microstructure of carbon atoms. Graphite was first discovered in 1779 and diamond form of carbon was discovered 10 years later. The interest on carbon had never stopped ever since then. Carbon fibre and fullerenes were discovered by researchers and scholars in the following two centuries. It was not until 1991 that the "material for 21st century [39]" and "the major millstone in nanoscale material science [40]" – carbon nanotube was discovered. (Fig. 2. 3 shows the structure of diamond, graphite, fullerene and carbon nanotube.)

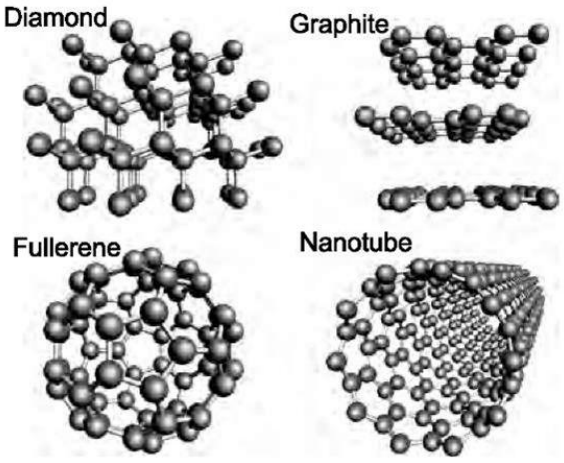


Fig. 2. 3 The schematic diagram of the structure of diamond, graphite, fullerene and carbon nanotube.

Mutil-walled carbon nanotube was first found by Japan scientist Sumio Iijima [41] as a product of the carbon-arc discharge method, which is similar to the method of preparing fullerenes [42]. The number of studies and experiments on carbon nanotube has been

significantly soared up ever since its discovery. The focus of various researches is utilizing CNT as promising reinforcements to enhance different material systems like polymer matrix, ceramic matrix and metal matrix, due to the exceptional mechanical and exciting physical properties of carbon nanotube, i.e. superior Young's/elastic modulus, high aspect ratio, outstanding thermal and chemical stability and high strength-to-weight ratio. In respect of this, CNT-reinforced matrix composites have been proposed for many automobile, aerospace, electrical and thermal applications.

2. 3. 1. The structure of carbon nanotube

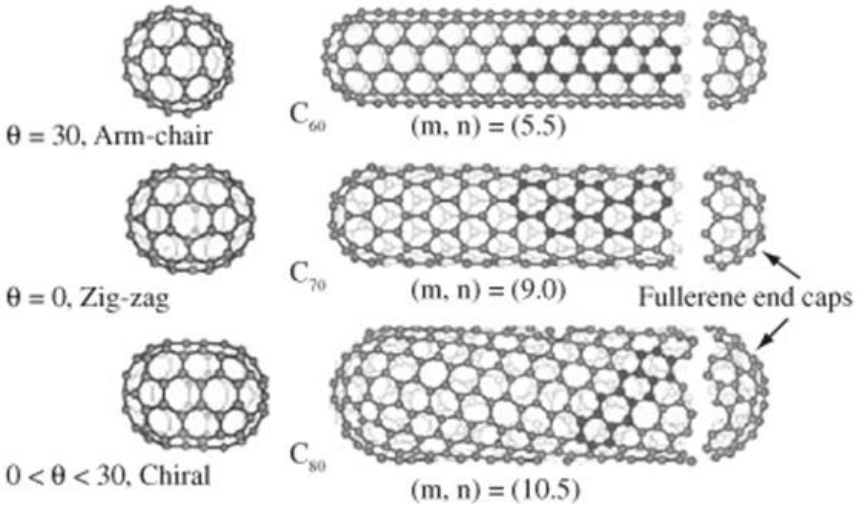


Fig. 2. 4 Single-walled carbon nanotube configurations with different caps.

CNT can be thought as sheets of graphite rolled into cylinders and capped with half-fullerenes at each end [43] (Fig. 2. 4). Ideal CNT have a seamlessly tubular structure are built by sp^2 carbon units [44], which equipped CNT with desirable chemical and thermal stability. CNT has an incredibly large aspect ratio so that it has a very strong tendency of

clustering due to the strong van der Waals attractive forces between the long and thin tubes.

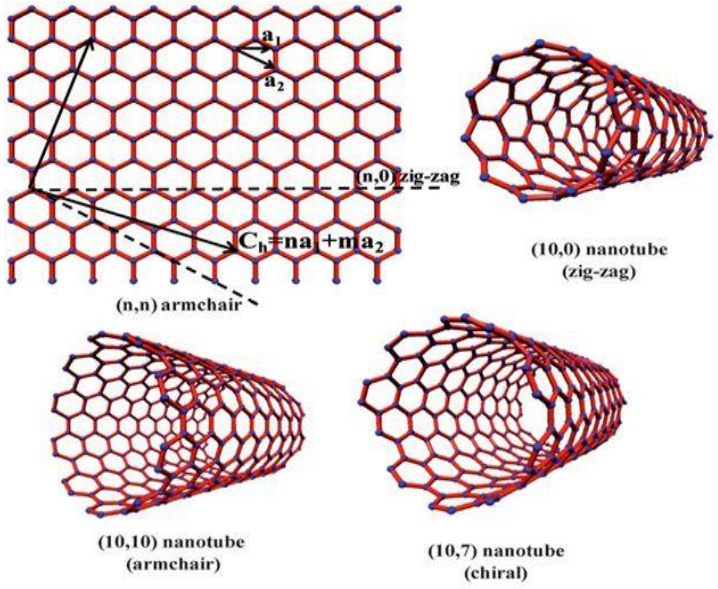


Fig. 2. 5 Configurations of armchair, zigzag and chiral structure of carbon nanotubes.

The individual nanotube has three different patterns of structure, namely armchair, zigzag and chiral, depending on the different way that hexagonal networks of carbon atoms rolled together [45] (as shown in Fig. 2. 5). These different groups can be distinguished by C_h, which is a vector showing the junction of two equivalent points on an open graphene sheet. C_h is determined by the equation:

$$C_h = na_1 + ma_2 \qquad (2.\ 3.\ 1.\ 1)$$

where a_1 and a_2 are standard unit cell vectors while n and m are the integers ($m \geq n$) representing possible nanotube structures. Another meaningful parameter is the angle between C_h and a_1, namely chiral angle (θ). When $n = m$, $\theta = 30°$ zigzag tube is obtained

and when $m = 0$ or $n = 0$, $\theta = 0°$ or $90°$ we get armchair tube. All the rest are known for chiral nanotubes ($n \neq m$, $0° < n, m < 90°$, $0° < \theta < 90°$) (Fig. 2. 4) [45].

2. 3. 1. 1. Single-walled and multi-walled carbon nanotube

CNT are normally either single-walled or multi-walled resulting from the different number of rolled graphite sheet layers (Fig. 2. 6). Single-walled carbon nanotube (SWNT) can be described as a cylindrical network of carbon atoms bonded by sp^2 bonding and capped by half fullerene (C_{60}) at each end, while multi-walled carbon nanotube (MWNT) is composed of several layers of graphite separated by a distance of 0.34nm [46]. Generally, the diameters of MWNT is in the range of 2-25 nm and the distance between each sheet is around 0.34 nm [47] while the diameter of SWNT is ranged from 1-2 nm [48]. Currently, the length and diameter of both produced MWNT and SWNT are much larger than before due to the significant development of fabrication methods[49]. Although MWNT generally revealed lower properties due to the existence of various defects in its structure than SWNT, it is stilled more widely investigated and studied because of its lower cost of synthesis.

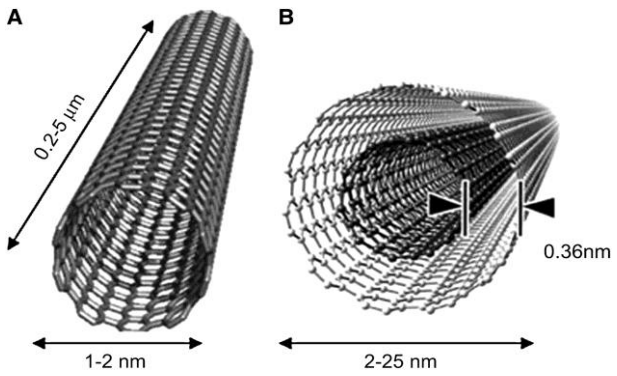


Fig. 2. 6 The schematic structure of SWNT (A) and MWNT (B).

2. 3. 1. 2. The morphology of carbon nanotube

According to A. M. K. Esawi and K. Morsi [50], MWNT, synthesized by chemical vapour deposition, showed two types of morphology: bent and entangled vs. stiff and straight. Fig. 2. 7 presents the different morphology of MWNT while Table 2. 1 summarizes the characteristics of the MWNT.

Table 2. 1 Specification of the MWNT used in the study of A. M. K. Esawi and K. Moris [50].

Morphology	Mean diameter	Average length	Length to diameter ratio
Bent and entangled	30 – 50 nm	10 – 20 μm	375
Stiff and straight	140 ± 30 nm	7 ± 2 μm	50

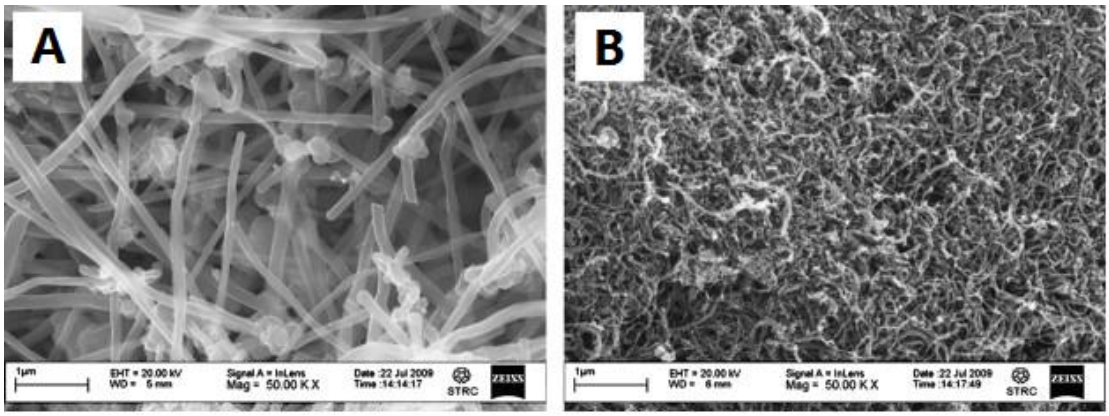


Fig. 2. 7 SEM images of (A) bent and entangled and (B) stiff and straight MWNT.

As can be seen from Table 2. 1, the small diameter MWNT have a very high length to diameter ratio comparing to that of large diameter MWNT (Fig. 2. 7. (A)) (375 vs. 50), which makes MWNT with small diameter vulnerable to form in bundles and shows a bent and entangled morphology (Fig. 2. 7. (B)). It is predicted that MWNT with smaller diameter

have a larger effective length in addition to its larger starting aspect ratio, which indicated a higher potential of MWNT for strengthening and stiffening the composites [50]. Nevertheless, Wang et al. [51] commented that small diameter MWNT will lead to more defects, porosity and deformation under the impact of mechanical alloying and weaken the properties of the composite. Hence, it is quite interesting to balance the separation of MWNT while keep its perfect tubular structure.

2. 3. 2. The synthesis of carbon nanotube

2. 3. 2. 1. Arc discharges

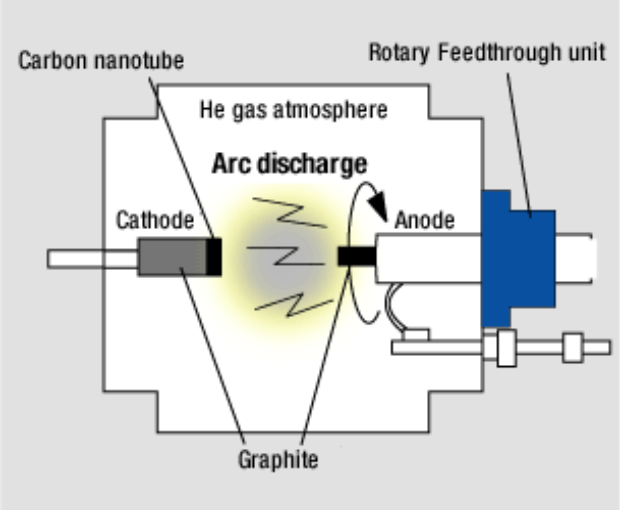


Fig. 2. 8 Schematic drawing of the electric arc discharge apparatus.

The arc discharge method, was the first available method fabricating both MWNT and SWNT, is the same route of producing fullerenes and has been employed for quite a long time to produce carbon fibre, which resulting in a disagreement that carbon nanotube were observed before 1991 but not recognized as such.

Electric arc discharge method is the most classic approach applied in fabricating carbon nanotube (Fig. 2. 8). In the process of this technique, an electric arc discharge is struck between two graphite electrodes under inert gas (helium, argon or other neutral atmosphere) at low pressure (between 50 and 700 mbar). One of the carbon rods is vaporized by discharge and MWNT was deposited on the other rod [52]. In 1993, Bethune et al. [53] and Iijima et al. [54] addressed that by adding metal catalysts (such as cobalt, iron or nickel) on a cathode, SWNT was condensed on the anode. One of the disadvantages of this technique is the gasification with oxygen or carbon dioxide is needed to purify the as-deposited carbon nanotube. Also, the gathering of carbon nanotube has to interrupt the ongoing reaction which would no doubt prolong the production cycle.

2. 3. 2. 2. Laser ablation

The laser ablation technique, another very powerful method to prepare CNT, was demonstrated in 1995 by Smalley's group at Rice University [55]. The apparatus used by this group is shown in Fig. 2. 9.

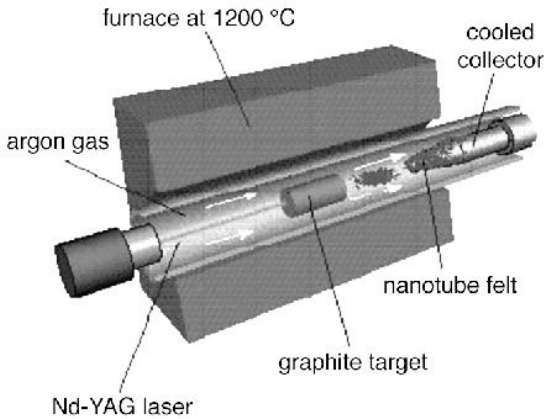


Fig. 2. 9 Schematics of a laser ablation set-up [56].

Similar to arc discharge, laser ablation is operated under helium or argon gas atmosphere to keep pressure at a very high temperature (1200 ℃). A very hot vapour plume is formed by high energy laser striking on the graphite target, and then the soot is cooled rapidly to grow carbon nanotube. Purification is also needed in the process to eliminate the carbonaceous impurities. Since the gas atmosphere and catalyst mix is the same as in the arc discharge process and other reaction conditions are very similar, laser ablation and arc discharge reactions probably occur with the same mechanism.

2. 3. 2. 3. Chemical vapour deposition (CVD)

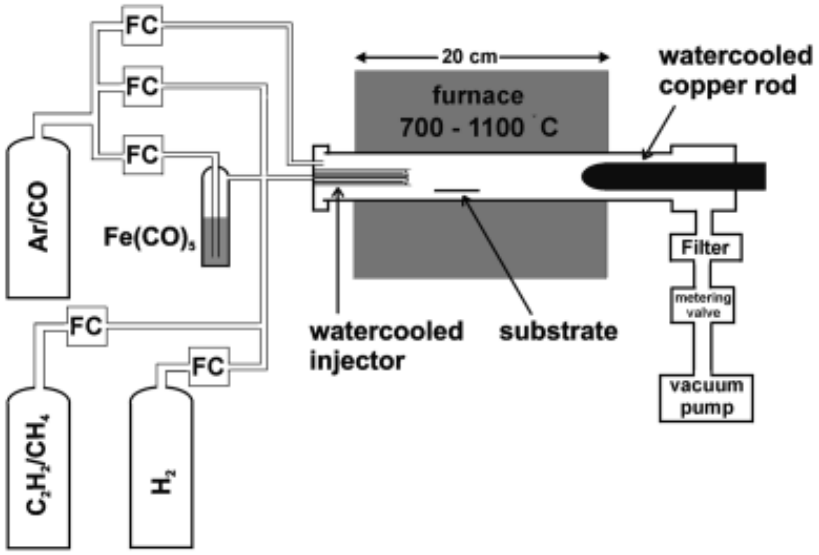


Fig. 2. 10 Scheme of chemical vapour deposition (CVD) reactor.

An alternative process is chemical vapour deposition (CVD) (Fig. 2. 10) which is the most common applied catalytic route in producing commercial MWNT. The fabrication of MWNT in CVD process involves a high temperature (500 ℃ - 1200 ℃) heating of a metal catalyst such as Fe, Co and Ni at a hydrocarbon gas atmosphere (e.g. carbon monoxide,

methane or acetylene), which leads to a catalytic dissociation of hydrocarbon molecules, and the precipitation of carbon atoms on the surface of metal particles. Fig. 2. 11 shows the MWNT prepared by CVD method.

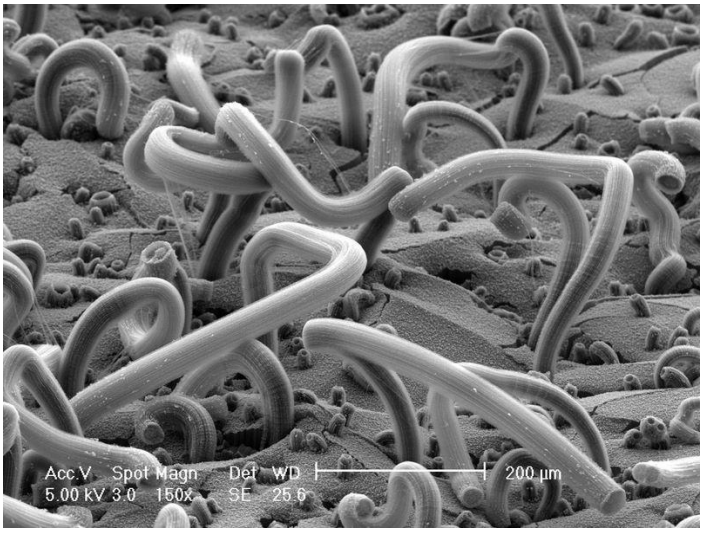


Fig. 2. 11 The SEM image of MWNT grown by CVD.

In CVD technique, SWNT was found to grow at a very high temperature on the well-distributed catalyst while MWNT formed at relatively lower temperature and even at the absence of metal catalyst [57]. The weakness of CVD method is the various impurities such as fullerenes, graphite compounds, amorphous and metal particles produced along with the growth of MWNT. Careful purification achieved by oxidative treatment is needed to remove the contaminations.

To summarize, various methods have been explored for the synthesis of carbon nanotube. Except the three main techniques, namely arc discharge, laser ablation and chemical vapour

deposition, other innovative routes such as plasma torch method and underwater AC electric arc method are attempted on some scale. But these novel methods are still not mature enough for commercial application. Generally, the carbon nanotube fabricated by catalyst method are cheaper and the quantities are controllable, however, the existence of defects and impurities makes their performance much lower than the expensive arc prepared ones. Even so, the low commercial price of MWNT produced by CVD makes them more popular in scientific research. Thus, the development and exploration of new technology to lower the fabrication cost of high quality carbon nanotube is clearly essential for its wide industrial application.

2. 3. 3. The properties of carbon nanotube

The distinctive characteristics of CNT are what sparked the intense interest of the scientific world. A. M. K Esawi et al. [58] described the properties of carbon nanotube as a combination of graphite and diamond: light weight, flexibility and electrical conductivity like graphite while strong, thermally conductive like diamond. Numerous research groups had added carbon nanotube to different matrix with the aim of strengthening, toughening and enhancing the thermal or electrical conductivity of the matrix material.

2. 3. 3. 1. Mechanical properties

Among all the outstanding performances, mechanical properties of carbon nanotube are greatly influenced by the strong carbon–carbon sp^2 bonding. The SWNT possesses a super

high Young's modulus of up to 5 TPa and a tensile strength as high as 52 GPa. In spite of showing a little lower mechanical behaviour (up to 1.8 TPa for elastic modulus and up to 63 GPa for tensile strength [21]), MWNT is more widely used due to the availability and cheaper price. Since the density of carbon nanotube is as low as 1.3 - 1.4 g/cm^3, the specific strength of it can be up to 48,000 kN·m/kg (that of high cabon steel is only 154 kN·m/kg) which is the highest value of materials that known by human beings [59]. In the October of year 2000, the researchers from the Pennsylvania State University found that the strength of SWNT is 100 times that of the same volume of steel while the weight of SWNT is just 1/6 to 1/7 of the weight of the later [60].

2. 3. 3. 2. Electrical properties

The distinct geometry and atoms arrangement of carbon nanotube allow carbon nanotube to have different electrical characteristics. For a specified carbon nanotube with certain *n* and *m* parameters (as mentioned in the section 2. 3. 1), if the difference of *n* and *m* is the integral multiple of 3, then the carbon nanotube is semi-conductive with a small band gap; when *n* and *m* are equal the carbon nanotube exhibits metallicity like copper; otherwise the carbon nanotube are semiconducting [22]. Theoretical calculation estimate the current density in metallic carbon nanotubes can be as high as 4×10^9 A/cm^2 which is 1000 times the electrical conductivity of copper, the second most conductive metal just after silver to the best knowledge of human beings [22].

2. 3. 3. 3. Thermal properties

Carbon nanotube possesses exceptional thermal conductivity along the axis direction but insulating perpendicular the axis, which is a property named 'ballistic conduction'. In 1999, J.W. Che, T. Cagin, and W.A. Goddard [23] numerically calculated the thermal property of carbon nanotube which nearly reached 2980 W/m/K. In 2005, the thermal conductivity of SWNT was experimentally measured to be around 3500 W/m/K [24] which is almost 10 times that of copper (385 W/m/K). What's more, carbon nanotube is theoretically expected to be stable below the temperature of 750 ℃ in air and 2800 ℃ in vacuum, which exhibits the possibility of applying carbon nanotube in high temperature fields [61].

2. 3. 4. The application of carbon nanotube

As a result of the remarkable properties, carbon nanotube have been projected for catalysts [62], sensors [63], field emission materials [64] and reinforcements for composites [65].

Since the discovery of carbon nanotube, its surprisingly impressive mechanical properties not only excited the scientific world but also sparked the interest and ideas of incorporating carbon nanotube into various matrixes to fabricate composites with dramatically enhanced tensile strength [66, 67], compressive strength [68], hardness [69, 70] and other specific mechanical characteristics. Polymer [71], metal and ceramic matrixes [65] all have been investigated as the matrix for carbon nanotube reinforced composite. Due to the relatively convenient mixing of carbon nanotube with various polymers, the carbon nanotube

reinforced polymer composite is most widely studied among all the carbon nanotube reinforced composite. On the other hand, because of the significant density difference and the poor wettability between carbon nanotube and metal/ceramic matrix as well as the severe agglomeration of carbon nanotube, metal/ceramic-carbon nanotube composites are rarely successfully fabricated and much less work has been done in these fields. The detailed description of the development of carbon nanotube reinforced composites can be found in the following section.

With the exceptional electrical conductivity, excellent chemical stability and, more importantly, large specific surface areas, carbon nanotube is successfully experimented as catalyst supporter to replace the conventional brittle alumina and silicon supporter in the field of heterogeneous catalysis [62]. Also, the combination of nano-sized dimension, seamless structure, stable chemical properties and superior electro-conductibility make carbon nanotube an ideal nano-probe (sensor and electron emitter) to replace the traditional electron emitters (like Spindt-type emitters) [72, 73] and improve the resolution of imaging (features such as DNA molecules is possible to be seen with the assistance of carbon nanotube emission tip) [74] as the electron field emission tip on scanning tunneling microscope (STM), atomic force microscopy (AFM) and electrostatic force microscopy (EFM) [75].

It is worth noticing that, to the best knowledge of the present author, very little practical products or industrial applications of carbon nanotube have been employed commercially,

which, in return, indicates a wide scope for the future research and development.

2. 3. 5. The characterization of carbon nanotube

Raman spectroscopy is the most used method to reveal the complementary structural information of carbon nanotube. In the Raman spectrum of carbon nanotube, the first order peaks exhibit the structure information of carbon nanotube which composed of D band at around 1350 cm^{-1} and G band that is typically located at 1580 cm^{-1} [76]. G band is observed for perfect sp^2 covalent bonding of hexagonal graphite which will therefore appear wider and smaller for badly structured and defect containing nanotubes [16]. On the other hand, D band is attributed to lattice defects, so it will increase and broaden with increasing amount of defects in the structure of nanotubes [76]. In addition, it is reported by other researchers [16] that the broadening of the D and G peaks indicates the amorphisation of nanotubes.

The intensity ratio of D band peak and G band peak (I_D/I_G) is often used to assess and evaluate the structure of CNT [16]. The more hexagonal graphite (the higher the G band peaks) and less defects (the lower the D band peaks) exist, the lower I_D/I_G will be. A better mechanical properties can be achieved in the final Al-CNT composite if lower I_D/I_G is maintained after various process, which implies more hexagonal graphite (e.g. high G band peak intensity) and less defective (e.g. low D band peak intensity). Fig. 2. 12 shows an example of Raman spectrum of MWNT.

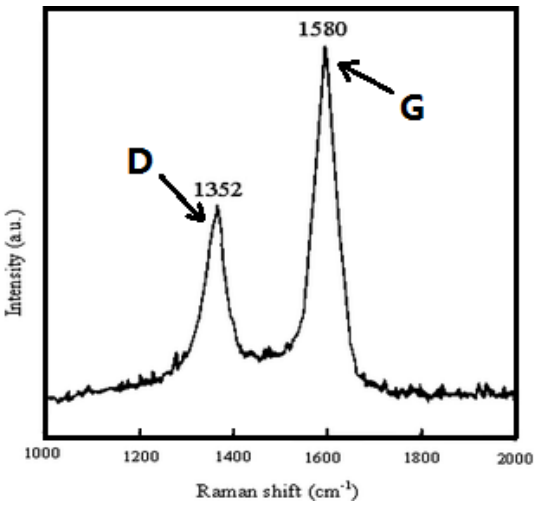


Fig. 2. 12 A typical Raman spectrum of MWNT.

2. 4. Carbon nanotube reinforced aluminium metal matrix

In 1991, the discovery of CNT by Iijima [41] revolutionized the whole scientific world. The superb capability and seamless structure of CNT is extremely attractive to the field of high-performance aerospace and automobile industries. Enormous numbers of experiments and simulations have been carried out to inducing CNT as reinforcement into different materials systems namely polymer, ceramic and metal matrix.

2. 4. 1. Composite material

Composite material is a macroscopic or microscopic scale, engineered or naturally existed, mixture of two or more constituent materials with significantly different physical or chemical properties with a recognizable interface between each component. This revolutionized material overcomes the vulnerabilities of conventional materials and satisfies the increasingly specific demands of all applications without accentuating flaws and defects.

2. 4. 2. Carbon nanotube reinforced composites

Taking the advantages of superior elastic modulus, high tensile strength and all the other excellent thermal and electrical characteristics of carbon nanotube, CNT reinforced composites have been developed and applied in diverse material systems such as polymer, ceramic and metal matrix system. The significant enhancement of the property of the carbon nanotube reinforced composite suggests the possibility of novel application of CNT reinforced composites, ranging from thermal management to automobile and aerospace industries.

2. 4. 2. 1. *CNT reinforced polymer composites*

Since the discovery of CNT, the majority of research on CNT composites is focused on polymer matrix, with only a small portion of ceramics and metals matrix being considered for this role. The main reason for this was that the relative ease of polymer processing, which often does not need high temperature and/or high pressure as needed for metals and ceramics matrix systems.

2. 4. 2. 1. 1. Processing techniques

Typically, the traditional fabrication method of polymer-CNT composites involves three main steps [77] which consist of dispersing CNT in a suitable solvent by mechanical blending, agitation or ultrasonication; mixing the aqueous CNT dispersions with solutions of polymer before casting the polymer-CNT mixture as films and evaporating the solvent. In

some cases, CNT needs to be pre-treated with acid to facilitate solubilisation [78].

The limitation of the solution mixing method, as stated above is that only common solvents that polymers can dissolve in can be used. Thus, another alternative, melt spinning is developed. In this technique, fibre-shaped, rather than films, polymer-CNT composite was produced by high shear force dispersing CNT in thermoplastic polymers (i.e. polypropylene and polystyrene) at an elevated temperature. In this case, blending energy and mixing temperature are often controlled to grow specific CNT fibre. No solvent is needed in this technique which is very compatible with current industrial practices [79]. In addition to the two most commonly utilized routes, many creative means such as in situ polymerization and latex technology have also been developed to satisfy the specific demands.

2. 4. 2. 1. 2. Mechanical properties of polymer-CNT composites

Both MWNT and SWNT are employed to enhance the properties of polymers such as polystyrene epoxy, nylon, and so on. The first systematic study of polymer-CNT, operated by Shaffer et al. [80], was quite disappointing that the acquired stiffness and Young's modulus was much lower than the theory calculated value. Nevertheless, the following studies by many other researchers proved the efficiency of using CNT to reinforce polymer materials.

In 2005, Margrave et al. [81] incorporated chemical functionalized SWNT into epoxy polymer, in which an increase of 18 % and 24 % in tensile strength and modulus

respectively was obtain with the addition of only 1.0 wt. % of SWNT. More exciting data of strengthening was achieved in the study of polystyrene-CNT composite by Andrews et al. [82, 83], which revealed that, after 1.0 wt. % CNT was added into the polystyrene matrix, the stiffness improved 48 % and 62 % with the addition of short (~15 μm) and long (~50 μm) carbon nanotube, respectively, while the tensile strength increased 25 % for both tubes added composites.

2. 4. 2. 1. 3. Other properties of carbon polymer-CNT composites

Although the intense attention has been focused on mechanical properties, the possibility of using carbon nanotube to improve other (electrical, thermal, optical and so on) characteristics of polymer has also been studied. To date, many researchers investigated the effect of CNT on the electrostatic dissipation [84] and conductivity [85] of polymers and achieved exciting results.

2. 4. 2. 2. *CNT reinforced ceramic composites*

Oxides possess high stiffness and splendid chemical and thermal stability, but weak in shear and tension. The objective of importing CNT into ceramic is to enhance its fracture toughness and strength. In contrast to the prosperity of polymer-CNT composite, CNT reinforced ceramic material system has been largely unexplored. This is resulting from the difficulty of uniformly dispersing CNT in ceramics and the poor wettability of CNT/ceramic interface which is rather challenging than CNT/polymer composites.

2. 4. 2. 3. CNT reinforced metal matrix composites

It is well recognized the materials used in aerospace and automobile industry demand high specific stiffness strength and low coefficient of thermal expansion (COE) while keep lightweight [86]. As the rapid development of modern engineering industries, conventional materials can no longer satisfy all the challenges, which results in the development of metal matrix composites in which the base metal matrix provides the ductility and the reinforcement (normally ceramics or high stiffness metal in fibre or particle form) supplies the strength.

Among all the CNT reinforced material systems, carbon nanotube reinforced metal matrix composite (CNT-MMC) is the most promising one in the application of automotive and aerospace industry. In recent years, many researchers put their emphasis on fabricating CNT-MMC by different processing routes using different metal matrix (Al, Mg, Cu and etc.) to be utilized as structural materials with extraordinary strength and functional materials with excellent electrical and thermal properties. To date, the research of CNT-MMC achieved some promising results, but several critical issues need to be addressed before the full potential of CNT in the metal matrix can be obtained.

Generally, the approaches of fabricating carbon nanotube reinforced aluminium composite can be summarized into two steps: the first step is the mixing of carbon nanotube with metal particles and the other step is the consolidation of the mixture.

2. 4. 2. 3. 1. The mixing of carbon nanotube and metal powders

To mix the carbon nanotube with metal powders, ball milling (mechanical alloying) is the most effective and commonly used method while chemical vapour deposition, electrochemical deposition and molecular level mixing were also attempted.

(a) Ball milling/mechanical alloying

Ball milling (BM), also known as mechanical alloying (MA), is a cold solid-state powder processing technique for powder grinding and blending [87]. In the ball milling/mechanical alloying process, powders are milled with or without milling media (i.e. stainless steel or ceramic ball bearings) and undergo repeatedly welding and fracturing, which yields powders with reduced particle size and homogenous distribution of each phase. More importantly, the severe plastic deformation during the BM/MA process introduces a large amount of strain and dislocation into the "as-milled" powders while severely reduces grain size. Thus, ball milling/mechanical alloying is employed to produce alloys from immiscible solids [88], composite with uniform dispersion of reinforcement [29, 34] and ultra-fine grain sized materials [89].

The most studies on the fabrication of CNT-MMC employed mechanical alloying method due to its high efficiency, controllable process and simplicity of operation. Esawi and Morsi [90, 91] ball milled 2.0 wt. % and 5.0 wt. % MWNT with aluminium powders for 48 h at 200 rpm with a ball-to-powder weight ratio of 10:1. The particles size of the "as-milled"

Al-5.0 wt. % MWNT powders is found much smaller than that of the "as-milled" Al-2.0 wt. % MWNT, which can be seen from Fig. 2. 13. More importantly, carbon nanotube were found to uniformly dispersed at the fracture surface of the ball-milled Al-2.0 wt. % MWNT particle as shown in Fig. 2. 14. This directly proved the effectiveness of dispersing carbon nanotube into metal powders.

A. H. Javadi et al. [92] and Z. Y. Liu et al. [93] employed ball milling to disperse 2.0 wt. % and 0.5 wt. % carbon nanotube into aluminium powders, respectively. Their results shown that carbon nanotube were well dispersed in the aluminium powders. Besides directly fabricating the carbon nanotube/aluminium mixture for compaction and consolidation, some researchers like T. Laha et al. [94], S. M. Zhou et al. [95] and B. Abbasipour et al. [96, 97] used ball milling to produce the precursor for their individual processing, which is discussed in detail in the following sections.

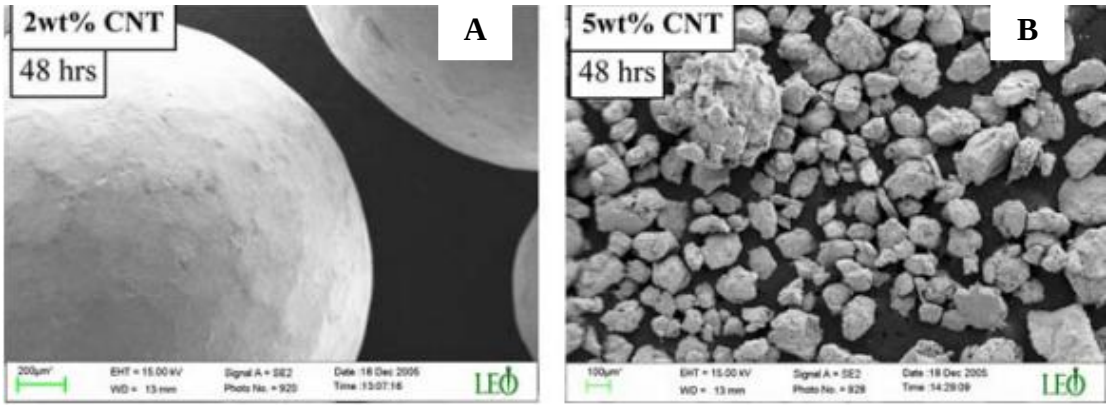


Fig. 2. 13 The SEM micrographs of mechanically alloyed Al - (A) 2.0 wt. % and (B) 5 .0 wt. % MWNT composite powders after 48 h.

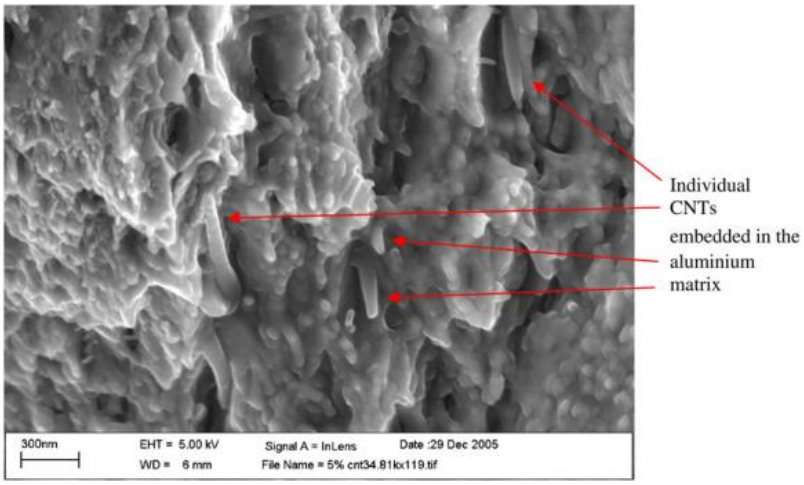


Fig. 2. 14 The deformed and fractured Al-2.0 wt. % MWNT particles, showing individual MWNT embedded in the aluminium particles after ball-milling of 48 h.

(b) Chemical vapour deposition

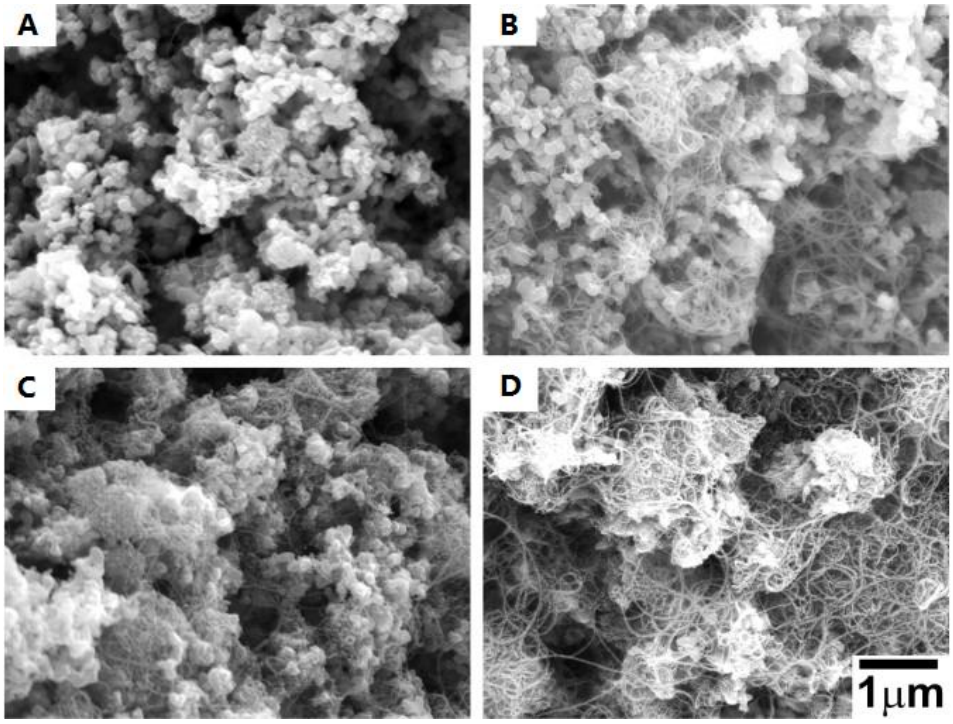


Fig. 2. 15 The FESEM images of the CNT–Al_2O_3 nanocomposites with CNT contents of (A) 3.19 wt. % (on 0.5 wt. % Co/Al_2O_3), (B) 7.39 wt. % (on 1.0 wt. % Co/ Al_2O_3), (C) 8.25 wt. % (on 2.0 wt. % Co/ Al_2O_3) and (D) 19.10 wt. % (on 4.0 wt. % Co/ Al_2O_3). The scale bar for each of these images is 1 μm.

To date, ball milling is the most effective and operative method in evenly dispersing CNT in metal matrix. However, it is reported that the violent crash led to the damage of CNT and worsen the properties of the composite. Thus, another competitive method: chemical vapour deposition was developed, which directly grew CNT on metal particles by catalysts. Zhang et al. [98] have prepared Al_2O_3-CNT composite material as depicted in Fig. 2. 15 This research demonstrates CVD method is very efficient and promising because it kept both the homogeneous dispersion and the intact structure of CNT in the metal matrix.

(c) Electrochemical deposition

Research into the preparation of CNT-MMC, by electrochemically co-deposition of CNT with metal particles from electrolytic solutions, has been investigated by some researchers, particularly as nano-composite coatings. The significant factor that affects the formation of thin composite coating is the evenly distribution of CNT in the bath and kept good suspension. Ball milling [99] and acid treatment [100] are employed to solve this problem. It has also been found that the content of CNT in composites is closely related to the frequency of current pulse [101].

C. Guo et al [101] electric-deposited carbon nanotubes and nickel onto carbon steel substrate and produced a roughly 37 μm thick of Ni-CNT coating. The plating parameters are listed in Table 2. 2. The researchers found that with increasing the current density, thicker and coarser Ni-CNT coating layers (as shown in Fig. 2. 16) were formed due to more Ni ions were reduced and deposited. However, the deposition rate of CNT in the plating bath was

relatively stable.

Table 2. 2 The synthesis parameters used in the electrical coating bath by C. Guo et al. [101].

Parameter		Value
Electrolyte	$NiSO_4$-$6H_2O$	280 g/L
	$NiCl_2$-$6H_2O$	35 g/L
	H_3BO_3	45 g/L
	CNT	0.3 g/L
Temperature		54 ±0.5 ℃
pH		4.0
Current density		2, 4, 8, and 12 A/dm^2
Deposition time		60 min

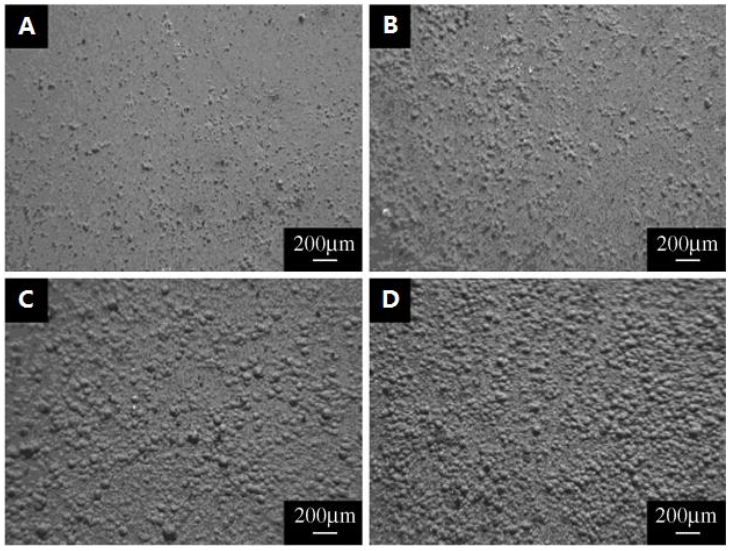


Fig. 2. 16 The surface morphology of Ni-CNT coating layers of different current density: (A) 2 A/dm^2, (B) 4 A/dm^2, (C) 8 A/dm^2 and (D) 12 A/dm^2.

(d) Molecular level mixing

Korean researchers S. I. Cha et al. [102], developed a novel ‘molecular level mixing’ technique to disperse 5.0 and 10.0 vol. % MWNT in copper oxide (CuO) powders and fabricated MWNT/Cu composite materials. This process includes the functionization and

dispersion of carbon nanotube in ethanol, mixing with Cu salt (copper acetate), ultrasonication promoting the attachment or integration of Cu ion with functional groups on the carbon nanotubes and drying (100-250 ℃, in air), calcination and reduction (250 ℃, hydrogen atmosphere, 3 h).

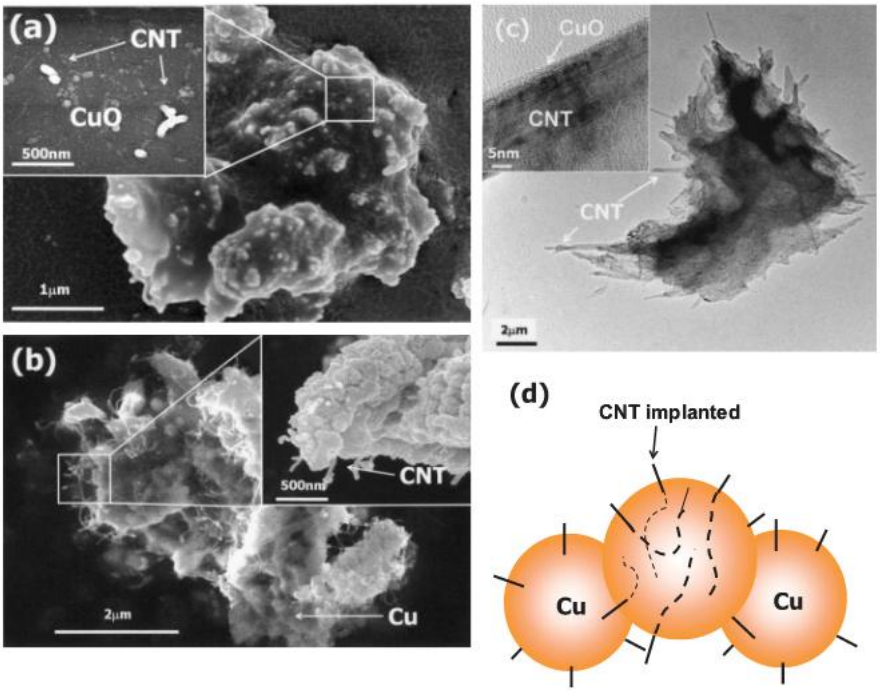


Fig. 2. 17 The individual carbon nanotube found on the surface of aluminium particles.

The SEM and TEM micrographs in Fig. 2. 17 clearly show the homogeneous distribution of MWNT in the CuO powders (which was reduced to Cu later after mixing). The TEM micrograph of polished bulk MWNT/Cu composite in Fig. 2. 17. (c) confirms the uniform dispersion of MWNT in copper matrix. Noticeably, the researchers implanted this molecular level mixing method to the fabrication of 0-1.8 vol. % CNT reinforced Al_2O_3 composite material. Although CNT agglomerates were observed on the fracture surface of the

composite. The Vickers hardness and fracture toughness were improved [103].

2. 4. 2. 3. 2. CNT-MMC composite consolidation

(a) Press and sinter route

The traditional sintering is the simplest method for producing CNT metal matrix composites, where Cu, Al and Mg based composites were produced. He et al. [104]. sintered a Al-5.0 wt. % CNT compact which was fabricated by chemical vapour deposited CNT on Al powders at 903 K for 0.5 h in the atmosphere of $CH_4/N_2/H_2$. The sintered Al-5.0 wt. % CNT composite showed a relatively high density of 96 % with the uniform distribution of CNT. Also, the pullouts and bridges of carbon nanotube revealed at the fracture surface were responsible for the improvement of 2.8 times and 4.3 times for tensile strength and hardness respectively over the pure aluminium powder.

(b) Equal-channel angular processing (ECAP)

Equal-channel angular processing (ECAP), one of novel severe plastic deformation techniques, has been successfully explored in the synthesis of CNT-Cu composite. In 2007, Quang et al. [105-107] have employed ECAP to produce Cu matrix composites with CNT content varying from 1.0 vol. % to 5.0 vol. %, which showed that CNT were much better uniformly dispersed in the metal matrix with the increasing passes through the channel. ECAP produced almost fully dense Cu-CNT composites with aligned CNT along the pressing direction. It is also found that the deformation caused by ECAP can damage the

perfect structure of CNT.

(c) Spark plasma sintering (SPS)

Spark plasma sintering (SPS) only take a few minutes to complete sintering rather than hours taken by conventional sintering. Due to the superior rapid heating rate of pulsed current, undesirable product can be avoided and nano-sized or nanostructure particles can be preserved. Liao et al. [36] reported a 0 - 2.0 wt. % MWNT enhanced Al-MMC fabricated by SPS at 500 °C with a holding time of 20 min under high vacuum (~10 Pa). Even though pores were detected in the composite marix as depicted in Fig. 2. 18, the density of the as-sintered samples reached around 95 %.

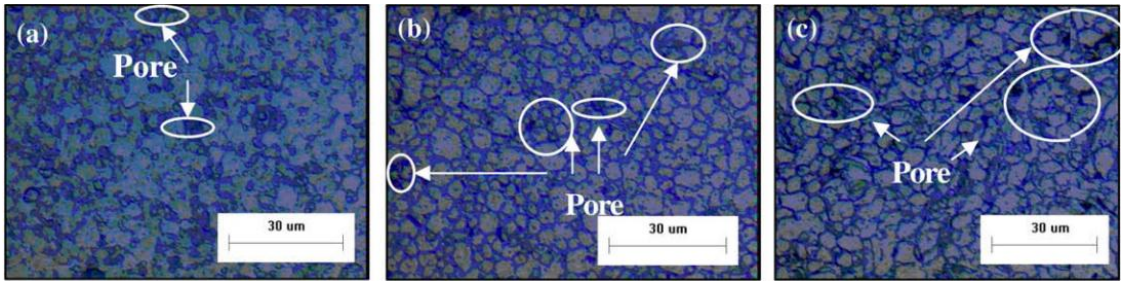


Fig. 2. 18 The microstructure of the SPSed (a) pure Al, (b) Al–0.5 wt. % MWNT, (c) Al–2.0 wt. % MWNT composite.

(d) Hot pressing

Hot pressing as a very promising densification technique is widely employed in the powder metallurgy field. Both compacted preform and loose powders can be easily shaped, consolidated and densified [108] under the high temperature and high pressure by particle deformation and rearrangement.

A. K. Shukla et al. [109] incorporated 5.0 and 10.0 vol. % MWNT (diameter: 15 ± 5 nm, length: 5 – 20 μm) and the same percentages of SWNT (diameter: < 2 nm) into copper (Cu) powders by high energy ball milling. The Cu-CNT mixture were mixed for 20 h at a speed of 200 rpm in argon atmosphere before they were consolidated under high vacuum (10^{-5} mbar) for 30 min at 700 ℃ with a constant stress of 30 MPa. It is measured that the relative density of all the as-produced bulk samples are over 95 % which is obviously benefit for the improvement of overall mechanical properties.

A. I. Rudskoy et al. [110] also used hot pressing to consolidate the mixture of aluminium powders (particle size: < 63 μm, purity: 99.5 wt. %) and in-situ grown carbon nanotubes. The Al-CNT mixture were pressed into pellets (diameter: 10 mm, height: 4 mm) at room temperature before being hot-pressed again at 480, 720 and 980 ℃ with a super high pressure of 5 GPa. The density of all the specimens were found exceeding 98 % of the theoretical value.

(e) Hot extrusion

Hot extrusion [111] have also been utilized in the manufacture of CNT-MMC but mainly as supplement processing. Liao et al. [36] extruded (500 ℃, extrusion ratio: 9:1, extrusion speed: 5 mm/s) the CNT-Al-MMC sample sintered by SPS, which presented a super high density of 99 %, comparing to only 95 % before hot extrusion. The alignment of CNT was also obtained after hot extrusion.

(f) Hot isostatic pressing (HIP)

Similar to hot pressing, hot isostatic pressing (HIP) technique employed high pressure and high temperature to optimize the density and properties of conventional materials. But the pressure and high temperature used in HIP process is much higher which can reach 310 MPa and more than 1350 ℃ respectively. More importantly, the stress applied to the material in HIP comes from every direction that makes the material shrink in a uniform way.

S. F. Bartolucci et al. [112] fabricated a carbon nanotube reinforced aluminium nano-composite by combining ball milling and HIP. 1.0 wt. % MWNT (diameter: < 15 nm, length: < 15-20 μm), 99.0 wt. % aluminium powders (particle size: < 22 μm) and 2.0 wt. % stearic acid were ball-milled by a high energy attritor for 1 h. Then the "as-milled" powders were HIPed at 375 ℃ for 20 min and the as-HIPed sample was near 100 % theoretical density as measured by Archimedes method. Similarly, J. Stein et al. [113] HIPed the ball milled mixture of 2.0 wt. % MWNT (diameter: 13-16 nm, length: 1-10 μm, purity: 98 wt. %) – AA5XXX (the detailed trademark was concealed by the authors) powder and achieved an over 99 % relative density.

(g) Stir casting

Casting is the most widely employed method in manufacturing bulk MMC materials in large scale. However, it is less effective in the fabrication of CNT-MMC due to the poor wettability of CNT with metal and the difficulty of evenly dispersing CNT in metal matrix. C.S. Goh et al. [114, 115] melted magnesium (Mg) and stirred with 0 – 2.0 wt. % carbon

nanotube by a twin blade impeller (mild steel with oxides coating to avoid iron contamination, 450 rpm, 5 min) at 750 ℃ in argon atmosphere. Although the hardness, ultimate tensile strength and ductility were increased by the addition of carbon naotube, the agglomerates of carbon nanotube were found in the as-casted magnesium.

(h) Compocasting

According to B. Abbasipour et al. [96, 97], an enhanced compocasting apparatus was developed and the schematically experimental set-up is showed in Fig. 2. 19. Instead of adding carbon nanotubes directly into the molten metal like other researchers, B. Abbasipour et al. deposited carbon nanotubes on the aluminium particles by Ni-P electroless plating to form Ni-P-CNT coatings on the surface of aluminium to reduce the agglomerates of CNT as well as improve the wettability between CNT and aluminium prior to the mixing and casting. To further enhance the interfacial wetting between aluminium and carbon nanotube, 1.0 wt. % magnesium was also added into the melt. The CNT coated aluminium particles were injected into the 1.0 wt. % Mg – Al melt at a constant temperature of 700 ℃ while being stirred at 500 rpm. The researchers found that with the addition of carbon nanotube, the equivalent diameter of grain size was much smaller and the density of the composite was reduced. No information of the distribution of carbon nanotube in the composite materials is given in the paper. Similarly, some other researchers employed nickel coating on carbon or graphite reinforcement to improve its wettability with aluminium and magnesium [116-118] , which led to the improvement of mechanical properties in the carbon nanotube reinforced metal composite.

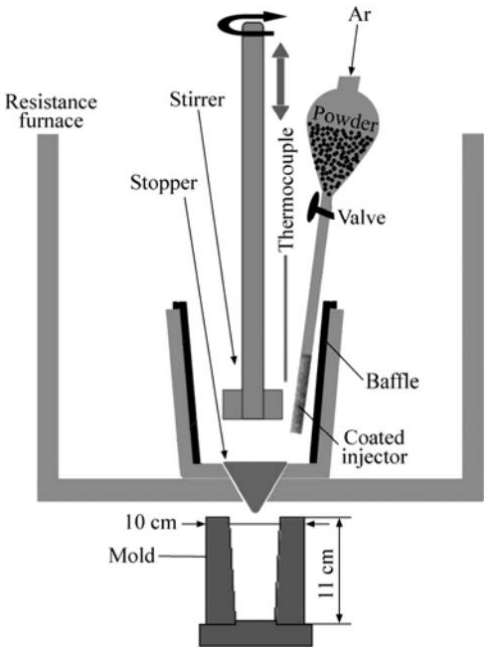


Fig. 2. 19 The schematic diagram of the apparatus used by B. Abbasipour et al. [96, 97].

(i) Melt Infiltration

Melt infiltration [119], as an very effective method of fabricating composite materials, is also employed by researchers to incorporate carbon nanotube into metal matrix. Fig 2. 4. 2. 3. 2. 3. (A) explained the mechanism of this technique schematically. Firstly, a porous solid structure (preform) with dispersed reinforcement needs to be prepared. Then a metal or alloy of lower melting point would be melt and the liquid phase would fill the pores of the porous solid to fabricate a dense composite.

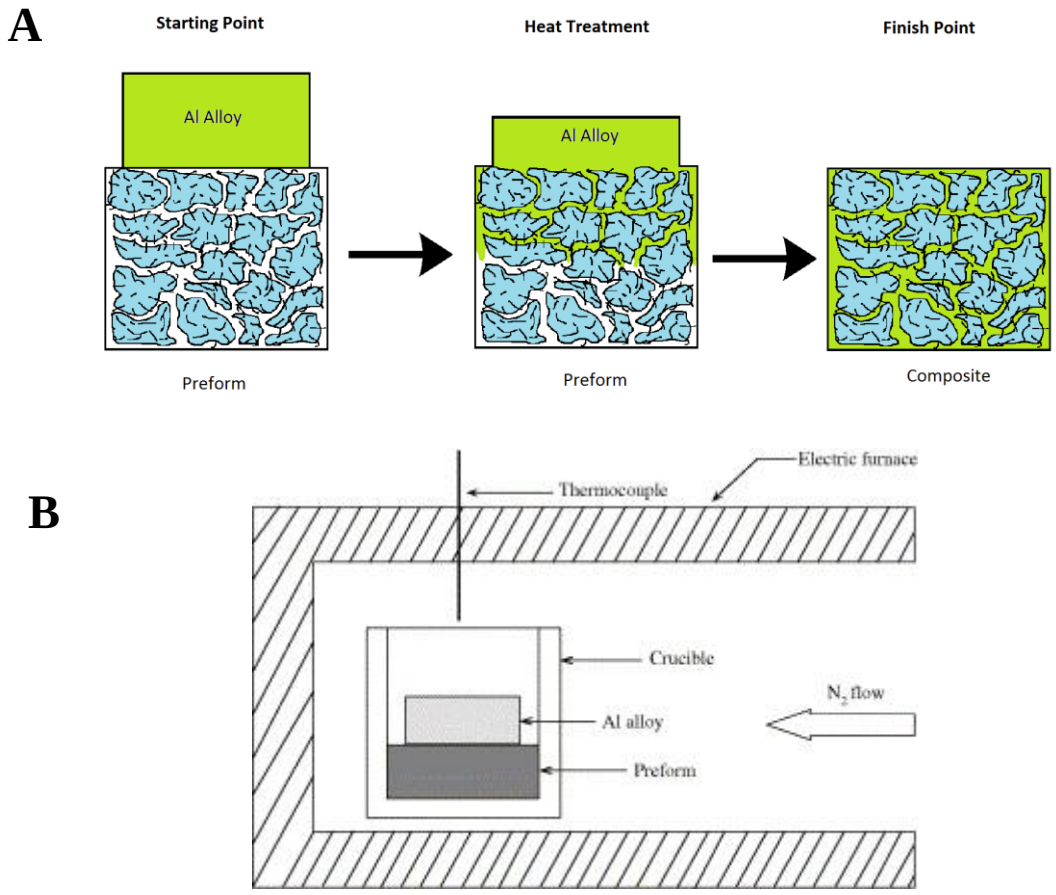


Fig. 2. 20 (A) The mechanism of melt infiltration; (B) The apparatus used by S.M. Zhou et al. [95] in their preparation of CNT/Al composite by melt infiltration method.

The most obvious advantages of this technique are that the high concentration of reinforcement was successfully incorporated into the matrix and the product after infiltration did not need extra machining. The critical procedure of obtaining a dense bulk material with uniform distribution of reinforcement is the control of infiltration parameters and the dispersion of reinforcement in the preform.

S. M. Zhou et al. [95] fabricated aluminium composites reinforced with CNT by pressureless infiltration method. In their experiment, multi-walled carbon nanotube of 0 – 20 vol. % was

added into a mixture of Mg (average particle size: 74 μm) and Al (average particle size: 100 μm) powders of a mass ratio of 2:7. The CNT, Mg and Al powders were then ball milled for 7 h in argon atmosphere at a speed of 300 rpm and the as-mixed composite powders were compacted into pellets (Ø 70 mm, thickness: 15 mm). Afterwards, Al alloy (commercial trademark LY12) was put on the top of the pellet as shown in Fig. 2. 20. (B) and heat treated in nitrogen atmosphere at 800 ℃ for 5 h. The researchers found that the presence of Mg in the mixture and the use of nitrogen gas are essential for the preparation of a dense bulk material, since Mg is quite active and prone to react with Al_2O_3 and residual O_2 to break the oxide layer. Nitrogen could react with both Al and Mg to promote the densification of the preform. The dispersion of carbon nanotube in the matrix was found homogeneous but the length of carbon nanotube was found to be seriously shortened after ball milling.

(j) Plasma spraying

Plasma spray technique was used by T. Laha et al. [94] to fabricate carbon nanotube reinforced aluminium composite materials (the schematic diagram of the plasma spray process is presented in the Fig. 2. 21). In their endeavour, spherical 23 wt. % Si-Al prealloyed powder (size: 15-45 μm) was employed due to the better followability of spherical shape of particles and relatively easiness of melting of small particle size during the continuous spray process. In order to achieve a uniform distribution, 10 wt. % carbon nanotubes (diameter: 40-70 nm, length: 0.5-2.0 μm) was ball milled with Al-Si powders for 48 h prior to the plasma spray process. The as-mixed composite powder was plasma sprayed by using argon and helium as carrier gas with a gun voltage and current of 35 V and 800 A

respectively. The 0.3 mm coating was moved off by quenched the deposition and 6061 Al spray holder into liquid carbon dioxide.

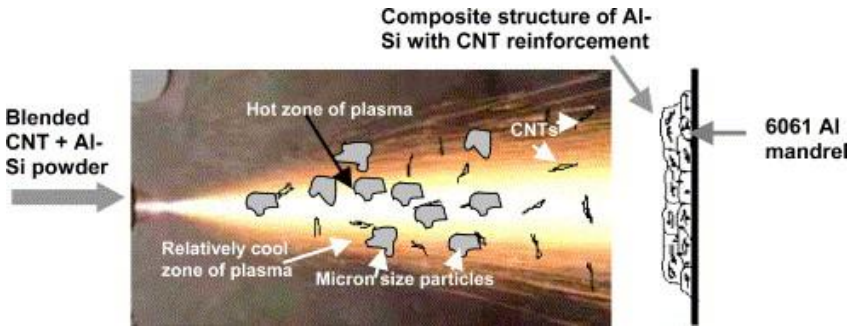


Fig. 2. 21 Schematic of plasma spray of 10 wt. % CNT-Si-Al composite powders.

Similar to the melt infiltration method, the homogenous distribution of carbon nanotube in the aluminium composite produced by plasma spray mainly rely on the mixing of Al-Si powders and carbon nanotube prior to the spray process. The characterization of composite coating revealed that the agglomerates of carbon nanotube existed both in the "as-milled" composite powders and as-sprayed coating layer (Fig. 2. 22). Also, some loosely bounded carbon nanotubes were blew off from the Al-Si particles and flied away from the target as shown in Fig. 2. 21. Moreover, the Raman spectrum of as-sprayed composite indicated the damage of carbon nanotube which is due to the high temperature (10,000 – 15,000 K) of plasma and high pressure in the process that may melt CNT or transfer carbon nanotube into other carbon allotrope like graphite, diamond or amorphous carbon.

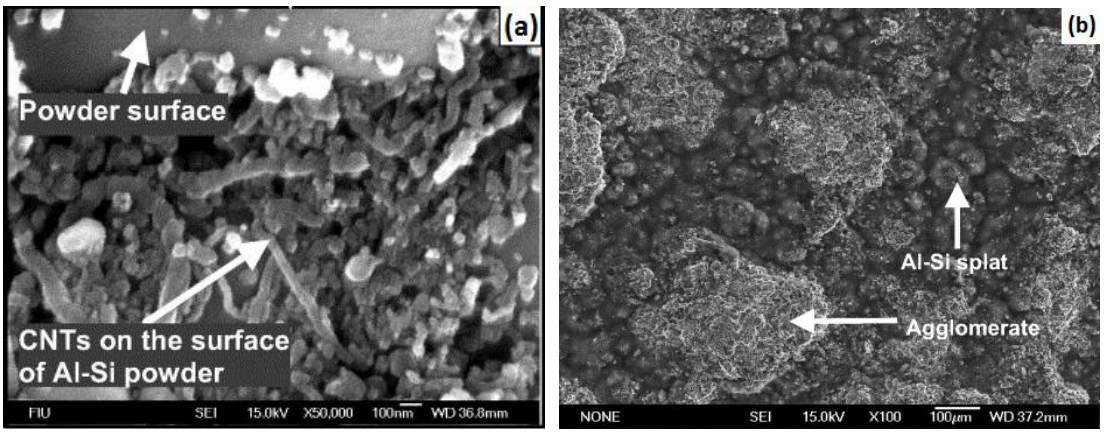


Fig. 2. 22 The SEM images of agglomerates of carbon nanotube found in (a) "as-milled" Al-Si powders and (b) as-sprayed Al-Si composite.

2. 4. 2. 3. 3. Mechanical properties of carbon nanotube/metal composites

(a) Hardness

According to S. F. Bartolucci et al. [112], 1.0 wt. % MWNT reinforced aluminium composite was fabricated by ball milling, then hot isostatic pressing and hot extrusion. The Vickers hardness of as-HIPed-and-extruded Al – 1.0 wt. % MWNT reached to 102 ± 1 Hv while that of the as-HIPed-and-extruded pure Al is 96 ± 7 Hv.

J. Z. Liao et al. [32, 36] employed high energy ball milling (milling time: 4 h, speed: 200 rpm, 2.0 wt. % stearic acid) to disperse carbon nanotube (diameter: 60-100 nm, length: 5-15 μm and purity ＞ 95 %) into aluminium powders (particle size: 5 μm, purity: 99.22 %). Al-0.5 wt. % CNT composite material was consolidated by spark plasma sintering and followed by hot extrusion. The as-produced Al-0.5 wt. % CNT composite has a Vickers

micro-hardness of 58 Hv which is 21 % higher than the value of pure Al (48 Hv) that experienced the same processing.

(b) Tensile strength

Tensile strength, as a very important engineering index, represents the maximum stress that the material can withstand before structural failure. B. Boesl et al. [120] prepared a 1.0 wt. % multi-walled carbon nanotube (diameter: 10-30 nm, length: 25-30 μm) reinforced aluminium composite by wet-mixing in acetone for 2 h and spark plasma sintering in vacuum at 500 ℃ and 80 MPa for 1 h with a heating rate of 50-60 ℃/min. An advanced in situ tensile test was conducted inside the chamber of scanning electron microscope. The tensile test result is shown in Fig. 2. 23. As measured in the experiment that the Al-1.0 wt. % MWNT showed 40 % higher tensile strength than the unreinforced Al specimen.

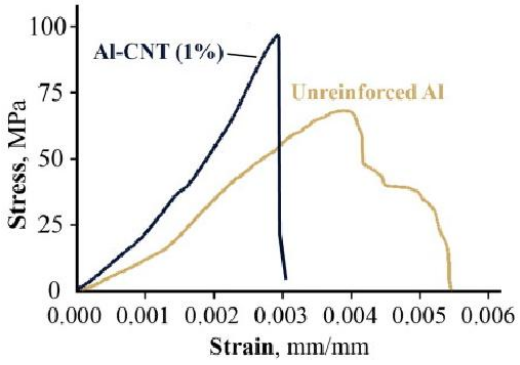


Fig. 2. 23 The strain-stress curves of pure Al and Al-1.0 wt. % MWNT composites.

X. D. Yang et al. [30] developed an approach to produce Al-CNT composite by growing carbon nanotube on the surfaces of Al powders by chemical vapour deposition (CVD) and then ball milling the composite powder to homogenise the distribution of CNT before

compaction, sintering and hot extrusion. The schematic diagram of the production process is depicted in Fig. 2. 24.

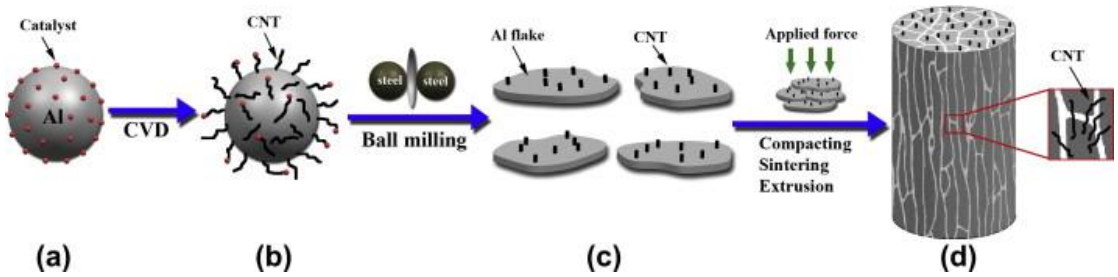


Fig. 2. 24 The schematic diagram of the fabrication process developed by X. D. Yang et al. [30]

The comparison between the tensile strength of the CNT/Al composite produced by Yang et al. and that fabricated by other researchers is presented in Table 2. 3. As can be seen that with the addition of 2.5 wt. % of carbon nanotube, the yield strength of the CNT/Al composite produced by Yang et al. enhanced from 159 MPa for the un-reinforced Al bulk material to 276 MPa (increased by 73.58 %) and the ultimate tensile strength is increased from 220 MPa to 334 MPa with an improvement of 51.82 %. The tensile strength of CNT/Al composite fabricated by other researchers are also listed in the Table 2. 3. It is obvious that the tensile strength of the composite with the addition of carbon nanotube enhanced significantly comparing to the strength of pure aluminium materials.

Table 2. 3 The properties comparison between the Al-CNT composites prepared by different approaches.

Reference	Composite processing technique	CNT content (wt. %)	Yield strength (MPa)	Ultimate tensile strength (MPa)	Elongation (%)
Yang et al. [30]	In situ CVD synthesis, milled for 90 min, sintering and hot extrusion	0	159	220	21.6
		2.5	276	334	17.9
Liao et al. [36]	Blended by can rolling, spark plasma sintering and hot extrusion	2	88	160	35
Esawi et al. [121]	Milled for 30 min, compacted and hot extrusion	2	–	254	–
Pérez-Bustamante et al. [122]	Milled for 300 min, vacuum sintering and hot extrusion	2	180	252	15.6
Esawi et al. [111]	Milled for 360 min, compacted and hot extrusion	2	–	348	7.9
Kwon et al. [20, 123]	Nanoscale dispersion, spark plasma sintering and hot extrusion	3.4	–	194	10.1

(c) Compressive strength

Compressive strength reveals the capability of materials withstand load before crushing and shattering which is critical for material selection and structure projection. However, a limited amount of research work on the compressive resistance of carbon nanotube reinforced metal composite has been published so far.

M. Jafari et al. [35] compared the microstructure and properties of the ball-milled and sintered Al2024 alloy and Al2024-1~3 vol. % MWNT composite. Both the Al2024 pre-alloyed powders and Al2024-MWNT mixtures were ball milled for 30 h at a speed of 500 rpm with 0.5 wt. % stearic acid as process control agent (PCA). The ball milled powders were subject to hot pressing at optimized pressing condition (500 ℃, 250 MPa and 30 min). The stress-strain profile of the compression test of the as-produced specimens is shown in Fig. 2. 25. As can be seen from the diagram that the compressive strength of nano-structured Al2024 alloy is 712 MPa while this of 1.0 vol. % MWNT and 2.0 vol. % MWNT reinforced Al2024 composites were remarkably improved to 740 and 810 MPa. However, when the loading of MWNT increased to 3 vol. %, the Al2024-3 vol. % MWNT composite displayed a brittle behaviour in the compression test. This is due to the agglomeration of MWNT in the metal matrix which impeded the densification process, accommodating the composite with more pores and lower density [35].

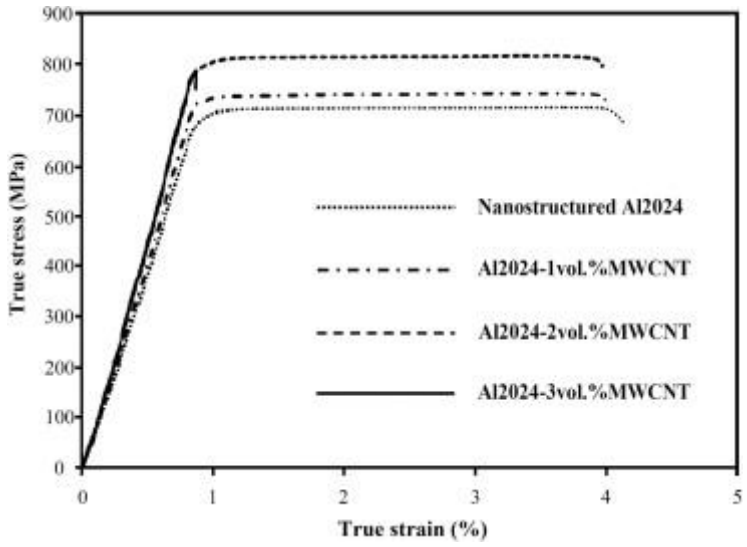


Fig. 2. 25 The stress-strain profile of the specimens produced by M. Jafari et al. [35].

T. Noguchi et al. [124] produced 0.8 vol. % and 1.6 vol. % MWNT reinforced Al composites by Nano-Scale Dispersion (NSD) method. In their study, 500 g of aluminium powders of 99.85 % purity and an average particle size of 28 μm, 10 g of magnesium powders of 99.8 % purity and an average particle size of 45 μm, 100 g of natural rubber and 10 g or 20 g of MWNT were mixed to form a precursor. Then the precursor was warm compacted at 800 ℃ for 1 h in nitrogen atmosphere. The as-produced composite was subject to compression test and the researchers found that with 1.6 vol. % loading of MWNTs, the compressive stress was strengthened sevenfold and reached to around 240 MPa.

2. 4. 2. 3. 4. Other properties of carbon nanotube/metal composites

(a) Electrical conductivity

Z. Y. Liu et al. [66] investigated the electrical properties of carbon nanotube reinforced aluminium matrix composite produced by powder metallurgy method. In their study, 1.5 vol. % carbon nanotube (diameter: 10-20 nm, length: ＜5 μm) and aluminium powders (particle size: ＜10 μm, purity: 99.8 %) were blended in a bi-axis mixer at 60 rpm for continuously 8 h with a ball to powder ratio of 1:1. The mixed powders were degassed in vacuum, hot pressed at 580 ℃ for 1 h and hot forged at 450 ℃. Unexpectedly, the electrical conductivity of the as-fabricated 1.5 vol. % carbon nanotube reinforced aluminium composite was poorer than that of the pure aluminium matrix. The reason for this phenomenon is the non-orientated distribution of carbon nanotube in the matrix could not assist the electrons efficiently transport towards the same direction. Also, the electron

diffraction at the Al/CNT interface worsened the electrical performance of the composite. Similar results were obtained and published by other researchers which are listed in Table 2. 4. Thus, it is deemed that the orientation of carbon nanotube in the matrix and the interface between carbon nanotube and matrix is critical to the electrical capability of the composite.

Table 2. 4 The electrical conductivity of Al/CNT composites fabricated by different techniques.

Reference	Matrix	CNT (vol. %)	Electrical conductivity (MS/m)
Z. Y. Liu et al. [66]	Al	0(FSP	33.9
		1.5(FSP	32.1
		1.5(Forged)	32.5
C. L. Xu et al. [33]	Al	0	29.4
		1.5	20.4
		6	15.2
Y. Feng et al. [125]	Ag	0	64.5
		2	55.5
		4	50
S. M. Uddin et al. [126]	Cu	0	59
		0.15	50
		0.6	45
		3	20
W. M. Daoush [127]	Cu	0	54.2
		5	45.7

(b) Thermal conductivity

J. H. Wu et al. [128] added 0 ~ 5.0 wt. % carbon nanotube into aluminium matrix and the thermal conductivity was measured. In the study, the researchers dispersed carbon nanotube (diameter: 20-30 nm, length: 10-30 μm) and Al powders (particle size: 3-5 μm) in ethanol, ultrasonicated for 30 min, stirred for 1 h and dried at 120 ℃ for 2 h. The mixture was then

consolidated by spark plasma sintering at 580 ℃ and 40 MPa for 10 min. The thermal conductivity of the Al-CNT composite of different CNT concentration is displayed in Fig. 2. 26. As can be seen that with 0.5 and 1.0 wt. % of carbon nanotube loading, the thermal conductivity increased from 185 W/m/K for the pure Al specimen to 199 and 193 W/m/K, respectively. However, further increasing the concentration of carbon nanotube in the aluminium matrix led to the deterioration of thermal properties.

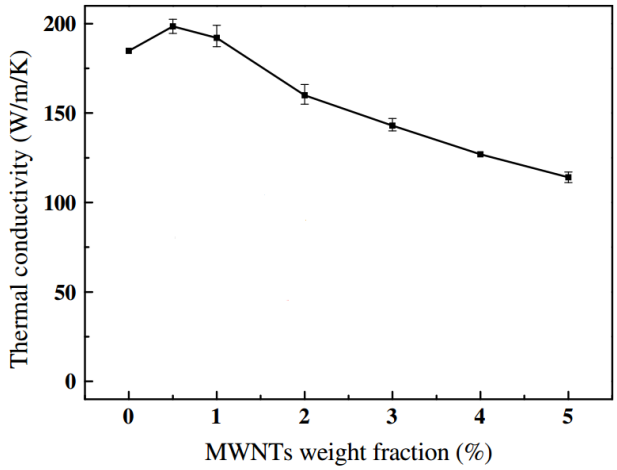


Fig. 2. 26 The thermal conductivity of CNT/Al composite as a function of the loading of carbon nanotubes.

S. Yamanaka et al. [129], S. Cho et al. [130] and K. Chu et al. [131] also reported analogous trend in their papers. J. H. Wu et al. [128] stated that the thermal performance degradation of the Al-CNT composite is due to the agglomeration of carbon nanotube as well as the thermal resistance at the interface. Clusters of carbon nanotube were clearly observed in the composite which is displayed in Fig. 2. 27. According to another paper published by the same group [132] the CNT agglomerates only possessed one third of the thermal

conductivity of the single carbon nanotube. Also, the existed carbon nanotube bundles increased the porosity and lowered the density of the composite. The accumulated pores scattered phonons and the gas phase in the pores has poorer thermal conductivity, thus the interfacial thermal resistance is increased.

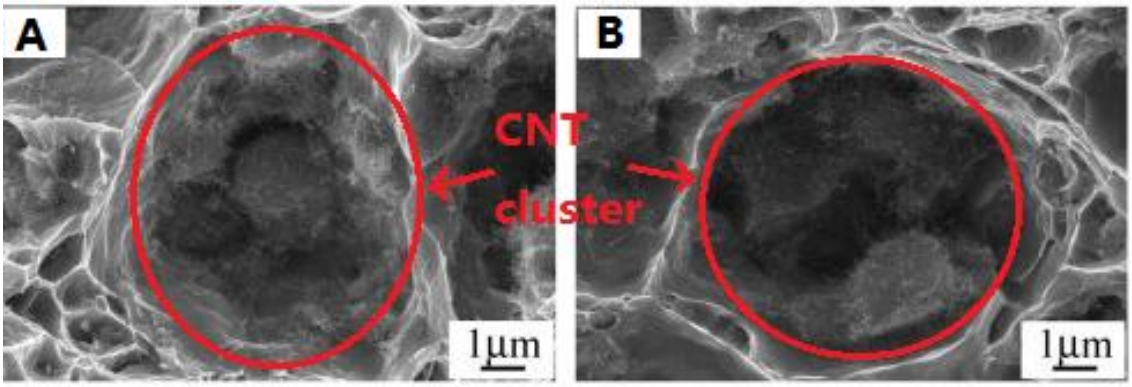


Fig. 2. 27 The SEM images of the fracture surface of CNT/Al composite: (A) 3.0 wt. % MWNT, (B) 5.0 wt. % MWNT.

2. 4. 2. 3. 5. CNT reinforced aluminium metal matrix composites

In the recent decade, great deals of research were carried out to incorporate CNT into metal matrix, especially Al matrix due to its low density and high strength-weight ratio. The introduction of CNT into Al matrix is focused on improving mechanical properties, such as strength and stiffness, while keeping lightweight.

To date, most of the Al-CNT composites fabricated by powder metallurgy method achieved dramatically enhancement in stiffness and strength. In 1998, Kuzumaki et al. [31] reported a

100% improvement in the tensile strength by adding 10 vol.% CNT into aluminium matrix. In the study of R. George et al. [133], both MWNT and SWNT were used in reinforcing aluminium, where their results showed that the Young's modulus of the composites increased by 12 % and 23 % with 0.5 vol.% and 2 vol.% addition of MWNT, respectively. However, the Al-SWNT composite with the same volume fraction of the reinforcement did not display a considerable increase in Young's modulus. On the contrary, the systematic study conducted by Esawi and Morsi [111] fabricated an Al-2.0 wt. % MWNT composite which presented a deterioration in both hardness and indentation modulus compared to pure aluminium due to the poor bonding between CNT and Al matrix.

Al-CNT composites manufactured by other routes also achieved positive results. He et al. [104] synthesized 6.5 vol. % CNT reinforced aluminium composites via chemical vapour deposition (CVD) method which obtained 184 % increase in tensile strength and 333 % increase in hardness. Deng et al. [134] made the Al-1.0 and 2.0 wt. % CNT composite by hot extrusion, in which the high temperature and high pressure promoted the formation of Al_4C_3. A desirable high density (98.4 %) and CNT pullouts in the Al-1.0 wt% CNT specimen was achieved whereas clusters and interfacial bonding was observed in the Al-2.0 wt. % CNT composite.

In summary, a lot of promising results were obtained in the fabrication of carbon nanotube reinforced aluminium composite materials, however, there is still a wide scope for the future work. The key issues are (1) the homogeneous distribution of CNT in matrix; (2) the

enhancement of interfacial bonding between CNT and aluminium; (3) the reaction between Al and carbon nanotube to form Al_4C_3; (4) the protection of CNT structure during processing.

2. 4. 3. Strengthening mechanism

The major aim of incorporating CNT into metal matrix is to achieve better mechanical properties such as higher tensile strength, stiffness and hardness in the bulk composites. Although the mechanism of CNT reinforced metal matrix is not yet clear, several possible models have been built by experienced experts, which are presented in the following sections.

2. 4. 3. 1. Grain refinement strengthening

Grain boundaries impede the movement of dislocation. It would require more energy for dislocation to traverse grain boundaries and further propagation, especially if the existed grain boundaries are randomly orientated. For a certain material and an applied pressure, smaller grain size provides more grain boundaries and the stress distributes on each grain is reduced. Thus, it demands more stress for the dislocation to penetrate the material, which improve the yield strength of materials [135]. The inversely proportional relationship of yield strength and grain size is denoted by the Hall-Patch equation [136] which is shown as follows:

$$\sigma_y = \sigma_i + K_y/\sqrt{D} \qquad (2.\,4.\,3.\,1.\,1)$$

where σ_y and σ_i are the yield stress and friction stress respectively, K_y is the Petch parameter and D is the grain size.

C. R. Bradbury et al. [70] ball milled 1.0 ~ 9.0 wt. % MWNT with elemental aluminium powders to produce Al-MWNT composite powders, which were then compacted at 570 MPa and extruded at 500 ℃. The hardness of the as-extruded composite was found increased with the reduction of grain size according to the Hall-Petch equation. D. Poirier et al. [137] ball milled 10 vol. % MWNT (diameter: 10-30 nm length: 0.5-50 μm) and aluminium powders (particle size: 7-15 μm, purity: 99.5 %) for 2 h and 5 h. The crystalline size of the composite powders was calculated by William-Hall equation based on the XRD patterns [138]. It is found that the grain size reached only 190 nm and 40 nm for the 2 h-milled and 4 h-milled powders respectively. The Vickers micro-hardness of the Al-10 vol. % MWNT composite powders were measured to be 168 ± 10 and 329 ± 11 after 2 h and 5 h milling respectively, under the effect of grain refinement strengthening.

2. 4. 3. 2. Dislocation strengthening

The work hardening happened in the ball milling process which would introduce more defects, vacancies and dislocations into the materials. Hence, the dislocation density increases and the average distance between each dislocation are shortened. Simultaneously, the dislocation generates stress field around themselves which would act as barriers to slow down or stop the motion of dislocation in the matrix, thus improve the yield strength of the

material. C. S. Goh et al. [139, 140], S. K. Thakur et al. [141] and S. M. L. Nai et al. [142] reported the addition of carbon nanotube into the soft metal matrix and increased the density of dislocations especially at the vicinity of carbon nanotube. C. S. Goh et al. [139, 140] also concluded that the strain in the matrix increased with increasing carbon nanotube concentration.

2. 4. 3. 3. Thermal mismatch strengthening

According to R. Geogre et al. [133], a thermal mismatch strengthening mechanism was proposed based on the Arsenault's reinforcing theory [143] for the Al-SiC composite. They considered the thermal expansion coefficients of carbon nanotube and aluminium are up to $10^{-6}\,K^{-1}$ and $23.6 \times 10^{-6}\,K^{-1}$ respectively. Obviously, there is a severe thermal expansion mismatch between carbon nanotube and aluminium, which is more pronouncedly exhibited when the temperature changes significantly. Especially, in the consolidation (heating and cooling cycle) of carbon nanotube reinforced metal composite, the vibration frequency and amplitude of carbon and aluminium atoms are different, thus stress fields are formed at the interfaces and more strain are induced into the matrix. Consequently, the dislocation density in the composite matrix is increased and they are beneficial for the obstruction of the propagation of dislocation and leads to the increase of yield strength. What's also worth noticing is that the thermal mismatch happens at the interface of matrix and reinforcement, since the carbon nanotube are in nano-scale, the metal-CNT composite tends to have more interfaces than the traditional coarse particles reinforced materials and in turn they possesses more dislocations and higher yield strength.

2. 4. 3. 4. Orowan loop strengthening

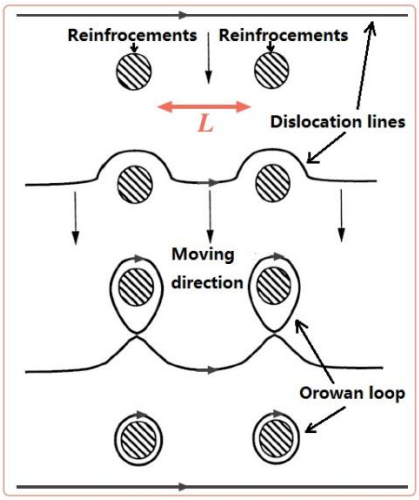


Fig. 2. 28 The schematic diagram of the pinning effect of reinforcements and the formation of Orowan loop.

R. Geogre et al. [133] and D. Lahiri et al. [144] reported an Orowan looping strengthening mechanism that considered the dispersed carbon nanotubes as pinning points which bend the moving lines of dislocations and resist the propagation of dislocations as shown in the schematic diagram in Fig. 2. 28. Also, the bypassed dislocations would leave dislocation loops (namely: Orowan loop) around the reinforcements which increase the difficulties for the following dislocations to traverse the Orowan loop encircled dispersolids or nano fibres.

2. 4. 3. 5. Load transfer strengthening

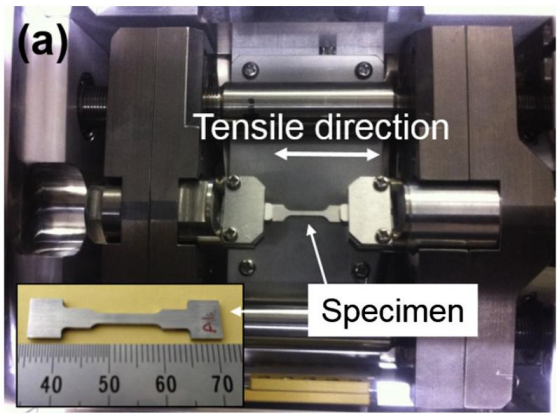


Fig. 2. 29 The configuration of the tensile specimen of the in situ tensile stage.

B. Chen et al. [145] conducted an advanced in situ observation of tensile test and studied the load transfer strengthening mechanism of Al-MWNT composite. The composite used in the experiment was 0.6 wt. % MWNT (diameter: up to 100 nm) reinforced aluminium powders (particle size: up to 150 μm, purity: 99.9 %) fabricated by ball milling (Al_2O_3 ball bearings, ball to powder ratio: 10 to 1, milling time: 4 h) and sparking plasma sintering (temperature: 550 ℃, pressure: 30 MPa, atmosphere: vacuum at 5 Pa, holding time: 30 min) followed by hot extrusion (temperature: 500 ℃, atmosphere: argon, ram speed: 0.5 mm/s and extrusion ratio: 12 to 1). The dog bone tensile specimen was machined from the as-prepared composite and the inset in the Fig. 2. 29 showed its configuration. In-situ tensile test was performed inside the vacuum chamber of a field emission scanning electron microscopy (FE-SEM, JEOL, JEM-6500F). The test was deliberately paused after certain periods of time in order to capture the actual dynamic fracture process. The evolution of carbon nanotube during the test is displayed in Fig. 2. 30.

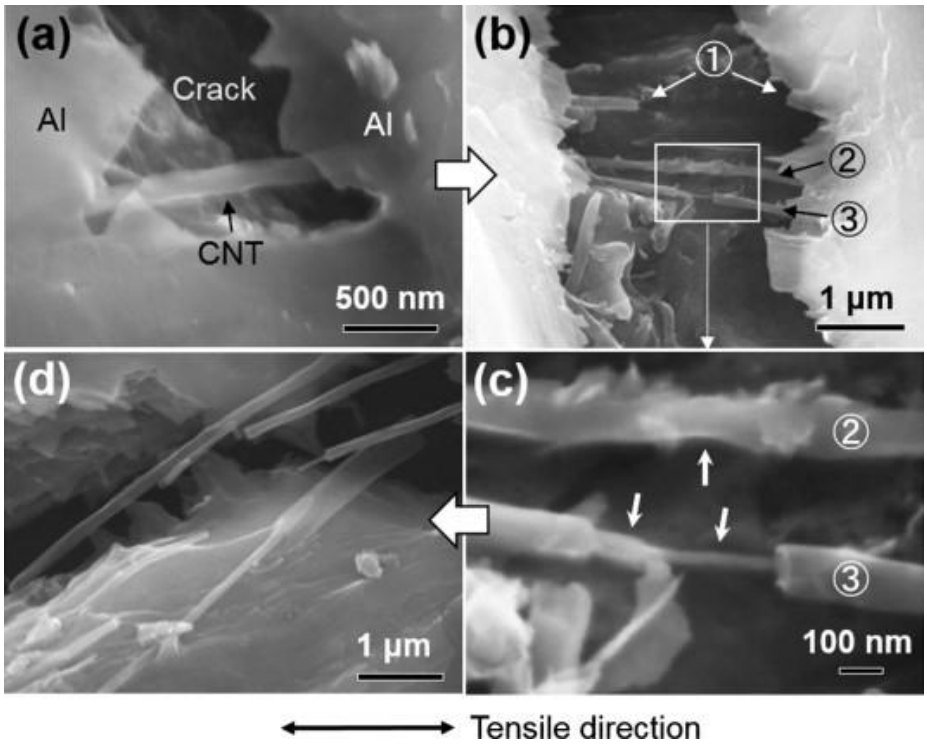


Fig. 2. 30 The in situ FE-SEM images of Al-MWNT composite under tensile test.

As can be seen from Fig. 2. 30. (a), an individual carbon nanotube (as point out by the black arrow) was found to bridge the split materials parts, which is vertical to the direction of crack develop. This is the direct evidence of the load transfer between carbon nanotube and aluminium matrix. Since the tensile strength of carbon nanotube is much higher than that of aluminium, the force of pulling managed to break the aluminium structure but when it encounter the tough carbon nanotube, the rate of crack propagation is slowed down or stopped. Therefore, higher energy or longer time of pulling is required in order to break the Al-MWNT composite. Similar bridging phenomena are also observed by other researchers like Z. Xia et al. [146] and B. Boesl et al. [120].

Further increase the force of pulling, some carbon nanotubes were noticed to be peeled off

and the inner tubes of small diameter were exposed which are presented in Fig. 2. 30. (b) to (d). K. T. Lau [147] simulated the fracture of fibrous reinforcements and found that the structural damage starts from the outermost layers of fibrous phase which is consistent with the observation of B. Chen et al. [145]. Besides, Cox [148] in 1952 built a shear lag model to explain the load transfer from matrix to the reinforcement by interfacial stress along the interface. It is envisaged that the contact surfaces between matrix and reinforcements are first under strain. Evidently, the carbon nanotube in the Fig. 2. 30. (c) and Fig. 2. 30. (d) displayed the slough of outer layers and the naked inner layer after breakage respectively, which support the hypothesis of Cox [148].

The shear lag model was employed by Kelly-Tyson [149] for the strength prediction of short fibre reinforced metal composites. It is estimated that when the length (l) of CNT is shorter than the critical length (l_c) that the strength of the CNT reinforced composite can be calculated by the equation:

$$\sigma_{\text{composite}} = \sigma_{\text{fibre}} V_{\text{f}} (\frac{l}{l_{\text{c}}}) + (1 - V_{\text{f}}) \sigma_{\text{matrix}} \qquad (2.\ 4.\ 3.\ 5.\ 1)$$

where the $\sigma_{\text{composite}}$ is the composite strength, $\sigma_{\text{fibre}}$is the CNT strength, σ_{matrix} is the matrix strength, V_{f} is the volume friction of CNT in the matrix, and l_c is given by:

$$l_{\text{c}} = \frac{\sigma_{\text{fibre}} d_{\text{fibre}}}{2\tau_{\text{matrix}}} \qquad (2.\ 4.\ 3.\ 5.\ 2)$$

Where d_{fibre} is the average diameter of the CNT and τ_{matrix} is the shear strength of

matrix ($\approx 0.5\ _{\text{matrix}}$).

H. J. Choi et al. [149] calculated the strength for the Al-4.0 vol. % MWNT composite, which is 434 MPa and 391 MPa for the 70 nm and 200 nm grain size materials respectively. The experimentally measured strength values are up to 403 MPa and 323 MPa, which are very close to the estimated values by the Kelly-Tyson equation.

2. 4. 4. Challenges

2. 4. 4. 1. Agglomeration and dispersion of carbon nanotube in matrix

The most critical challenge in manufacturing Al-CNT composites (also common in the CNT reinforced ceramic and polymer system) is the agglomeration and dispersion of CNT in the matrix, which results from the intricate entanglements of long and smooth CNT and the strong van der Waals forces of attraction between CNT. The mechanical properties of carbon nanotube metal matrix composite such as tensile strength, Young's modulus and hardness are directly related to the dispersion of reinforcements in the metal matrix. Thus, the homogeneous distribution of CNT in the matrix is indispensable in uniformly translating the superior characteristics of CNT into composite matrix. Agglomeration and clustering of CNT in the composite will lead to the deterioration of the overall mechanical properties. Especially when it comes to the incorporation of higher loading of carbon nanotube into the matrix, the dispersion problem is more pronounced.

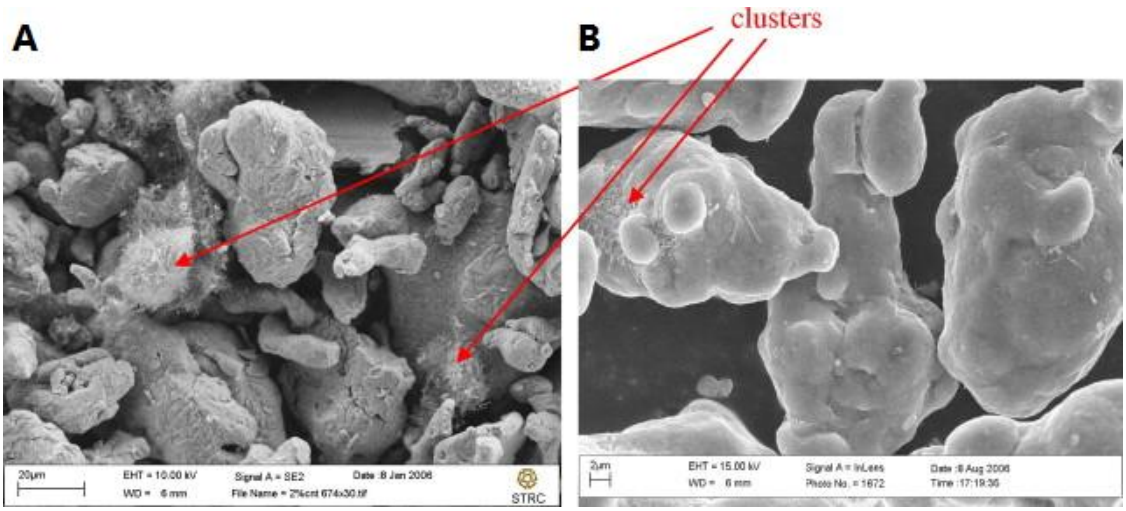


Fig. 2. 31 The SEM micrographs of carbon nanotube agglomerates found in the (A) tubular shake-mixed at 46 rpm and (B) ball milled at 300 rpm Al-2.0 wt. % MWNT composite powders.

A. M. K. Esawi and M. A. E. Borady [28] employed both turbula shaker-mixer (speed: 46 rpm, time: 5 h) and planetary ball mill (speed: 300 rpm, time: 5 h) to disperse 0.5, 1.0 and 2.0 wt. % of carbon nanotube (diameter: 140 nm, length: 3-4 μm) into aluminium (particle size: up to 75 μm) powders. After mixing, carbon nanotube agglomerates were found in both powder groups with 2.0 wt. % CNT as indicated by red arrows in the Fig. 2. 31.

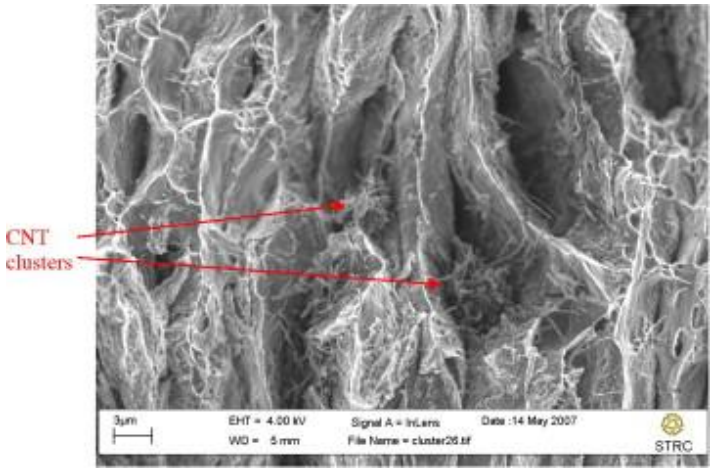


Fig. 2. 32 CNT agglomerates found on the fracture surface of the ball-milled and hot-rolled Al-1.0 wt. % CNT.

The carbon nanotube clusters were also observed in the fracture surface of the ball-milled and hot-rolled Al-1.0 wt. % CNT which is shown in Fig. 2. 32. The stress-strain profiles of the as-produced bulk Al-CNT composite are presented in Fig. 2. 33. It is evident from the Fig. 2. 33 that with the increased amount of CNT, the ultimate tensile strength of the composite was reduced which is due to the difficulty in the deagglomeration and uniformly distribution of carbon nanotube in the matrix. The CNT bundles showed poor wettability in metal matrix, increased the porosity and reduced the density of the composite, leading to a deterioration of the mechanical properties of the composite.

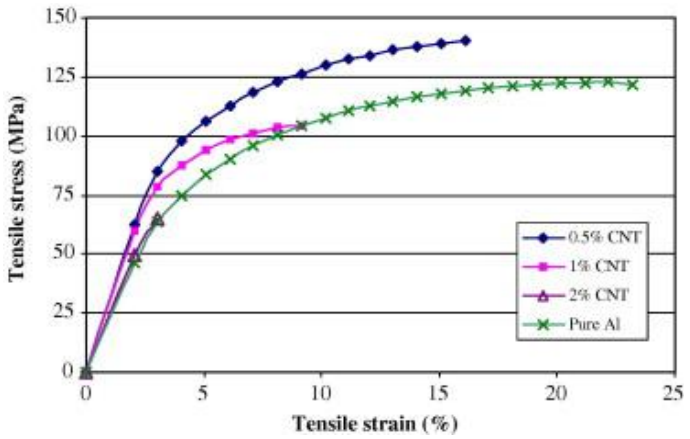


Fig. 2. 33 The tensile stress-strain curves of bulk Al-CNT composite with various CNT concentrations.

Likewise, M. Jafari et al. [35] also found MWNT agglomerates (as depict in Fig. 2. 34 (A)) in the Al2024-1.5 vol. % MWNT composite powders which was subjected to 1 h ball milling. The density of the as-produced composite was found to decrease with increasing concentration of carbon nanotube as shown in Fig. 2. 34 (B). The reason of this phenomenon is because of the agglomeration and un-uniformly distribution of carbon nanotube in the

matrix.

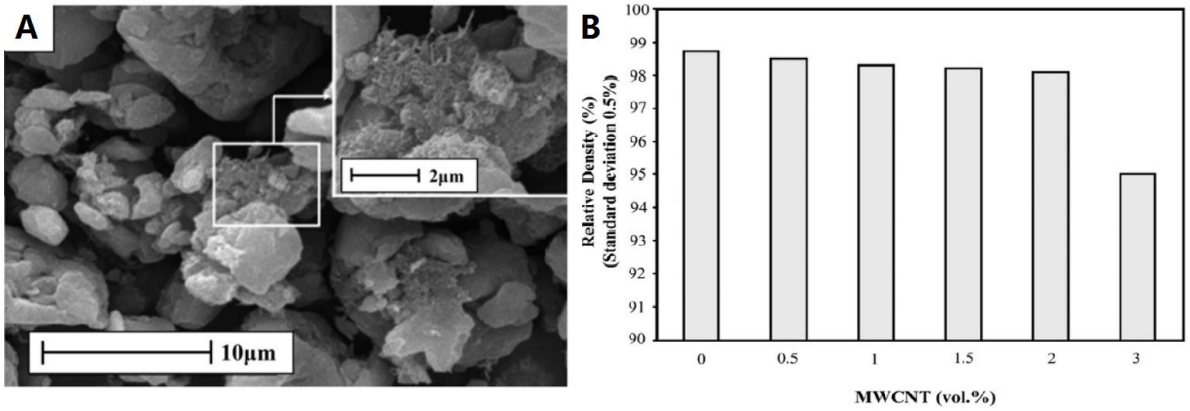


Fig. 2. 34 (A) The CNT agglomerates found in the Al2024-1.5 vol. % MWNT composite powders; (B) the relative density of the Al-CNT composite with various carbon nanotube loadings.

2. 4. 4. 2. Interfacial bonding between matrix and carbon nanotube

The interface between CNT and metal matrix is extremely critical since it is the channel of load transfer from the matrix to the reinforcement [150]. Hence powerful interface would significantly improve the strength of matrix while the poor interface would lead to lower strength and insufficient utilization of the superior characteristics of CNT [151]. Additionally, the product of interfacial reaction is critical to enhance the interface between matrix and reinforcements and enhance the strength of the composites [151].

According to K. P. So et al. [152, 153], the surface tension of aluminium is 995 mN/m [154] while that of carbon nanotube is only one twentieth the value: 45.3 mN/m [155]. Since there is a significant difference between the surface tension of aluminium and carbon nanotube,

tight bonds at the interface are not easy to be achieved. Also, the active aluminium atoms are prone to form alumina (Al_2O_3) which would worsen the contact and integration between the matrix and reinforcements.

Kwon et al. [123] reported that a thin layer of Al_4C_3 formed at the interface of Al-5.0 wt.% CNT composite by spark plasma sintering at 600 ℃ followed by hot extrusion at 400 ℃, which obtained a 128 % improvement of tensile strength from 85 to 194 MPa. Kwon et al. [123] reported that the formation of small amounts of Al_4C_3 in the CNT-MMC helps the load transfer by pinning CNT to the matrix and enhancing the interface strength. In the fabrication of MWNT-Cu composite via powder metallurgy route [156, 157], wettability between MWNT and copper was improved by coating Ni on the MWNT surface during liquid phase sintering. However, T. Kuzumaki et al. [158] concluded that the mechanical properties of the as-produced carbon nanotube reinforced titanium composite was degraded due to the formation and growth of Al_4C_3 along the reactive prism planes in the structure of carbon nanotube. Therefore, the formation of aluminium carbide in the composite is still controversial.

2. 4. 4. 3. The structure of carbon nanotube in Al-CNT composite

Since the superior performances and properties of carbon nanotube are result from its specific length to diameter ratio and seamless structure, it is crucial to preserve the tubular structure of carbon nanotube in the composite in order to achieve its full potential.

Z. Y. Liu et al. [93] produced Al-MWNT composite by ball-milling 0.5 wt. % multi-walled carbon nanotube (diameter: 10-20 nm, length: 5 μm) with 99.5 wt. % aluminium for 2, 4, 6, 8 and 12 h at 300 rpm with a ball to powder ratio 8 to 1. The Raman spectra of ball-milled composite powders were measured, the intensity of G band and D band peak were recorded and the intensity ratio of G band peak and D band peak (I_G/I_D) were calculated and listed in the Table 2. 5.

Table 2. 5 The I_G/I_D of the Al-0.5 wt. % MWNT composites powders that were ball-milled for different time in Z. Y. Liu et al. [93]'s experiment.

Milling time (h)	0	2	4	6	8	12
I_G/I_D	0.85	0.82	0.77	0.71	0.62	0.53

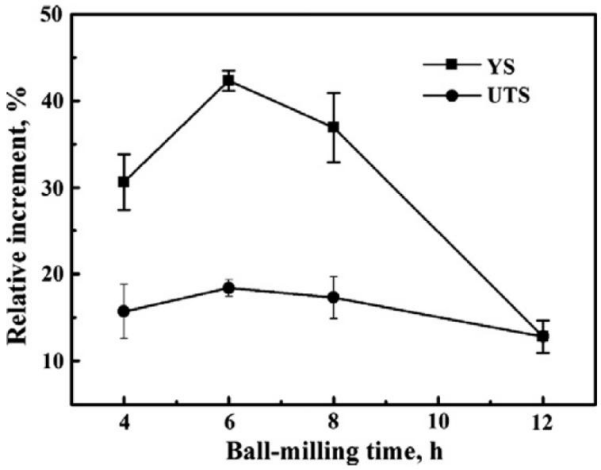
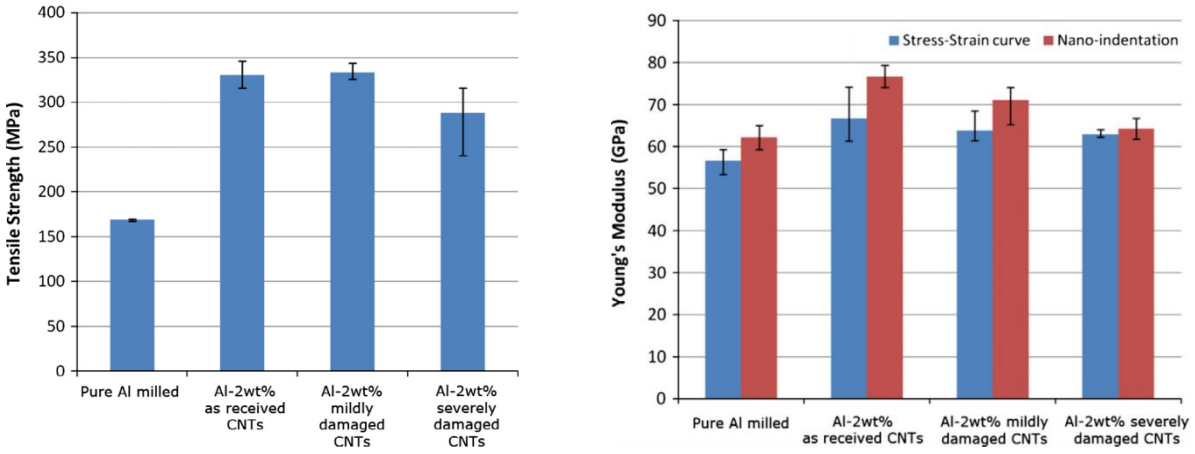


Fig. 2. 35 The yield strength (YS) and ultimate tensile strength (UTS) of the Al-0.5 wt. % CNT composite produced by Z. Y. Liu et al. [93].

As can be seen from the Table 2. 5 that with increasing milling time the I_G/I_D increased, which means more defects and dislocations were introduced into the structure of carbon nanotube in the Al-0.5 wt. % MWNT composite of longer milling time. Fig. 2. 35 illustrates

the relative increment of yield strength (YS) and ultimate tensile strength (UTS) of the as-produced Al-0.5 wt. % MWNT composite. It is clear that both the relative increment of yield strength and ultimate tensile strength of the as-produced Al-0.5 wt. % MWNT composite kept increasing until ball milling after 6 h. However, further increasing the ball milling time the increment of the yield strength and ultimate tensile strength decreased due to the serious damage to the CNT structure during ball milling process. Thus, it is concluded that the structure damage of carbon nanotube is disadvantaged towards the utilization of full characteristics of carbon nanotube into the composite matrix.

M. T. Z. Hassan et al. [159] investigated the effect of damaged structure of carbon nanotube on the Al-CNT composite. Ball milling was utilized to introduce defects and dislocations into carbon nanotube and two groups (namely: mildly damaged and seriously damaged) of damaged carbon nanotube were produced. Then 2.0 wt. % of each as-damaged carbon nanotube were further ball milled with aluminium, cold compacted and hot extruded. The tensile strength, Young's modulus and nano-indentation of the as-produced composite are shown in Fig. 2. 4. 4. 3. 2. (a) and Fig. 2. 4. 4. 3. 2. (b). It is found that the composite with mildly damaged carbon nanotube displayed 97.5 % higher tensile strength and 14.2 % higher Young's modulus than pure aluminium matrix while the seriously damaged carbon nanotube displayed only 71 % and 3.3 % enhancement for the tensile strength and Young's modulus, respectively, than the pure aluminium matrix. Thus, it proves the importance of the tubular structure of carbon nanotube in the composite matrix.



A B

Fig. 2. 36 The (A) tensile strength, (B) Young's modulus and nano-indentation measured for the Al-2.0 wt. % CNT composite prepared by M. T. Z. Hassan et al. [159].

2. 5. Powder metallurgy

Powder metallurgy is a novel technology with a long history. According to the archaeological research, the Egyptian utilized carbon reduces the iron oxide to obtain iron sponge and make iron wares in about 3000 BC [160]. In the 4th century, the Indian ironsmith employed the sinter-forging method to build the Delhi Iron Pillar [161]. Modern powder metallurgical technique was commenced in the 19th century with the production of carbides and porous bronze. After the Second World War, further advances and improvement took place due to the introduction of various net-shape ferrous and non-ferrous products [162]. Nowadays, powder metallurgy as a relatively mature technique has been widely employed in a variety of industrial production. Especially, additive manufacturing, including 3D printing, selective laser melting and selective laser sintering, as a novel member of PM family is predicted to revolutionize the manufacturing and production industry in the near future.

2. 5. 1. The advantages of powder metallurgy

The global attention of both academic and industrial fields are drawn by powder metallurgy which is due to the relatively simple requirement for facilities, economic price, low energy consumption, possibility of manufacturing refractory materials and controllable properties of products.

As the powder metallurgical technique produces near net shape components with close dimensional tolerances, little (less than 3 %) raw material is wasted in the process and few or no further machining or finishing is required, which shortens the production cycle and save the capital of raw materials and secondary processing. This is extremely beneficial to large scale production. Nowadays, manufacturing industries like automobile, aerospace and other transportation sectors consume roughly 80 % of structural powder metallurgy part production [163].

Also, although traditional casting largely contributed to the development of modern industries, materials today made by conventional methods can no longer satisfy the requirement of fabricating new materials. For example, refractory materials like Mo, W, Ta, and Nb as well as their alloys and intermetallics which have very high melting point (higher than 2000 ℃ [164]) that are mainly produced by high temperature powder metallurgy method in industry. In contrast, the fabrication of these materials would consume folds of more energy by slip casting method [164].

What's more, powder metallurgy technique can secure the homogeneity of materials while some traditional moulding and processing methods can easily result in precipitation of certain components and worsening the overall properties of products. The development of composite broadened the application and enhanced the properties of modern materials. However, elements with huge density and dimension difference are prone to see the lighter and smaller composition agglomerate together. To solve this problem, powder metallurgy approach was employed by a lot of researchers to produce homogenous composites like ceramic particulates [165] and nano-fibres reinforced metal matrix composite. Additionally, the morphology of the powders and the microstructure of the bulk materials are controllable, so the properties and performances of the as-produced products can be tailored by powder metallurgy technique.

2. 5. 2. The powder metallurgy process

Each step of powder metallurgy technique is straight forward and highly efficient. The schematic diagram of the manufacturing procedures of powder metallurgy is presented in the Fig. 2. 37. The detailed procedures are introduced in following sections.

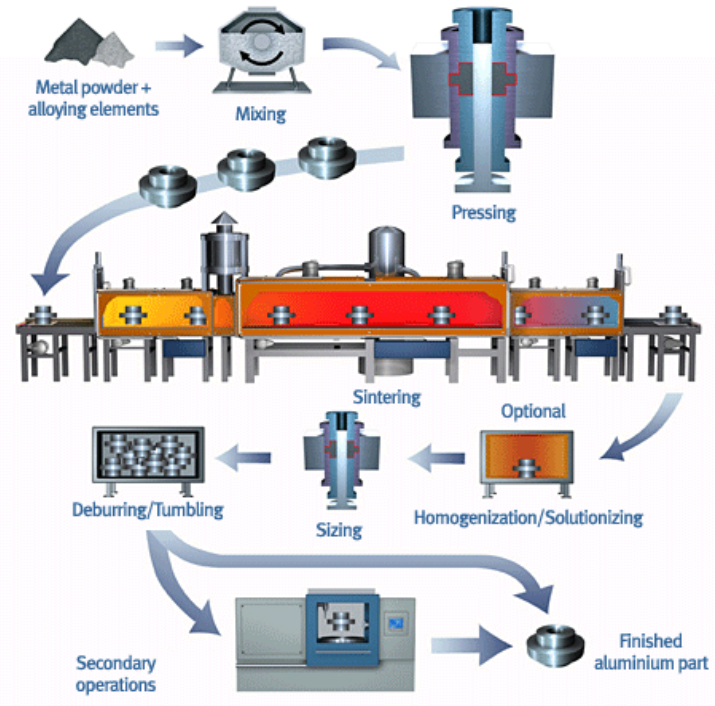


Fig. 2. 37 The schematic diagram of powder metallurgy production procedures [166].

2. 5. 2. 1. Powder production

As can be learnt from the name of powder metallurgy, this technique employs diverse powder (metal, alloy or ceramic) as raw materials to manufacture engineering components of determined shape and designed properties. Powders of different particle size, morphology and microstructure are vital to the final properties of powder metallurgical products. To meet the specified requirement for various powders, diverse techniques of powder production were explored and invented.

2. 5. 2. 1. 1. Mechanical milling and grinding

Mechanical grinding and milling are the most original powder preparation method which is mainly employed to produce ceramic particulates. As the brittle nature of ceramic materials,

they are vulnerable to break apart under certain impact. On the other hand, as most metals exhibit plastic manners under external pressure, grinding and milling is not very effective in large scale production of metal powders. Thus, generally, brittle powders are placed in ball mill and subjected to high-energy collision from milling balls. Subsequently, fine powders with uniform composition are yielded.

2. 5. 2. 1. 2. Atomization

For large scale industry production of metal powders, atomization of metal melt is the most reliable and widely applied approach. It is been used to produce metal powders like: lead, tin, zinc, copper, nickel iron and aluminium as well as pre-alloyed powder like brass, bronze, high speed steel and stainless steel. Melt atomization involves three main processes namely: heating and melting, atomization and solidification of metal.

The atomization technique can be classified by the different ways of disintegration energy introduced into the melt. Among all the specific atomization approaches, gas and liquid atomization are the most important processes for the industrial powder production. The former is mainly employed for the production of low melting point metals while the latter is mainly responsible for iron base powders. Depending on the requirements for the properties of the powders to be produced, different gases such as air, argon, nitrogen and helium are used to atomize the metal melt into fine particles (1 μm~1 mm). Similarly, water atomization mainly used water to produce powders. Other techniques like centrifugal atomization and vacuum atomization are also employed in powder production but in smaller

scales.

2. 5. 2. 1. 3. Chemical methods

Chemical methods are also utilized in powder production. The main mechanism of this process is using reduction agent gases (like hydrogen, ammonia and natural gas) or solids (like carbon, or reactive metals like Na, Ca and Mg) to reduce compounds such as oxides, carbonates, nitrates and halogenides. Generally, the reduction reaction can be summarized by the following equation:

$$\mathrm{MeO} + \mathrm{RA} = \mathrm{Me} + \mathrm{RAO} \qquad (2.\,5.\,2.\,1.\,3.\,1)$$

where MeO is the substance to be reduced, RA is the reduction agent, Me is the reduced metal and RAO is the oxidized reduction agent. As the complexity of the processes, it is only applied in small scale or laboratory powder production for powders with some special required properties, composition or microstructure.

2. 5. 2. 2. *Blending and mixing*

For powder metallurgy technique, powder mixing or blending is required before further processing. Blending is defined as the mixing of the particles having the same chemical composition to homogenize the particle size distribution while mixing is to mingling the particles of different nominal composition and uniform the distribution of each constituent in the mixture. Additionally, various lubricants and binders can be added and dispersed into the

powder mixture at this stage to alleviate the friction between powders and die set and assist die filling, pressing and product ejection. Very often, ball bearings made of hard ceramic or metal alloy are added into the mixture as milling media to improve the efficiency and effectiveness of mixing as well as shorten the mixing time. To homogenize active powders, inert gases like argon or nitrogen are needed to fill the milling chamber to prevent the possible reaction.

2. 5. 2. 3. Shaping and pressing

To manufacture products with specific geometry, as-mixed powders are poured into pre-designed die sets which have the cavity and groove of the product shape and dimension, then mechanical compacted under the applied external pressure. The ejected as-pressed material body is called green compact or preform. The control of lubrication, pressure, ramp rate, dwell time and eject rate are essential for producing green compacts with favourable and uniform density.

2. 5. 2. 4. Consolidation

After compaction, the particles in the green compacts are mechanically bonded which is too weak for the working condition. Also, the density of the material is still too low and the high porosity makes the preform fragile and vulnerable. Therefore, further densification is needed to comprehensively enhance the density and properties of the products. Conventionally, the green compacts are placed in the furnace (sometimes with protective atmosphere like: argon

and nitrogen or reduce atmosphere like: hydrogen and ammonia) and heated up to a temperature close to (solid state sintering) or exceed (liquid state sintering) the melting point of one constituent for a certain period of time. Similar to the compaction stage, the atmosphere, heating rate, dwell time, and cooling rate are adjustable to obtain the products with desirable microstructure and properties. Nowadays, other technologies like hot pressing, hot isostatic pressing (HIP) and spark plasma sintering (SPS), which apply pressure and temperature on the green compacts at the same time, were developed to simplify the production process, shorten the processing time and more importantly enhance the densities and properties of the products.

2. 5. 2. 5. Finishing operations

Theoretically, the as-sintered products are ready for application. For some specific cases, post processing such as homogenization, solutionizing, sizing and deburring/tumbling are required to further enhance the quality of the products.

Chapter 3. Experiment and characterization

3. 1. Introduction

This chapter presents a detailed description of the starting materials, the materials processing and analytical characterization methods used in this study.

The first section describes the raw materials used in the experiment together with information on suppliers, purity, form, dimension etc.

The second section provides a detailed description of the powder mixing and composite fabrication parameters, including the composition of composite, the ball to powder weight ratio, milling speed, milling time, atmosphere, compaction pressure, sintering temperature, dwell time and etc.

The third section describes diverse techniques of characterization employed in the project to study the powder characteristics, microstructure and properties of composites. The particle size (distribution) was determined used laser particle sizer. The microstructure and composition of composites were characterised using a combination of optical microscopy, scanning electron microscopy (SEM), energy dispersive X-Ray spectroscopy (EDS) and transmission electron microscopy (TEM). The structure of carbon nanotube was studied using Raman spectroscopy. The mechanical properties (e.g. tensile strength and hardness) of samples were determined using Vickers hardness and tensile test methods. Thermal stability

of the sample was studied using differential scanning calorimetry (DSC). Finally, the densities of compacted and sintered samples were measured using Archimedes method.

3. 2. Pristine materials

3. 2. 1 Aluminium

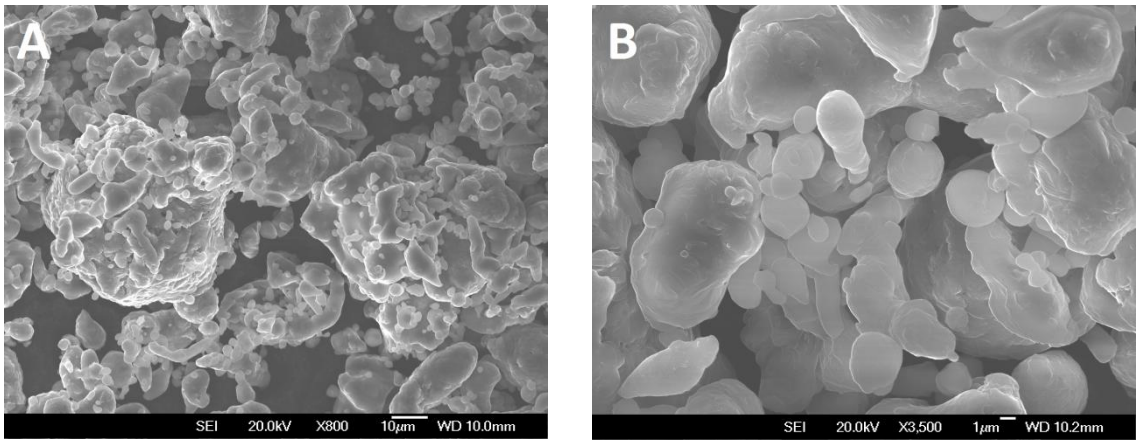


Fig. 3. 1 The SEM micrograph of pristine elemental aluminium powders (-75 μm). (A) under low magnification (800×) and (B) under high magnification (3500×).

Three types of elemental aluminium powders were used in the study. An argon gas atomized aluminium powder, of a particle size up to 75 μm and a purity of 99.7 % produced by ECKA Granulate GmbH & Co. KG, was selected as the matrix constituent of composite. Fig. 3. 1 illustrates the size, shape and topography of the aluminium powders (-75 μm). It is evident from the Fig. 3. 1. (A) that the sizes of pristine aluminium particles are in a relatively wide range and the shapes of these particles are irregular.

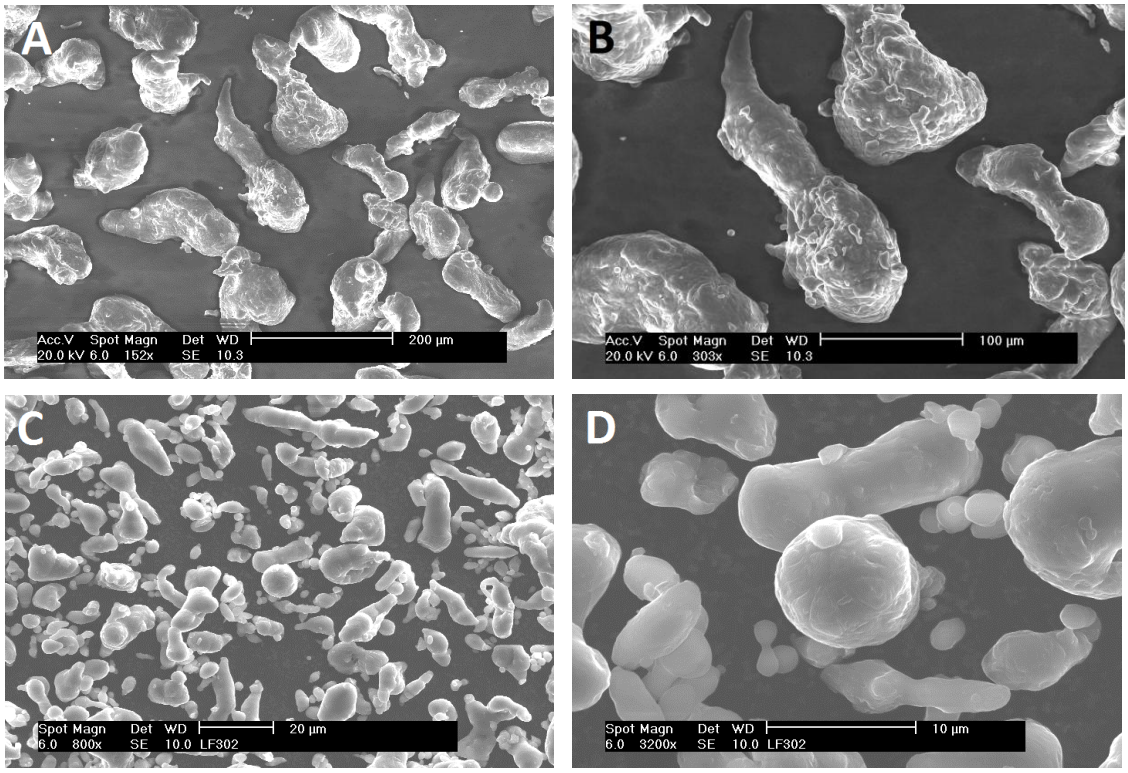


Fig. 3. 2 SEM micrograph of (A) and (B) showing the morphology of pristine elemental aluminium powders (75 µm – 106 µm) and (C) and (D) showing the morphology of pristine elemental aluminium powders (-10 µm). (A) and (C) are under low magnification; (B) and (D) are under high magnification.

Another two types of elemental aluminium powders, purchased from the Aluminium Powder Company Limited (AlPoCo), were employed to study the effect of process control agent on the ball-milled Al-MWNT composite powders. One of them was which has a purity of 99.9 % and a particle size ranged from 75 µm to 106 µm. The morphology of this type of elemental aluminium powders is shown in the Fig. 3. 2. (A) and (B). The third type of elemental aluminium powders has a purity of 99.97 % and a powders size smaller than 10 µm. Fig. 3. 2 (C) and (D) presents the irregular shape and smooth surface of the third type of element aluminium powders.

3. 2. 2 Carbon nanotube

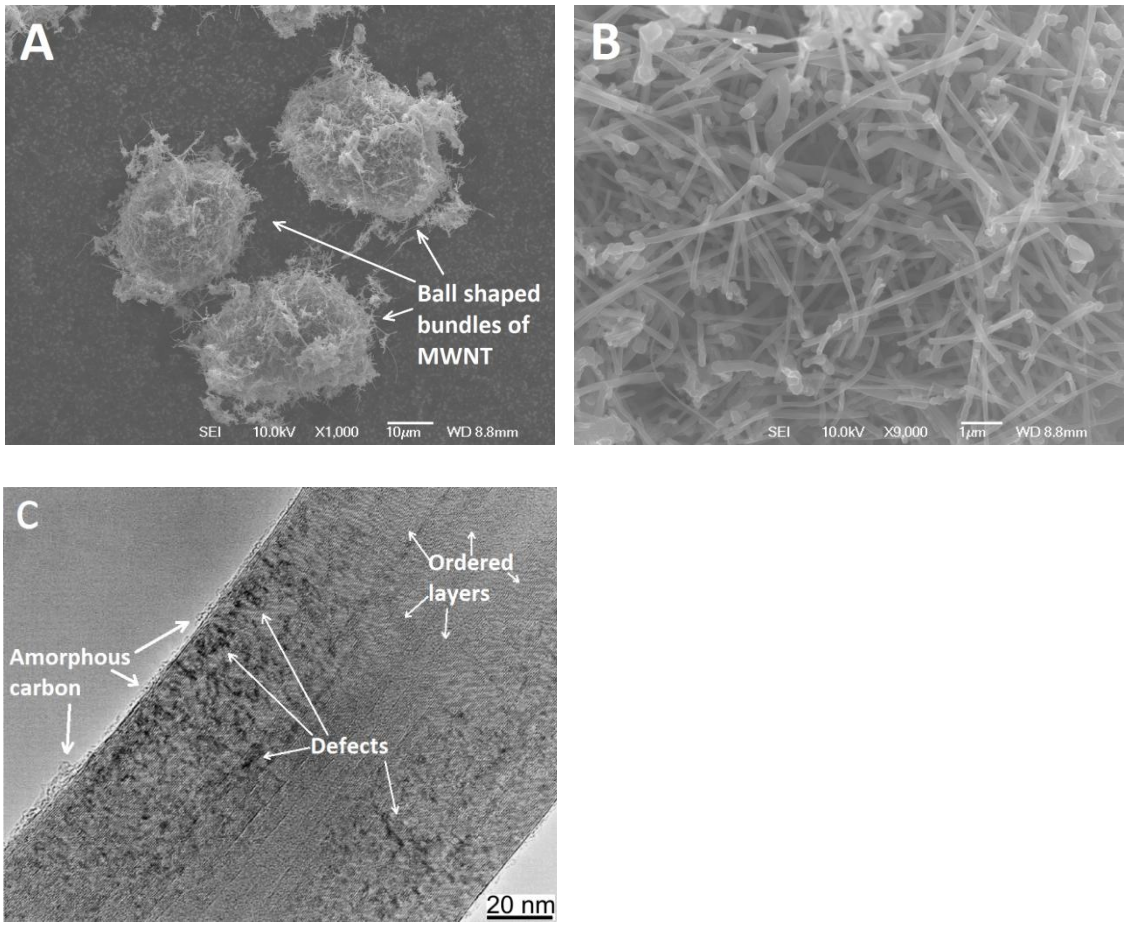


Fig. 3. 3 (A) the SEM micrograph of raw MWNT clusters; (B) the high magnification SEM micrograph of pristine MWNTs and (C) high resolution TEM micrograph of MWNT supplied by MER Corporation.

Corresponding to the elemental aluminium powders used in the project, three different types of multi-walled carbon nanotube (MWNT) was employed in the study. The first type of MWNT, 140 ± 30 nm in diameter and 7 ± 2 μm in length synthesized by chemical vapour deposition (CVD) method, were purchased from Materials and Electrochemical Research Corporation (M.E.R. Corporation). This type of MWNT was not only ball milled with elemental aluminium powders to yield Al-MWNT composite powders but also pressed and

sintered as reinforcements in the Al-MWNT composite.

Fig. 3. 3. (A) and (B) show the SEM micrograph of the pristine multi-walled carbon nanotube. They are randomly woven together to give ball-shaped bundles with an average diameter of around 25 μm. These clusters are the biggest challenges for the manufacture of effective MWNT-Al composites because many researchers have found MWNT agglomerates [28, 31, 32, 35, 36] of different sizes in the metal matrix after various processing including hot extrusion [31], mechanical alloying [91], hot pressing [33], plasma spray [94] and hot rolling [28]. It is obvious that MWNT were in straight and long tubular shape which has fewer tendency to agglomerate than curved and entangled MWNT according to A. M. K. Esawi et al. [50]. Also, a high resolution TEM micrograph of MWNT, provided by Materials and Electrochemical Research Corporation, demonstrating its multi-layer microstructure (around 170 layers) is presented in the Fig. 3. 3. (C). Amorphous carbon on the surface and defects inside the structure of MWNT are marked in the Fig. 3. 3. (C) as well.

The other two types of MWNT are supplied by Sigma Aldrich Co. and Cheap Tubes Inc.. Fig. 3. 4 shows SEM micrographs of these raw multi-walled carbon nanotubes used in this study. The MWNT of an average diameter of 6-9 nm and an average length of 5 μm supplied by the Sigma-Aldrich Co. is shown in the Fig. 3. 4 (A). The MWNT of an average diameter of 10-30 nm and an average length of 10-30 μm supplied by the Sigma-Aldrich Co. is shown in the Fig. 3. 4 (B). It is clear in the Fig. 3. 4 that both types of MWNT are curved

and agglomerated together which is due to the strong van der Waals force of attraction between the long and thin tubes. According to A. M. K. Esawi et al. [167], reported that the MWNT of smaller diameter are more prone to bent and entangled which resulted in more difficulties to disperse the MWNT in the matrix compared to the straight MWNT of larger diameter.

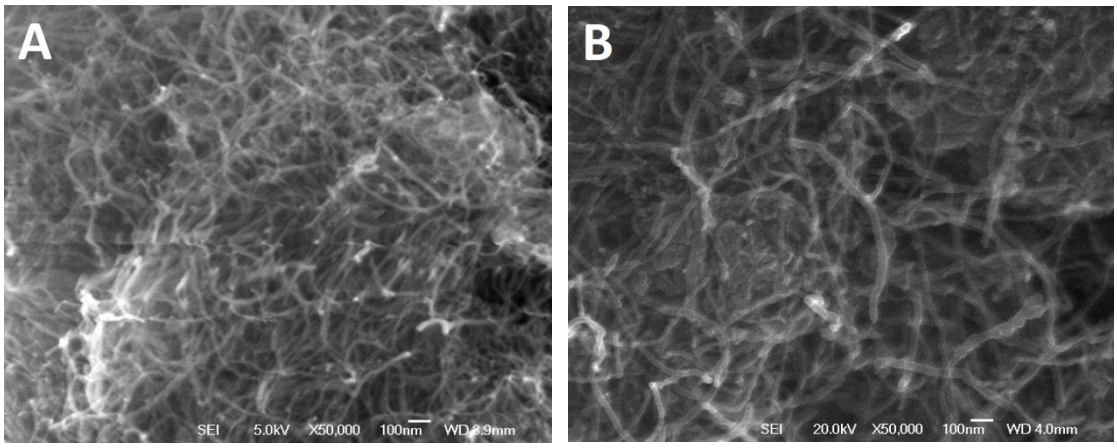


Fig. 3. 4 SEM micrographes showing clusters of pristine multi-walled carbon nanotube: (a) MWNT of diameter 6-9 nm and average length 5 μm, supplied by the Sigma-Aldrich c; and (b) MWNT of diameter 10-30 nm and average length 10-30 μm, supplied by the Cheap Tubes Inc..

3. 3. Materials processing

3. 2. 3 Powder mixing

A Fritsch planetary mono mill (model: PULVERISETTE 6 classic line) was employed in the mixing and dispersion of carbon nanotube into aluminium powders for different length of milling time. A batch of AISI 420 stainless steel balls of a diameter of 10 mm purchased from the Atlas Ball and Bearing Co. Ltd. was used as milling balls. The ball to powder

weight ratio was kept at 10:1. Either 1.0 wt. % of stearic acid ($C_{18}H_{36}O_2$) or 1.0 wt. % of ethanol was added in each run as process control agent (PCA) to prevent the severe welding of the ductile aluminium during the ball milling process. Another action taken against the welding of the particles was to pause for 20 min after the ball milling for each 20 min. This helps to cool down the milling materials and milling media, in order to avoid the milling pot to reach to high enough temperature for the welding of aluminium powders. Loading of metal powders, process control agent and stainless steel milling balls into the milling pot were carried out in the glove box in argon atmosphere to avoid exposure of powder to oxygen. The speed of milling was set to 250 revolutions per minute (rpm) and the milling time varied from 5 hours to 20 hours.



Fig. 3. 5 An image of Fritsch planetary mono mill (model: PULVERISETTE 6 classic line).

3. 2. 4 Pressing of powder

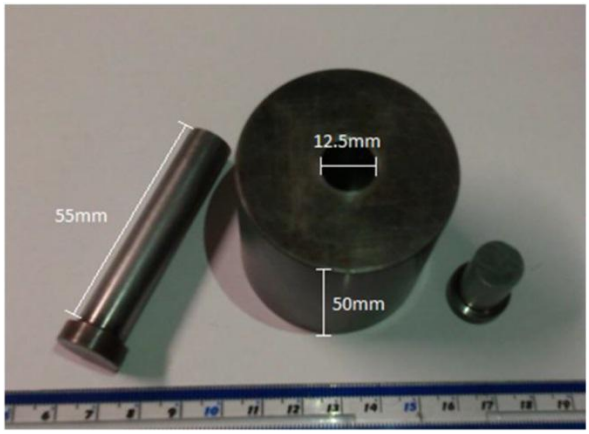


Fig. 3. 6 A photograph of a punch and die set used to prepare the cylindrical samples.

A cylindrical tool steel punch and die set (Fig 3. 2. 4. 1) were used to shape 1.7 g of powders into discs of 12.5 mm diameter and 1.2 mm high, so that the disc samples were suitable for XRD sample holder for subsequent microstructural characterisation. The internal and external diameters of the die are 12.5 mm and 40 mm, respectively. The height of the die is 50 mm. A punch of a length of 55 mm was used to press the powders.

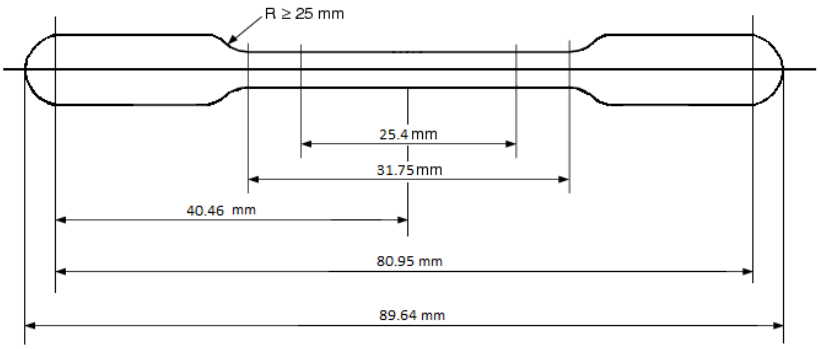


Fig. 3. 7 The schematic diagram of tensile test specimen based on MPIF Standard 10.



Fig. 3. 8 The pressed and sintered tensile test specimen.

Tensile test specimens of geometry and dimension according to the Metal Powder Industrial Federation (MPIF) standard 10 (Fig. 3. 7) were produced using a machined die set made from H13 hardened tool steel. Fig. 3. 8 presents the as-produced pressed and sintered tensile test specimen.



Fig. 3. 9 A photograph of hydraulic press supplied by Eco Hydraulic Presses.

A 30 tons hydraulic press supplied by Eco Hydraulic Presses (as shown in Fig. 3. 9) was employed to compact the powder samples at a constant pressure of 475 MPa. This pressure was chosen because it is the minimum pressure required for maximum compact density of Al as determined from previous studies [168]. The pressure dwelling time for the production of cylindrical samples and tensile specimens were set to 30 s and 60 s, respectively. The lubricant (commercial name: KenoLube® P11) from Höganäs Sweden was used to lubricate the die sets before each pressing to reduce the friction and wear of the die set.

3. 2. 5 Sintering of powder



Fig. 3. 10 A photograph of ELITE horizontal tube furnace used in the project.

All compacted specimens were sintered in the horizontal tube furnace as shown in the Fig. 3. 10, (Model: TSH16/25/180-2416) manufactured by Elite Thermal System Limited (ELITE) at a heating rate of 10 ℃/min and holding at 630 ℃ for 1 h in dynamic flow nitrogen gas at 3 L/min.

3. 4. Characterization

3. 4. 1 Sample grinding and mounting

The powders and sintered specimens were firstly mounted in bakelite by the ATM Opal OP460 mounting machine (Fig. 3. 11). The as-mounted samples were then wet ground (using water) with silicon carbide sandpaper following the grade order: 120, 240, 400, 800, 1200, 2500 and 4000. Afterwards, the ground samples were polished using Diaduo 6 μm and 1 μm lubricant and MDMOL 6 μm and 1 μm polishing clothes, respectively. This was followed by the polishing using OP-S colloidal silica suspension. The grinding and polishing processes were carried out using a Struers LaboPol-5 grinding and polishing machine (Fig. 3. 12).



Fig. 3. 11 OPAL 460 ATA sample mounting machine.



Fig. 3. 12 Struers LaboPol-5 grinding and polishing machine.

3. 4. 2 Etching

Keller's reagent was used to etch the surface of as-polished surfaces of the samples to reveal their microstructure. The composition of Keller's reagent is shown in the Table 3. 1. Each sample was immersed in the etchant for roughly 10 s and washed by water before being dried by a hair drier.

Table 3. 1 The chemical composition of Keller's reagent.

	Chemical Composition
Keller's Reagent	5ml nitric acid (HNO_3) 3ml hydrochloric acid (HCl) 2ml hydrofluoric acid (HF) 190ml distilled water

3. 4. 3 Optical microscopy



Fig. 3. 13 The Zeiss microscope (model: Axioskop 2 MAT with HAL 100 halogen lamp).

A Zeiss microscope (model: Axioskop 2 MAT with HAL 100 halogen lamp), as shown in the Fig. 3. 13, was employed in the examination of the cross section microstructure of both powder and sintered samples.

3. 4. 4 Scanning electron microscopy (SEM)

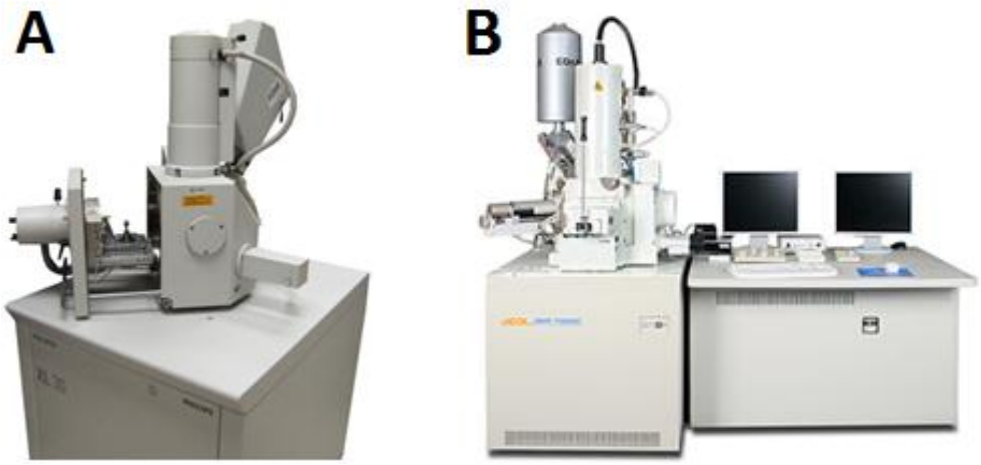


Fig. 3. 14 A photograph of (A) Philips-XL30 SEM and (B) JEOL JSM-7000F FESEM.

A scanning electron microscopy of Philips-XL30 (Fig. 3. 14. (A)) and a field emission scanning electron microscopy (FESEM) of JEOL JSM-7000F (Fig. 3. 14. (B)) were employed to characterize the morphology of "as-milled" particles and the microstructure of sintered samples. The powder samples were first uniformly dispersed on the thin adhesive carbon disc while the sintered samples were loaded into the SEM holder directly before they were characterized by SEM with secondary electron imaging model, operated at 5 to 20 kV. The energy-dispersive X-ray spectroscope (EDX) was used to identify the composition of each sample.

3. 4. 5 Vickers micro-hardness test



Fig. 3. 15 Mitutuoyo hardness testing machine.

The hardness of powders and as-sintered samples were measured using Vickers micro-harness test. A Mitutuoyo model: MVK-H1 hardness testing machine, as shown in the Fig. 3. 15, was employed and a constant load of 10 kgf and a dwell time of 5 s was utilized

in the test. At least 10 hardness measurements were taken for each sample and an average harness was determined.

3. 4. 6 Tensile test



Fig. 3. 16 A universal tensile testing machine with Zwick/Roell 1484 frame.

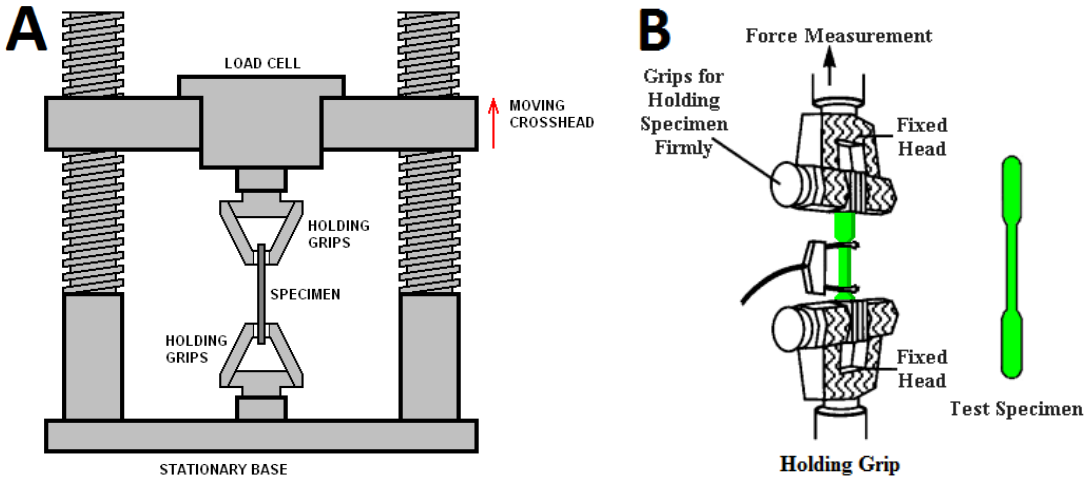


Fig. 3. 17 The schematic diagram of (A) the setup of the tensile testing machine and (B) the tensile specimen on the grips and clamped by the extensometer.

Tensile test specimens were prepared according to Metal Powder Industries Federation (MPIF) Standard 10 as mentioned in the previous section. A universal tensile testing machine with a Zwick/Roell 1484 frame and a pair of instron grips showed in Fig. 3. 16 were used to measure the tensile properties of the sintered sample. Each tensile test specimen was tightly clamped by the grip pair and subjected to a tension rate of 0.5 mm/min (Fig. 3. 17. (A)). The elongation of the specimen was monitored by an extensometer of a gauge length of 20 mm (Fig. 3. 4. 5. 2. (B)). The force and extension were recorded by a computer, which were then converted to stress and strain plots.

3. 4. 7 Apparent density and tapped density

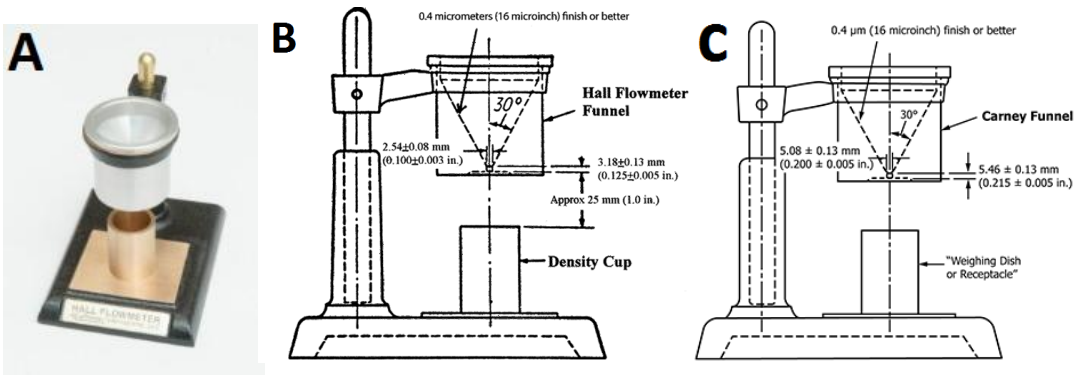


Fig. 3. 18 (A) an image and (B) a schematic diagram of Hall Flowmeter apparatus and (C) schematic diagram of Carney apparatus.

Apparent density of powders refers to the mass and volume ratio of a certain type of powders that are loosely packed in a confined space, while tapped density denotes the density of a powder which is intentionally vibrated or tapped.

The apparent densities of the powder were tested according to MPIF Standard 4 and MPIF Standard 28 for the free-flowing and non-free-flowing metal powders respectively. The Hall Flowmeter apparatus (as shown in Fig. 3. 18. (B)) was used for the free flowing powders while the Carney apparatus (as shown in Fig. 3. 18. (C)) was used for the non-free flowing powders. The setup of the Hall apparatus and Carney apparatus are basically the same except the diameter of the orifices at the bottom of the Carney funnel (5 mm/0.20 in.) is doubled that of the Hall funnel (2.54 mm/0.10 in.)

In the measurement of apparent density, the powders were poured into the funnel and filled the density cup of a volume of 25 ± 0.05 cm^3 until the powders overflowed. Then a stainless steel ruler was used to level the powders to the top of the density cup. The apparent density of the powder was calculated by dividing the mass of the powders left in the density cup with the volume of the density cup. Five measurements were done for each powder sample and an average value was calculated.

The procedures of measuring the tapped density of powders are similar to that of the apparent density. Except that the density cup containing the powder were tapped using the vibration of the control sieve shaker (Restch, AS200 basic) at a rate of 250 rpm taps per minute so that densification can take place. The density cup was always refilled with powders if the volume of the powders in the density cup decreased. This procedure is repeated until no further decrease of the volume of the powder take place.

3. 4. 8 Green density, sintered density and relative density

The green density and sintered density of the specimens were measured according to the Archimedes' principle. The mass of the specimens in air (M_{air}) were weighed and recorded prior to immerse them into distilled water. The specimens immersed in water were placed in a sealed container. A vacuum pump was utilized to extract the air inside the specimens and make sure the water filled the pores. Then the mass of the specimen in the water (M_{water}) was measured. Subsequently, the density ($D_{measured}$) of the specimen was calculated by the equation:

$$D_{measured} = \rho_{water} \times M_{air} / (M_{air} - M_{water}) \quad (3.\ 4.\ 8.\ 1)$$

where the ρ_{water} is the density of water at room temperature. The relative density ($D_{relative}$) is calculated by the following equation:

$$D_{relative} = D_{measured} / D_{theory} \quad (3.\ 4.\ 8.\ 2)$$

where D_{theory} is theoretical density.

3. 4. 9 X-ray diffraction (XRD)



Fig. 3. 19 A photograph of Inel EQUINOX 3000 X-ray diffractometer used in the project.

An X-ray diffractometer of Inel EQUINOX 3000 was used to study the phase composition and grain size of the samples, The X-ray is powered by a generator of 3500 watts and the acquisition angle (2θ) is ranged from 0° - 130 °. The radiation and wavelength of the X-ray is Cu K-alpha and 0.15418 nm respectively.

In some cases, the grain size of the sintered composite are calculated by the full width at half maximum (FWHM) according to the William-Hall method [138, 169].

$$B_{\text{sample}} \cos\theta = \frac{K\lambda}{D} + 4\varepsilon \sin\theta \qquad (3.\ 4.\ 9.\ 1)$$

where B_{sample} represents the peak broadening due to grain size , D is the grain size in nanometer, λ is the wavelength of the radiation (0.15418 nm), K is a constant equal to 0.94.

ε is the strain in the material and θ is the Bragg diffraction angle.

The instrument contribution of peak broadening is subtracted by the equation:

$$B_{\text{sample}}^{\ 2} = B_{\text{total}}^{\ 2} - B_{\text{instrument}}^{\ 2} \qquad (3.\ 4.\ 9.\ 2)$$

where B_{total} is the measured peak broadening and $B_{\text{instrument}}$ is the broadening due to the imperfectness of the diffractometer.

3. 4. 10 Differential scanning calorimetry (DSC)



Fig. 3. 20 A photograph of NETZSCH DSC (model: 404 C CELL).

A NETZSCH DSC (model: 404 C CELL) (Fig. 3. 20) was employed to study the phase transformation in the specimen by measuring the heat flow through the sample with respect to those through a reference standard upon heating to elevated temperatures. Both pristine and "as-milled" powders of a mass of 20 mg were loaded into a DSC alumina crucible of a diameter of 6.5 mm with an alumina (Al_2O_3) lid. All samples were subjected to a heating rate of 10 ℃/min from ambient temperature to 700 ℃ in dynamic flow argon gas at a flow

rate of 5 L/min.

3. 4. 11 Raman spectroscopy



Fig. 3. 21 A photograph of Raman spectroscope (Renishaw inVia Raman microscope).

The structure of carbon nanotube was studied using a Renishaw-InVia Raman microscope (Fig. 3. 21) with an argon green laser light (wavelength: 532 nm, laser powder: 100%, scanning time: 100 s). The powder samples were evenly spread on the surface of a thin glass slice prior to Raman spectroscopy.

3. 4. 12 Particle size analysis

The particle size and the size distribution of the "as-milled" powders were examined using particle size analyser as shown in Fig. 3. 22. The model of the particle size analyser is HELOS/KR with disperser combination OASIS/L and dosing unit VIBRI/L Sympatec, operated with a laser of wavelength: 632.8 nm, laser power of 5 mW. Dry particles were poured through the lenses and the intensity of diffracted laser beam automatically recorded

and analysed to determine the size of particle.



Fig. 3. 22 A photograph of particle size analyser (HELOS/KR with dry/wet disperser combination OASIS/L and dosing unit VIBRI/L).

D_{50}, which represents the particle size that half of the particle population are below and half above this diameter, is used to reveal the median particle size change in the mechanical alloying process [51, 170].

3. 5. Preparation of powder and bulk specimen

Various powder and bulk specimens were prepared for different purposes in the project. The detailed processing procedures are introduced here.

To study the effect of process control agent on the ball-milled Al-1.0 wt. % MWNT composite powders, 1.0 wt. % of process control agent: either stearic acid and ethanol was added into the Al-1.0 wt. % MWNT powders (either elemental aluminium powders (75-106 μm) with 1.0 wt. % MWNT(D: 6-9 nm, L: 5 μm) or elemental aluminium powders (-10um) with 1.0 wt. % MWNT (D: 10-30 nm, L: 10-30 μm)). The mixtures were then ball milled for 1-10 h at a constant speed of 250 rpm in argon atmosphere. For comparison, Al-1.0 wt. %

MWNT composite powders were also ball milled without any process control agent. The "as-milled" Al-1.0 wt. % MWNT powders were then pressed at 475 MPa and sintered at 630 ℃ for 1 h in nitrogen atmosphere. The names for each specimen are listed in the Table 3. 2. The detailed property measurement and microstructure characterization of the as-produced specimens can be found in chapter 4.

Table 3. 2 The definition of the name of the specimens in chapter 4.

Aluminium	**MWNT**	**Process control agent**	**Milling Time (h)**	**Name**
99.0 wt. % Elemental aluminium powders (75-106 μm)	1.0 wt. % MWNT (*D*: 6-9 nm, *L*: 5 μm)	/	5	Al(75-106 μm)MWNT_BM5
		1.0 wt.% stearic acid	1	Al(75-106 μm)MWNT_1ST_BM1h
			5	Al(75-106 μm)MWNT_1ST_BM5h
			10	Al(75-106 μm)MWNT_1ST_BM10h
		1.0 wt.% ethanol	1	Al(75-106 μm)MWNT_1ET_BM1h
			5	Al(75-106 μm)MWNT_1ET_BM5h
			10	Al(75-106 μm)MWNT_1ET_BM10h
99.0 wt. % Elemental aluminium powders (-10 μm)	1.0 wt. % MWNT (*D*: 10-30 nm, *l*: 10-30 μm)	/	5	Al(-10 μm)MWNT_BM5
		1.0 wt.% stearic acid	1	Al(-10 μm)MWNT_1ST_BM1h
			5	Al(-10 μm)MWNT_1ST_BM5h
			10	Al(-10 μm)MWNT_1ST_BM10h
		1.0 wt.% ethanol	1	Al(-10 μm)MWNT_1ET_BM1h
			5	Al(-10 μm)MWNT_1ET_BM5h
			10	Al(-10 μm)MWNT_1ET_BM10h

To study the effect of milling time on the microstructure and mechanical properties of the aluminium materials, elemental aluminium powders (- 75 μm) were ball milled for 5-20 h at a constant speed of 250 rpm in argon atmosphere. The "as-milled" elemental aluminium

powders were then pressed at 475 MPa and sintered at 630 ℃ for 1 h in nitrogen atmosphere. The names for each specimen are listed in the Table 3. 3. The detailed property measurement and microstructure characterization of the as-produced specimens can be found in chapter 5.

Table 3. 3 The definition of the name of the specimens in chapter 5.

Material	Process control agent	Ball milling time (h)	Name
100% Elemental aluminium powders (-75um)	1.0 wt. % stearic acid	0	Pure Al(-75um)
		5	Pure Al(-75um)_BM5h
		10	Pure Al(-75um)_BM10h
		15	Pure Al(-75um)_BM15h
		20	Pure Al(-75um)_BM20h

To study the effect of milling time on the microstructure and mechanical properties of the Al-1.0 wt. % MWNT composite materials, 1.0 wt. % MWNT (*D*: 140 ± 30 nm and *l*: 7 ± 2 μm) were ball-milled with elemental aluminium powders (- 75 μm) for 5-20 h at a constant speed of 250 rpm in argon atmosphere. The "as-milled" Al-1.0 wt. % MWNT composite powders were then pressed at 475 MPa and sintered at 630 ℃ for 1 h in nitrogen atmosphere. The names for each specimen are listed in the Table 3. 4. The detailed property measurement and microstructure characterization of the as-produced specimens can be found in chapter 6.

Table 3. 4 The definition of the name of the specimens in chapter 6.

Material	Process control agent	Ball milling time (h)	Name
100% elemental Al powders	1.0 wt. % stearic acid	0	Pure Al(-75um)
1.0 wt. % MWNT (*D*: 140 ± 30 nm and *l*: 7 ± 2 μm) and 99. wt. % elemental Al powders (-75um)		5	Al(-75um)_1MWNT_BM5h
		10	Al(-75um)_1MWNT_BM10h
		15	Al(-75um)_1MWNT_BM15h
		20	Al(-75um)_1MWNT_BM20h

To study the effect of different concentration of MWNT on the microstructure and mechanical properties of the Al-MWNT composite materials, 0.5 wt. %, 1.0 wt. % and 2.0 wt. % of MWNT (*D*: 140 ± 30 nm and *l*: 7 ± 2 μm) were ball-milled with elemental aluminium powders (- 75 μm) for 15 h at a constant speed of 250 rpm in argon atmosphere. The "as-milled" Al-MWNT composite powders were then pressed at 475 MPa and sintered at 630 ℃ for 1 h in nitrogen atmosphere. The names for each specimen are listed in the Table 3. 5. The detailed property measurement and microstructure characterization of the as-produced specimens can be found in chapter 7.

Table 3. 5 The definition of the name of the specimens in chapter 7

Material (wt. %)		**Process control agent**	**Ball milling time (h)**	**Name**
Al (-75um)	**MWNT** (*D*: 140 ± 30 nm, *l*: 7 ± 2 μm)			
99.0	0.5	1.0 wt. % stearic acid	15	Al(-75um)_0.5MWNT_BM15h
	1.0			Al(-75um)_1.0MWNT_BM15h
	2.0			Al(-75um)_2.0MWNT_BM15h

Chapter 4. The effect of process control agent on the Al-1.0 wt. % MWNT composite powders

4. 1. Introduction

This chapter is concerned with the study of the effect of process control agent (PCA) on the resultant Al-1.0 wt. % MWNT composite powders processed by high energy ball milling. Two groups of Al and CNTs powders (Group 1: Al (75-106 μm) with 1.0 wt. % MWNT (*D*: 6-9 nm, *L*: 5 μm), group 2: Al (-10 μm) with 1.0 wt. % MWNT (*D*: 10-30 nm, *l*: 10-30 μm)) were selected for this study to demonstrate the necessity of using process control agent (i.e. stearic acid or ethanol) to prevent excessive welding in the ball milling of Al-1.0 wt. % MWNT composite powder. Also, the effect of different process control agent on the ball-milled MWNT and Al-1.0 wt. % MWNT composite powders is analysed. The name of the materials used in this chapter can be found in the Table 3. 2.

4. 2. Results

4. 2. 1 The morphology of the ball-milled Al-1.0 wt. % MWNT composite powders

4. 2. 1. 1. *No PCA*

Fig. 4. 1 presents the SEM micrographs showing the morphology of the ball-milled Al-1.0 wt. % MWNT composite powders without adding any process control gent. Fig. 4. 1. (A) shows that the Al(75-106)MWNT composite powders ball-milled for 5 h have smooth

surfaces, spherical and disc-like shape and an average particle size of approximately 2 mm, which is about 10 times the size of the pristine elemental Al (75-106um) powders. Similarly, the Al(-10um)MWNT composite powders with no PCA ball-milled for 5 h also showed an significant increase in the particle size and reached an average of around 400 μm. The morphology of the ball-milled Al(-10um)MWNT composite powders is displayed in the Fig. 4. 1. (B). These particles have irregular shape and a relatively wide size distribution.

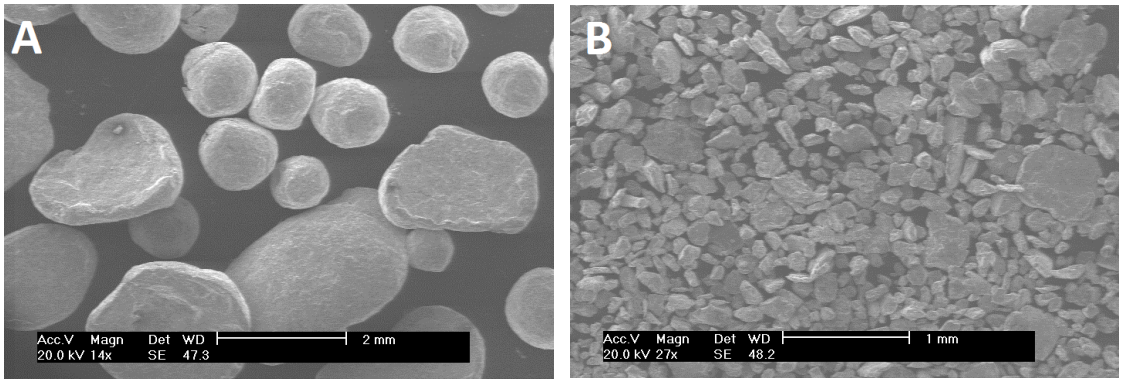


Fig. 4. 1 SEM micrographs of Al-1.0 wt. % MWNT milled for 5 h without the addition of PCA. (A) for Al(75-106)MWNT_BM5h and (B) for Al(-10)MWNT_BM5h.

4. 2. 1. 2. *1.0 wt. % Stearic acid*

In contrast to the evolution of the ball-milled Al-1.0 wt. % MWNT composite powders without any PCA, the composite powders ball-milled with 1.0 wt. % of stearic acid shown different morphology and shape, as shown in the Fig. 4. 2 Comparing Fig. 3. 2. (A) and Fig. 4. 2. (A), it can be seen that large pristine Al(75-106 μm) powders were first flattened into flake shape after being milled for 1 h. As the milling time increased to 5 h, although the laminar morphology remained (Fig. 4. 2. (B)), the average size of particles milled for 5 h decreased slightly and the surfaces became rougher comparing to the Al(75-106 μm)MWNT

composite powders milled for 1 h. Further increasing the milling time to 10 h, the shape of particles became granular and particle size decreased further (Fig. 4. 2. (C)).

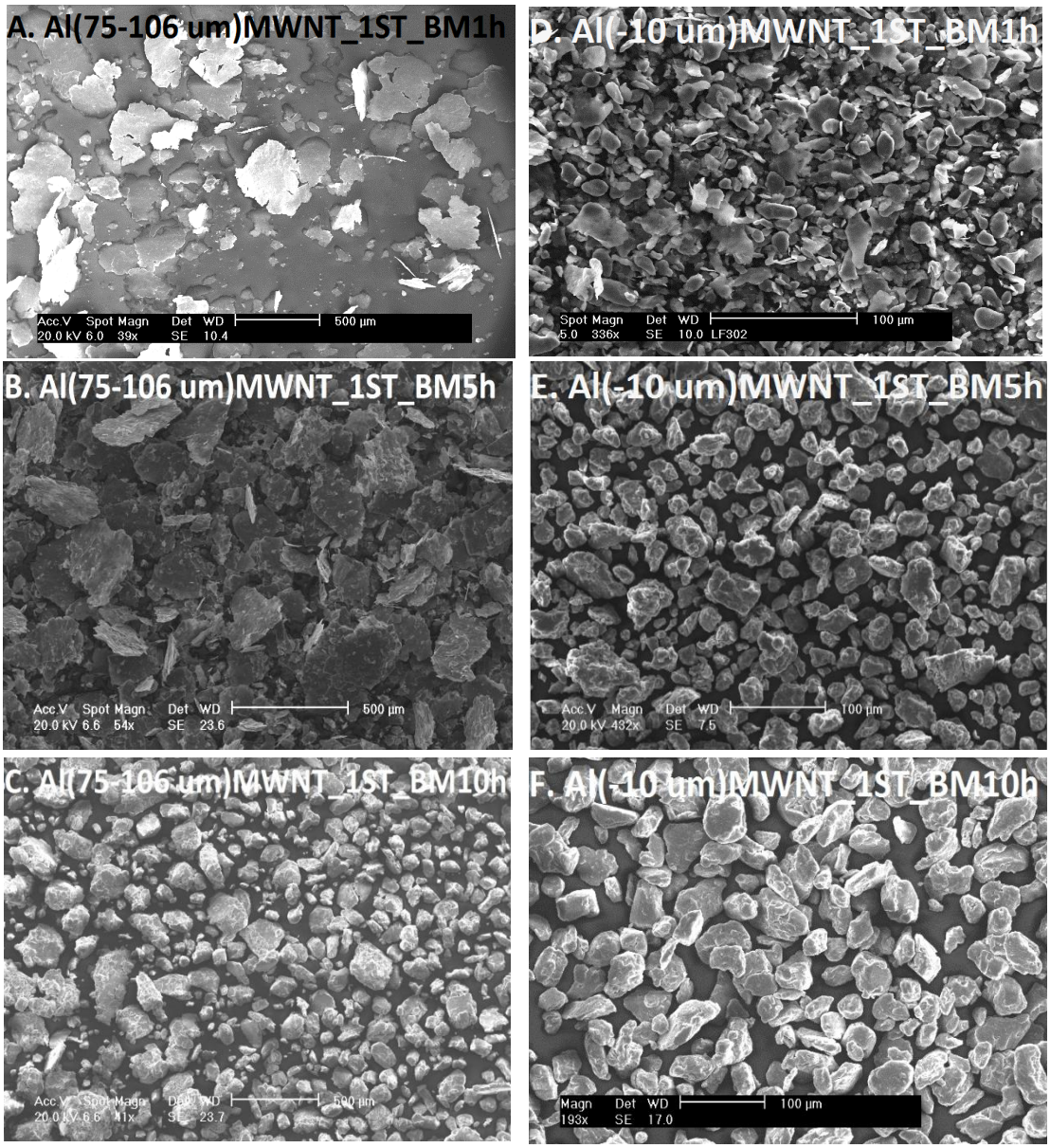


Fig. 4. 2 SEM micrographs showing morphology of the Al-1.0 wt. % MWNT composite powders that ball milled with 1.0 wt. % stearic acid as process control agent for 1 to 10 h. (A)–(C) for Al(75-106 μm)MWNT_1ST_BM1h-10h and (D)–(F) for Al(-10 μm)MWNT_1ST_BM1h-10h.

Fig. 4. 2. (D) – (F) displays the SEM images of the Al(-10 μm)MWNT composite powders

with 1.0 wt. % stearic acid as PCA after ball milling for 1-10 h. It can be seen from the Fig. 4. 2. (D) that the Al(-10 μm)MWNT composite powders (-10 μm) showed flake shape after ball milling for 1 h. As the milling time increased to 5 h, the shape of the composite powders changed into granular and the particle size increased slightly. Further increasing the milling time to 10 h, the granular shape of the composite powders retained and the particle size was further increased.

4. 2. 1. 3. 1.0 wt. % Ethanol

Fig. 4. 3 shows the morphology of the Al-1.0 wt. % MWNT composite powders that ball milled with 1.0 wt. % ethanol as process control agent for 1 to 10 h. It can be seen from the Fig. 4. 3. (A) that the 1 h ball-milled Al(75-106 μm)MWNT_1ET (1.0 wt. % ethanol) composite powders showed disc-like shapes and smooth surfaces. As the milling time increased to 5 h, the particle size of the composite powders was significantly reduced and the shape of particles changed to thin flake with sharp edges, as shown in Fig. 4. 3. (B). When the milling time increased to 10 h, the particle size of the Al(75-106 μm)MWNT_1ET composite powders was further reduced and the shape of particle was granulated.

Similar to the evolution of the Al(75-106 μm)MWNT powders in the ball milling, the particle size of the Al(-10 μm)MWNT composite powders with the addition of 1.0 wt. % ethanol kept an decreasing trend with the increasing milling time. As can be seen from the Fig. 4. 3. (D), that the Al(-10 μm)MWNT composite powders was deformed and flattened slightly after ball milling for 1 h. Further increasing the milling time to 5 h, the composite

powders became much finer showing thin flake morphology (Fig. 4. 3. (E)). When the time of milling increased to 10 h, the particle size of the composite powders was further reduced and fine particles even agglomerated together.

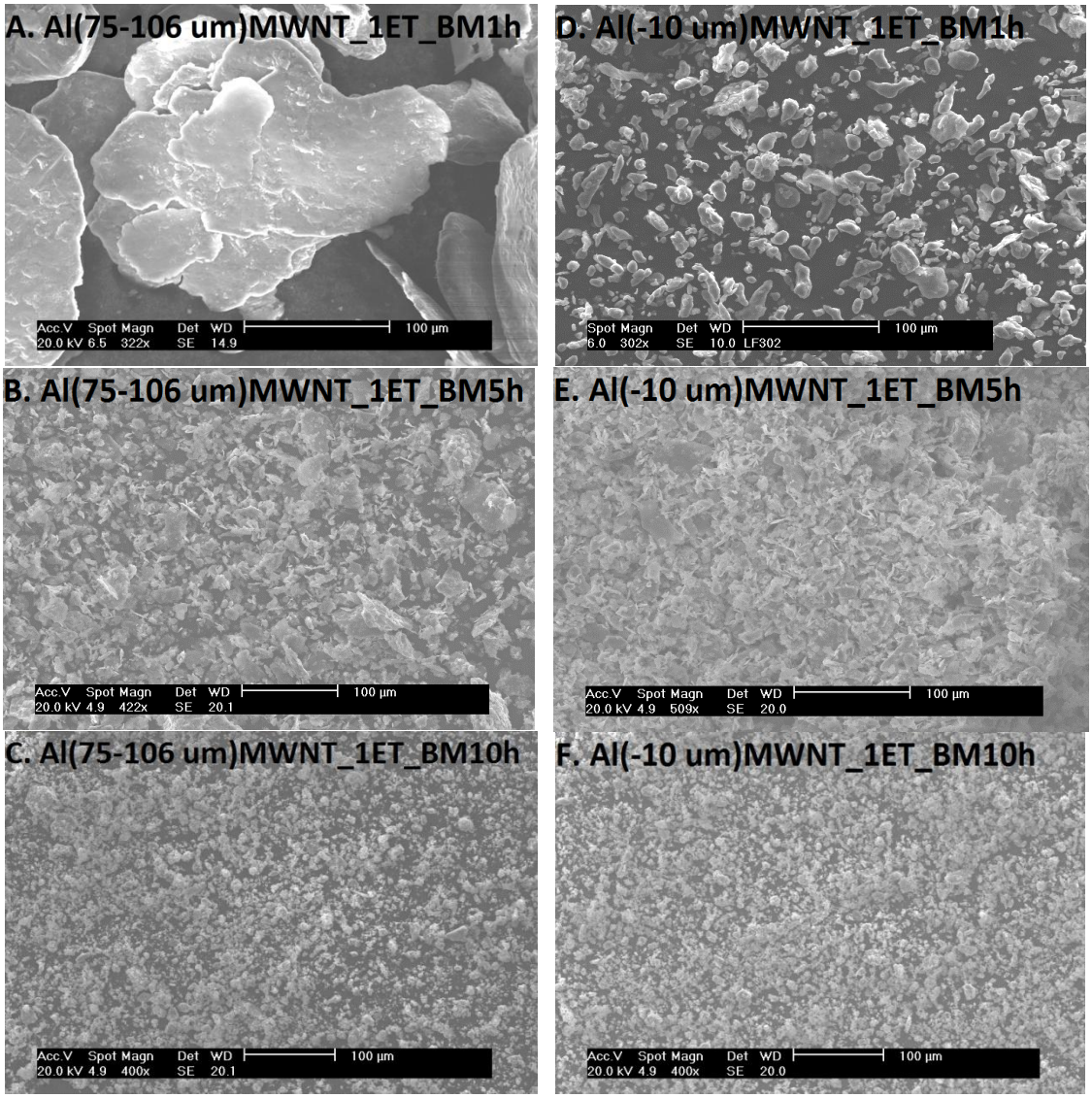


Fig. 4. 3 SEM micrographs showing morphology of the Al-1.0 wt. % MWNT composite powders that ball milled with 1.0 wt. % stearic acid as process control agent for 1 to 10 h. (A)–(C) for Al(75-106 μm)MWNT_1ET_BM1h-10h and (D)–(F) for Al(-10 μm)MWNT_1ET_BM1h-10h.

4. 2. 2 The particle size distribution of the ball-milled Al-1.0 wt. % MWNT composite powders

To quantitatively study the evolution of the Al-1.0 wt. % MWNT composite powders with PCA in the ball milling process, particle size distribution of the ball-milled composite powders were measured and recorded by particle size analyser. Fig. 4. 4 and 4. 2. 2. 2. 1 plot the cumulative particle size distribution of the Al-1.0 wt. % MWNT composite powders ball-milled for 1-10 h with 1. 0 wt. % stearic acid and 1.0 wt. % ethanol as process control agent, respectively.

4. 2. 2. 1. *1.0 wt. % Stearic acid*

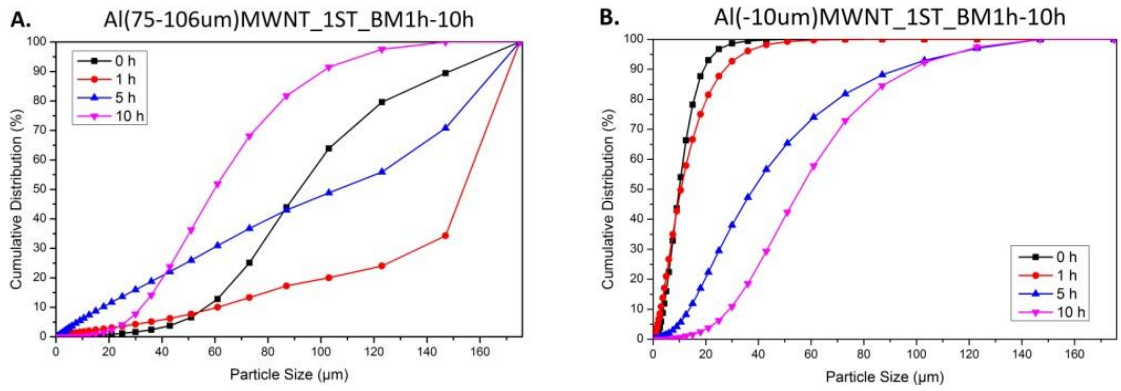


Fig. 4. 4 Cumulative particle size distribution of Al-1.0 wt. % MWNT composite powders with 1.0 wt. % stearic acid as process control agent for 1-10 h of ball milling. (A) for Al(75-106 μm)MWNT_1ST_BM1h-10h and (B) for Al(-10 μm)MWNT_1ST_BM1h-10h.

Fig. 4. 4. (A) presents the cumulative particle size distribution of the ball milled Al(75-106 μm)MWNT composite powders using 1.0 wt. % stearic acid as process control agent. As can be seen from the Fig. 4. 2 .2. 1. 1. (A) that after ball milling for 1 h, the particle size of the composite particles was significantly shifted into the range of larger than 140 μm.

Increase the milling time to 5 h, the overall particle size of the composite powders reduced and the amount of particles below 140 µm evidently increased. Further increasing the milling time, the particle size of the composite powders distinctly shifted to the range that 90 % of the powders were smaller than 100 µm.

Fig. 4. 4. (B) shows the cumulative particle size distribution of the Al(-10 µm)MWNT composite powders ball milled with 1.0 wt. % stearic acid for 1 – 10 h. It is clear that the particle size of the ball milled Al(-10 µm)MWNT composite powders did not change much after ball milling for 1 h besides the particles larger than 20 µm increased slightly. After ball milling for 5 h, the Al(-10 µm)MWNT composite powders significantly shifted to larger particle size that some particles even larger than 100 µm. Further increasing the milling time to 10 h, the amount of particle in the range 20 – 90 µm mainly increased.

4. 2. 2. 2. 1.0 wt. % Ethanol

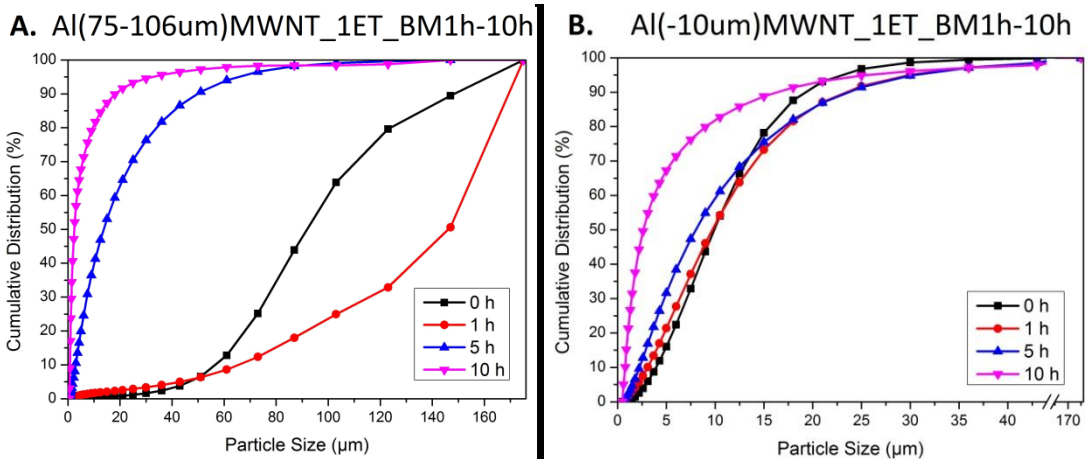


Fig. 4. 5 Cumulative particle size distribution of Al-1.0 wt. % MWNT composite powders with 1.0 wt. % ethanol as process control agent for 1-10 h of ball milling. (A) for Al(75-106 µm)MWNT_1ET_BM1h-10h and (B) for Al(-10 µm)MWNT_1ET_BM1h-10h.

Fig. 4. 5. (A) plots the cumulative particle size distribution of Al(75-106 μm)MWNT composite powders with 1.0 wt. % ethanol as process control agent ball milled for 1-10 h. As can be seen from the Fig. 4. 5. (A) that the particle size of the 1 h ball milled Al(75-106 μm)MWNT composite powders significantly increased and 50 % of the powders are larger than 100 μm. Further increasing the milling time to 5 h, the particle size remarkably shifted back to the smaller range with 90 % of the powders are smaller than 60 μm. When the milling time increased to 10 h, the particle size was further reduced that 90% of the powders are below 10 μm.

Fig. 4. 5. (B) depicts the cumulative particle size distribution of the ball milled Al(-10 μm)MWNT composite powders using 1.0 wt. % ethanol as process control agent. It is obvious in the Fig. 4. 5. (B) that the composite powders larger than 15 μm increased slightly after milling for 1 h. Increasing the milling time to 5 h, only the particles below 13 μm increased moderately. However, the particle size was significantly reduced after 10 h of ball milling that 80 % of the powders are smaller than 10 μm.

4. 2. 2. 3. The comparison of median particle size (D_{50}) between different process control agent

D_{50}, the median diameter of powders, was chosen to compare the representative particle size of ball milled powders, which is also used by other researchers [171]. The median diameters of the Al-1.0 wt. % MWNT composites ball milled with or without process control agent were illustrated in the Table 4. 1. As can be seen from the Table 4. 1 that the particle size of

the 5 h ball-milled Al(75-106um)MWNT and Al(-10um)MWNT composite powders without any PCA reached 2 mm and 400 μm, respectively.

Table 4. 1 The D_{50} of ball-milled Al-1.0 wt. % MWNT particles (um)

Process Control Agent	Non		1.0 wt. % Stearic Acid			1.0 wt. % Ethanol		
Milling Time (h)	0	5	1	5	10	1	5	10
Al(75-106um)MWNT	-	2000	153.70	112.83	59.78	146.50	13.74	2.43
Al(-10um)MWNT	-	400	10.58	38.03	55.95	9.72	8.02	2.64
Pristine elemental Al(75-106um)	91.87	-	-	-	-	-	-	-
Pristine elemental Al(-10um)	9.92	-	-	-	-	-	-	-

For the Al(75-106um)MWNT composite powder using 1.0 wt. % stearic acid as PCA, the particle size was first increased significantly from 91.87 μm (pristine Al(75-106um)) to 153.70 μm after ball milling for 1 h. After milling for 5 h and 10 h, the particle size of the composite was reduced steadily to 112.83 μm and 59.78 μm, respectively. However, the particle size of the Al(-10um)MWNT composite powders ball milled with 1.0 wt. % stearic acid kept an increasing trend with increasing milling time. As can be seen from the Table 4. 1 that the particle size of the Al(-10um)MWNT composite increased slightly from 9.92 μm to 10.58 μm after 1 h of ball milling. Further increasing the milling time to 5 h and 10 h, the particle sizes were further increased to 38.03 μm and 55.95 μm, respectively.

Similar to the Al(75-106um)MWNT composite powder using 1.0 wt. % stearic acid as PCA, the particle size of the Al(75-106um)MWNT composite powder ball milled with 1.0 wt. %

ethanol was increased first then decreased with the increasing milling time. It can be seen from the Table 4. 1 that the particle size of the Al(75-106um)MWNT composite powders increased to 146.50 μm after ball milling for 1 h before reducing to 13.74 μm and 2. 43 μm after further milling for 5 h and 10 h respectively. However, the particle size of the ball milled Al(-10um)MWNT composite powders using 1.0 wt. % ethanol as process control agent kept a decreasing trend with increasing milling time. The particle size was first slightly reduced to 9.72 μm after ball milling for 1 h and then steadily decreased to 8.02 μm and 2.64 μm after ball milling for 5 h and 10 h, respectively.

4. 2. 3 The Raman spectra of the MWNT in the ball-milled Al-1.0 wt. % MWNT composite powders

Raman spectroscopy is employed to reveal the structural information of MWNT after ball milling with aluminium powders. It is known that the peak at around 1350 cm^{-1} in the Raman spectrum of MWNT is called D band peak which represents the defects in the structure of MWNT [76]. Another peak located at around 1580 cm^{-1} is named G band peak which shows the ordered vibration of carbon atoms in the structure of MWNT [16]. The Raman spectra of the ball-milled Al-1.0 wt. % MWNT is presented in the Fig. 4. 6 and Fig. 4. 7.

4. 2. 3. 1. 1.0 wt. % Stearic acid

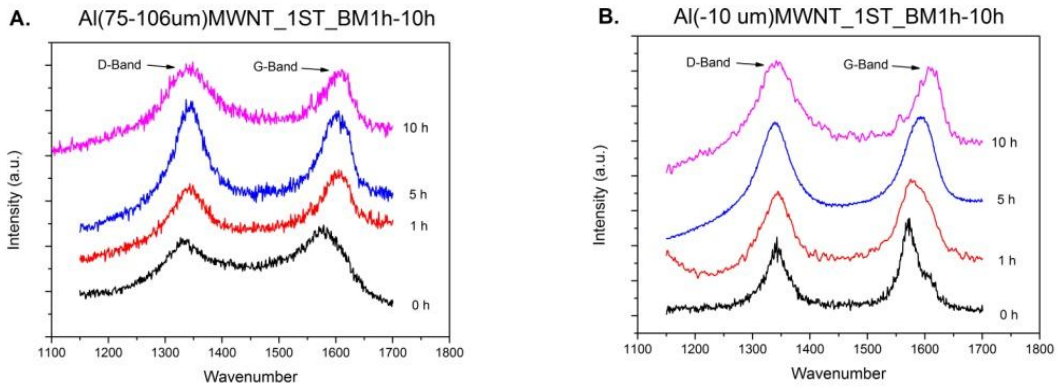


Fig. 4. 6 Raman spectra of Al-1.0 wt. % MWNT composite powders with 1.0 wt. % stearic acid as process control agent ball milled for 1-10 h. (A) for Al(75-106 μm)MWNT_1ST_BM1h-10h and (B) for Al(-10 μm)MWNT_1ST_BM1h-10h

The Raman spectra of the MWNT in the Al(75-106 μm)MWNT composite powders using 1.0 wt. % stearic acid as process control agent is plotted in the Fig. 4. 6. (A). It can be seen that the D band peak is lower than the G band peak in the Raman spectrum of the pristine MWNT (*D*: 6-9 nm, *L*: 5 μm). When the composite powders were ball milled for 1 h, the relative intensity of D band peak slightly increased. Further increasing the milling time to 5 h and 10 h, the peaks of D band are higher than the peaks of G band.

Fig. 4. 6. (B) depicts the Raman spectra of MWNT (*D*: 10-30 nm, *L*: 10-30 μm) in the ball milled Al(-10 μm)MWNT composite using 1.0 wt. % stearic acid as process control agent. As can be seen from the Fig. 4. 6. (B) that the intensity of the D band peak is noticeably lower than that of the G band peak in the pristine MWNT (*D*: 10-30 nm, *L*: 10-30 μm). Increasing the milling time to 1 h, the relative intensity of D band peak increased

correspondingly. When the milling time increased to 5 h and 10 h, the intensity of the D band peak just exceeded that of the G band peak.

4. 2. 3. 2. 1.0 wt. % Ethanol

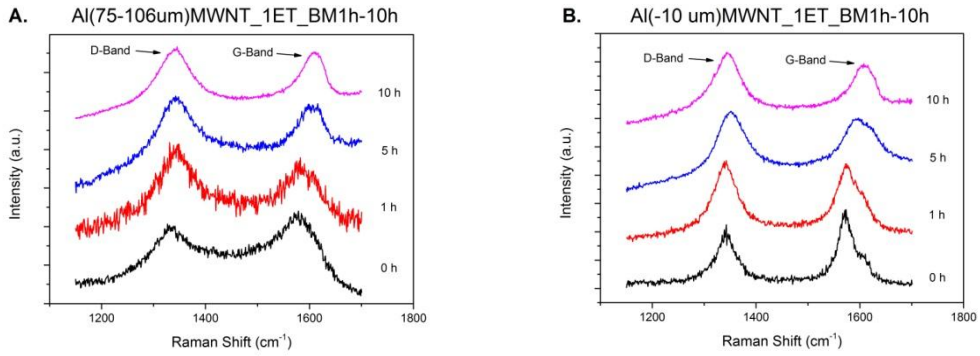


Fig. 4. 7 Raman spectra of Al-1.0 wt. % MWNT composite powders with 1.0 wt. % ethanol as process control agent for 1-10 h of ball milling. (A) for Al(75-106 μm)MWNT_1ET_BM1h-10h and (B) for Al(-10 μm)MWNT_1ET_BM1h-10h

Fig. 4. 7. (A) shows the Raman spectra of MWNT (*D*: 6-9 nm, *L*: 5 μm) in the Al(75-106 μm)MWNT composite using 1.0 wt. % ethanol as process control agent. As can be seen that just after 1 h of ball milling, the intensity of the D band peak is already higher than that of the G band peak. Further increasing the milling time to 5 h and 10 h, the relative intensity of D band peak and G band peak did not change noticeably.

Fig. 4. 7. (B) presents the Raman spectra of the MWNT (*D*: 10-30 nm, *L*: 10-30 μm) in the ball milled Al(-10 μm)MWNT composite with the addition of 1.0 wt. % ethanol as process control agent. Similar to the ball milled Al(-10 μm)MWNT composite_1ET (1.0 wt. % ethanol), the D band peak of the MWNT in the ball milled Al(-10 μm)MWNT composite

exceeds that of the G band peak after just 1 h of ball milling. Further increasing the milling time to 5 h and 10 h, the D band peak and G band peak kept the relative intensity.

4. 2. 3. 3. The comparison of I_D/I_G of MWNT between different process control agent

To assess and evaluate the structure evolution of the MWNT in the ball milling of Al-1.0 wt. % composite, the intensity ratio of D band peak and G band peak (I_D/I_G) is calculated and illustrated in the Table 4. 2 and Table 4. 3.

Table 4. 2 The I_D/I_G of the MWNT in the ball milled Al-1.0 wt. % MWNT composite powders with 1.0 wt. % stearic acid as process control agent.

Milling Time	0 h	1h	5h	10h
Al(75-106 μm)MWNT_1ST	0.85	0.87	0.98	0.99
Al(-10 μm)MWNT_1ST	0.90	0.95	0.98	0.98

As can be seen from the Fig. 4. 2. 3. 3. 1 that the I_D/I_G of the ball milled Al(75-106 μm)MWNT composite powders employed 1.0 wt. % stearic acid as process control agent showed an increase with the increasing milling time. The I_D/I_G in the pristine MWNT (*D*: 6-9 nm, *L*: 5 μm) is 0.85 which increased to 0.87 after ball milling for 1 h. When the milling time increased to 5 h and 10 h, the I_D/I_G increased further to 0.98 and 0.99, respectively.

Similarly, the I_D/I_G of the ball milled Al(-10 μm)MWNT with 1.0 wt. % stearic acid increased steadily with the increasing milling time. The I_D/I_G of the Al(-10 μm)MWNT_1ST composite powders increased from 0.90 (pristine MWNT (*D*: 10-30 nm, *L*: 10-30 μm)) to

0.95 after ball milling for 1 h. Further increasing the milling time to 5 h and 10 h, the I_D/I_G was increased to 0.98.

Table 4. 3 The I_D/I_G of the MWNT in the ball milled Al-1.0 wt. % MWNT composite powders with 1.0 wt. % ethanol as process control agent.

Milling Time	0 h	1 h	5 h	10 h
Al(75-106 μm)MWNT_1ET	0.85	0.94	1.10	1.11
Al(-10 μm)MWNT_1ET	0.90	1.01	1.01	1.03

Table 4. 3 depicts the I_D/I_G of the Al-1.0 wt. % MWNT composite powders ball milled with 1.0 wt. % ethanol for 1-10 h. Although the overall increasing trend of the I_D/I_G in the materials using 1.0 wt. % stearic acid and 1.0 wt. % ethanol as process control agent are similar, the degree of increasing is higher in the materials employed 1.0 wt. % ethanol.

As can be seen from the Table 4. 3. that the I_D/I_G of the ball milled Al(75-106 μm)MWNT_1ET (1.0 wt. % ethanol) composite powders increased significantly from 0.85 (pristine MWNT (*D*: 6-9 nm, *L*: 5 μm)) to 0.90 after ball milling for 1 h. Further increasing the milling time to 5 h and 10 h, the I_D/I_G was further increased to 1.10 and 1.11 respectively. Similarly, the I_D/I_G of the Al(-10 μm)MWNT composite powder with 1.0 wt. % stearic acid increased evidently after just 1 h of ball milling from 0.90 (pristine MWNT (*D*: 10-30 nm, *L*: 10-30 μm)) to 1.01 before reaching 1.03 after ball milling for 10 h.

4. 3. Discussion

4. 3. 1 The effect of process control agent on the Al-1.0 wt. % MWNT composite powders

It can be seen from the Fig. 4. 1 that the particle size of the 5 h ball milled Al(75-106)MWNT and Al(-10 μm)MWNT composite powders without any process control agent reached approximately 2 mm and 400 μm respectively. Obviously, these big particles are not ideal for any engineering use. On the contrary, the Al(75-106)MWNT and Al(-10 μm)MWNT composite powders ball milled with either 1.0 wt. % of stearic acid or ethanol as process control agent kept an average particle size below 160 μm (Fig. 4. 2 .1. 2. 1, Fig. 4. 3 and Table 4. 1)

The reason for the growth of particle size is the excessive cold welding of ductile Al powder as compare to fracturing of particle resulted from strain hardening [16] during the ball milling process. High kinetic energy milling balls not only deformed the soft Al particles but also welded them together when the clean and flat surfaces were brought into contact, which led to the increase of particle size. In contrast, the addition of PCA (i.e. ethanol or stearic acid) gradually dispersed and covered the surfaces of Al particles during the ball milling process. This formed a barrier over the fresh fractured surfaces of Al particles that inhibited particle welded together by preventing the contact and diffusion of Al particles. In addition, the PCAs reduced the tendency of welding between ductile Al powders and stainless steel milling balls and inner walls of milling pots [172]. Thus, the presence of PCA in the Al-1.0

wt. % MWNT led to a smaller particle size as compared to those milled without PCA.

Therefore, it is necessary to add PCA into the ductile powders prior to the ball milling to prevent the excessive welding of powders and yield fine particles during the ball milling process.

4. 3. 2 The effect of different process control agent on the Al-1.0 wt. % MWNT composite powders

It is worth notice from the Table 4. 1 that the particle size obtained is different in both Al(75-106)MWNT and Al(-10 μm)MWNT composite powders after milling for the same time when different process control agents were used. As can be seen from Table 4. 1 that with the addition of 1.0 wt. % stearic acid, the median particles size of Al(75-106)MWNT reached 112.83 μm and 59.78 μm after ball milling for 5 h and 10 h respectively. While for the powders of Al(75-106)MWNT milled with 1.0 wt. % ethanol, the median size significantly decreased to 13.74 μm and 2.43 μm after milling for the same 5 h and 10 h individually.

Similar trend is also found in the ball-milled Al(-10 μm)MWNT composite powders. The median particle size of the "as-milled" Al(-10 μm)MWNT with 1.0 wt. % stearic acid is 38.03 μm and 55.95 μm for a milling time of 5 h and 10 h (Table 4. 1), respectively. However, when 1.0 wt. % ethanol was applied as process control agent, much finer particles was obtained. The Al(-10 μm)MWNT composite powders ball milled with 1.0 wt. % stearic

acid for 5 h and 10 h yielded powders with median particle sizes of 8.02 μm and 2.64 μm (Table 4. 1), respectively. These results indicate that ethanol is more effective in reducing particle size in ball milling than the same amount of stearic acid. Similar results are reported by other researchers [173].

Although the reason for the different impact of stearic acid and ethanol on ball-milled particles is not fully understood yet, several possible reasons were proposed. It is reported [174] that the mobility of the liquid state PCA is better than that of the solid state PCA. Since ethanol is a liquid which can reach the cracks on the particles that solid state stearic acid powders cannot reach easily. Also, it is possible that ethanol in a liquid phase absorbed less impact energy from milling balls than stearic acid as the solid form of stearic acid may be deformed by the impacting balls. Therefore, the kinetic energy transfer to the Al powder containing the CNT was greater in the case of ethanol resulting in more fracturing leading to finer particle size as compared to stearic acid case.

Another possible explanation is the different molecule size which affects the absorption of PCA on mixture surfaces [175]. A ethanol molecule (C_2H_5OH) has 5 C-H bond whereas a stearic acid molecule ($CH_3(CH_2)_{16}COOH$) has 35 C-H bond. Based on the length and angle of C-H bond, it can be understood that the stearic acid molecule is much bigger than ethanol molecule. Therefore, for the same weight, the amount of ethanol molecule is more than that of the molecule of stearic acid. The increase of molecule amount when using ethanol may enhance the ability of preventing the welding of ductile Al particles by covering more

surfaces of aluminium during the ball milling process.

4. 3. 3 The effect of different process control agent on the structure of MWNT

Comparing the same starting materials (Al(75-106)MWNT or Al(-10 μm)MWNT) ball milled with 1.0 wt. % of stearic acid or ethanol, the obtain I_D/I_G of the ball milled powders is different. As can be seen from the Table 4. 2 and Table 4. 3 that the I_D/I_G of the Al(75-106)MWNT composite powders ball milled with 1.0 wt. % ethanol increased to 1.11 after milling for 5 h and peaked at 1.12 for 10 h. However, when 1.0 wt. % of stearic acid was applied, the I_D/I_G of the Al(75-106)MWNT composite powders only increased 0.98 and 0.99 after milling for 5 h and 10 h respectively.

Similarly, the I_D/I_G of the ball milled Al(-10 μm)MWNT composite powders with 1.0 wt. % of ethanol reached at 1.01 and 1.03 after milling for 5 h and 10 h respectively, while the I_D/I_G was only 0.98 when 1.0 wt. % of stearic acid was applied for the same milling time (Table 4. 2 and Table 4. 3). Overall, the I_D/I_G of the composite powders ball milled with 1.0 wt. % ethanol is higher than that of the composite powders ball milled with 1.0 wt. % stearic acid.

The difference between the I_D/I_G of the ball-milled composite powders when 1.0 wt. % of ethanol and 1.0 wt. % stearic acid was applied means that the more defects were introduced into the structure of MWNT when 1.0 wt. % of ethanol was added in the composite powders

than that with 1.0 wt. % of stearic acid. It is known that if the size difference between the MWNT and aluminium particles is reduced, the chances for them to be impacted by milling balls would come close. On the other hand, the presence of relatively big aluminium particles would reduce the chances for MWNT to be hit by the ball bearings. Since the application of 1.0 wt. % ethanol in the composite powders tend to yield finer composite particles (Table 4. 1), the MWNT in the composite powders are more likely to be stroke or impacted by the milling balls. Therefore, the structure of MWNT was more severely damaged when 1.0 wt. % ethanol was applied in the ball milling of the Al-1.0 wt. % MWNT composite.

4. 4. Summary

The effect of process control agent on the particles and the structure of MWNT in ball-milled Al-1.0 wt. % MWNT composite powders can be summarised as follows:

1. The use of process control agent such as ethanol and stearic acid prevents the excessive welding of aluminium particles during ball milling process. The application of process control agent is necessary in the ball milling of the Al-1.0 wt. % MWNT composite powders.

2. The application of 1.0 wt. % ethanol yields finer composite particles with smaller D_{50} values than that of 1.0 wt. % stearic acid.

3. The application of 1.0 wt. % ethanol was found to introduce more defects into the structure of MWNT than 1.0 wt. % stearic acid under the same milling condition. Therefore, 1.0 wt. % stearic acid was chose for the following study.

Chapter 5. The effect of ball milling on the microstructure and mechanical properties of aluminium materials

5. 1. Introduction

This chapter introduces the properties and microstructure of both pristine and high energy ball milled aluminium powders before and after pressing and sintering. More specifically, the evolution of the aluminium particles during the ball milling process is investigated by SEM and particle size analysis. Vickers micro-hardness test and ASTM standard tensile test were employed to study the mechanical properties of the ball-milled aluminium powders and sintered bulk specimens, respectively. The microstructure of the as-produced powders and sintered specimens were revealed by optical microscopy and SEM respectively. The definition of the names of each material studied in this chapter is listed in the Table 3. 3.

5. 2. The effect of ball milling on aluminium powders

5. 2. 1 Results

5. 2. 1. 1. *Morphology*

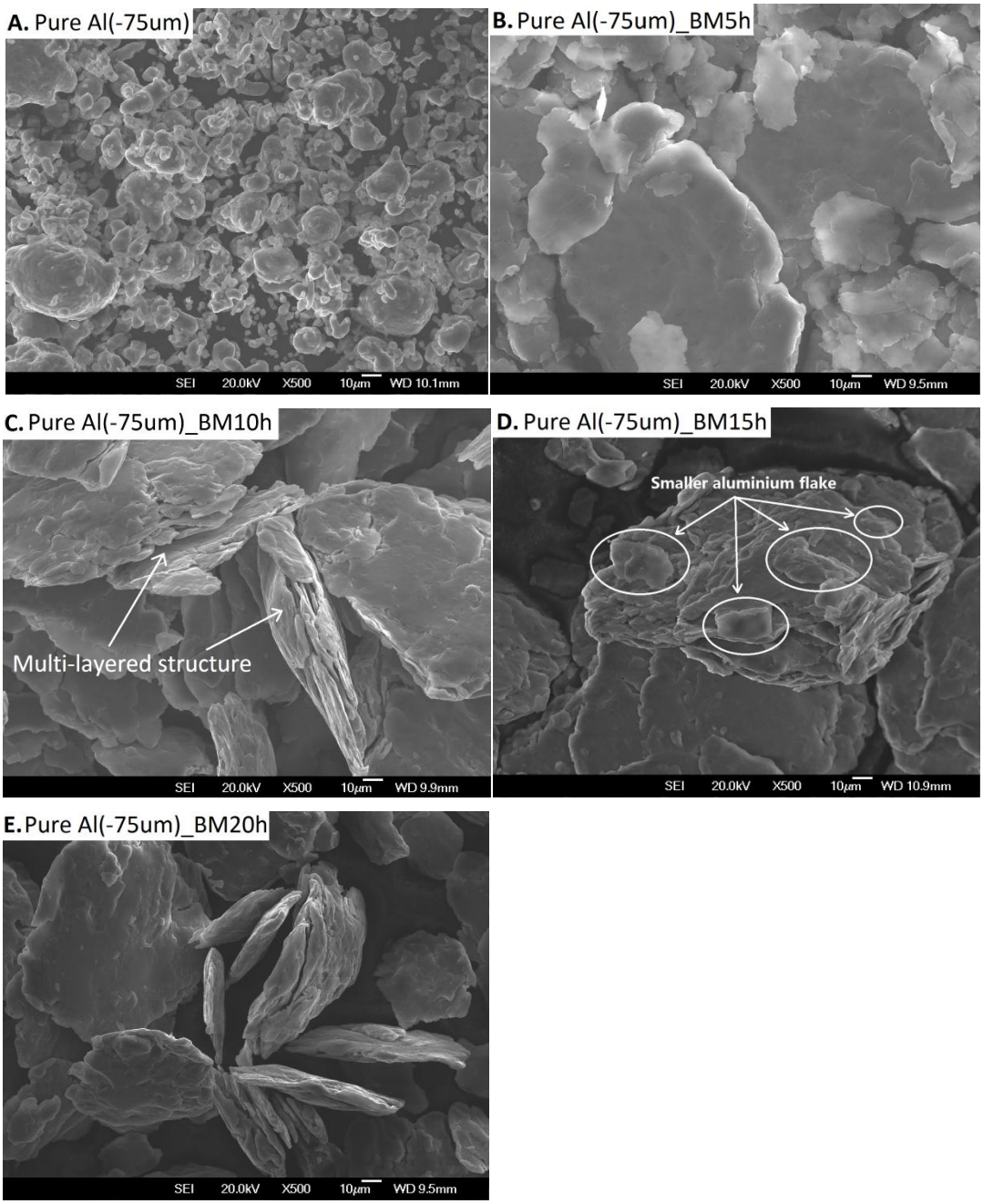


Fig. 5. 1 Secondary electron micrographs showing the morphology of the aluminium powders ball milled for (A) 0 h, (B) 5 h, (C) 10 h, (D) 15 h and (E) 20 h (Magnification: 500×).

More specifically, it can be seen from the Fig. 5. 1. (B) that the 5 h ball-milled aluminium powders have single layer structure and laminated morphology with increased particle size and smooth surface, as compared to the starting Al powder (Fig. 5. 1. (A)). After ball milling for 10 h, both the particle size and thickness were further increased. The surfaces of the 10 h ball-milled aluminium powders became rough and multi-layer structure is visibly observed as indicated by arrows in the Fig. 5. 1. (C) which is indication of welding. For 15 h milling time, the thickness of particles increased further and the surface of the aluminium particles become even rougher. Especially, smaller aluminium flakes were found attached to large aluminium particles (indicated in the Fig. 5. 1. (D)). For 20 h milling, the ball-milled aluminium powders showed a more uniform particle size distribution, the edges of aluminium particles became rounded and the ratio of length or width to the thickness decreased.

Table 5. 1 The content of oxygen element on the surfaces of the ball-milled aluminium particles, measured by EDX at 5 kV

Specimen	**Composition of oxygen on the particle surface (wt. %)**
Pristine pure Al(-75um)	0.23
Pure Al(-75um)_BM5h	0.91
Pure Al(-75um)_BM10h	1.46
Pure Al(-75um)_BM15h	1.85
Pure Al(-75um)_BM20h	2.17

Table 5. 2. 1. 1. 1 shows the average oxygen content on the surfaces of the ball-milled aluminium particles which was measured by EDX using a voltage of 5 kV. It is worth noticing that the concentration of oxygen on the aluminium particles increased with the

increasing of ball milling time.

5. 2. 1. 2. Cross-section

Fig. 5. 2 shows the cross-section microstructure of the ball-milled aluminium powders by optical microscope taken at magnifications of 100× and 500×. As can be seen from the Fig. 5. 2. (A) and (B) that grains of the gas atomised pristine aluminium particles are equiaxed without obvious preferable orientation of growth. Also, the micro-pores inside the particles are visible under the optical microscope, as indicates by the red circles in the Fig. 5. 2. (B).

According to Ternovoi et al. [176], these pores are formed due to the diffusion of high velocity gas into the aluminium particles during the atomization process and they were trapped within the aluminium particles in the following solidification process. Hence pores were clearly presented on the cross-section of pristine atomized aluminium particles.

In the Fig. 5. 2. (C) and (D), the 5 h ball-milled aluminium particles shows the cross-section of flattened laminated layers of aluminium. The micro-pores inside the aluminium particles are still visible as indicates by red circles in the Fig. 5. 2. (D). Most of the aluminium flake kept individual particle shape and only little welding is observed which is corresponding to the SEM observation in the Fig. 5. 1. (B). Comparing all the cross-section of the ball milled aluminium powders, the 5 h ball-milled aluminium powders possessed the lowest average thickness which is around 6 μm.

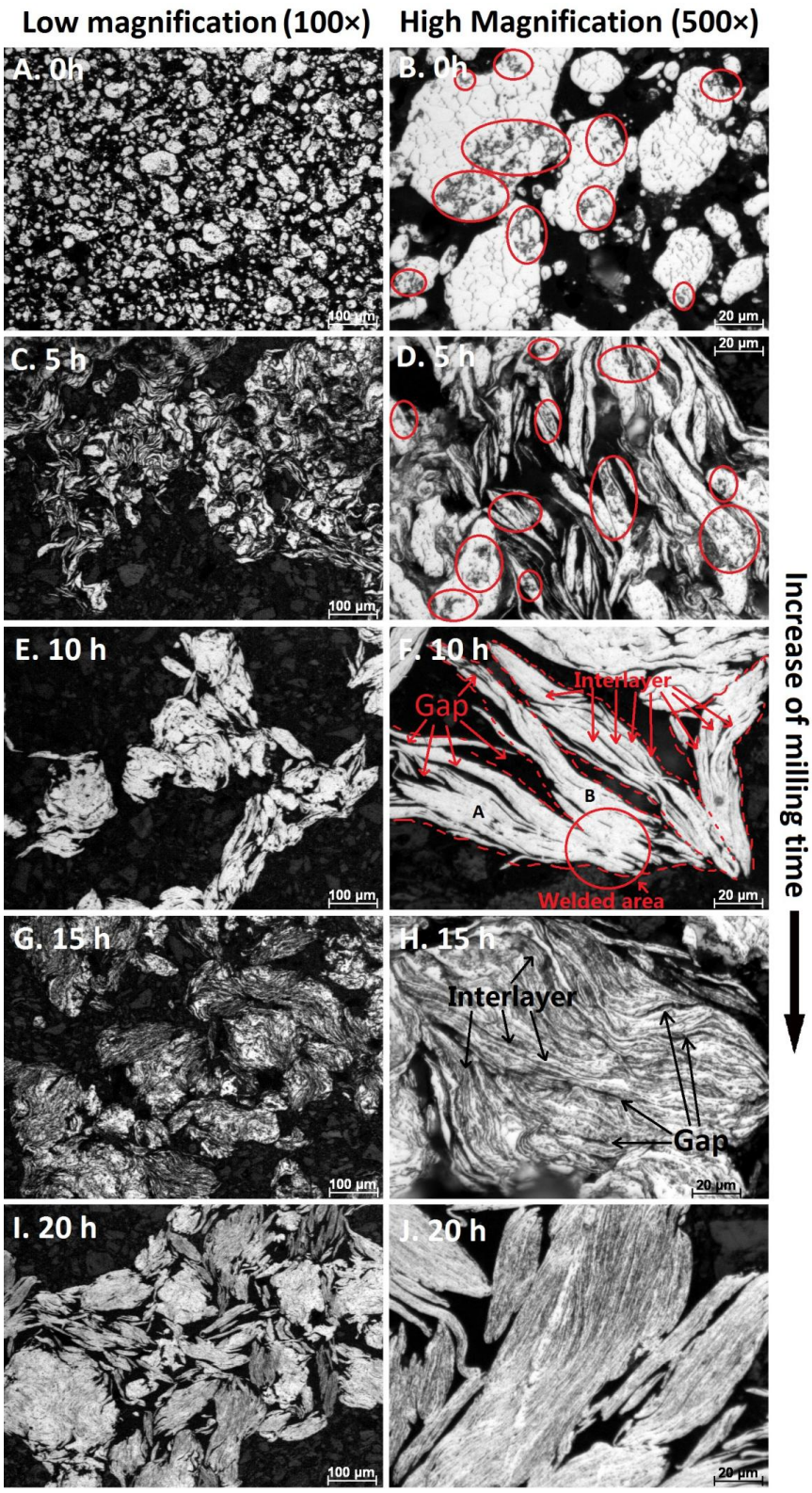


Fig. 5. 2 The optical micrographs showing the cross-section of the aluminium powders ball-milled for (A)-(B) 0 h, (C)-(D) 5 h, (E)-(F) 10 h, (G)-(H) 15 h and (I)-(J) 20 h. The red circles in (B) and (D) indicate the pores inside the particles. The red circle in (F) indicates the welded area inside the aluminium particle.

When the ball milling increased to 10 h, distinct multi-layered structure is observed in the 10 h ball-milled aluminium powders which is showed in the Fig. 5. 2. (F). As can be seen from the Fig. 5. 2. (F), the thickness of the ball-milled aluminium flake increased to approximately 20 μm while the average thickness of the interlayer inside the ball-milled particle is around 3 μm (as indicated by arrows in the Fig. 5. 2. (F)). Although some area inside the aluminium flakes already welded together like the area marked by the red circle in the Fig. 5. 2. (F), the gap between each layer are still visible like the gaps inside the particle A and B in the Fig. 5. 2. (F).

For milling time of 15 h, it can be seen from the Fig. 5. 2. (G) and (H) that although the overall thickness of the ball-milled aluminium particles is increased, the average thickness of the interlayer inside the multi-layer structure is decreased further to around 1 μm. Also, the number of layers inside each aluminium particles is increased and the gap between each interlayer is further reduced that no big or long gap was found in the cross-section of the 15 h ball-milled aluminium particle.

To understand the composition of the black points and lines showed in the Fig. 5. 2. (H), SEM was employed to characterize the cross-section of the ball-milled aluminium particles. Fig. 5. 3 (A) and (B) are the secondary electron micrograph and the backscattered micrograph of the same area on the cross-section of the 15 h ball-milled aluminium particle. The areas marked by the red circles in the Fig. 5. 3 (B) demonstrate the existence of

micro-pores and micro-gaps inside the 15 h ball-milled aluminium particle.

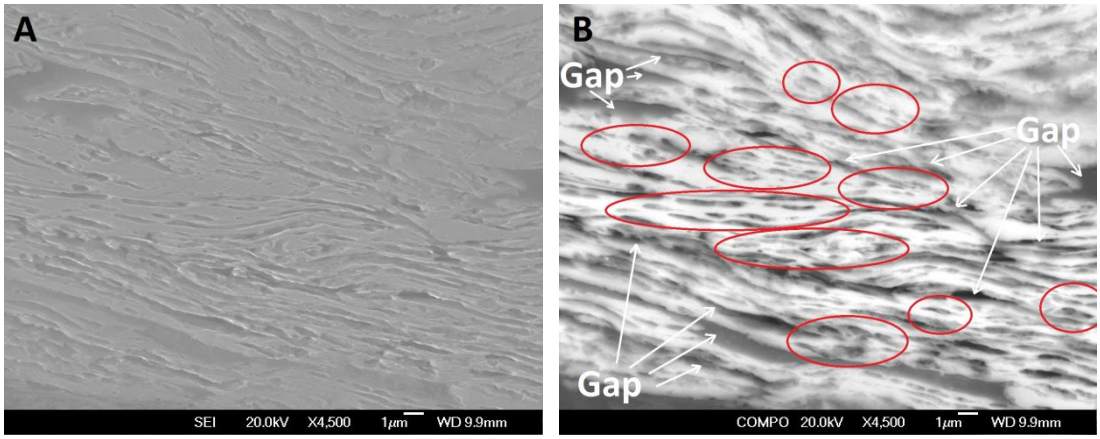


Fig. 5. 3 The secondary electron (A) and the backscattered (B) micrographs of the same area on the cross-section of the 15 h-ball-milled aluminium particle. The red circles in (B) indicate the micro-pores and micro-gaps inside the particle.

Fig. 5. 2 (I) and (J) show the cross-section of 20 h ball-milled aluminium particles. After ball milling for 20 h, the internal microstructure of the ball-milled aluminium particles are homogenized. The average thickness of each interlayer inside the aluminium particle are uniformed and reduced to below 1 μm. More detailed microstructure of the 20 h ball-milled aluminium powders can be found in the Fig. 5. 4, which presents the secondary electron (A) micrograph and backscattered electron micrograph (B) of the same area on the cross-section of the 20 h ball-milled aluminium particles. Comparing to the 15 h ball-milled aluminium powders (Fig. 5. 2 .1. 2. 2), it is clear that fewer micro-gaps and smaller micro-pores were found in the 20 h ball-milled aluminium powders, but the micro-pores found on the cross-section were uniformly distributed in the particle.

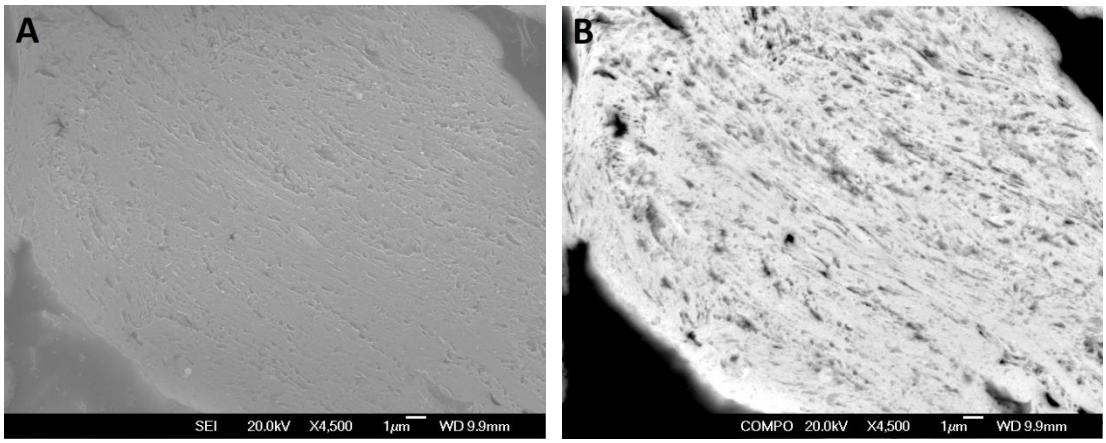


Fig. 5. 4 The secondary electron (A) and the backscattered electron (B) micrographs of the same area on the cross-section of the 20 h ball-milled aluminium particles.

5. 2. 1. 3. Particle size distribution

While the SEM micrographs in the Fig. 5. 1 provide the qualitative data of the characterisation of pristine aluminium and ball-milled aluminium powders, the particle size analysis quantified the distribution of aluminium particle size before and after ball milling. The differential particle size distribution of the ball-milled aluminium powders is plotted in the Fig. 5. 5. As can be seen from the Fig. 5. 5, the particle size peaks for the prisitine aluminium is below 25 μm. After ball milling for 5 h, the peak of particle size significantly shifted to around 70 μm with a broader size range, which is corresponding to the flattening of aluminium particles as shown in the Fig. 5. 1. (B). Further increasing the milling time to 10 h, the particles in the range of 25 μm to 50 μm was decreased while the particles in the 100 μm to 150 μm was increased. In addition, the particles over 200 μm were found. These changes of the particle size distribution all suggest the increase of the average particle size.

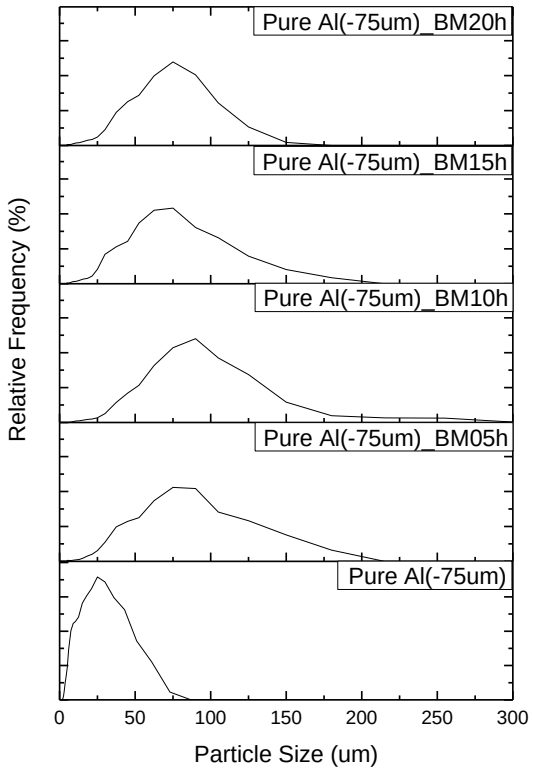


Fig. 5. 5 The differential particle size distribution of aluminium powders before and after ball milling.

However, after ball milling for 15 h, the ball-milled aluminium particles shifted back into smaller size range and the particles distributed in the size range greater than 200 μm were no longer observed (Fig. 5. 5). For 20 h ball-milled aluminium powders, the particles between 150 μm and 200 μm disappeared and the amount of the particles between 25 μm and 50 μm was decreased. More importantly, the particle size distribution was more concentrated and the intensity of the main peak was increased which indicates the welding and work hardening/fracturing in the ball milling process reached a dynamic equilibrium.

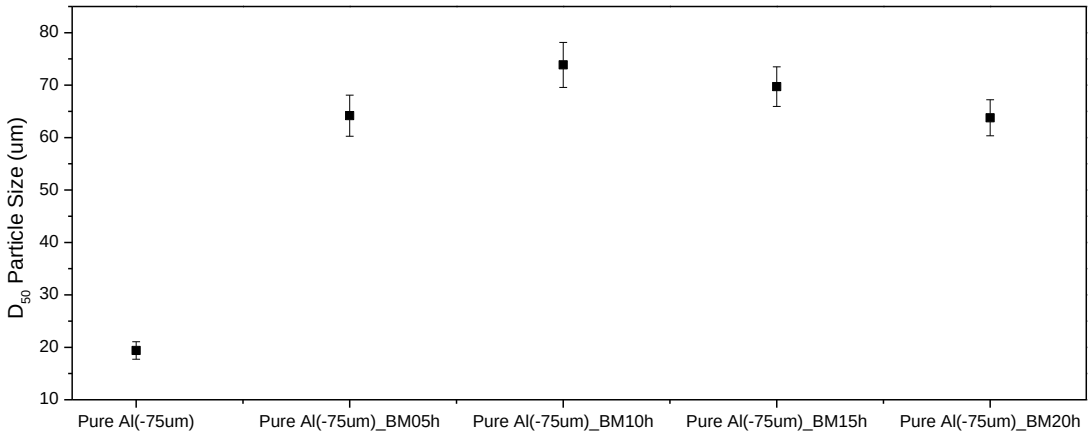


Fig. 5. 6 The median particle size (D_{50}) of both pristine and ball-milled aluminium powders.

The median particle size (D_{50}) of the pristine and ball-milled powders was plotted in the Fig. 5. 6. As can be seen from the Fig. 5. 6 that the median particle size of the raw aluminium powders was only 19.40 ± 1.68 μm. Nevertheless, the median particle size of the aluminium particles that ball milled for 5 h and 10 h reached 64.18 ± 3.92 μm and 73.86 ± 4.29 μm respectively. Further increasing the milling time to 15 h and 20 h, the median particle size decreased to 69.71 ± 3.77 μm and 63.78 ± 3.43 μm, respectively.

5. 2. 1. 4. X-ray diffraction

Fig. 5. 7 shows the X-ray diffraction patterns of the pristine and ball-milled aluminium powders. As can be seen from the Fig. 5. 7 that only five major peaks, corresponding to the (111), (200), (220), (311) and (400) lattice planes of aluminium were exhibited without notable peak shifting. No other XRD peak was found which means either the absence of other phase or the concentration of the phase were too low that the X-ray diffractometer used in the current experiment did not have adequate resolution. What's also worth noting is that the XRD peaks broadened with increasing milling time.

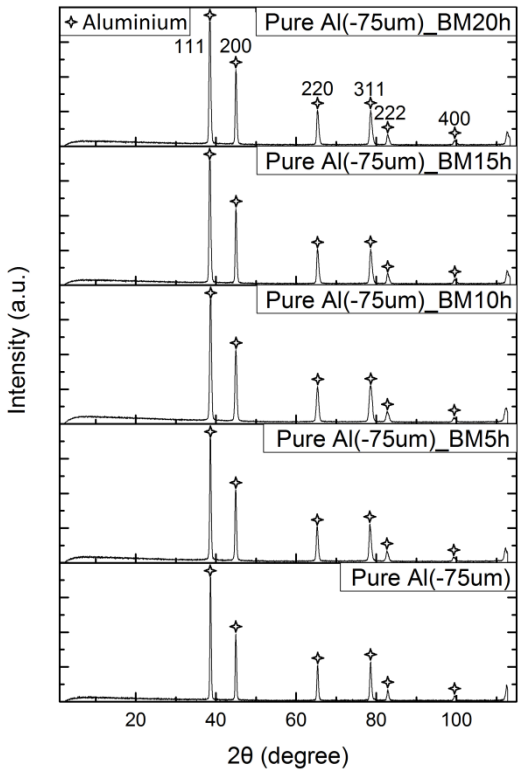


Fig. 5. 7 The XRD patterns of the pristine and ball-milled aluminium powders.

5. 2. 1. 5. Differential scanning calorimetry

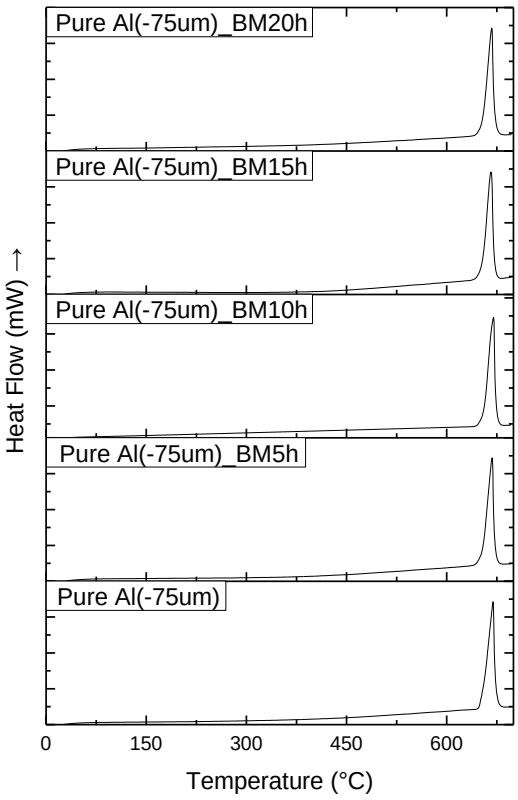


Fig. 5. 8 The differential scanning calorimetric (DSC) curves of the pristine and ball-milled aluminium powders.

The thermal analysis of the aluminium powders was carried out and the corresponding differential scanning calorimetric curves are presented in the Fig. 5. 8. It is apparent from the Fig. 5. 8 that all the ball-milled aluminium powders absorbed similar amount of energy when they were heated from ambient temperature (25 ℃) to 700 ℃ at a constant heating rate of 10 ℃ /min in argon atmosphere. The DSC peak at around 660 ℃ is due to the melting of aluminium powders. No other noticeable exothermic and endothermic peak was observed which indicates no significant chemical reaction occurred in the heating process.

5. 2. 1. 6. Vickers micro-hardness

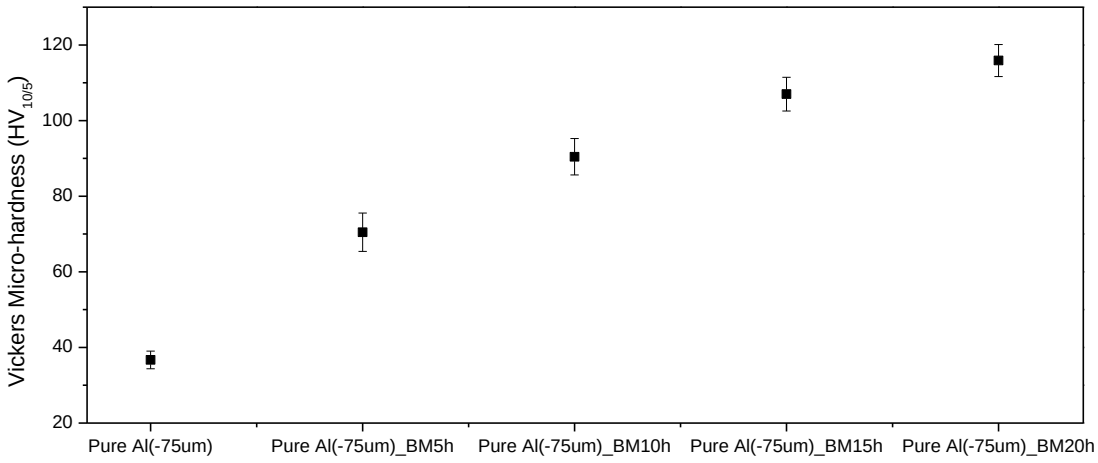


Fig. 5. 9 The Vickers micro-hardness of the pristine and ball-milled aluminium powders.

The hardness of powders is a significant parameter in the industry and engineering field of powder metallurgy since it influences the compatibility and formability of powders. The Vickers micro-hardness of the pristine and ball-milled aluminium powders was measured and plotted in Fig. 5. 9. It is notable that the hardness of the ball-milled aluminium particles increased with increasing milling time.

More specifically, the pristine aluminium has a Vickers micro-hardness of 36.70 ± 2.33 $HV_{10/5}$. In comparison, the hardness of the ball-milled aluminium powders was improved to 70.48 ± 5.06 $HV_{10/5}$ and 90.43 ± 4.81 $HV_{10/5}$ after ball milling for 5 h and 10 h, respectively. At longer ball milling time, the increment of the hardness was reduced. The Vickers micro-harnesses of the 15 h ball-milled and 20 h ball-milled aluminium particles were 107 ± 4.45 $HV_{10/5}$ and 115.88 ± 4.24 $HV_{10/5}$ respectively.

5. 2. 2 Discussion

5. 2. 2. 1. The effect of ball milling on the structure of aluminium powders

Generally, there are two processes competing in the typical high energy ball milling [51, 87] namely welding and work hardening (fracturing). Specifically, welding is due to the soft and ductile aluminium particles being collided by the high energy and high speed moving milling balls which reduces the diffusion distance of powders. Also, the inner temperature of the milling pot increases because of the impact and friction between milling media (e.g. milling balls and milling pots), between milling media and powder, as well as between powders. Some researchers reported that the temperature in the milling pot reached to 250 ℃ [177]. Subsequently, the increased temperature promotes the atomic diffusion between powders, the aluminium powders are welded together and the overall particle size increases. Since the increase of particle size is not favourable in most cases, cooling methods like water circulation of milling pot and pause cycle in the milling process for a certain time interval are used to prevent the over-temperature and excessive welding.

The other process occurs in the high energy ball milling is work hardening (also known as strain hardening or cold working). The shear effect of the high energy milling ball increases the density of strain, defects and dislocations in the crystal structure of powders. This increases the hardness and brittleness of powders, ultimately fractures the powders, leading to reduction of the particle size. In general, the competition between welding and work

hardening during the ball milling process governs the resultant particle size, shape and microstructure of the ball-milled powders.

According to the morphology observation and the microstructure analysis by SEM (Fig. 5. 1) and optical microscopy (Fig. 5. 2), the schematic diagram of the evolution of aluminium particles in the ball milling process is presented in the Fig. 5. 10.

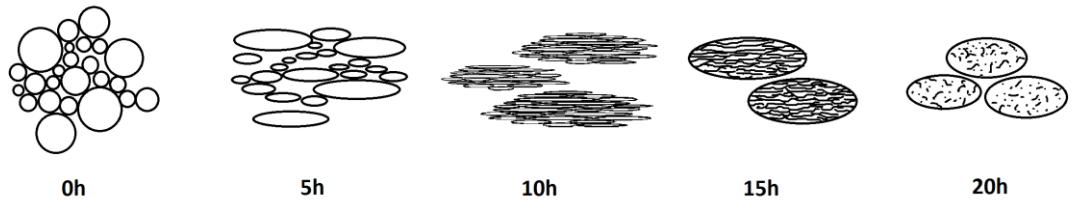


Fig. 5. 10 The schematic diagram of the evolution of aluminium particles during ball milling process.

As can be seen from the Fig. 5. 1. (A), the pristine aluminium particles have smooth surfaces and relatively equiaxed spherical shape. Also, the pristine aluminium powders composed of a combination of large and small particles which can be seen from the morphology in the Fig. 5. 1. (A)) and particle size distribution in the Fig. 5. 5. Therefore, the pristine aluminium powders in the Fig. 5. 10. (0 h) are represented by spherical particles with various particle sizes.

After ball milling for 5 h, the aluminium powders were flattened and severely plastic deformed under the severe impact of milling balls, showing a single-layered disc like-shape (Fig. 5. 1. (B)). Also, the overall surface area of the aluminium powders was significantly

increased (Fig. 5. 1. (B)) while the thickness of the aluminium powders was significantly reduced to around 6 μm at this stage. Moreover, most of the aluminium powders are still separated and welding is not significant, which can be seen from the cross-section of the powders (Fig. 5. 2. (D)). Hence, the deformed and separated particles are used to depict the 5 h ball-milled aluminium particles in the Fig. 5. 10 (5h).

When the ball milling time increase to 10 h, multi-layered structure in the ball-milled particles was formed on a large scale (Fig. 5. 1. (C)) due to more particles were welded together. The collision of milling balls reduced the thickness of the interlayer inside the ball-milled aluminium particles to approximately 3 μm (Fig. 5. 2. (E) and (F)) in spite of the overall median particle size was significantly increased to 73.86 ± 4.29 μm. Also, relatively large gaps between each interlayer of aluminium were observed in the ball-milled powders (Fig. 5. 2. (F)). Thus, the structure of the 10 h ball-milled aluminium particles are denoted by the particles with relatively thick layers of welded aluminium (Fig. 5. 10 (10h)).

Further increasing the milling time to 15 h, the number of interlayer inside the ball-milled aluminium powders were noticeably increased (Fig. 5. 2. (H)) due to more aluminium flakes were welded together. Also, the average thickness of the interlayer in the ball-milled aluminium particles was further reduced to around 1 μm (Fig. 5. 2. (H)) under the impact of milling ball. Moreover, a certain number of particles were fractured by milling balls so that the median particle size was slightly reduced to 69.71 ± 3.77 μm. Therefore, the aluminium powders ball-milled for 15 h were represented by the particles with multi-layered structure

of relatively long micro-gaps and thin interlayers (Fig. 5. 10 (15h)).

After 20 h of ball milling, the multi-layered structure in the 20 h ball-milled aluminium powders was not as noticeable as before (Fig. 5. 4) because the most of the micro-gaps were welded under the collision of milling balls. Also, the accumulation of strain and dislocations inside the ball-milled particles reduced the ductility of the aluminium powders thus more particles were fractured and the median particle size was further decreased to 63.78 ± 3.43 μm. Moreover, the microstructure of the 20 h ball-milled aluminium powders were uniformed and only micro-pores and short micro-gaps dispersed in the cross-section (Fig. 5. 4). Hence, the powders with internal micro-gaps and micro-pores were seen in 20 h ball-milled aluminium particles (Fig. 5. 10 (20h)).

In summary, the welding process was more pronounced from the start of milling up to 10 h, giving coarser median particle size and multi-layered microstructure. Conversely, work hardening process dominated in longer milling times of 15 h and 20 h, yielding particle of finer median particle size. Similar behaviour of aluminium particles in the mechanical alloying process was also reported by other researchers [178].

5. 2. 2. 2. The effect of ball milling on the hardness of aluminium powders

It is worth noting that the width of the XRD peaks increased with the increasing milling time. According to William-Hall equation [179, 180], the broadening of XRD peaks is due to the

refinement of grain size and/or the increasing of lattice strain. Obviously, under the impact of high energy milling balls, aluminium particles underwent severe plastic deformation and the grain size was reduced during the ball milling process. Specifically, in the early stage of ball milling, plastic deformation proceeds by slip and twinning at low and moderate strain rates resulted from ball milling. With increasing milling time, the density of dislocation increases and the crystal disintegrates into subgrains at heavily strained region. Further increasing the milling time, deformation occurs at newly formed shear bands which consist of a dense network of dislocation and the grain size of the powders is further reduced [87].

The enhancement of the particle hardness of ball-milled aluminium particles with the increasing of milling time is due to the repeated welding and fracturing which increased the density of the dislocations and defects in the particles. Therefore, the overall intensity of lattice strain in the ball-milled aluminium powders was increased, the grain size of the aluminium powders was reduced and the amount of grain boundaries were increased with the increasing milling time, which are supported by the broadening of XRD peaks as shown in the Fig. 5. 7. Obviously, the increased dislocation density [181] and the area of grain boundaries [182] in the ball-milled powders impede dislocation motion and contribute to the toughening of particles. Especially, with the increasing milling time, the lattice strain increased while the grain size reduced, hence the hardness of the ball-milled aluminium particles increased with increasing milling time [183]. In other words, the energy required for the particle failure increases with the increasing milling time due to the enhancement of the particle hardness [87].

However, the high hardness in the ball-milled aluminium particles is not always positive and useful. Because it requires more pressure and energy to compact the powders to achieve relatively high density that suitable for the following consolidation and post-treatment, which is discussed in detail in the following sections.

5. 2. 3 Summary

According to the preparation and characterization of the ball-milled aluminium powders, the data analysis and integrated discussion in the previous sections, the following results can be summarized:

1. Under the effect of welding and work hardening, the median particle size of the ball-milled aluminium powders increased with milling time for the first 10 h before decreased with longer milling time in excess of 10 h.

2. The aluminium particles were deformed into flake shape after ball milling for 5 h by slip and twinning of the lattice under the impact of milling balls. Then multi-layered microstructure was formed by the welding between particles. Afterwards, the micro-gaps between each interlayer inside the ball-milled particles were decreased and they gradually welded together with increasing milling time.

3. No obvious compound was formed in the ball milling of aluminium powders since

no other extra peak was found in the XRD and DSC data.

4. The hardness of the ball-milled elemental aluminium powders increased with milling time, because of the increased lattice strain and grain boundaries impeded the propagation of dislocations.

5. 3. The effect of ball milling on the sintered aluminium materials

To study the effect of ball milling on the sintered aluminium materials fabricated by the ball-milled aluminium powders, conventional press-and-sinter route was employed to produce the sintered aluminium materials. Both the green and sintered density of the green compact and sintered bulk specimens were measured using Archimedes' method. Optical microscopy and scanning electron microscopy (SEM) were employed to reveal the microstructure of the sintered specimens. The crystal structure of the sintered materials was characterized by XRD. The hardness and tensile strength of the sintered materials were also measured.

5. 3. 1 Results

5. 3. 1. 1. Cross-section

The microstructure of the sintered specimens fabricated using pristine aluminium and

ball-milled aluminium powder was revealed by the optical micrographs showed in the Fig. 5. 11. As can be seen from the Fig. 5. 11. (A) and (B) that the cross section microstructure of the sintered specimens produced using pristine aluminium powders showed mainly equiaxed grain structure. However, the cross section microstructure of the sintered specimen fabricated using 5 h ball-milled aluminium powders, showed layer like structure (Fig. 5. 11. (C) and (D)) [184] due to flake-like morphology of the ball-milled powders (Fig. 5. 1. (B)). Further increasing milling time to 10 h and longer, the layered structure remained in the matrix and the amount of pores in the matrix increased significantly. As it can be seen in the Fig. 5. 11. (E), (I) and (J) that pores are marked by the black circles. It is found that these pores are mainly distributed along the boundaries and the size of the pores increased with the increasing milling time.

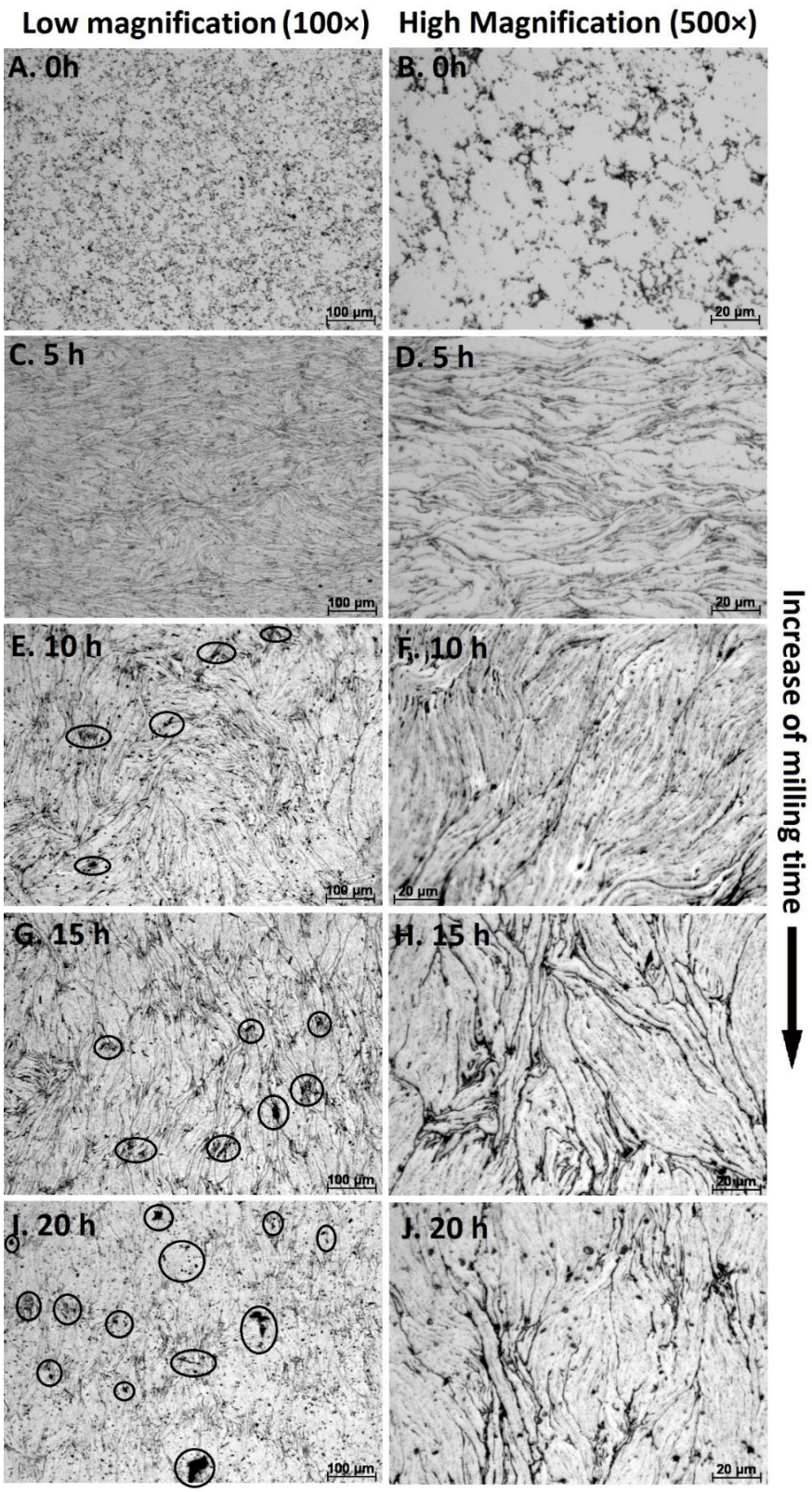


Fig. 5. 11 The optical micrographs showing the microstructure of the sintered specimens fabricated using pristine aluminium and ball-milled aluminium powders. (A) and (B) for 0 h, (C) and (D) for 5 h, (E) and (F) for 10 h, (G) and (H) for 15 h and (I) and (J) for 20 h. The micrographs in the left row (A, C, E, G, I) and right row (B, D, F, H, J) are under the magnification of 100× and 500×

respectively. The circles in (E), (G) and (I) marked the pores inside the aluminium matrix.

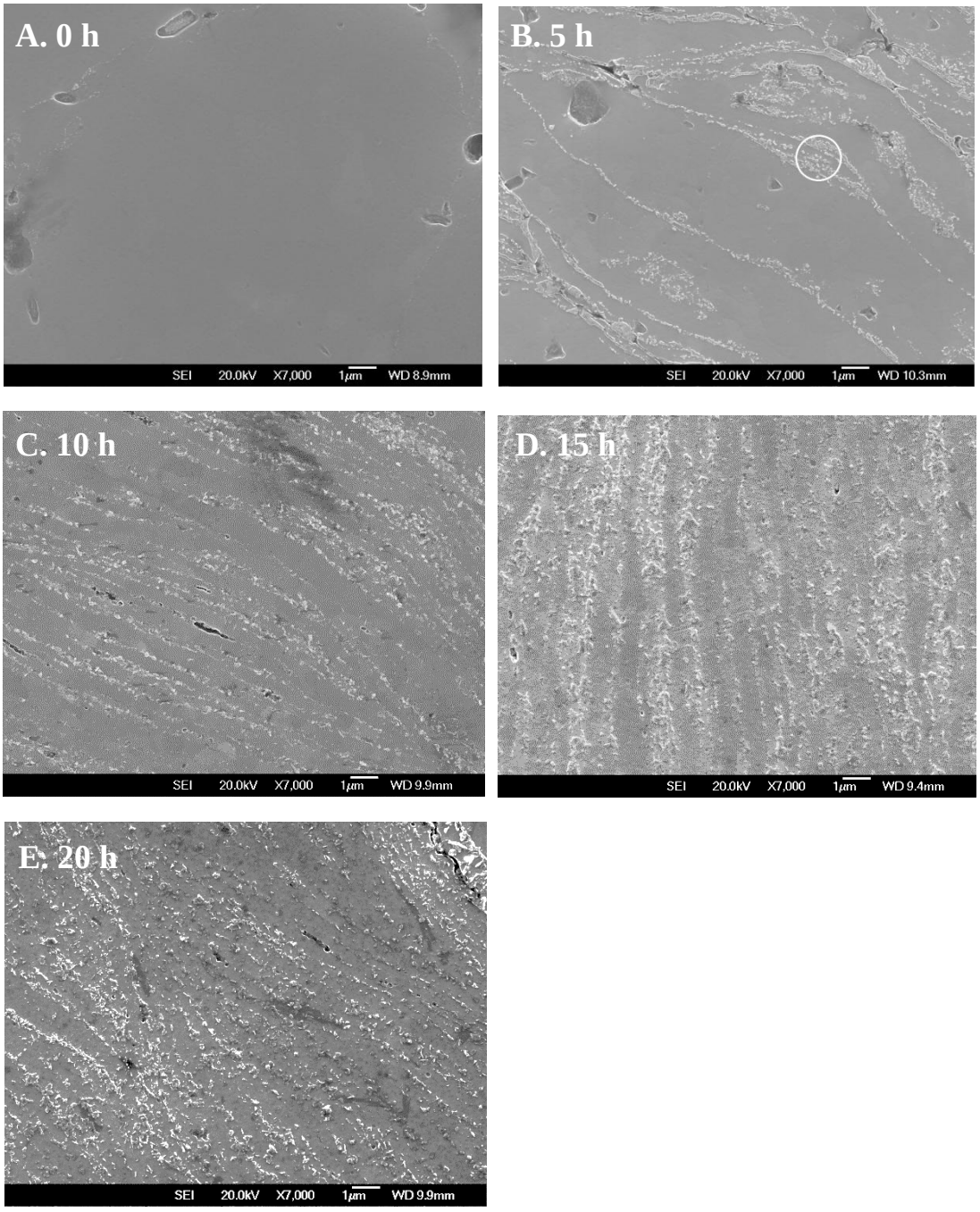


Fig. 5. 12 The SEM micrographs showing the cross-section of the sintered specimens fabricated using pristine aluminium (A) and ball-milled aluminium powders (B for 5 h, C for 10 h, D for 15 h and E for 20 h). Magnification: 7000×. The circle in (B) shows the region where EDX was applied.

The cross-section of the sintered bulk specimens was also studied by SEM. Fig. 5. 12

presents the cross-section microstructure of the sintered specimens fabricated using pristine and ball-milled aluminium powders. It is clear from the Fig. 5. 12 that the sintered pristine aluminium specimen exhibits smooth and clean surface. However, the cross-section of the sintered specimens fabricated using 5 h or longer time ball-milled aluminium powders show some nanosized particles. EDX was employed to study the composition of these nanoparticles and several regions on the cross section like the area indicated by the circle in Fig. 5. 12. (B) were characterized. It is found that the nanoparticles contained averagely 59.73 wt. % of aluminium and 40.27 wt. % of oxygen, which suggested these nanoparticles were alumina [183, 185].

Also, it is worth noticing that nanosized alumina particles are not randomly distributed in the cross-section of sintered aluminium materials. Instead, they are in lines and the distance between each line decreased with the increasing milling time. Furthermore, the amount of alumina nanoparticles on the cross-section of the sintered specimens is proportional to the milling time. More alumina nanoparticles were found on the sintered specimens fabricated using longer time ball-milled aluminium powders.

5. 3. 1. 2. Sintered density

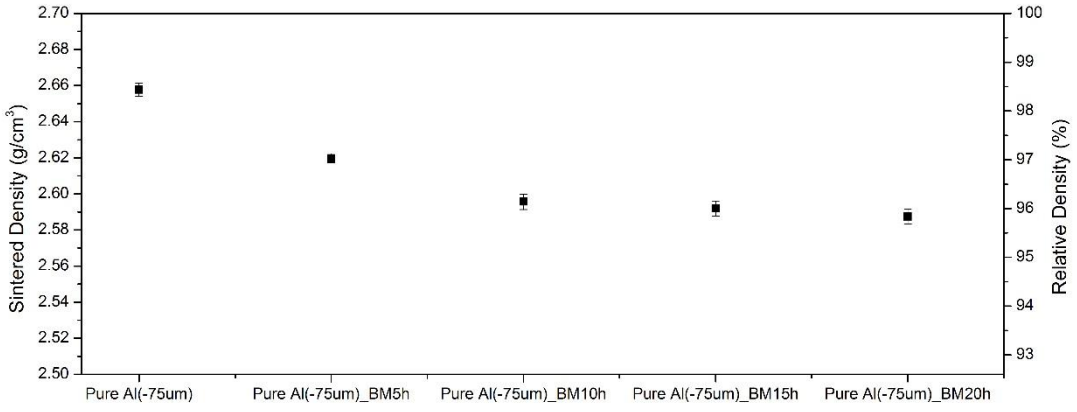


Fig. 5. 13 The sintered density of bulk specimens fabricated using pristine and ball-milled Al powders.

The sintered density of the bulk specimens prepared using pristine and ball-milled aluminium powders are shown in Fig. 5. 13. It can be seen from Fig. 5. 13 that the sintered density of the bulk aluminium specimens displays a steady decreasing trend with the increasing milling time. The sintered specimen of pristine aluminium shows a density of 2.66 g/cm^3 (relative density: 98.43 ± 0.11 %). The sintered density of specimens prepared from 5 h ball-milled and 10 h ball-milled Al powder decreased to 2.62 g/cm^3 (relative density: 97.03 ± 0.10 %) and 2.59 g/cm^3 (relative density: 96.13 ± 0.16 %), respectively. For 15 h and 20 h milling time, the sintered density decreased further to 2.59 g/cm^3 (relative density: 96.00 ± 0.15 %) and 2.58 g/cm^3 (relative density: 95.83 ± 0.15 %).

5. 3. 1. 3. X-ray diffraction

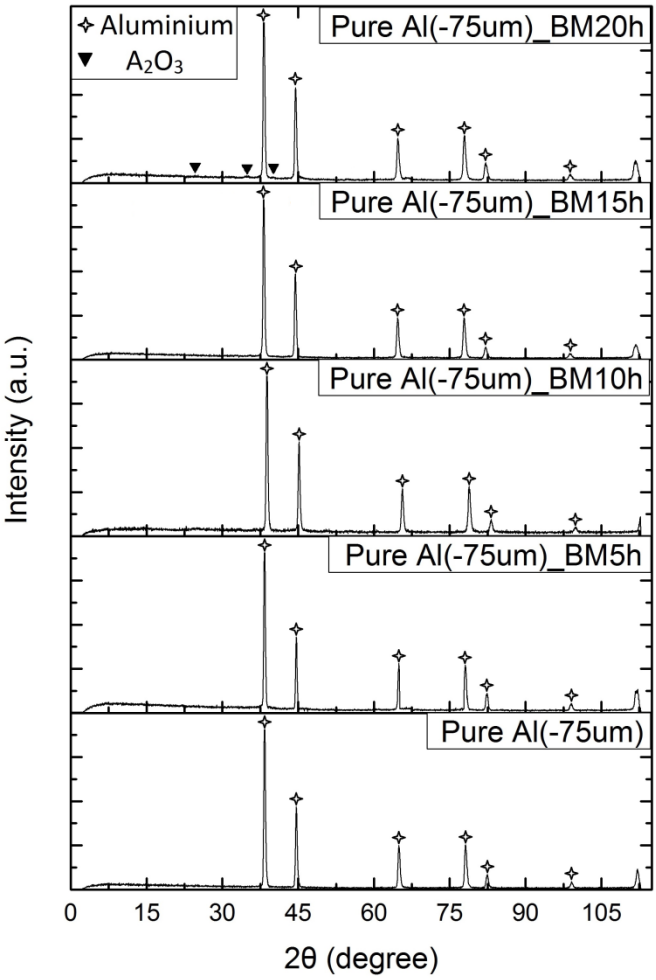


Fig. 5. 14 XRD patterns of the sintered specimens fabricated using pristine and ball-milled aluminium powders.

XRD patterns of the sintered specimens produced using pristine and ball-milled aluminium powders are presented in Fig. 5. 14. The XRD peaks confirm that Al is the only element found in the matrix fabricated using pristine aluminium and 5-15 h ball-milled aluminium powders, which is marked by 'stars' in the Fig. 5. 14. The characteristic peaks of alumina were found in the aluminium matrix fabricated using 20 h ball-milled aluminium powders, as indicated by black triangles in Fig. 5. 14.

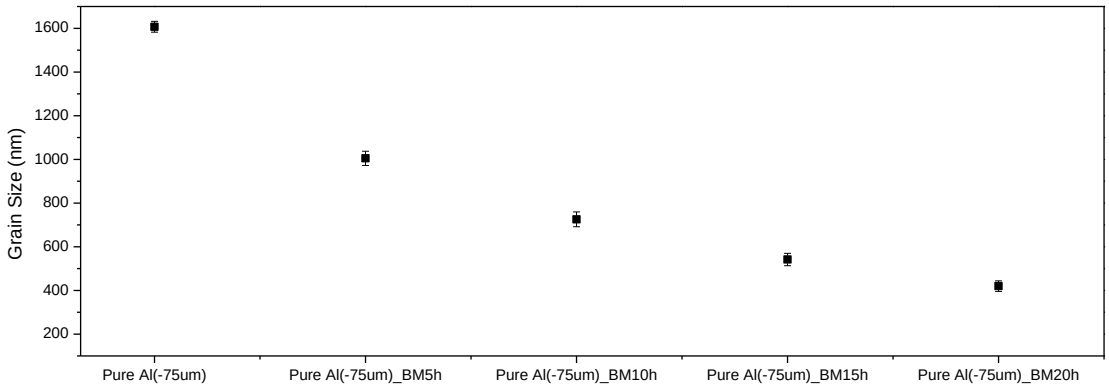


Fig. 5. 15 The grain size of the sintered specimens produced using pristine and ball-milled aluminium powders.

The grain size of the sintered specimens is calculated by the William-Hall equation (equation 3. 4. 9. 1). The values of the grain size are shown in the Fig. 5. 15. It is apparent from the Fig. 5. 15 that the grain size of the sintered specimens decreased with the increasing milling time. More specifically, the grain size of the sintered specimen using pristine aluminium powders was determined as 1.61 μm. However, the grain size of the sintered specimens fabricated using 5 h ball-milled Al powder reduced to 983.53 ± 32.53 nm. At higher milling time, the grain size decreased to 541.56 ± 28.45 nm and 419.74 ± 24.08 nm for the sintered specimens prepared using 15 h ball-milled and 20 h ball-milled aluminium powders respectively.

5. 3. 1. 4. Vickers micro-hardness

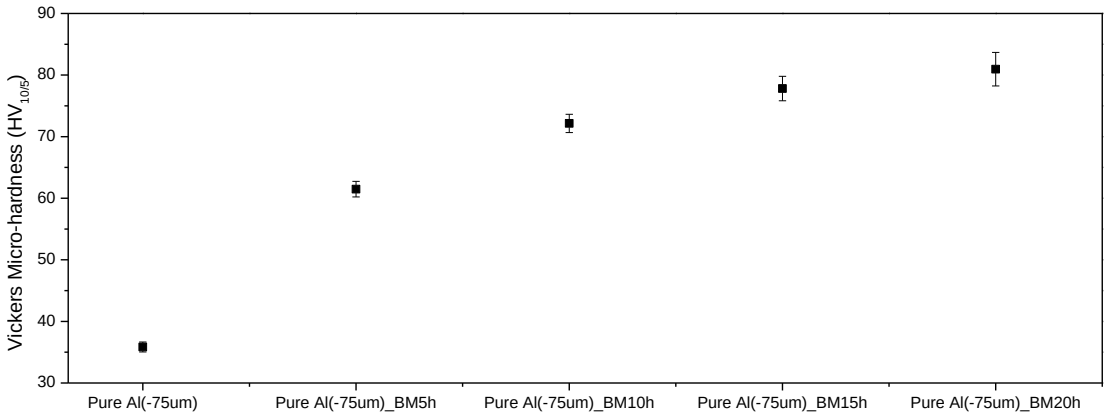


Fig. 5. 16 Vickers micro-hardness of the bulk specimens fabricated using the pristine and ball-milled aluminium powders.

The Vickers hardness values for the sintered specimens fabricated using the pristine and ball-milled aluminium powders are displayed in the Fig. 5. 16. It is obvious that the hardness of the sintered bulk specimens kept an increasing trend with the increase milling time. The sintered bulk specimens of pristine aluminium showed a relatively low micro-hardness which is only 35.85 ± 0.8 $HV_{10/5.}$ However, the hardness values of the sintered specimens using 5 h and 10 h ball-milled aluminium powders increased to 61.48 ± 1.27 $HV_{10/5}$ and 72.15 ± 1.49 $HV_{10/5}$, respectively. Further increasing the milling time, the micro-hardness values of sintered specimens using powders ball-milled for 15 h and 20 h increased further to 77.81 ± 1.98 $HV_{10/5}$ and 80.96 ± 2.72 $HV_{10/5}$ respectively.

5. 3. 1. 5. Tensile properties

The strain-stress curves for the sintered specimens fabricated using the pristine and

ball-milled aluminium powders are shown in Fig. 5. 17. The corresponding mechanical properties obtained from tensile test are listed in Table 5. 2. It can be seen from Table 5. 2 that the sintered specimen fabricated using pristine aluminium powders possesses a good ductility but relatively low strength. On the contrary, the sintered specimens fabricated using ball-milled aluminium powders exhibit poorer ductility but much higher strength.

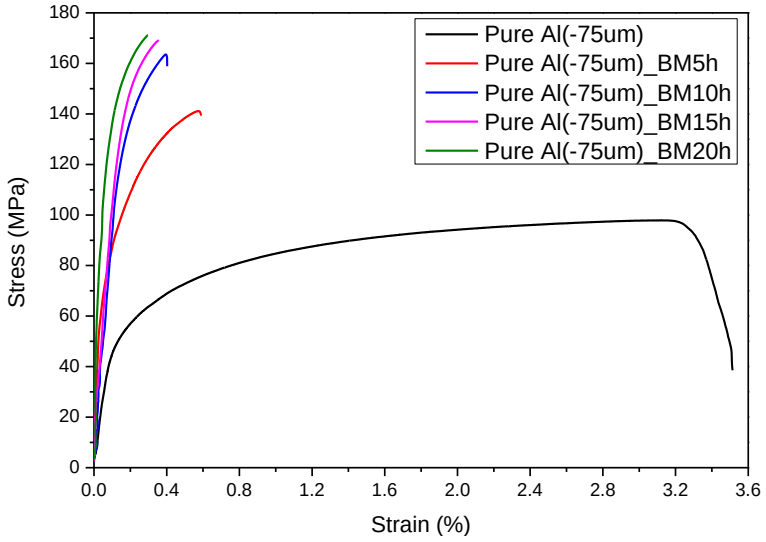


Fig. 5. 17 The strain-stress curves of the sintered specimens fabricated using the pristine and ball-milled aluminium powders.

Table 5. 2 The mechanical properties of the sintered specimens fabricated using the ball-milled Al powders.

Materials	**Yield strength (MPa)**	**Ultimate tensile strength (MPa)**	**Maximum strain before failure (%)**
Pure Al(-75um)	52.62 ± 1.74	97.87 ± 4.89	3.51 ± 0.08
Pure Al(-75um)_BM5h	87.13 ± 4.06	141.11 ± 7.06	0.59 ± 0.03
Pure Al(-75um)_BM10h	95.41 ± 5.28	163.52 ± 8.18	0.40 ± 0.02
Pure Al(-75um)_BM15h	106.35 ± 6.55	169.00 ± 8.45	0.36 ± 0.02
Pure Al(-75um)_BM20h	115.30 ± 7.20	171.21 ± 8.08	0.30 ± 0.02

More specifically, the sintered specimen of pristine aluminium shows relatively low strength

(UTS: 97.87 ± 4.89 MPa) and good ductility (maximum strain before failure: 3.51 ± 0.18 %) which are typical characteristics of aluminium material. On the other hand, the UTS of the sintered specimens produced from 5 h and 10 h ball-milled aluminium powders significantly increased to 141.11 ± 7.06 MPa and 163.52 ± 8.18 MPa, respectively. They are 44.18 % and 67.07 % higher than that of the sintered pristine aluminium specimen, respectively. Moreover, the UTS of the sintered specimens increased further to 169.00 ± 8.45 MPa and 174. 21 ± 8.08 MPa when 15 h and 20 h ball-milled aluminium powders were used respectively.

However, the ductility of the sintered specimens fabricated using ball-milled aluminium powders was severely decreased. The maximum strain before failure remarkably reduced to 0.59 ± 0.03 % and 0.40 ± 0.02 % for the sintered specimens using 5 h and 10 h ball-milled aluminium powders. The maximum strain before failure of the sintered specimens produced from 15 h and 20 h ball-milled aluminium powders were further decreased to 0.36 ± 0.02 % and 0.30 ± 0.02 % respectively, which are only one tenth that of the sintered pristine aluminium specimen.

5. 3. 2 Discussion

5. 3. 1. 1. The formation of Al_2O_3 in the sintered aluminium materials

As can be seen from the SEM image in Fig. 5. 12 and the XRD patterns in the Fig. 5. 14 that

the amount of the nanoparticles in the cross-section was increased in the sintered specimens using powders milled for longer time. Obviously in the Table 5. 2. 1. 1. 1 that the oxygen content on the surfaces of the ball-milled aluminium particles are proportional to the milling time. This indicates that the formation of alumina is partially contributed by the oxygen introduced in the ball milling process.

Also, according to the cross-section of the ball-milled aluminium particles (Fig. 5. 3 and Fig. 5. 4), no obvious alumina nanoparticles is found in the microstructure of the ball milled powders. This suggests that the alumina is mainly formed in the sintering process. One possible source of the oxygen is the air trapped between the flake aluminium layers in the compaction process. They reacted with aluminium to form alumina in the sintering process.

Another possible source of oxygen is stearic acid. It was ball milled with aluminium as the process control agent to prevent excessive welding of aluminium particles. Due to the repeated fracturing and welding of aluminium particles in the ball milling process, stearic acid continuously contacted the freshly formed aluminium powder surfaces and gradually dispersed into the aluminium particles. Subsequently, the oxygen in the stearic acid reacted with aluminium and formed alumina in the sintering process. Thus, the alumina nanoparticle were found on the cross-section of the sintered specimen and the amount of alumina nanoparticles increased in the sintered specimens fabricated using aluminium powders ball milled for longer time.

It is reported [186, 187] that the presence of Al_2O_3 formed a barrier to the contact and diffusion of aluminium atoms in the sintering process, which subsequently deteriorated the densification process. This along with the increased hardness of the ball-milled aluminium powders, which degraded the green density of the compacts, resulted in the decrease of sintered density of the bulk specimens. Also, the increased amount of pores inside the sintered specimens leaded to the insufficient bonding between aluminium particles and these pores acts as nucleation sites for plastic instability [188], which resulted in the failure of the specimens with lower ductility [189]. Moreover, some researchers found that the mismatch in coefficient of thermal expansion (CTE) (Al_2O_3: 5.30 10^{-6}/K versus Al: 23.6 10^{-6}/K) [190] and elastic modulus (Al_2O_3: 300 GPa versus Al: 69 GPa) between the metal matrix and nanoparticles is accommodated during sintering, cooling and straining process [191]. Simultaneously, defects, dislocations and residual stresses [192] are introduced into the region around the Al_2O_3 nanoparticles which resulted in the debonding of the interface [193] and the initiation and premature of crack [194].

In order to improve the density of the aluminium-based materials, Schaffer et al. [195, 196] and Kondoh et al. [197] added magnesium into aluminium which formed spinel ($MgAl_2O_4$) and disrupted Al_2O_3 film and enabled densification process for successful sintering. Other mechanical processing techniques like hot extrusion [28, 31, 32], hot rolling [28], hot pressing [31, 33-35] and HIP [198] were employed by other researchers to improve the density of the aluminium-based composite and further enhance the properties of the aluminium-based materials.

5. 3. 1. 2. The strengthening mechanism of the sintered aluminium materials

Table 5. 3 Comparison of the predicted and experimentally measured yield strength of the sintered aluminium materials.

Sintered materials	Estimated yield strength by Hall-Petch equation (MPa)	Experimentally measured yield strength (MPa)
Pristine Al	-	54.77
Pure Al(-75um)_BM05h	91.30	87.13
Pure Al(-75um)_BM10h	99.35	95.41
Pure Al(-75um)_BM15h	110.44	106.35
Pure Al(-75um)_BM20h	121.51	115.30

According to the theory of strengthening by grain refinement (as introduced in the section 2. 4. 3. 1), the calculation was made to estimate the yield strength of the sintered aluminium materials. For comparison, both the experimentally measured and estimated yield strength are listed in Table 5. 3. 1. 2 .1. As can be seen in the Table 5. 3. 1. 2. 1 that the experimentally measured yield strength of the sintered aluminium material increased by 65 % and 81 % to 87.13 MPa and 95.41 MPa with 5 h and 10 h of ball milling, respectively, compared to that of sintered pristine aluminium. Further increasing the milling time to 15 h and 20 h, the corresponding experimentally measured yield strength of the sintered aluminium material was improved to 106.35 MPa and 115.30 MPa, respectively. Overall, the experimental yield strength of the sintered aluminium materials increased with increasing milling time. Similarly, the estimated yield strength of the sintered aluminium material show a similar increasing trend with increasing milling time. More importantly, the values of the experimentally measured and estimated yield strength are closely correlated.

This demonstrates that the grain refinement mechanism is responsible for the strengthening in sintered aluminium specimens fabricated using ball-milled aluminium powders.

However, it is worth noting that the experimentally measured yield strengths are all lower than the estimated values. This is due to the lower density of the sintered aluminium as compared to its bulk theoretical density used in the estimation of the yield strength (Fig. 5. 13). The Hall-Petch equation does not take the density of material into consideration and assumes all the materials are fully dense. Obviously, the relative density of the sintered aluminium materials is below 100% (Fig. 5. 13) and it decreased with the increasing milling time. Pores are found in the cross section microstructure of sintered specimens (Fig. 5. 11). In the mechanical test, lower density reduced the effective area of materials to sustain the same stress. Thus, the resultant high stress concentration and insufficient bonding at pores located areas lead to the material deforms or fractures early than expected [199].

Moreover, certain amount of Al_2O_3 nanoparticles were formed in the aluminium matrix during the sintering process as can be seen from Fig. 5. 12. According to J. R. Groza et al. [200] and E. A. Bloch et al. [201], the presence of fine and evenly distributed particles within the matrix would obstruct and impede the motion of dislocations by forming Orowan loop [202]. Thus, the hard Al_2O_3 nanoparticles formed in the sintered aluminium materials may also contribute to the strengthening of the matrix. However, since the amount of Al_2O_3 formed in the aluminium matrix is not measured, the quantitative analysis of the dispersion strengthening by Al_2O_3 is not yet made.

Therefore, it can be conclude that grain refinement is the main strengthening mechanism in the sintered aluminium materials fabricated using ball-milled elemental aluminium powders. The low density is the main reason for the deterioration of the mechanical properties. The Al_2O_3 nanoparticles formed in the matrix of the sintered aluminium specimens may also enhance the sintered aluminium through dispersion strengthening.

5. 3. 3 Summary

The following conclusion of the sintered specimen prepared using ball-milled aluminium powders can be drawn:

1. The grain size of the sintered specimen prepared using ball-milled powder was steadily reduced with increasing milling time due to the violent impact and collision of milling balls to the Al powder.

2. The tensile strength and Vickers micro-hardness of the pressed and sintered specimen prepared using ball-milled powder increased with increasing milling time because of the reduction of grain size and the increased of Al_2O_3 nanoparticles that hinder the propagation of dislocation.

Chapter 6. The effect of ball milling on the microstructure and mechanical properties of multi-walled carbon nanotube reinforced aluminium composite

6. 1. Introduction

This chapter is concerned with the study of the effect of milling time on the microstructure and mechanical properties of the high energy ball milled carbon nanotube reinforced aluminium composite provided before and after sintering.

It is reported that the grain size of the ball-milled powder is inversely proportional to the milling time due to the severe plastic deformation [183, 203, 204] in the ball milling process. Also, the homogeneity of carbon nanotube [29, 30] in the ball-milled powder is improved with the increasing milling time. It is known that finer grain size of the ball-milled particles and more uniform distribution of carbon nanotube in the ball-milled powders are beneficial to achieve better mechanical properties in the bulk composite. However, it is also worth noting that the level of damage and amount of defects in the structure of carbon nanotube increased with increasing milling time [93]. The lost of essential tubular structure of carbon nanotubes deteriorates the characteristics (i.e. mechanical, electrical and thermal properties) of carbon nanotube and degrades the overall properties of the bulk composite [33, 93]. Therefore, it is critical to find the most appropriate milling time to obtain ball-milled

powders consisting of a homogeneous dispersion of carbon nanotube in a refined matrix microstructure, while maintaining the structure of carbon nanotube, in order to maximize the properties of the as-produced Al-CNT composite.

Hence in the current study, 1.0 wt. % MWNT was added into 99.0 wt. % elemental aluminium powders (-75 μm) and ball milled for 5 h to 20 h. The ball-milled powders were then prepared to form bulk specimens using press and sintering route. The microstructure of powders and sintered bulk specimens were characterized by a combination of XRD and SEM. The structure of MWNT was characterized using Raman spectroscopy. The mechanical properties (i.e. hardness and tensile strength) of the composite powders and sintered specimens were determined by Vickers micro-hardness and tensile test methods. The names of the material groups investigated in this chapter are listed in Table. 3. 5. 3.

6. 2. The effect of ball milling on the Al-1.0 wt. % MWNT composite powders

6. 2. 1 Results

6. 2. 1. 1. Morphology

6. 2. 1. 1. 1. The evolution of aluminium powders

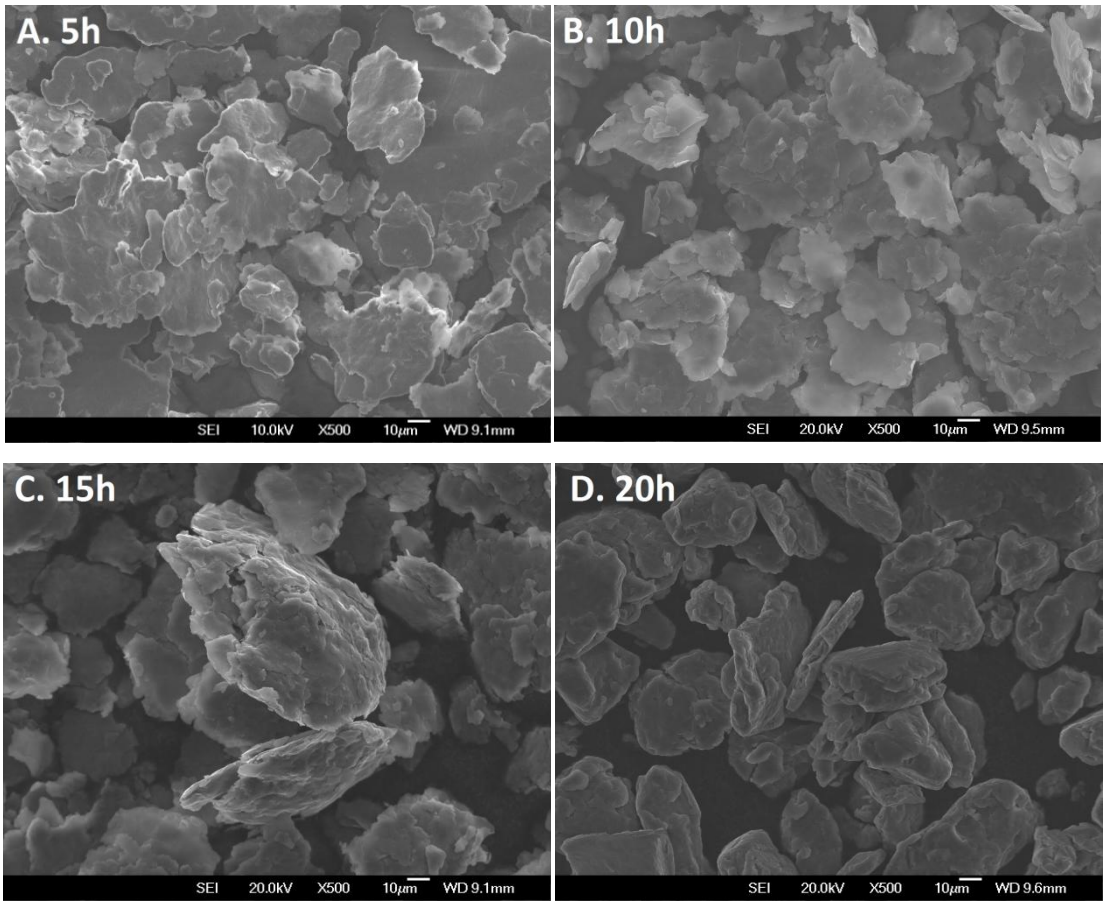


Fig. 6. 1 The SEM micrographs showing the morphology of the Al-1.0 wt. % MWNT composites powders that ball-milled for (A) 5 h, (B) 10 h, (C)15 h and (D) 20 h.

The morphology of the ball-milled Al-1.0 wt. % MWNT composite powders is shown in Fig.

6. 1. As can be seen from the Fig. 6. 1. (A) that the flake shape and smooth surface found in the 5 h ball-milled Al-1.0 wt. % MWNT composite powders, are very similar to those characteristics found in the 5 h ball-milled elemental aluminium powders (Fig. 5. 1. (B)). Further increasing the milling time to 10 h led to rougher surfaces and increased particle thickness, as shown in Fig. 6. 1. (B). This indicates that the welding of aluminium flakes occurred during the ball milling process. After ball milling for 15 h (Fig. 6. 1. (C)), the composite powders became lenticular in shape with reduced amount of coarse particles and further increased particle thickness.

However, the morphology of the Al-1.0 wt. % MWNT composite powders that were ball milled for 20 h are evidently different from that of the other ball-milled powders. As can be seen from the Fig. 6. 1. (D) that the thickness of the Al-1.0 wt. % MWNT composite powders increased to around 10 μm and the rounded particle edges were observed. Especially, the composite powders are more granular and equiaxed than the composite powders ball milled for 15 h. According other researchers' work [205, 206], the granular shape of the ball milled powders is a sign of dynamic equilibrium state of ball milling.

6. 2. 1. 1. 2. The dispersion of MWNT

Fig. 6. 2 shows the MWNT found in the ball-milled composite powders. After 5 h milling, the 25 μm bundles of MWNT (Fig. 3. 3. (A)) were broke down. However, smaller agglomerates of MWNT (around 5 μm) are still found on the surface of the 5 h ball-milled Al-1.0 wt. % MWNT composite powders (as circled by dashed lines shown in Fig. 6. 2. (A)).

As the time of ball milling increased to 10 h, only individual MWNT was observed on the particle surface as indicated by the arrows in Fig. 6. 2. (B).

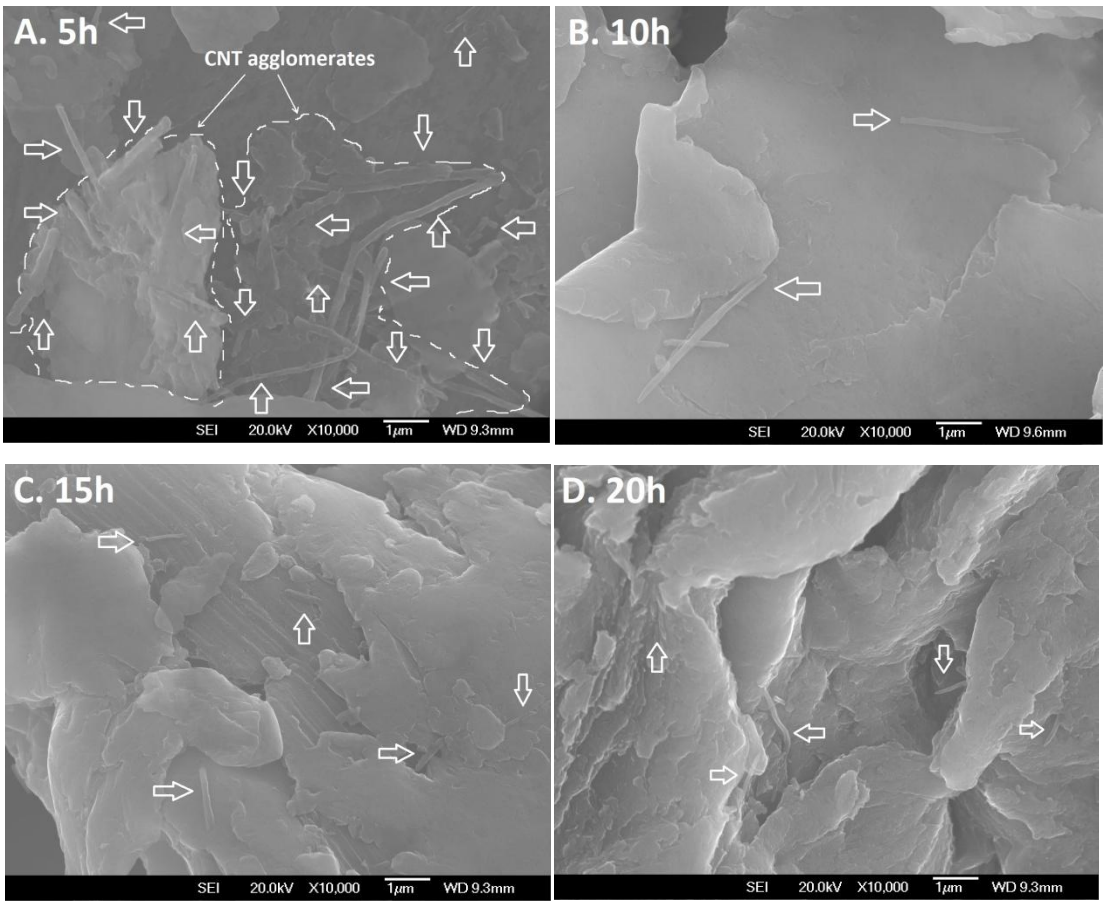


Fig. 6. 2 The SEM micrographs showing the multi-walled carbon nanotube in the Al-1.0 wt. % MWNT composites powders, prepared after ball milling for (A) 5 h, (B) 10 h, (C) 15 h and (D) 20 h (The arrows indicate the presence of MWNT and the dash lines in (A) indicate the presence of MWNT agglomerates).

At higher milling time of 15 h, the length of the individual MWNT on the surface of the powder was evidently shortened to 1-2 μm from 7 μm in the pristine MWNT (Fig. 3. 3. (B)). Especially, some of the MWNT were partially covered by the aluminium layers and only their ends were revealed as indicated by the arrows in Fig. 6. 2. (C). At even higher milling

time of 20 h, less MWNT was observed on the surface of the particles. However, more of them were found inside the ball-milled aluminium powders as demonstrated by the fractured surface showing the embedded MWNT inside the ball-milled particles in Fig. 6. 2. (D).

6. 2. 1. 2. Cross section

The cross-sectional microstructure of ball-milled Al-1.0 wt. % MWNT composite powders is shown in Fig. 6. 3. It is clear from Fig. 6. 3. (A) and (B) that the 5 h ball-milled composite powders had flake-like shape and the particle thickness varied from around 3 μm to 20 μm. Especially, rounded and smooth particle edges (Fig. 6. 3. (B)) were found in the "as-milled" powders, with some particles retained the near-spherical shape (Fig. 6. 3. (A)). These features are very similar to the characteristics of the 5 h ball-milled elemental aluminium powers shown in the Fig. 5. 2. 1. 2. (D).

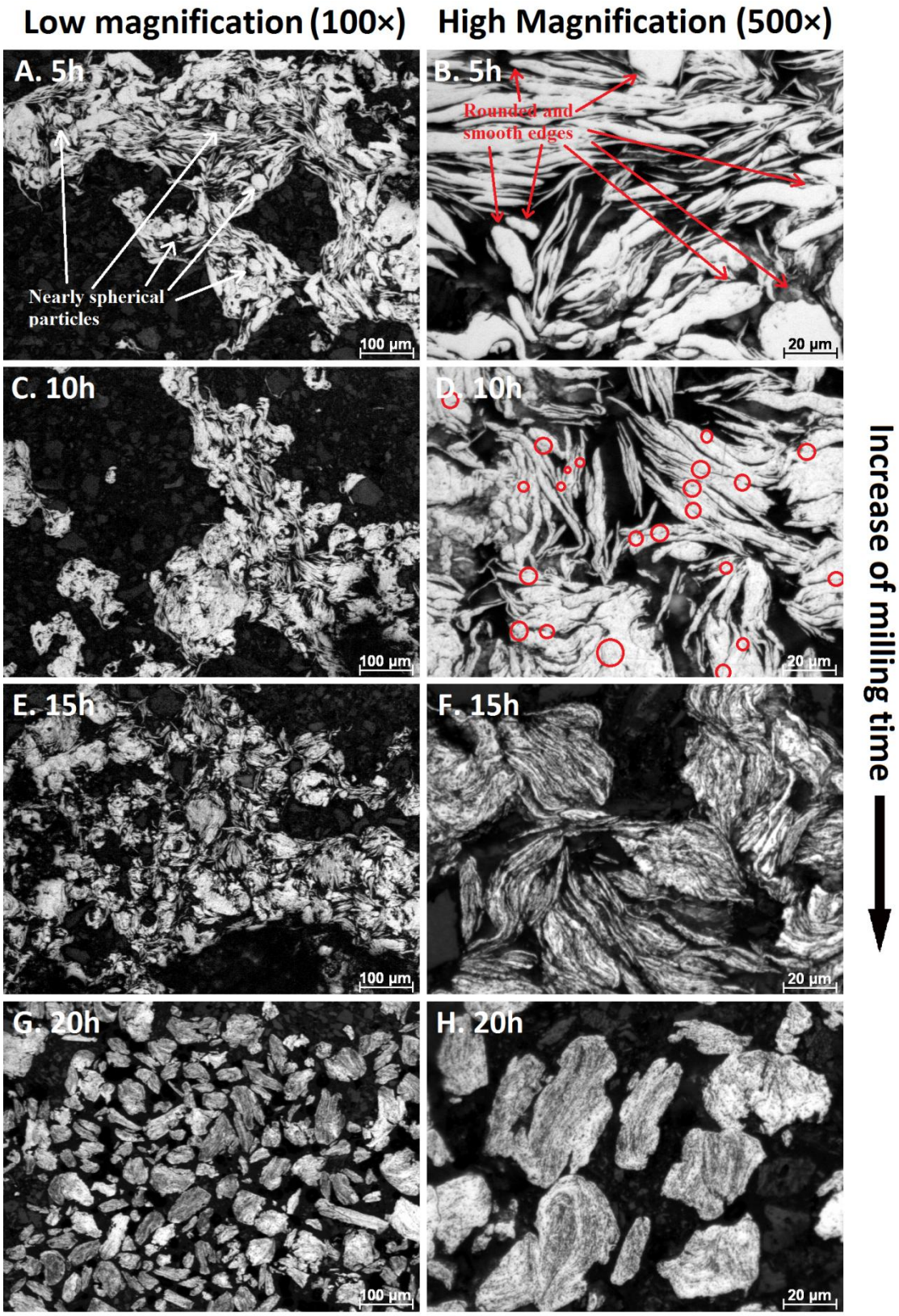


Fig. 6. 3 Optical micrographs showing the cross-section of ball-milled Al-1.0 wt. % MWNT composite powders. The micrographs are labelled according to the milling time: (A) and (B) for 5 h, (C) and (D) for 10 h, (E) and (F) for 15 h, and (G) and (H) for 20 h. The images in the left column

(A, C, E and G) and in the right column (B, D, F and H) are taken at magnifications of 100× and 500× respectively. The red circles in (D) indicate the welded region in the ball-milled powders.

As the milling time increased to 10 h, the welding between aluminium particles was visible, as marked by circles in Fig. 6. 3. (D). But the welding process only occurred on a small scale since no excessive welding was observed. Also, the thickness difference of the interlayers was reduced and the gaps between each interlayer inside the 10 h ball-milled aluminium particles are noticeable. Comparing to the cross-section of the 10 h ball-milled elemental aluminium particles (Fig. 5. 2. 1. 2. (F)), smaller particle sizes were found in the 10 h ball-milled Al-1.0 wt. % MWNT composite powders (Fig. 6. 3. (D)).

At a higher milling time of 15 h, Fig. 6. 3. (E) and (F) show a multi-layered structure in the ball-milled composite powders. Smaller particles size and thinner particle thickness were found in the 15 h ball-milled Al-1.0 wt. % MWNT composite powders as compared to those found in the 15 h ball-milled elemental aluminium particles (Fig. 5. 2. 1. 2. (H)). At even longer milling time of 20 h, rounded edges of ball-milled Al-1.0 wt. % MWNT composite powders have been observed and the thickness of powders was uniform and reduced to about 20 μm. More importantly, the multi-layered structure inside the ball-milled Al-1.0 wt. % MWNT composite particles became less obvious. No distinct interlayer inside the ball-milled particles was observed under the magnification of 500× (Fig. 6. 3. (H)).

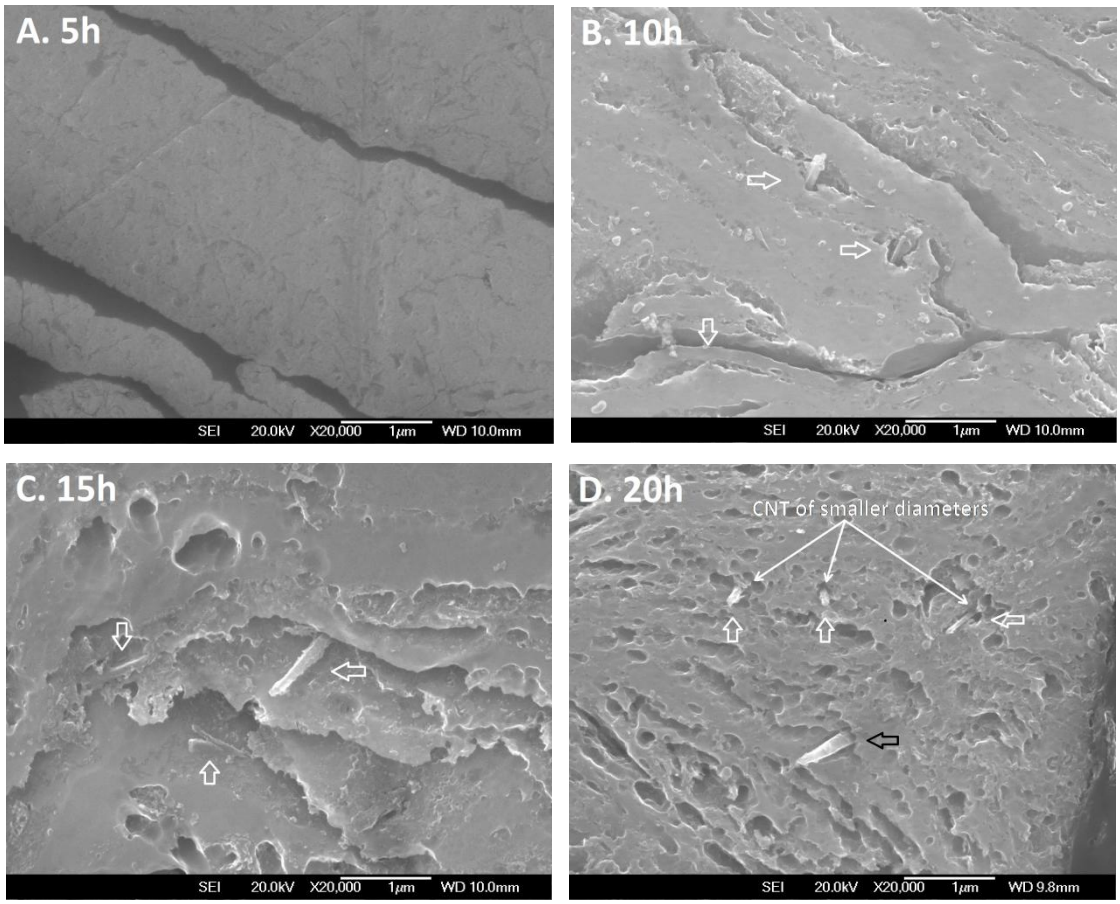


Fig. 6. 4 The SEM micrographs showing the MWNT found in the cross-section of the Al-1.0 wt. % MWNT composite powders that were ball-milled for (A) 5 h, (B) 10 h, (C) 15 h and (D) 20 h. Magnification: 2000×. The arrows indicate the presence of MWNT.

Fig. 6. 4 shows the MWNT found in the cross-section of the ball-milled Al-1.0 wt. % MWCNT particles. It is evident from the Fig. 6. 4. (A) that no MWNT was observed in the cross-section of the 5 h ball-milled Al-1.0 wt. % MWCNT composite particles. After ball milling for 10 h, MWNT were found between the relatively thick interlayers as indicated by arrows in Fig. 6. 4. (B). Further increasing milling time to 15 h, the MWNT were observed between the interlayers inside the ball-milled Al-1.0 wt. % MWCNT composite particles (Fig. 6. 4. (C). When the milling time increased to 20 h, MWNT and miro-pores were distributed inside the ball-milled Al-1.0 wt. % MWCNT composite particles (Fig. 6. 4. (D)).

It is worth noticing that the diameter of the MWNT was reduced after ball milling for 20 h (Fig. 6. 4. (D)).

6. 2. 1. 3. Particle size distribution

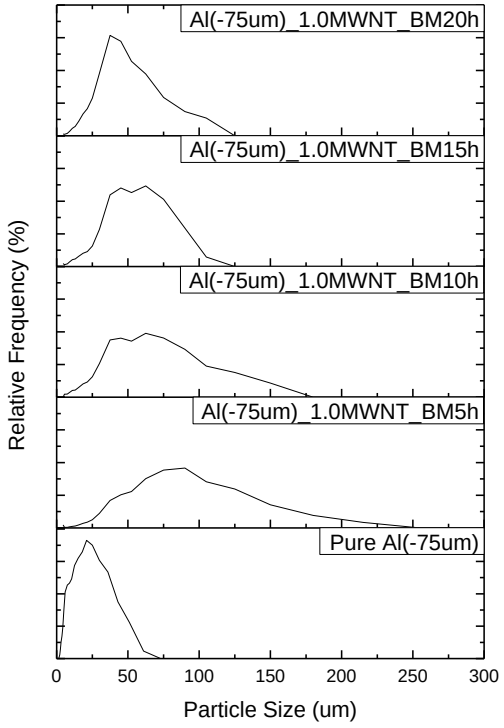


Fig. 6. 5 The particle size distribution of the ball-milled Al-1.0 wt. % MWNT composite powders.

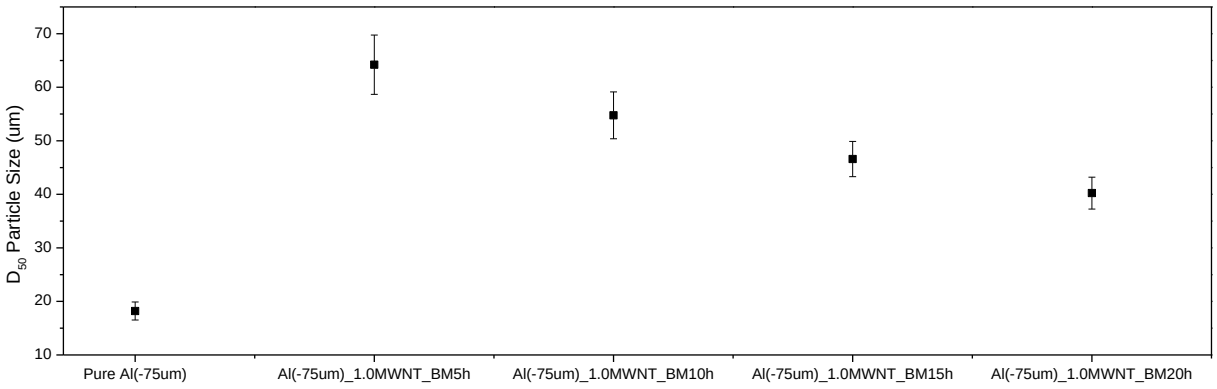


Fig. 6. 6 The median particle size (D_{50}) of the ball-milled Al-1.0 wt. % MWNT composite powders.

Figures 6. 2. 1. 3. 1 and 6. 2. 1. 3. 2 show the particle size distribution and median particle size of the ball-milled Al-1.0 wt. % MWNT composite powders as a function of milling time, respectively. It can be seen that the particle size of the pristine aluminium powders have a narrow size range (< 75 μm) with D_{50} of 19.40 ± 1.68 μm. After ball milling for 5 h, the particle size distribution of the ball-milled Al-1.0 wt. % MWNT composite powders was noticeably broadened (up to 238 μm) and the median particle size (D_{50}) significantly increased to 64.21 ± 5.53 μm. At high milling time of 10 h, the broadening of particle size distribution reduced and the median particle size decreased to 54.75 ± 4.38 μm. Further increasing the milling time to 15 h and 20 h, the distribution of the particle size became less broaden and the D_{50} decreased to 46.59 ± 3.30 μm and 40.23 ± 2.99 μm, respectively.

6. 2. 1. 4. X-ray diffraction

The XRD patterns of the ball-milled Al-1.0 wt. % MWNT composite powders were plotted in Fig. 6. 7. As can be seen from the Fig. 6. 7 that only the characteristic peaks of aluminium (as marked by stars) appeared which suggests no other phase was formed during the ball milling process or the content of the newly formed phase is too low to be detected by the current X-ray diffractometer. The full width at high maximum (FWHM) of the XRD peaks increased with increasing milling time. This indicates the refinement of the grain size and the increase of strain in the ball-milled powder.

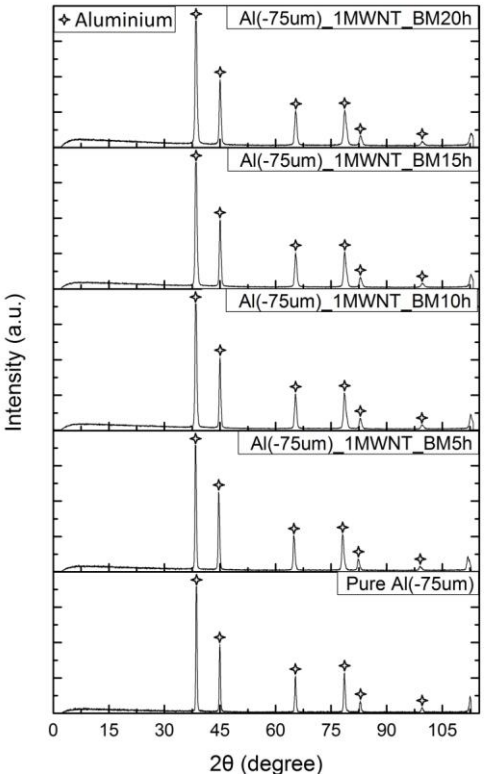


Fig. 6. 7 The XRD patterns of the ball-milled Al-1.0 wt. % MWNT composite powders.

6. 2. 1. 5. Raman spectroscopy

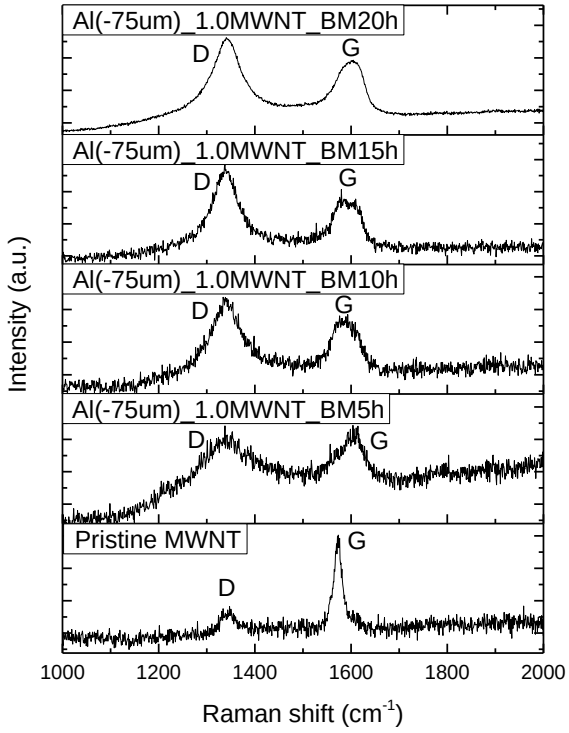


Fig. 6. 8 The Raman spectra of the ball-milled Al-1.0 wt. % MWNT composite powders.

Generally, the Raman spectrum of carbon nanotube has two distinctive peaks namely D band peak and G band peak. The former peak is at around 1350 cm^{-1}, which represents the defects in the MWNT structure while G band peak is at about 1590 cm^{-1}, which indicates the vibration of carbon atoms from an ordered structure. Fig. 6. 8 plots the Raman spectra of the pristine carbon nanotube and the carbon nanotube in the ball-milled Al-1.0 wt. % MWNT composite powders.

It can be seen from the Fig. 6. 8 that the Raman spectrum of the pristine MWNT shows the intensity of G band peak significantly exceeds that of D band peak, which suggests a relatively highly ordered MWNT structure. However, the D band peak and G band peak in the Raman spectra of the 5 h ball-milled Al-1.0 wt. % MWNT composite powders exhibits nearly equal intensity. Further increasing the milling time to 10 h and upwards, the intensity of D band peak is noticeably higher than that of G band peak. This indicates the amount of defects in the structure of carbon nanotube in the ball-milled Al-1.0 wt. % MWNT composite powders increased with the increasing milling time.

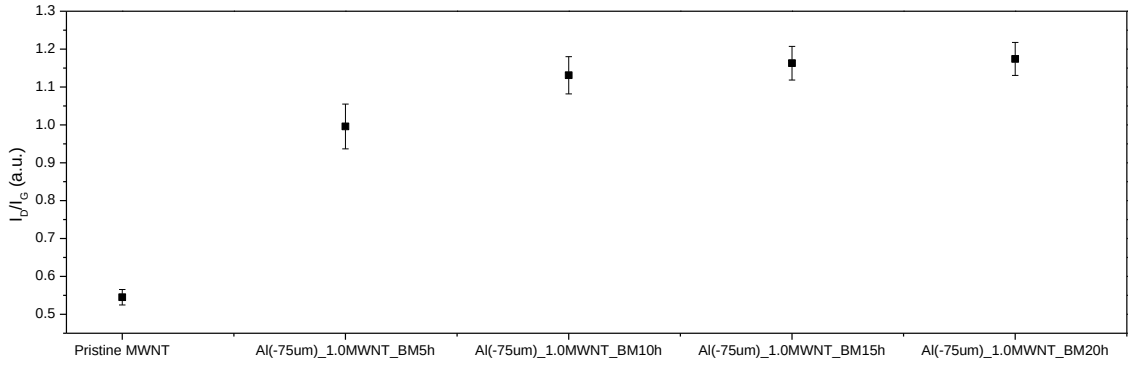


Fig. 6. 9 The I_D/I_G of the ball-milled Al-1.0 wt. % MWNT composite powders.

Generally, the intensity ratio of D band peak and G band peak (I_D/I_G) [207-209] was employed to evaluate the integrity of MWNT structure and the concentration of defects in MWNT. Thus, the current author used I_D/I_G of the ball-milled Al-1.0 wt. % MWNT composite powders to quantify the structure evolution of carbon nanotube in Al powder during the ball milling process. Fig. 6. 9 presents the specific I_D/I_G value of the carbon nanotube in the ball-milled Al-1.0 wt. % MWNT composite powders. As can be seen from the Fig. 6. 9 that the I_D/I_G of the pristine carbon nanotube is very low and it is only around 0.55. This indicates that the pristine carbon nanotube is highly ordered with little defects.

However, the I_D/I_G of the carbon nanotube in the ball-milled composite powders almost doubled and reached 0.99 ± 0.06 after ball milling for 5 h. Further increasing the milling time cause the I_D/I_G ratio to increase at small increment. When the Al-1.0 wt. % MWNT composite powders were ball milled for 15 h and 20 h, the I_D/I_G ratio of the carbon nanotube in the ball-milled powders further increased to 1.16 ± 0.04 and 1.17 ± 0.04, respectively.

6. 2. 1. 6. Vickers micro-hardness

To evaluate the properties of the ball-milled Al-1.0 wt. % MWNT composite powders, the hardness of the powders was measured by the Vickers hardness tester. Fig. 6. 10 shows the plot of hardness versus milling time. It is clear in Fig. 6. 10 that the Vickers micro-hardness of the ball-milled Al-1.0 wt. % MWNT composite powders is steadily improved with increasing milling time.

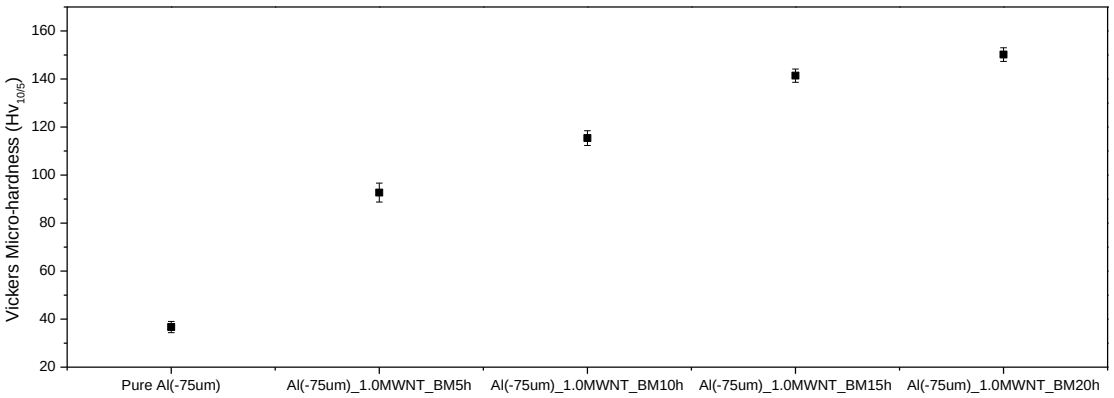


Fig. 6. 10 The Vickers micro-hardness of the ball-milled Al-1.0 wt. % MWNT composite powders.

Specifically, the hardness of the aluminium powders increased from 36.7 ± 2.3 $HV_{10/5}$ (the hardness of the unmilled pristine elemental aluminium powders) to 82.7 ± 3.9 $HV_{10/5}$ after ball milling for 5 h with the addition of 1.0 wt. % MWNT. Further increasing milling time to 10 h and 15 h increased the hardness of the ball-milled composite powders to 115.4 ± 3.1 $HV_{10/5}$ and 141.4 ± 2.8 $HV_{10/5,}$ respectively. At even higher milling time of 20 h, the hardness of the ball-milled composite powders reached to 150 ± 2.8 $HV_{10/5}$.

6. 2. 2 Discussion

6. 2. 2. 1. *The evolution and distribution of MWNT in the ball-milled Al-1.0 wt. % composite powders*

Fig. 6. 2. 2. 1. 1 presents a schematic diagram showing the distribution of MWNT in the ball-milled Al-1.0 wt. % MWNT composite powders. According to the SEM micrographs in Fig. 6. 2. (A), after ball milling for 5 h, large MWNT clusters of approximately 25 μm found

in the pristine MWNT (Fig. 3. 3 (A)) was de-agglomerated. However, smaller MWNT agglomerates about a size of 5 μm were still found on the surfaces of the 5 h ball-milled Al-1.0 wt. % MWNT composite powders. Due to the fact that the ball milling process resulted in plastically deformed aluminium powders with a limited welding of particles, no MWNT was found inside the 5 h ball-milled aluminium particles (Fig. 6. 4. (A)). At this stage, some big clusters of MWNT were de-agglomerated by the mixing effect of milling balls. A mixture of individual and agglomerated MWNT was mainly dispersed on the surfaces of the aluminium particles (Fig. 6. 2. 2. 1. 1. (5 h)).

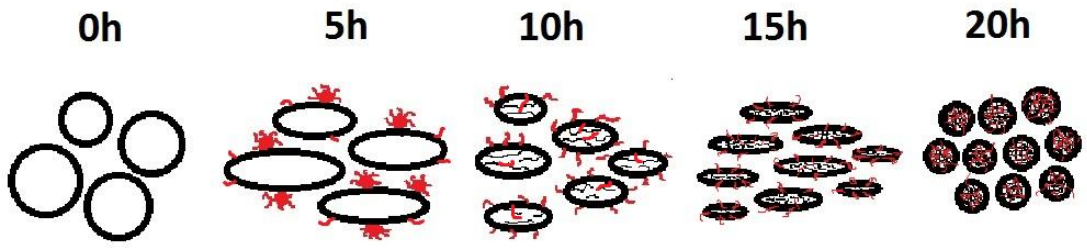


Fig. 6. 11 A schematic diagram showing the distribution of MWNT in the ball-milled Al-1.0 wt. % MWNT composite powders. The black circles represent the ball-milled composite particles. The red lines outside and inside the ball-milled composite particles indicate MWNT while the black lines inside the ball-milled composite powders represents the micro-gaps or micro-pores.

Increasing the milling time to 10 h, no obvious MWNT agglomerates but individual MWNT were found on the surfaces of the 10 h ball-milled Al-1.0 wt. % MWNT composite powders (Fig. 6. 2. (B)). This indicates the de-agglomeration of MWNT by the milling balls. Also, the level of particle welding by the impact of milling balls increased, leading to the trapping of some MWNT at the boundaries of the welded region of aluminium particles (Fig. 6. 4. (B)

and Fig. 6. 3. (D)).

When the milling time increased to 15 h, the MWNT found on the surfaces of ball-milled Al-1.0 wt. % MWNT composite powders were partially covered by the welded flake-shaped aluminium particles (Fig. 6. 2. (C)). Under the violent impact of milling balls, the aluminium particles were further deformed and elongated. Thus, the thickness of each aluminium layer is noticeable thinner than that of the 10 h ball-milled composite powders (Fig. 6. 4. (C)). Also, more surfaces of aluminium particles attached with dispersed MWNT were welded together, therefore, more MWNT were found trapped by the welded aluminium particles (Fig. 6. 4. (C))

Further increasing milling time to 20 h, little MWNT was dispersed on the outmost surfaces of the 20 h ball-milled Al-1.0 wt. % MWNT composite powders. Instead, under the repeated welding and fracturing in the ball milling process, most of the MWNT were found inside the ball-milled aluminium particles (Fig. 6. 4. (D)).

On the whole, the MWNT were first de-agglomerated and distributed on the surface of the aluminium particles. Then, under the impact of the severe and intensive deformation, repeatedly fracturing and welding in the ball milling process, MWNT were gradually dispersed into the ball-milled aluminium particles. This demonstrates ball milling is a feasible method to incorporate MWNT into aluminium powders.

6. 2. 2. 2. The structure evolution of MWNT in the ball-milled Al-1.0 wt. % composite powders

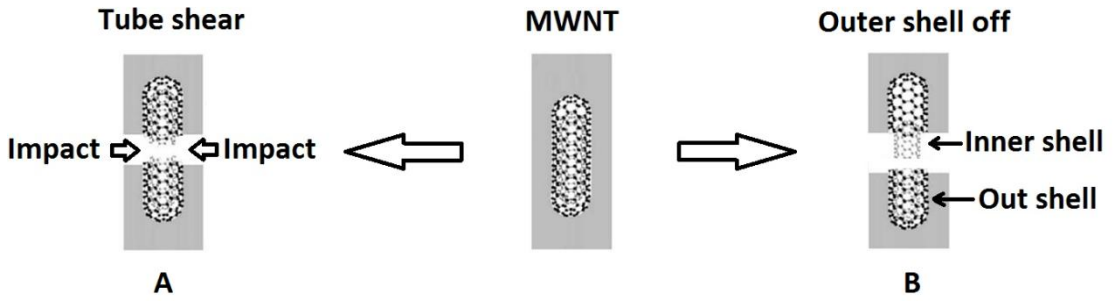


Fig. 6. 12 The breakage of MWNT by (A) tube shear (i.e. shear loading) and (B) outer shell off (i.e. axial tensile loading).

Although MWNT was dispersed into aluminium powders by ball milling, it is worth noting that the structure of MWNT was damaged to some extent. According to the I_D/I_G of the ball-milled Al-1.0 wt. % MWNT composite powders in Fig. 6. 9, the I_D/I_G value increased with increasing milling time. This indicates that defects were introduced into the structure of MWNT by ball milling and the degree of damage deteriorated with increasing milling time. Apparently, in the high energy ball milling process, carbon nanotube is strongly affected by the friction and impact of milling balls and aluminium particles as well as the collision between milling balls and milling pot wall. They all contribute to the deterioration of the structure of carbon nanotube.

A typical negative impact of the ball milling on the MWNT is the length reduction. It can be seen from the Fig. 6. 2. (A) that the length of the MWNT in the Al-1.0 wt. % MWNT composite powders was around 5 μm after ball milling for 5 h. However, the length of the

MWNT was severely decreased to 3.5 μm and 4 μm after ball milling for 10 h and 15 h, respectively. According to Shekar et al. [210], the tensile strength of MWNT is significantly higher than the shear strength of MWNT. Yu et al. [211], Barber et al. [212] and Cooper et al. [213] have reported that the shear strength of MWNT is between 35 MPa and 375 MPa while Peng et al. [214] measured the tensile strength of multi-walled carbon nanotube to be up to 100 GPa. Thus, the anisotropic mechanical properties of MWNT implies that MWNT are vulnerable to be fractured under shearing than axially tensile loading conditions, as illustrated in Fig. 6. 12. (A).

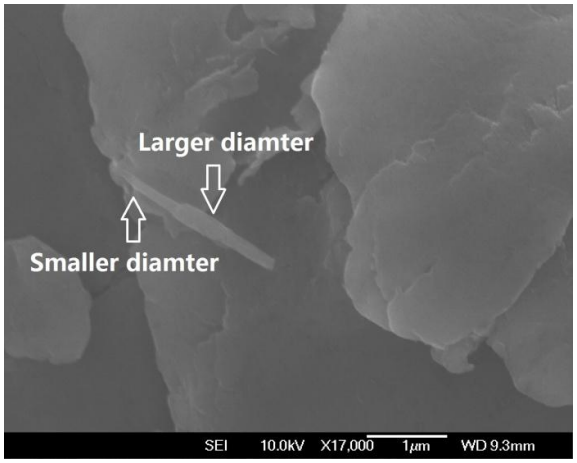


Fig. 6. 13 The SEM micrograph showing the damaged carbon nanotube on the Al-1.0 wt. % MWNT composites powders which were ball-milled for 15 h.

Another common degradation of the MWNT by ball milling is the ‘outer shell off’ as shown in Fig. 6. 12. (B). Under the impact of milling balls and the friction in the ball milling process, some MWNT lost their outer layers of carbon atom sheets which leads to the reduction of MWNT diameter. Fig. 6. 13 shows the MWNT found on the surfaces of the 15 h ball-milled Al-1.0 wt. % CNT composite powders. It can be seen that the diameter of the

right part of the MWNT are larger than that of the left part which are indicated by the arrows. This is because the inter-layer π-bond (van der Waals force, length: 0.34 nm [215, 216], energy: 0.02 meV [217]) in the multi-walled carbon nanotube is much lower than the covalent σ-bond (bond length: 0.142 nm [218], energy: 2.6 eV - 2.8 eV [219]) between the carbon atoms in the same layer composing the strong sp^2 bonding [26]. Therefore, the weak shear interactions between adjacent shells and tubes resulted in the outermost shells of MWNT are prone to be torn apart from the inner shells which is illustrated in Fig. 6. 12. (B). Other defects like torsion, bending and buckling of carbon nanotube structure in the ball milling process are also reported by other researchers [220].

6. 2. 2. 3. The effect of MWNT on the ball-milled aluminium powders

As can be seen from the Fig. 5. 6 that the median particle size of the elemental aluminium powders ball-milled for 15 h and 20 h were 69.71 ± 3.77 μm and 63.78 ± 3.43 μm, respectively. However, the median particle size for the 15 h and 20 h ball-milled Al-1.0 wt. % MWNT composite powders were 46.59 ± 3.30 μm and 40.23 ± 2.99 μm, respectively. Obviously, the median particle size of the ball-milled powders was reduced when 1.0 wt. % MWNT was added into the aluminium powders. This can be explained by the presence of MWNT between aluminium particles, which act as barriers that prevent the direct contact of aluminium particles during ball milling. Consequently, less ball-milled aluminium particles were welded together by ball milling and smaller particles of the ball-milled Al-1.0 wt. % MWNT composite powders were resulted.

6. 2. 3 Summary

This part of the study is focused on understanding the evolution and dispersion of MWNT in the ball-milled Al-1.0 wt. % MWNT composite powders. The following highlights of this study can be summarized:

1. 1.0 wt. % MWNT was homogeneously dispersed into Al powders by high energy ball milling at the expense of the degradation of MWNT structure.

2. The addition of 1.0 wt. % MWNT to the aluminium powders promoted the yielding of finer particles after ball milling, as compared to the ball-milled elemental aluminium powders using the same milling time.

6. 3. The effect of ball milling on the sintered Al-1.0 wt. % MWNT composite material

6. 3. 1 Results

6. 3. 1. 1. *Cross-section*

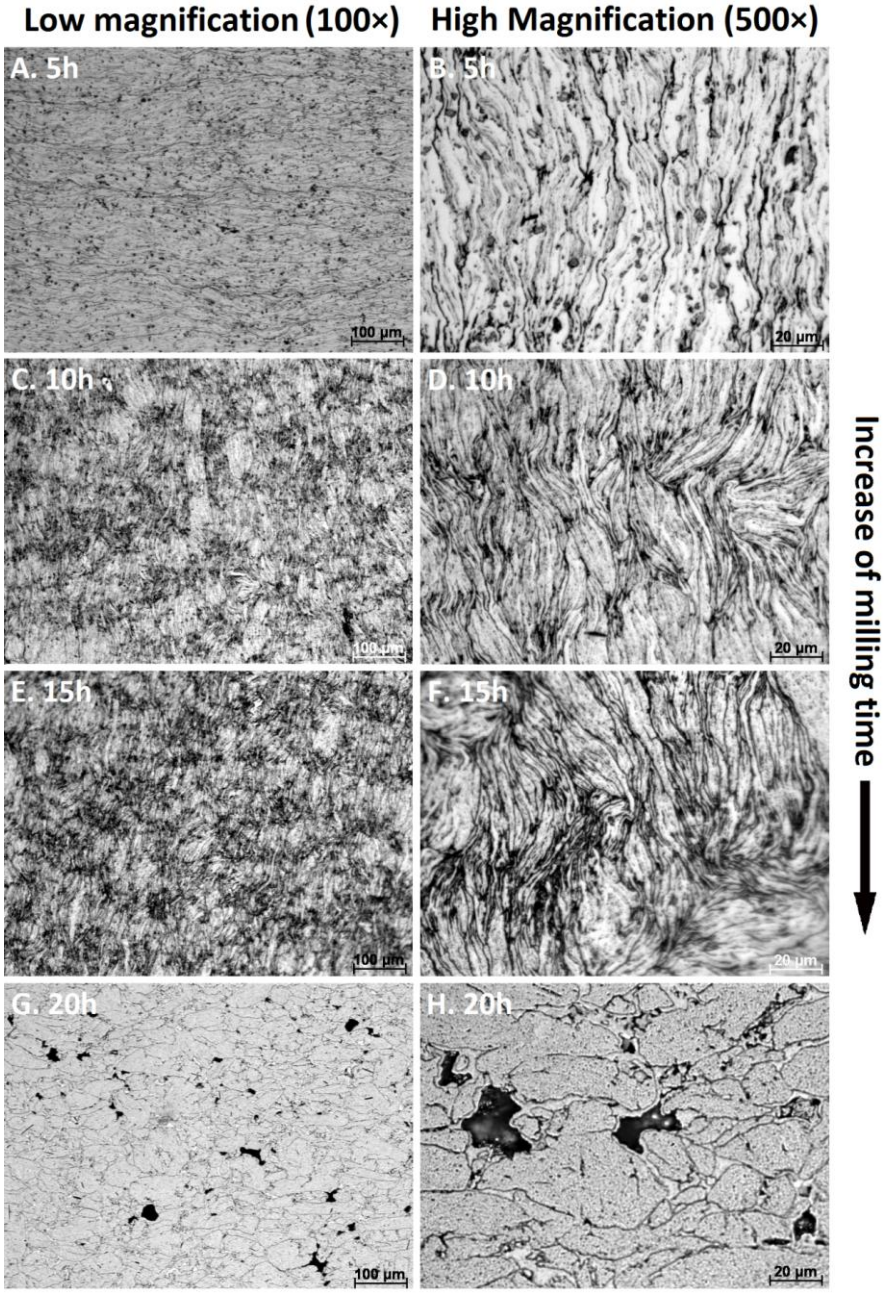


Fig. 6. 14 The optical micrographs showing the cross-section of the sintered Al-1.0 wt. % MWNT specimens using composite powder ball milled for (A) and (B) 5 h, (C) and (D) 10 h, (E) and (F) 15

h and, (G) and (H) 20 h. The images in the left column (A, C, E, G) and right column (B, D, F, H) are taken at magnifications of 100× and 500×, respectively.

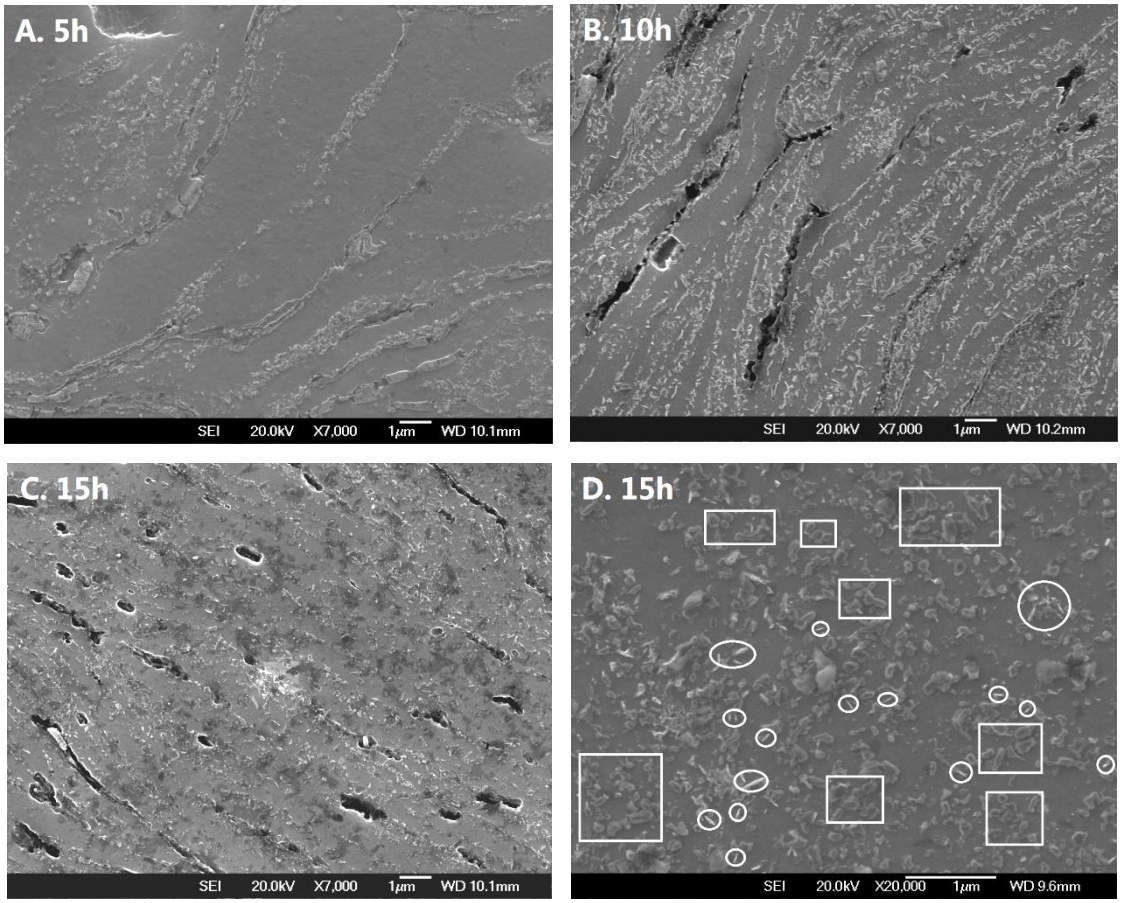


Fig. 6. 15 The SEM micrographs showing the cross-section of the sintered Al-1.0 wt. % MWNT specimens using composite powder ball milled for (A) 5 h, (B) 10 h, (C) and (D) for 15 h. (A)-(C) and (D) are taken at magnifications of 7000× and 20,000×, respectively. The rectangles and circles in (D) indicate the presence of Al_2O_3 and Al_3C_4, respectively.

The cross-sectional microstructure of the sintered Al-1.0 wt. % MWNT composite specimens are shown in Fig. 6. 14. The microstructure of sintered specimens using composite powders milled for 5 h to 15 h consisted of layered structure, as shown in Fig. 6. 14. (A)-(F). The amount of layer boundaries (i.e. not grain boundary) increased and the

thickness of interlayer decreased with increasing milling time. Similar to the ball-milled and sintered pure aluminium specimens (Fig. 5. 12), alumina (Al_2O_3) nano-particles were found in the sintered Al-1.0 wt. % MWNT composite materials as shown in the Fig. 6. 15. (A)-(D). In addition, needle-shaped aluminium carbide (Al_4C_3) [221, 222] in nano size were found in the sintered Al-1.0 wt. % MWNT composite and identified by EDX at a voltage of 5 kv. The Al_2O_3 nano particles and needle-shaped Al_4C_3 in the cross-section of the sintered Al-1.0 wt. % MWNT composite specimen produced using 15 h ball-milled composite powders are indicated by rectangles and circles in Fig. 6. 15. (D), respectively. The amount of Al_2O_3 and Al_4C_3 in the sintered Al-1.0 wt. % MWNT composite specimens with increasing milling time. The formation of Al_4C_3 is also reported by other researchers in the fabrication of carbon fibre [223, 224] and multi-walled carbon nanotube [225-227] reinforced aluminium composites.

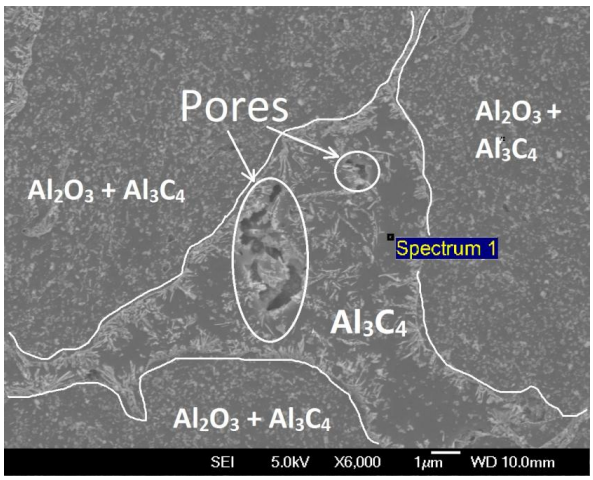


Fig. 6. 16 The SEM micrograph of the cross-section of the sintered Al-1.0 wt. % MWNT composite specimens using 20 h ball-milled composite powders. The white line is the boundary that separates Al_3C_4 rich region and a mixture of Al_2O_3 and Al_3C_4.

However, the microstructure of the sintered composite specimen using Al-1.0 wt. % MWNT

composite powders milled for 20 h consisted of equiaxed grain structure with presence of large pores (Fig. 6. 14. (G) and (H)). Also, mixtures of Al_2O_3 nanoparticles and needle-shaped Al_4C_3 were uniformly dispersed in the matrix as found in the cross-section of the sintered Al-1.0 wt. % MWNT specimen (Fig. 6. 16). In addition, Al_4C_3 rich region at the inter-granular region was identified by EDX as indicated in Fig. 6. 16.

6. 3. 1. 2. The dispersion of MWNT in the sintered Al-1.0 wt. % MWNT composite

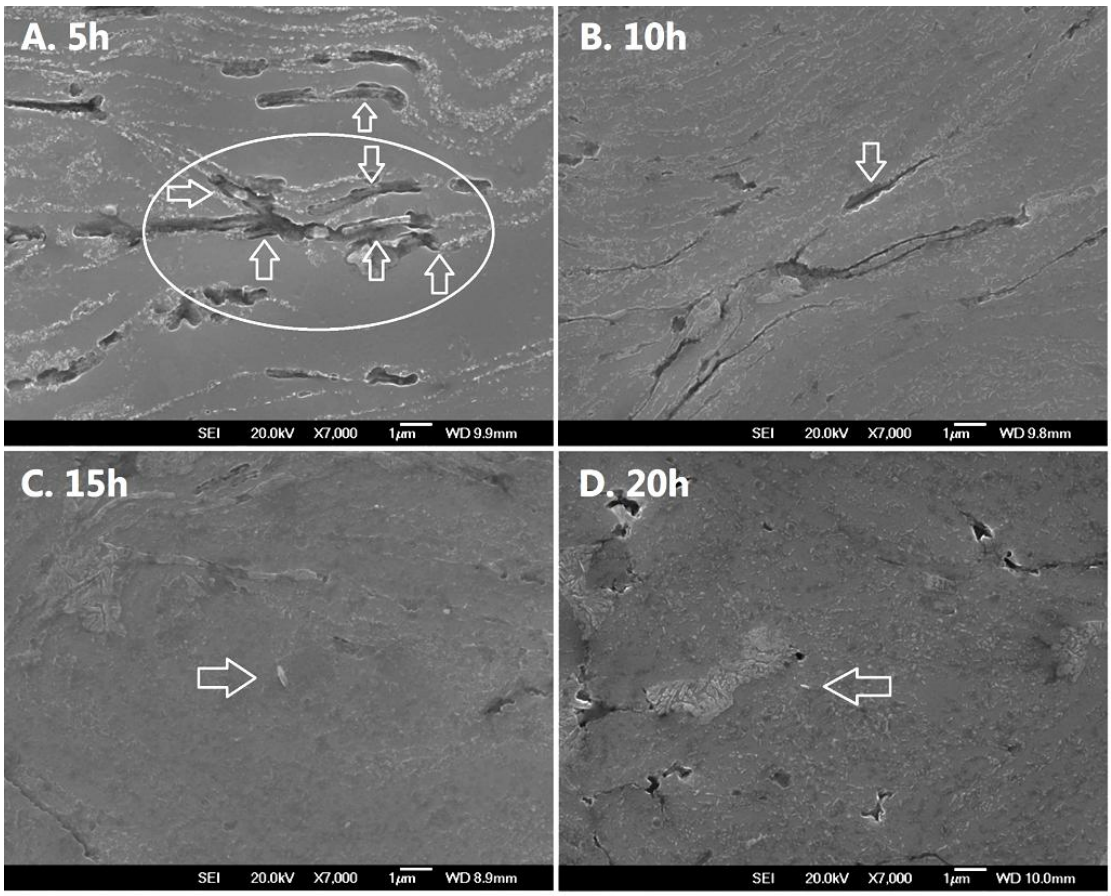


Fig. 6. 17 SEM micrographs showing the MWNT found in the matrix of the sintered Al-1.0 wt. % MWNT composite specimens. The arrows and the circle in (A) indicate the presence of MWNT and cluster of MWNT in the composite matrix.

The dispersion of MWNT in the sintered Al-1.0 wt. % MWNT composite specimens is depicted in Fig. 6. 17. As can be seen from Fig. 6. 17. (A) that several MWNT were found clustered together at the boundaries in the sintered Al-1.0 wt. % MWNT composite specimens using 5 h ball-milled composite powders. In Fig. 6. 17. (B), individual MWNTs were distributed at the boundary in the sintered specimen produced from the 10 h ball-milled Al-1.0 wt. % MWNT composite powders. The sintered specimens fabricated using 15 h and 20 h ball-milled Al-1.0 wt. % MWNT composite powders show MWNT distributed in the composite matrix in Fig. 6. 17. (C) and (D) respectively. It is worth noting that the diameter of the MWNT found at the cross-section decreased in the sintered Al-1.0 wt. % MWNT composite produced from ball-milled composite powders of longer milling time.

6. 3. 1. 3. Sintered density

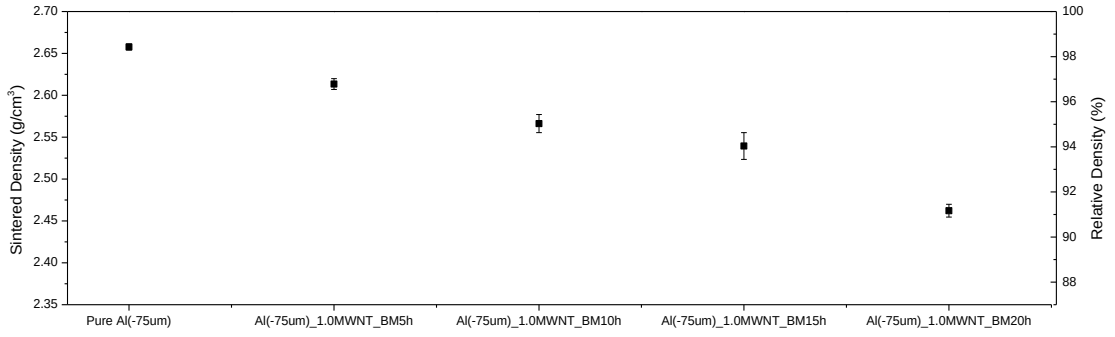


Fig. 6. 18 Sintered density of the composite specimens produced using the ball-milled Al-1.0 wt. % MWNT composite powders.

Fig. 6. 18 shows the densities of the sintered Al-1.0 wt. % MWNT composite specimens. It is obvious in Fig. 6. 18 that the density of sintered specimen fabricated using the ball-milled Al-1.0 wt. % MWNT composite powders decreased with increasing milling time. The

density for the sintered elemental aluminium is 2.66 g/cm^3 (relative density: 98.43 ± 0.11 %). However, the sintered densities of the Al-1.0 wt. % MWNT composite produced using 5 h and 10 h ball-milled composite powders noticeable reduced to 2.61 g/cm^3 (relative density: 96.67 ± 0.24 %) and 2.57 g/cm^3 (relative density: 95.04 ± 0.40 %), respectively. Further increasing milling time to 15 h and 20 h, the density of the Al-1.0 wt. % MWNT composite were further decreased to 2.54 g/cm^3 (relative density: 94.03 ± 0.59 %) and 2.46 g/cm^3 (relative density: 91.53 ± 0.28 %), respectively.

6. 3. 1. 4. X-ray diffraction

In order to study the crystal structure of the sintered Al-1.0 wt. % MWNT specimens fabricated from the ball-milled Al-1.0 wt. % MWNT composite powders, X-ray diffraction patterns were obtained and the spectrum are shown in Fig. 6. 19. It is apparent that five characteristic peaks of aluminium crystal structure corresponding to (111), (200), (220), (311) and (400) crystallographic planes are presented in all the sintered specimens. Also, the XRD peak of Al_4C_3 was observed in the sintered Al-1.0 wt. % MWNT composites fabricated from the 10 h to 20 h ball-milled composite powders. Additionally, Al_2O_3 peaks were found in the 20 h ball-milled and sintered Al-1.0 wt. % MWNT composite.

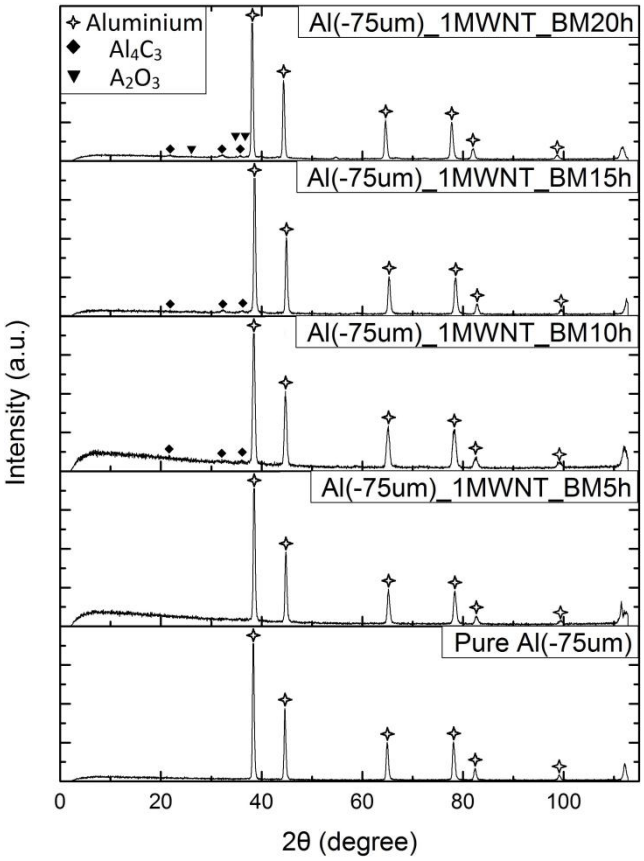


Fig. 6. 19 The XRD patterns of the sintered Al-1.0 wt. % MWNT composite fabricated using ball-milled Al-1.0 wt. % MWNT composite powders.

It is noteworthy that the peak intensity of Al_4C_3 in the matrix increased with increasing milling time. This suggests that more Al_4C_3 was formed in the sintered composite which was produced using the composite powders ball milled for longer time. According to other researchers [225, 228], Al_4C_3 were formed by the reaction of Al with amorphous carbon, defective sites and open ends on MWNT which were resulted from the structural damage of MWNT during the ball milling process. In the current research, the Raman spectra and I_D/I_G of the sintered Al-1.0 wt. % MWNT composite (Fig. 6. 8 and Fig. 6. 9) demonstrated the damage degree of the MWNT structure increased with increasing milling time. Therefore, the amount of amorphous carbon and defective sites reacted with aluminium increased with

the increase milling time. This increased the amount of Al_4C_3 formed in the Al-1.0 wt. % MWNT composite specimens prepared from powders ball milled for longer time.

What's also worth noticing is that the width of each XRD peak is broadened and it increased with the increasing milling time, as compared to the elemental aluminium specimen. According to T. Ungár [229], the broadening of the XRD peaks arises from the grain size refinement and the increase of lattice imperfectness. During the high energy ball milling process, the intensive mechanical deformation generated a large amount of lattice strain, structural defects and grain refinement into the ball-milled composite powders [230], leading to the peak broadening in the XRD spectra of the Al-1.0 wt. % MWNT composite.

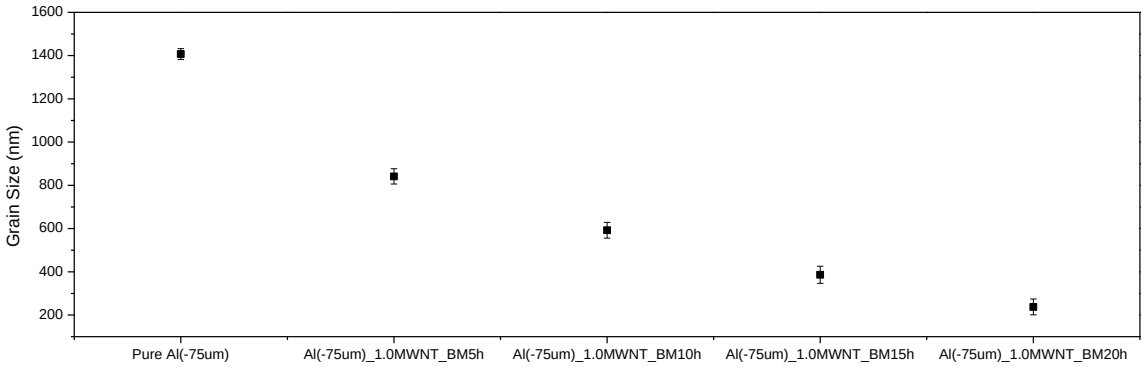


Fig. 6. 20 The grain size of the sintered Al-1.0 wt. % MWNT composite calculated by the William-Hall equation.

To quantitatively study the effect of ball milling on the crystal structure of the sintered Al-1.0 wt. % MWNT composite specimens, the grain size of the sintered composite specimens is calculated from the full width at half maximum (FWHM) according to the William-Hall equation (equation: 3. 4. 9. 1). The calculated grain size of the as-prepared

bulk composite specimens is shown in Fig. 6. 20. Overall, the grain size of the sintered Al-1.0 wt. % MWNT composite specimens decreased with increasing milling time. As can be seen from the Fig. 6. 20 that the grain size is significantly reduced from 1.6 μm to 841.39 ± 35.35 nm for the sintered pristine aluminium and the sintered Al-1.0 wt. % MWNT composite specimen prepared using the powders ball-milled for 5 h, respectively. When the milling time increased to 15 h and 20 h, the grain size decreased to 386.19 ± 39.54 nm and 237.63 ± 36.57 nm for the sintered Al-1.0 wt. % MWNT composite specimens fabricated using 15 h and 20 h ball-milled composite powders, respectively. The fine grain size of the sintered Al-1.0 wt. % MWNT composite fabricated using 20 ball-milled composite powders was demonstrated by the TEM micrograph (Fig. 6. 21).

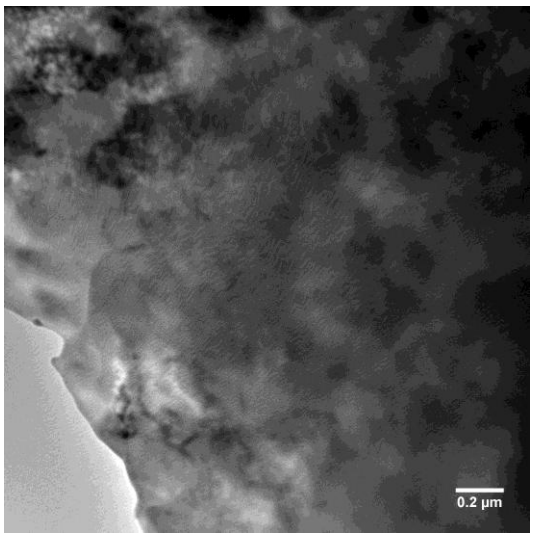


Fig. 6. 21 TEM micrograph of the sintered Al-1.0 wt. % MWNT composite fabricated using the 20 ball-milled composite powders.

6. 3. 1. 5. Raman spectroscopy

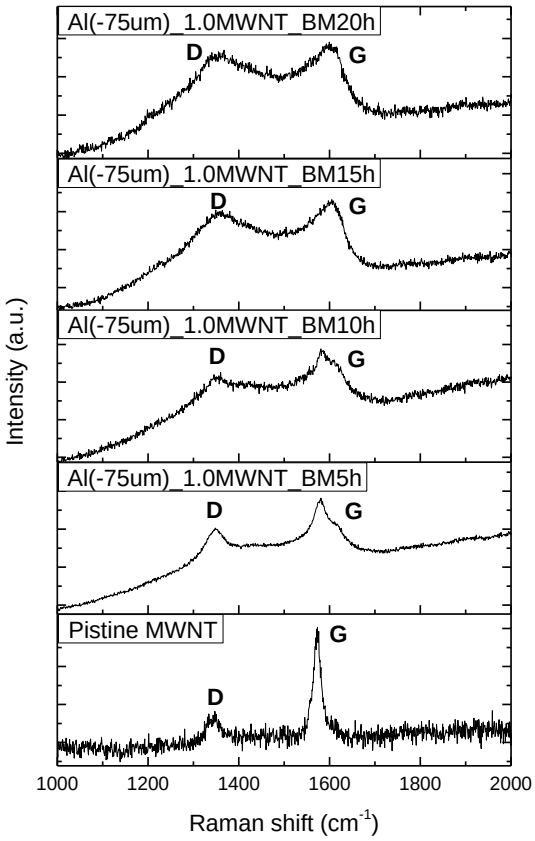


Fig. 6. 22 The Raman spectra of sintered composite specimens fabricated using the ball-milled Al-1.0 wt. % MWNT composite powders.

The structure of MWNT in the sintered Al-1.0 wt. % MWNT composite specimen is characterised by Raman spectroscopy and the Raman spectra are plotted in Fig. 6. 22. The intensity of the G band peak in the Raman spectrum of the pristine carbon nanotube is remarkably higher than that of the D band peak, which indicates a perfect crystal structure of the pristine MWNT. However, the relative intensity of the D band peak in the sintered Al-1.0 wt. % MWNT composite produced using ball-milled composite powders increased with increasing milling time. This suggests the introduction of a certain amount of defects into the structure of MWNT as a result of the ball milling process.

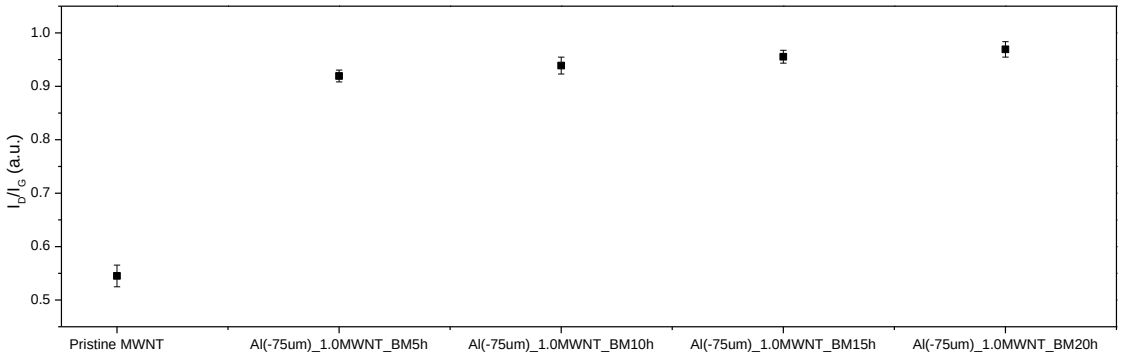


Fig. 6. 23 The I_D/I_G of the sintered composite specimens fabricated using the ball-milled Al-1.0 wt. % MWNT composite powders.

The I_D/I_G of the sintered composite specimens is calculated from the Raman spectra presented in Fig. 6. 22. Apparently, the I_D/I_G of the pristine MWNT in Fig. 6. 23 is very low and only at round 0.55. Nevertheless, the I_D/I_G of the 5 h ball-milled and sintered Al-1.0 wt. % MWNT composite powders is doubled and reached to 0.92 ± 0.01. Further increasing the ball milling to 10 h (Al(-75um)_1.0MWNT_BM10h) and 20 h (Al(-75um)_1.0MWNT_BM20h), the I_D/I_G of the sintered Al-1.0 wt. % MWNT composite specimens was further increased to 0.94 ± 0.02 and 0.97 ± 0.01, respectively.

6. 3. 1. 6. Vickers micro-hardness

The Vickers micro-hardness of sintered Al-1.0 wt. % MWNT composites specimens was measured and the results are given in Fig. 6. 24. Overall, the hardness of the sintered Al-1.0 wt. % MWNT composite specimen increased with increasing milling time. The hardness for the sintered Al-1.0 wt. % MWNT composite produced from 5 h and 10 h ball-milled composite powders are 73.09 ± 3.88 $HV_{10/5}$ and 90.98 ± 3.07 $HV_{10/5}$, respectively. When the

milling time increased to 15 h and 20 h, the hardness for the sintered Al-1.0 wt. % MWNT composite reached to 102.9 ± 4.46 $HV_{10/5}$ and 114.85 ± 4.87 $HV_{10/5}$, respectively. Also, it is worth noting that the hardness of the sintered Al-1.0 wt. % MWNT composite materials were found significantly higher than that of the sintered elemental aluminium specimens made from powders ball-milled for the same length of time (Fig. 5. 16).

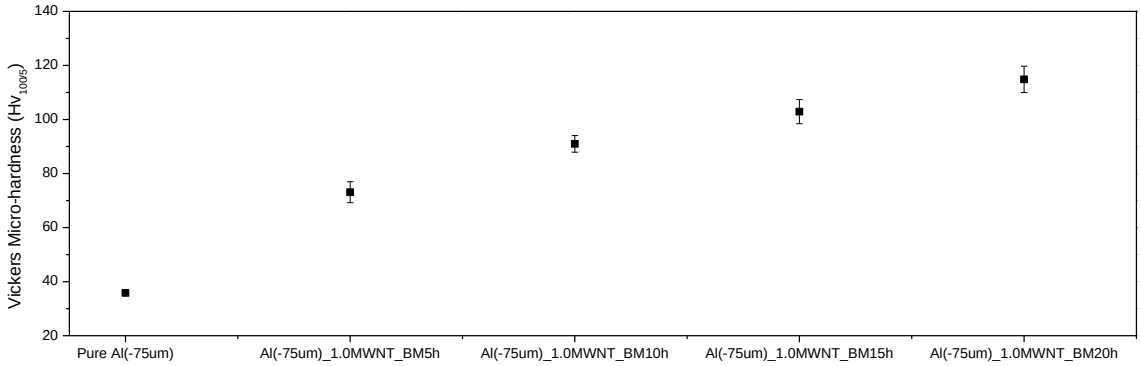


Fig. 6. 24 The Vickers micro-hardness of sintered Al-1.0 wt. % MWNT composite specimens fabricated using the ball-milled Al-1.0 wt. % MWNT composite powders.

6. 3. 1. 7. Tensile properties

Fig. 6. 25 shows the stress-strain curves of the sintered elemental aluminium and Al-1.0 wt. % MWNT composite specimens. It is apparent in Fig. 6. 25 that the sintered elemental aluminium specimen exhibited the best ductility but lowest strength among all the sintered specimens. On the contrary, the ductility of the sintered Al-1.0 wt. % MWNT composite specimens was seriously reduced but their tensile strength is considerably increased.

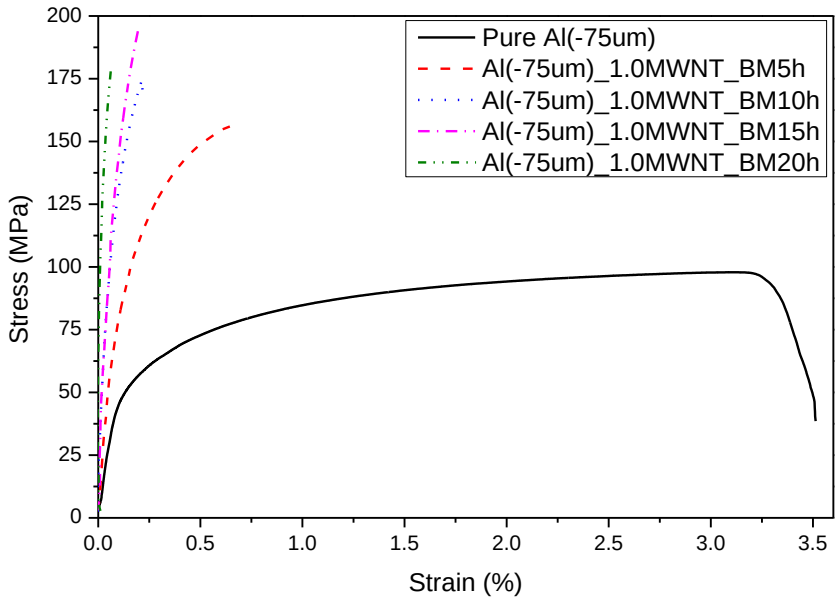


Fig. 6. 25 The stress-strain curves of the bulk composite specimens fabricated using elemental aluminium and ball-milled Al-1.0 wt. % MWNT composite powders.

Table 6. 1 The mechanical properties of the sintered elemental aluminium and composite specimens fabricated using the ball-milled Al-1.0 wt. % MWNT composite powders

Materials	**Yield strength (MPa)**	**Ultimate tensile strength (MPa)**	**Maximum strain before failure (%)**
Pure Al(-75um)	52.62 ±1.74	97.87 ±4.89	3.51 ±0.08
Al(-75um)_1.0MWNT_BM5h	97.77 ±5.96	156.02 ±7.40	0.65 ±0.06
Al(-75um)_1.0MWNT_BM10h	108.95 ±6.88	174.54 ±8.43	0.22 ±0.05
Al(-75um)_1.0MWNT_BM15h	124.76 ±8.35	195.84 ±9.49	0.20 ±0.02
Al(-75um)_1.0MWNT_BM20h	131.15 ±9.72	179.22 ±8.61	0.06 ±0.02

The mechanical properties of the sintered Al-1.0 wt. % MWNT composite specimens are illustrated in Table. 6. 3. 1. 7. 1. As can be seen from Table 6. 1 that the ultimate tensile strength (UTS) of the sintered elemental aluminium composite is 97.87 ±4.894 MPa. The UTS of the sintered Al-1.0 wt. % MWNT composite specimens steadily increased with increasing ball milling. When the Al-1.0 wt. % MWNT composite powders was ball milled for 5 h, the UTS of the sintered Al-1.0 wt. % MWNT composite significantly increased to

156.02 ± 7.40 MPa. The UTS of the sintered Al-1.0 wt. % MWNT composite reached to a maximum value of 195.84 ± 9.49 MPa at the milling time of 15 h. However, when the milling time increased to 20 h, the UTS of the sintered Al-1.0 wt. % MWNT composite was reduced to 179.22 ± 8.61 MPa.

Contrary to the trend of the UTS of the sintered composite, it can be seen from Table 6. 1 that the maximum fracture strain of the sintered composite specimen decreased with increasing milling time. The maximum fracture strain of the sintered elemental aluminium specimen is as high as 3.51 ± 0.18 %. Nevertheless, after only ball milling for 5 h, the maximum failure strain of the sintered Al-1.0 wt. % MWNT composite is severely reduced to 0.65 ± 0.06 %. At longer milling time of 15 h and 20 h, the maximum failure strain of the sintered composite further decreased to 0.20 ± 0.02 and 0.06 ± 0.02.

6. 3. 1. 8. Fracture surface

Fig. 6. 26 illustrates the fractographs of the sintered Al-1.0 wt. % MWNT composite specimens after tensile test. It can be seen in Fig. 6. 26. (A) that the fracture surface of the sintered elemental aluminium specimen shows extensively plastic deformation and dimple features, which is the typical sign of energy absorption and ductile fracture. Also, the sintered Al-1.0 wt. % MWNT composite fabricated using the 5 h ball-milled composite powders shows some plastic deformed areas Fig. 6. 26. (B) which supports the maximum fracture strain in Table 6. 1.

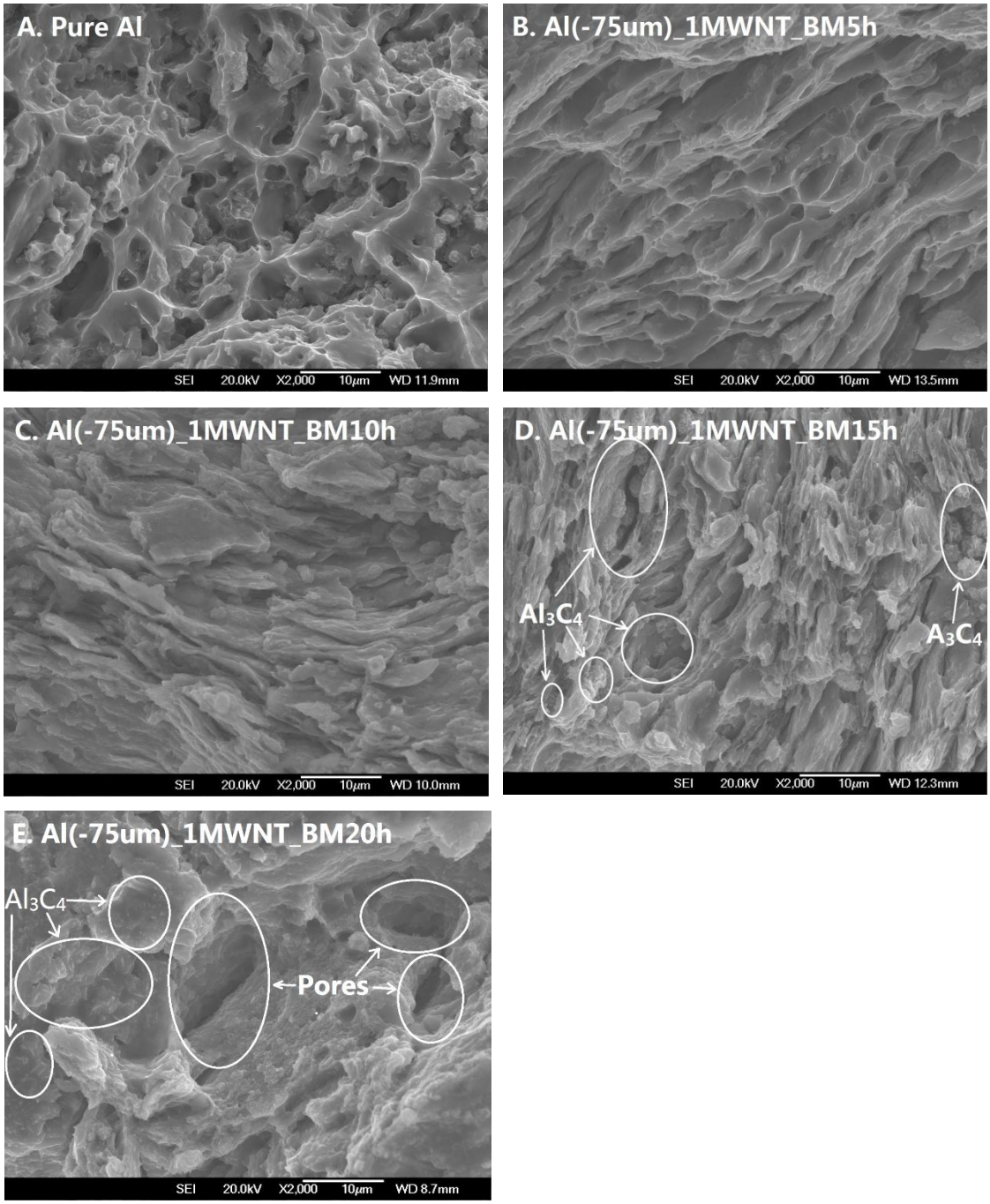


Fig. 6. 26 The fracture surfaces of the sintered Al-1.0 wt. % MWNT composite specimens subjected to ASTM standard tensile test.

However, when the milling time increased to 10 h (Fig. 6. 26. (C)) and 15 h (Fig. 6. 26. (D)), the fracture surface of sintered Al-1.0 wt. % MWNT specimen did not contain any significant dimple fracture. This indicates that the specimen failed by brittle manner. Moreover,

relatively large pores and Al_3C_4, as marked by the circles in Fig. 6. 26. (E), were found at the centre of the recessed areas on the fracture surfaces of the sintered composite produced using the 20 h ball-milled composite powders. This suggests that the pores and Al_3C_4 in the composite matrix are the nucleation points of cracks.

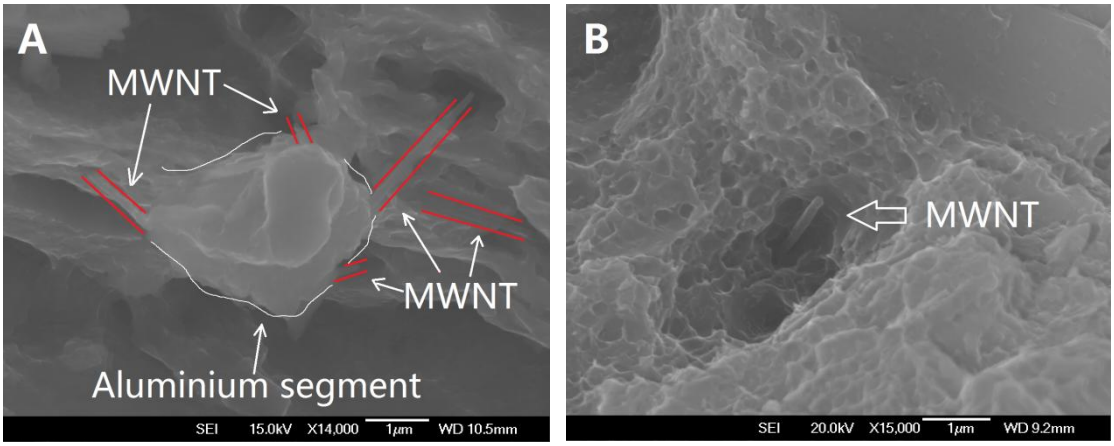


Fig. 6. 27 The MWNT found at the fracture surfaces of the sintered Al-1.0 wt. % MWNT composite specimen using 15h ball-milled powders, subjected to ASTM standard tensile test. Red lines outline the orientation of MWNT.

Fig. 6. 27 presents the MWNT found on the fracture surfaces of the sintered Al-1.0 wt. % MWNT composite specimens fabricated using the (A) 15 h and (B) 20 h ball-milled composite powders. As can be seen from the Fig. 6. 27. (A) that a segment of aluminium particles (as outlined by the white lines) was dragged by MWNT (as outlined by the red lines and indicated by white arrows) which are embedded in the composite matrix. This demonstrates the effective load sharing of MWNT from the aluminium matrix. Also, a dispersed individual MWNT was observed at the fracture surface of the sintered composite specimen fabricated using the 20 h ball milled composite powders as indicated in Fig. 6. 27.

(B). The alignment of paralleling to the tension direction indicate the contribution of the MWNT in the strengthening of composite materials.

6. 3. 2 Discussion

6. 3. 2. 1. The evolution and dispersion of MWNT in the sintered Al-1.0 wt. % MWNT composite

The homogeneous dispersion of carbon nanotube in the metal powders has been so far the most significant challenge in the field of CNT reinforced metal matrix composite [231]. It influences the performance and properties of the final composite products. Specifically, due to the poor bonding and the surface tension difference between carbon nanotube and aluminium [232]. the agglomeration of CNT is vulnerable to form pores inside the composite matrix, leading to lower strength, increased brittleness and deteriorated overall properties of the composite [233]. On the contrary, good dispersion of carbon nanotube leads to the better utilitisation of the characteristics of MWNT and remarkable enhancement of the properties [234].

Fig. 6. 2 and Fig. 6. 17 shows the dispersion of MWNT in the matrix of the sintered Al-1.0 wt. % MWNT composite. As can be seen that after the 5 h, several MWNT were still found clustered together and distributed at the boundaries (Fig. 6 .3. 1. 2. 1. (A)). This is accordance with the dispersion of MWNT on the 5 h ball-milled Al-1.0 wt. % MWNT composite powders as showed in Fig. 6. 2. (A). Increasing the milling time to 10 h, individual MWNT was found at boundaries (Fig. 6 .3. 1. 2. 1. (B)). When the milling time

increased to 15 h and 20 h, the MWNT was dispersed inside the matrix of the sintered Al-1.0 wt. % MWNT composite. Overall, the distribution of MWNT in the sintered Al-1.0 wt. % MWNT composite corresponded to the dispersion of MWNT in the ball-milled Al-1.0 wt. % MWNT composite powders (Fig. 6. 4). Ball milling is demonstrated to be effective in incorporating MWNT into aluminium metal matrix.

However, under the intensive impact and friction of the milling balls and the fracture of the composite particles, the structure of carbon nanotube is vulnerable to be bent, distorted and damaged. In addition, defects and amorphous carbon can be formed [227]. As can be seen from the Fig. 6. 23 that the I_D/I_G of the sintered Al-1.0 wt. % MWNT composite increased with increasing milling time. Similar increasing trend of the I_D/I_G is also reported by other researchers like Yang et al. [30], Liu et al. [93], Borkar et al. [235] and Chandran et al. [236] in the ball-milled MWNT reinforced metal composite materials.

The direct evidence of the degradation of MWNT structure is the shortening of their length as shown in Fig. 6. 2. Also, Castillejos et al. [237] reported that the presence of amorphous carbon in MWNT increased the intensity of D band peaks. Ci et al. [228] and Kurita et al. [227] found that Al_4C_3 was preferentially formed at defective sites, open ends of MWNTs and amorphous carbon rich region. In the current study, a certain amount of amorphous carbon and defects in MWNT was formed in after the ball milling process. This contributes to the increase in the intensity of D band peak and the I_D/I_G of the sintered Al-1.0 wt. % MWNT composite (Fig. 6. 23). In addition, the amount of the amorphous carbon, defective

sites and open ends of MWNT increased with increasing milling time. Subsequently, they reacted with aluminium and formed Al_3C_4 during the sintering process. Therefore, Al_3C_4 was found at the fracture surface (Fig. 6. 26 and Fig. 6. 28) and cross-section (Fig. 6. 15) of the sintered Al-1.0 wt. % MWNT composite. Also, the characteristic peaks of Al_3C_4 appeared in the XRD pattern (Fig. 6. 19) of the sintered Al-1.0 wt. % MWNT composite.

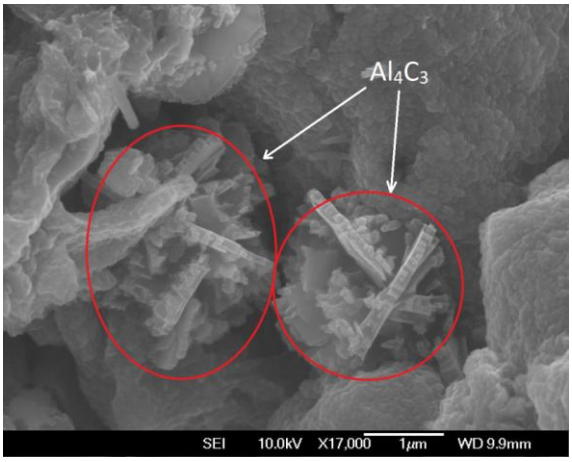


Fig. 6. 28 The Al_4C_3 found at the fracture surface of sintered Al-1.0 wt. % MWNT composite specimens fabricated by the 20h ball-milled composite powders.

6. 3. 2. 2. The strengthening of the sintered Al-1.0 wt. % MWNT composite

Table 6. 2 presents the experimentally measured and estimated yield strengths of the sintered Al-1.0 wt. % MWNT composite based on models of grain refinement strengthening (Hall-Petch equation, section 2. 4. 3. 1) and shear lag strengthening (Kelly-Tyson equation, section 2. 4. 3. 5). As can be seen from the Table 6. 2 that the experimentally measured yield strength of Al-1.0 wt. % MWNT composite increased from 97.73 MPa to 108.95 MPa after ball milling for 5 h and 10 h respectively. For longer milling time of 15 h and 20 h, the

experimentally measured yield strength increased to 124.76 MPa and 131.15 MPa, respectively. Overall, the experimentally measured yield strength of the sintered Al-1.0 wt. % MWNT composite increased with increasing milling time.

Table 6. 2 Comparison of the estimated and experimentally measured yield strength of the sintered Al-1.0 wt. % MWNT composite materials.

Sintered materials	**Estimated yield strength by Hall-Petch equation (MPa)**	**Estimated yield strength by Kelly-Tyson equation (MPa)**	**Experimentally measured yield strength (MPa)**
Al(-75um)_1.0MWNT_BM5h	94.32	130.21	97.73
Al(-75um)_1.0MWNT_BM10h	106.87	145.14	108.95
Al(-75um)_1.0MWNT_BM15h	125.45	161.44	124.76
Al(-75um)_1.0MWNT_BM20h	151.99	-[1]	131.15

It can be seen from the Table 6. 2 that the estimated yield strength of the Al-1.0 wt. % MWNT composite materials calculated by both Hall-Petch equation and Kelly-Tyson equation, showed increasing trends with increasing milling time. More importantly, the experimentally measured yield strength of the Al-1.0 wt. % MWNT composite are more closely correlated to that calculated by the Hall-Petch equation. This indicates that grain refinement mechanism played a more significant role in the strengthening of Al-1.0 wt. % MWNT composite materials fabricated by the ball-milled Al-1.0 wt. % MWNT composite powders.

[1] No reference yield strength of matrix available

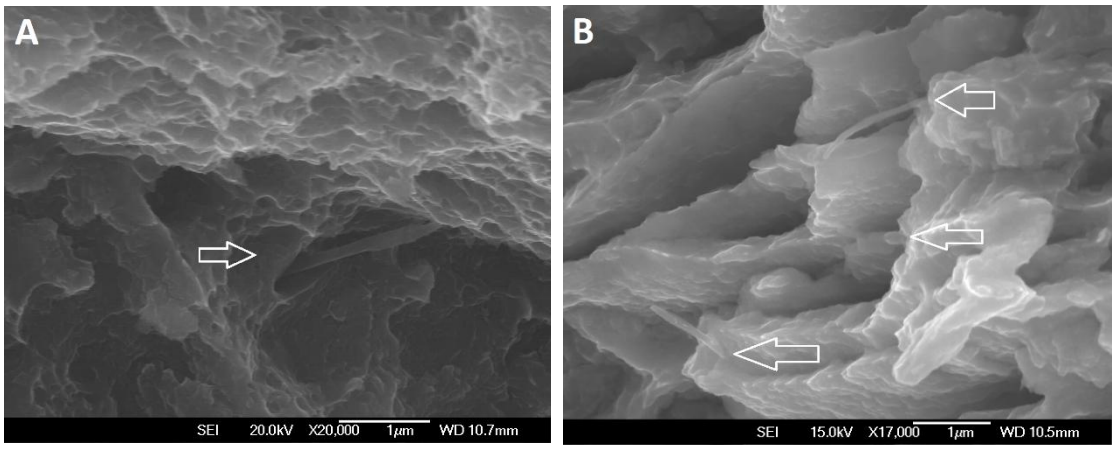


Fig. 6. 29 The MWNT found in the fracture surface of the sintered Al-1.0 wt. % MWNT composite materials with ball milling for (A) 5 h and (B) 10 h. The arrow indicates the presence of MWNT. (A) presents bridging and (B) presents pull-out.

However, it is worth noticing that the Hall-Petch equation does not take the density of the material into consideration. This implies that sintered density below the theoretical density would result in the deterioration of mechanical properties due to the presence of voids. Nevertheless, the experimentally measured yield strength of the Al-1.0 wt. % MWNT composite materials with ball milling for 5 h and 10 h (relative sintered density of 97 % and 95 %, respectively, Fig. 6. 18) are greater than the estimated values by the Hall-Petch equation which assumes the materials are 100 % dense. This can be explained by the load transfer effect [238-240] by MWNT in the matrix. R. George [133] deemed that the composite utilized the stiffness of MWNT through the transfer of load from the matrix to MWNT by interfacial shear stress. B. Chen et al. [145] experimentally demonstrated the shear lag effect in the MWNT reinforced aluminium composite by in situ observation in the tensile test (as introduced in the section 2. 4. 3. 5). Similar crack bridging and pull-out of MWNT on the fracture surface of the sintered Al-1.0 wt. % MWNT composite is observed

and shown in Fig. 6. 27 and Fig. 6. 29. Apparently, in Fig. 6. 29. (A), a MWNT is bridged over the two separated sections on the fracture surface of the sintered Al-1.0 wt. % MWNT composite. Fig. 6. 29. (B) shows the evidence of pull-out of MWNT in the fracture surface, as highlighted by arrows. This demonstrates the contribution of load transfer effect of MWNT to the strengthening of the Al-1.0 wt. % MWNT composite.

Moreover, when the milling time increased to 15 h and 20 h, the corresponding experimentally measured yield strength (i.e. 124.76 MPa and 131.15 MPa) of the Al-1.0 wt. % MWNT composite are lower than the estimated yield strength (i.e. 125.45 MPa and 151.99 MPa) of the composite. This can be explained by the decrease of the sintered density (Fig. 6. 18) which degrades the mechanical properties of the Al-1.0 wt. % MWNT composite. Also, the reinforcing effect from MWNT was reduced with increasing milling time since the structure of MWNT was damaged during the ball milling process. Especially, the degree of damage is proportional to the milling time (Fig. 6. 22 and Fig. 6. 23).

Furthermore, Al_2O_3 and Al_3C_4 are formed in the matrix of the sintered Al-1.0 wt. % MWNT composite (Fig. 6. 15). These hard phases may hinder the propagation of dislocations in the matrix and improve the mechanical properties of the composite. Especially, other researchers [241, 242] also reported that the formation of Al_3C_4 in the Al-MWNT composite enhanced the interface between MWNT and aluminium. Subsequently, this improves the efficiency of load transfer between aluminium matrix and MWNT. However, the presence of Al_2O_3 and Al_3C_4 in the composite matrix is also reported to generate local strains and debonding at the interface due to the mismatch of elastic modulus and thermal expansion

coefficients between aluminium and Al_2O_3 and Al_3C_4 [243]. This embrittles the composite and reduces the ductility of the composite [223, 224].

6. 3. 3 Summary

The sintered Al-1.0 wt. % MWNT composite specimens were prepared using ball-milled composite powders. According to the characterization of the sintered Al-1.0 wt. % MWNT composite, following conclusions can be drawn:

1. 1.0 wt. % MWNT was homogeneously dispersed in the matrix of the sintered composite by ball milling at the expense of the degradation of MWNT structure.

2. The ultimate tensile strength and the yield strength of the sintered Al-1.0 wt. % MWNT composite specimens increased with increasing milling time, while the maximum failure strain of the sintered Al-1.0 wt. % MWNT composite specimens reduced with increasing milling time.

3. The strengthening of the sintered Al-1.0 wt. % MWNT composite materials is mainly due to gain refinement and load transfer effect. The Al_2O_3 and Al_3C_4 formed in the matrix may also contribute to the enhancement of the mechanical properties of the sintered Al-1.0 wt. % MWNT composite.

Chapter 7. The effect of multi-walled carbon nanotube concentration on the microstructure and mechanical properties of Al-MWNT composite materials

7. 1. Introduction

This chapter presents a detailed study of the effect of various amount (0.5, 1.0, 2.0 wt. %) of MWNT on the microstructure and tensile properties of the 15 h ball-milled Al-MWNT composite powders before and after sintering.

The microstructure of the 15 h ball-milled Al-MWNT composite powders and the sintered Al-MWNT composite was investigated by a combination of optical microscopy and SEM. The crystal structure of the specimens is characterized by XRD. The structure of multi-walled carbon nanotube was studied by Raman spectroscopy. The tensile properties of the sintered Al-MWNT composite were measured according to ASTM standard tensile test.

The explanation of the names of the as-fabricated materials introduced in this chapter can be found in Table 3. 5.

7. 2. The effect of multi-walled carbon nanotube concentration on the Al-MWNT composite powders

7. 2. 1 Results

7. 2. 1. 1. *Morphology*

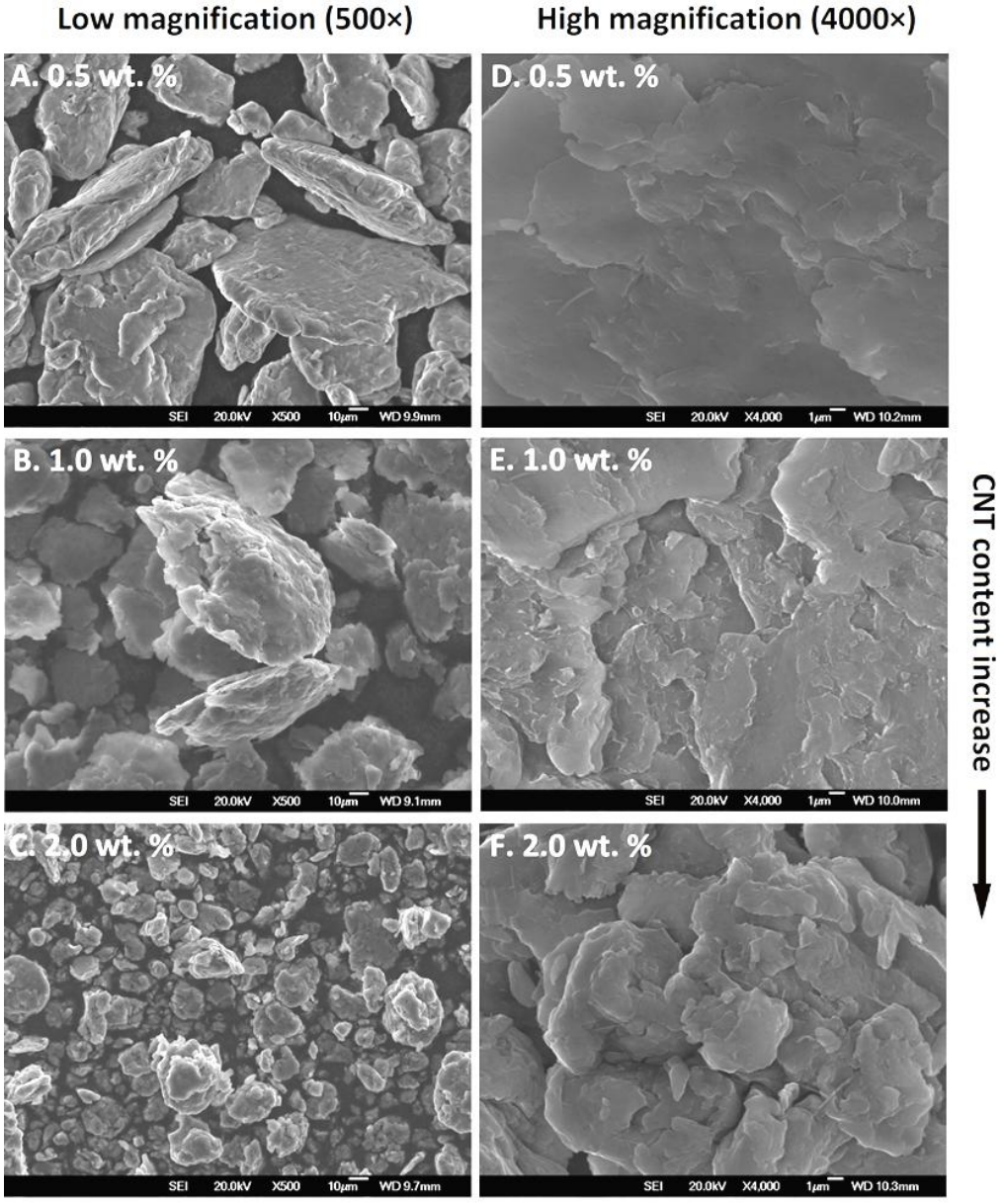


Fig. 7. 1 SEM micrographs showing the morphology of the ball-milled Al- (A) and (D) 0.5 wt. %, (B) and (E) 1.0 wt. % and, (C) and (F) 2.0 wt. % MWNT composites powders (magnification: (A)-(C): 500×, (D)-(F): 4000×).

The morphology of ball-milled Al-MWNT composite powders is studied by SEM using secondary electron imaging mode and the micrographs taken at magnification 500× (left column) and 4000× (right column) are presented in Fig. 7. 1. The ball-milled Al-MWNT composite powders containing 0.5 wt. % MWNT has an average particle size of around 60 μm (Fig. 7. 1. (A)). However, at higher MWNT content of 1.0 wt. %, the average size of the ball-milled Al-MWNT composite particles decreased slightly to about 45 μm. At even higher content of 2.0 wt. % MWNT, the average particle size of the composite powders reduced significantly to around 20 μm. In general, the mean particle size of the ball-milled Al-MWNT composite powders decreased with increasing MWNT content.

Also, it can be seen from Fig. 7. 1 that the shape and roughness of the ball-milled Al-MWNT composite powders varied with the content of MWNT. Al-0.5 wt. % MWNT composite powders have disc-shape morphology with smooth surfaces and rounded edges. However, the morphology changed to a lenticular shape as the MWNT content increased to 1.0 wt. %. In addition, the surface of ball-milled Al-1.0 wt. % MWNT composite particles became rougher while the edges of the particles became sharper. When the addition of MWNT increased to 2.0 wt. %, the ball-milled composite powders were granulated and equiaxed. Especially, small granular particles were observed on the surface of ball-milled Al-MWNT composite particles as shown in Fig. 7. 1. (F).

7. 2. 1. 2. The dispersion of multi-walled carbon nanotube

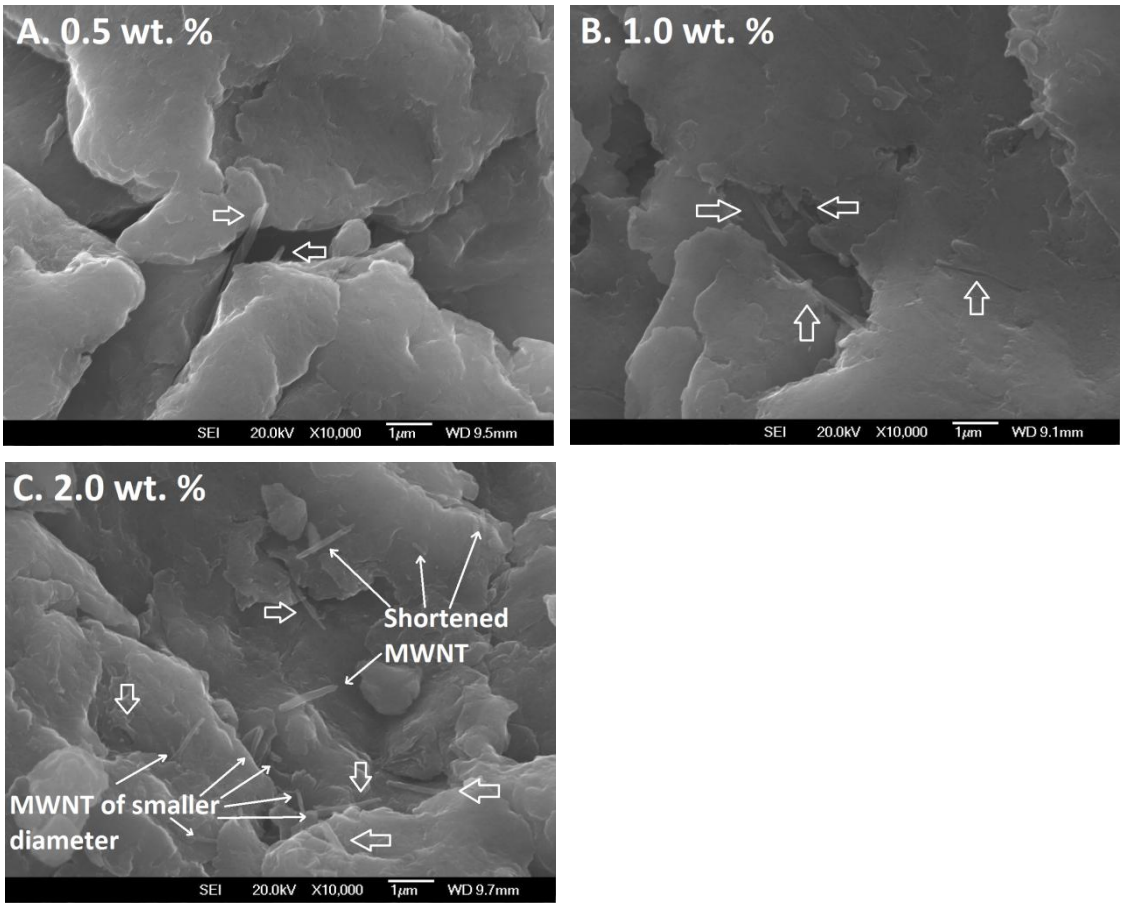


Fig. 7. 2 SEM micrographs showing the MWNT on the ball-milled Al-(A) 0.5 wt. %, (B) 1.0 wt. % and (C) 2.0 wt. % MWNT composites powders. The arrows indicate the presence of MWNT.

The distribution of multi-walled carbon nanotube in the ball-milled Al-MWNT composite powders is investigated by SEM. Fig. 7. 2 shows the MWNT found on the surface of ball-milled Al-MWNT composite powders (as indicated by arrows). As can be seen from the Fig. 7. 2. (A) that most surface area of the ball-milled Al-0.5 wt. % MWNT composite powders are MWNT free and the MWNT are found to be embedded inside the aluminium particles. As the MWNT concentration increased to 1.0 wt. %, most of the MWNT were partially covered by the aluminium flakes (Fig. 7. 2. (B)). Further increasing the MWNT

content to 2.0 wt. %, MWNT were found inside the aluminium particles as well as on the surfaces of the ball-milled Al-2.0 wt. % MWNT composite powders. Although no significant MWNT agglomerates were observed, it is noteworthy that the length of MWNT found on the surface of the ball-milled Al-2.0 wt. % MWNT composite powders after ball milling is shortened to around 1.2 μm comparing to 7 ± 2 μm in the pristine MWNT (as indicated in Fig. 7. 2. (C)). Similarly, the diameter of some of the MWNT distributed on the surface of the ball-milled Al-2.0 wt. % MWNT composite powders were reduced from 140 ± 30 nm (the average diameter of the pristine MWNT) to 50-70 nm (as indicated in Fig. 7. 2. (C)).

In general, no obvious agglomerates of MWNT were found on the surface of the 15 h ball-milled Al-MWNT composite powders with concentration of MWNT as high as 2.0 wt. %. This demonstrates the feasibility of employing ball milling to disperse relatively high concentration of MWNT in aluminium powders. However, it cannot be ignored that structural damage was introduced into MWNT since both length and diameter of MWNT were found reduced after 15 h of ball-milling.

7. 2. 1. 3. Cross section

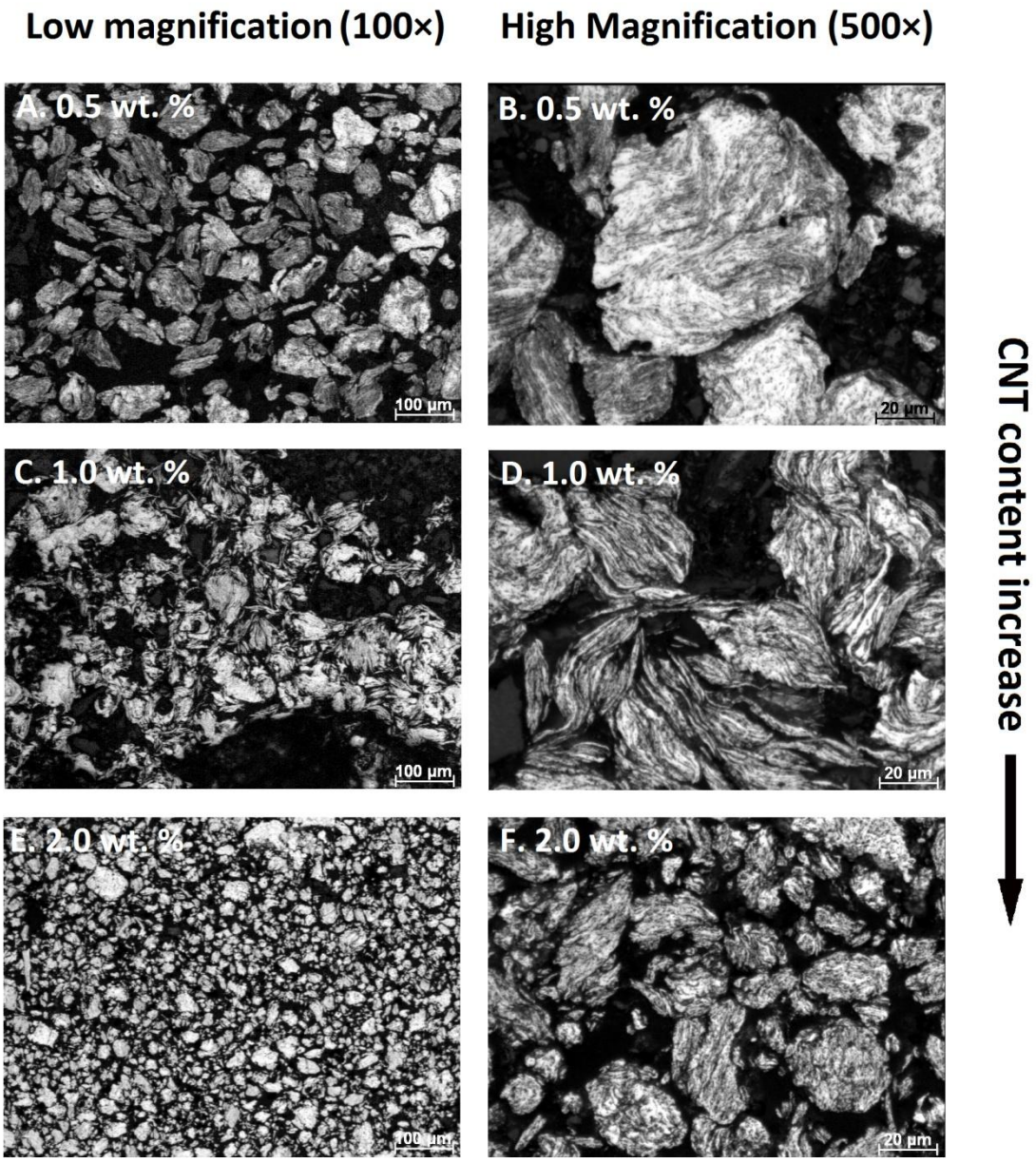


Fig. 7. 3 Optical micrographs showing the cross-section of the ball-milled Al- (A) and (B) 0.5 wt. %, (C) and (D) 1.0 wt. % and, (E) and (F) 2.0 wt. % MWNT composite powders (magnification: (A), (C) and (E): 100×, (B), (D) and (F): 500×).

Fig. 7. 3 shows optical micrographs of cross-section of 15 h ball-milled Al-MWNT composite powders with varied amount of MWNT. The 15 h ball-milled Al-0.5 wt. %

MWNT composite powders comprised of laminated structure with several interlayers (Fig. 7. 3. (A) and (B)). Also, the boundaries between some interlayers are not very distinct and continuous. At higher MWNT content of 1.0 wt. %, a finer multi-layered structure was obtained and the inter-boundaries are clearly observed in the 15 h ball-milled Al-1.0 wt. % MWNT composite particles (Fig. 7. 3. (C) and (D)). The average interlayer thickness reduced to around 2 μm. At even higher MWNT concentration of 2.0 wt. %, the interlayer thickness of the 15 h ball-milled Al-2.0 wt. % MWNT decreased to below 1um (Fig. 7. 3. (E) and (F)). In general, the ball-milled Al-MWNT composite particles consisted of laminated structure after ball milling. The thickness of interlayers reduced with increasing MWNT concentrations.

The distribution of MWNT in the 15 h ball-milled Al-MWNT composite powders was studied by SEM. Fig. 7. 4 shows the MWNT found in the cross-section of the 15 h ball-milled Al-MWNT composite powders. The individual MWNT was found homogeneously embedded in the cross-section of the 15 h ball-milled Al-0.5 wt. % MWNT composite particles as indicated by the arrow (Fig. 7. 4. (A)). For the 15 h ball-milled Al-1.0 wt. % MWNT composite powders, MWNT was found among the multi-layered structure of the ball-milled composite particles (Fig. 7. 4. (B)), and no obvious agglomeration of MWNT was observed. However, when the content of MWNT increased to 2.0 wt. %, some MWNT were found to cluster together as marked by the rectangles in Fig. 7. 4. (C), which is more clearly seen in the micrograph taken at higher magnification (Fig. 7. 4. (D))

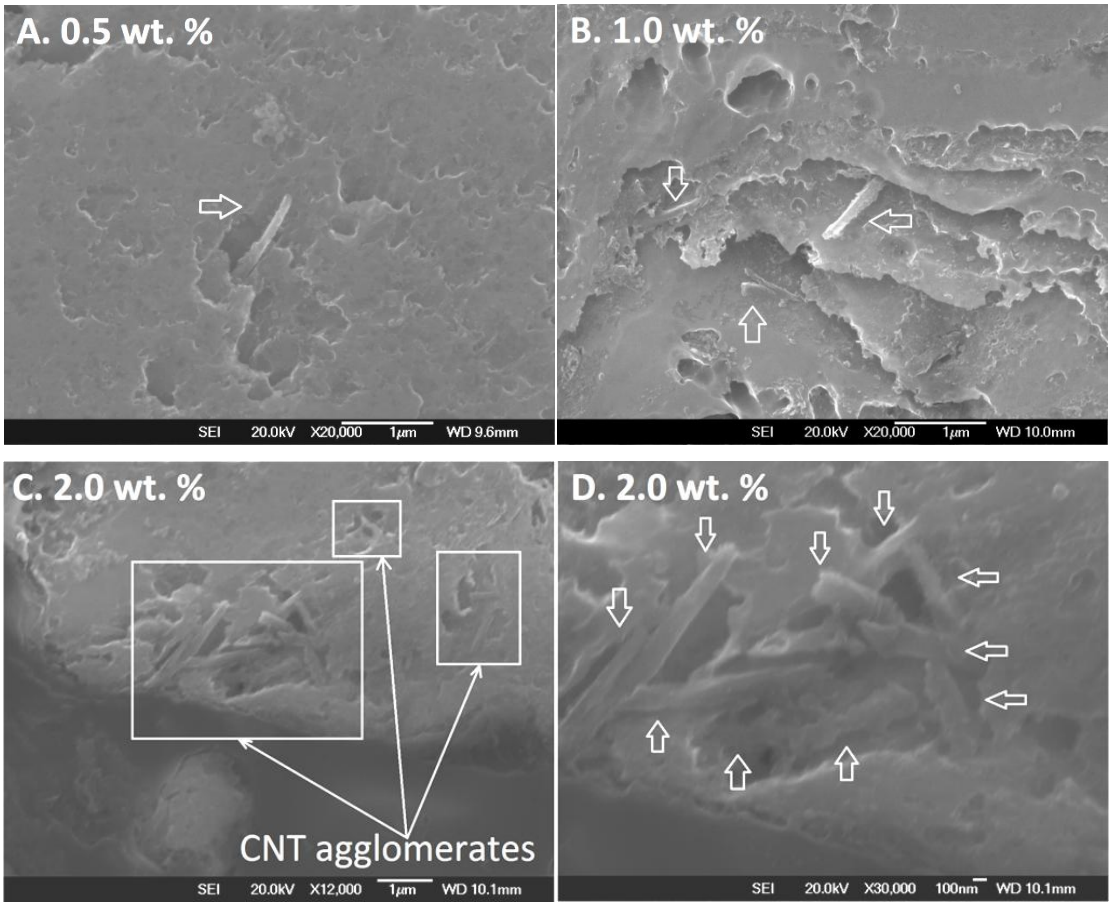


Fig. 7. 4 SEM micrographs showing the MWNT found on the cross-section of Al-(A) 0.5 wt. %, (B) 1.0 wt. % and, (C) and (D) 2.0 wt. % MWNT composite powders.

7. 2. 1. 4. Particle size distribution

The particle size distribution and the median particle size of the 15 h ball-milled Al-MWNT composite powders are presented in Fig. 7. 5 and Fig. 7. 6, respectively. The 15 h ball-milled Al-0.5 wt. % MWNT composite powders exhibit a broad size distribution ranging from below 1.63 μm to 210 μm (Fig 7. 2. 1. 4. 1). However, at MWNT concentration of 1.0 wt. %, the population of the powders below 100 μm increased moderately. Few particles in the range between 125 and 210 μm were also detected. At even higher MWNT content of 2.0 wt. %, the powder size was significantly reduced and a majority population of powder has

sizes below 50 μm.

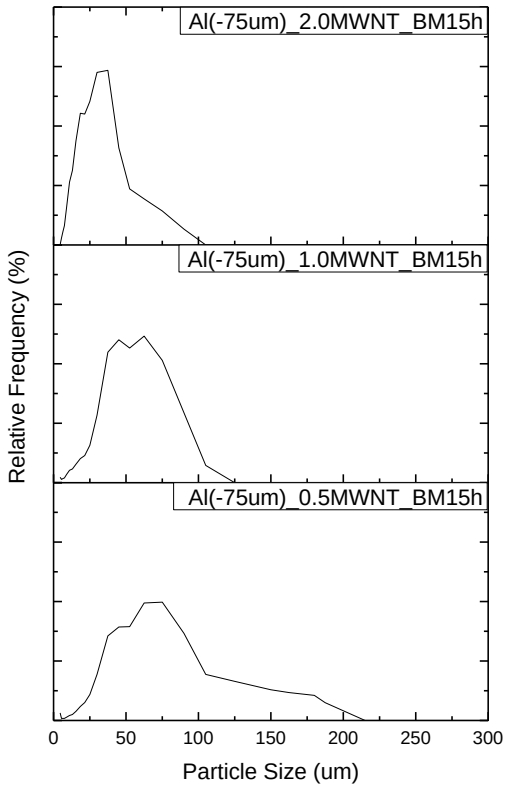


Fig. 7. 5 The particle size distribution of the ball-milled Al-MWNT composite powder.

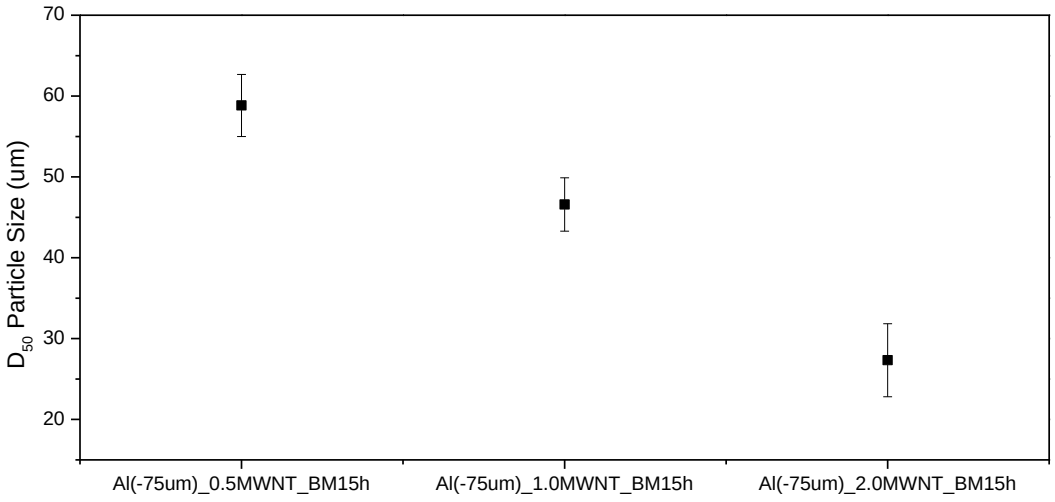


Fig. 7. 6 The median particle size (D_{50}) of the ball-milled Al-MWNT composite powders.

The median particle size (D_{50}) of the 15 h ball-milled Al-MWNT composite powders versus

the MWNT concentration, was plotted in Fig. 7. 6. The median particle size of the Al-0.5 wt. % MWNT composite powders is 58.84 ± 3.84 μm. When 1.0 wt. % and 2.0 wt. % MWNT was applied, the median particle size decreased to 46.59 ± 3.30 μm and 27.33 ± 2.52 μm, respectively. In general, the median particle size of the ball-milled Al-MWNT composite powders decreased with increasing the MWNT concentration.

7. 2. 1. 5. X-ray diffraction

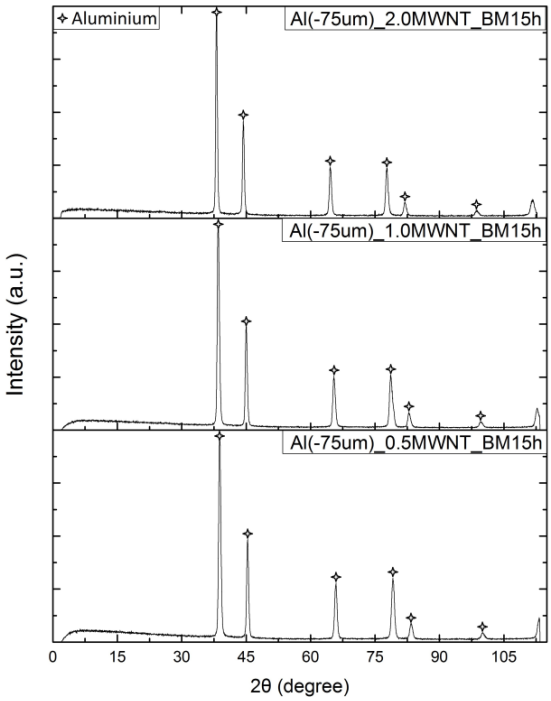


Fig. 7. 7 The XRD patterns of the 15 h ball-milled Al-MWNT composite powders.

Fig. 7. 7 shows XRD spectra of 15 h ball-milled Al-MWNT composite powder with various MWNT contents of 0.5, 1.0 and 2.0 wt. %. The characteristic peaks of aluminium, corresponding to the crystallographic plane of (111), (200), (220), (311) and (400), are found in all XRD spectra independent of the concentration of MWNT. This indicates that no

obvious chemical reaction was occurred and no significant new phase was formed in the 15 h ball-milled Al-MWNT composite powders. However, the width at half maximum (FWHM) of the XRD peaks were broadened with increasing MWNT content. This implies that the grain refinement and the higher level of lattice strain in the crystal structure with increasing MWNT concentration. Similar trend has also been reported by T. Ungár et al. [229].

7. 2. 1. 6. Raman spectroscopy

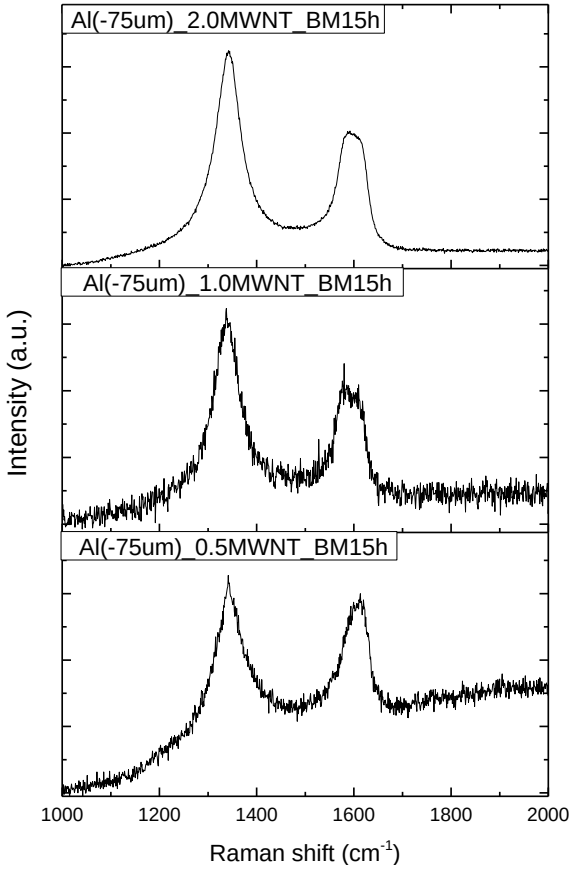


Fig. 7. 8 The Raman spectra of the 15 h ball-milled Al-MWNT composite powders.

Raman spectroscopy was utilised to characterize the structure of the MWNT in the 15 h ball-milled Al-MWNT composite powders. The Raman spectra and the I_D/I_G of the 15 h

ball-milled Al-MWNT composite powders are shown in Fig. 7. 8 and Fig. 7. 9, respectively. As can be seen from Fig. 7. 8 that the relative intensity of D band peak is slightly higher than that of the G band peak in the 15 h ball-milled Al-0.5 wt. % MWNT composite powders. At higher MWNT content of 1.0 wt. %, the peak intensity of D band is significantly greater than that of the G band. At even higher MWNT of 2.0 wt. %, the difference in peak intensities between the D and G band become greater. Generally, the difference in peak intensities between D and G bands increased with the increasing MWNT concentration in the 15 h ball-milled Al-MWNT composite powders.

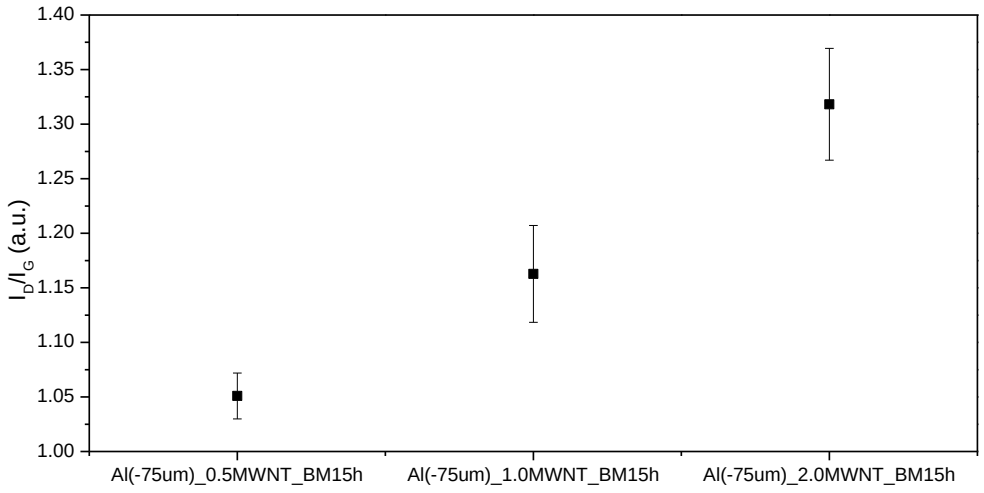


Fig. 7. 9 The I_D/I_G of the 15 h ball-milled Al-MWNT composite powders.

The quality of MWNT structure in the 15 h ball milled Al-MWNT composite powders containing 0.5, 1.0 and 2.0 wt. % of MWNT was measured using the I_D/I_G ratio obtained from the Raman spectra (Fig. 7. 8). The I_D/I_G of the Al-0.5 wt. % MWNT composite powders was found to be 1.05 ± 0.02. However, it increased to 1.16 ± 0.04 and 1.32 ± 0.05 for the 15 h ball-milled Al-1.0 wt. % MWNT and 2.0 wt. % MWNT composite powders,

respectively.

7. 2. 1. 7. Vickers micro-hardness

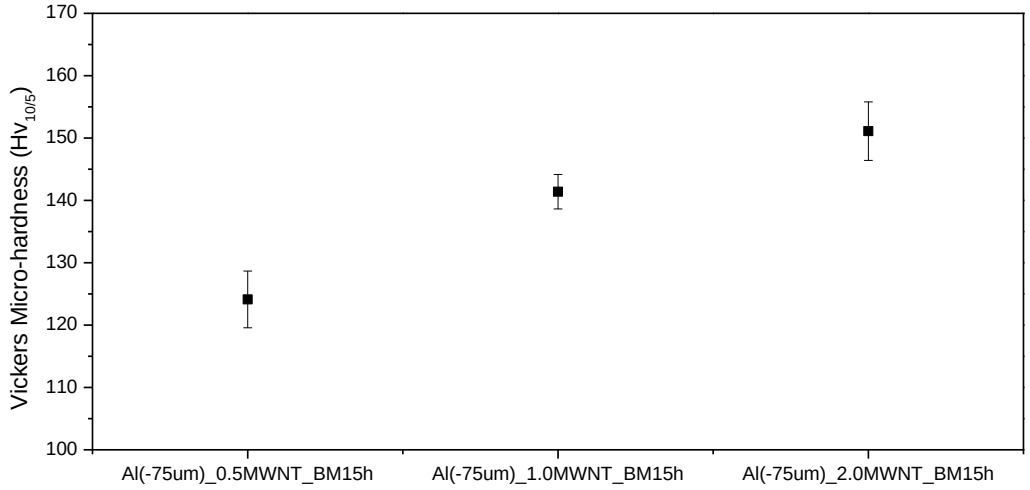


Fig. 7. 10 The Vickers micro-hardness of the 15 h ball-milled Al-MWNT composite powders.

The hardness of the 15 h ball-milled Al-MWNT composite powders is shown in Fig. 7. 10. It is clear that the hardness of the ball-milled Al-0.5 wt. % MWNT is 104.12 ± 4.55 $HV_{10/5}$. When the content of MWNT increased to 1.0 wt. % and 2.0 wt. %, the hardness of the 15 h ball-milled Al-MWNT composite powders increased to 141.40 ± 2.76 and 151.11 ± 4.69 $HV_{10/5}$, respectively. In general, the hardness of the ball-milled Al-MWNT composite powders increased with increasing MWNT content.

7. 2. 2 Discussion

7. 2. 2. 1. The dispersion of MWNT in the ball-milled Al-MWNT composite powders

According to the Fig. 7. 4, the individual MWNT are found inside the 15 H ball-milled Al-0.5 wt. % MWNT and Al-1.0 wt. % composite powders and no obvious agglomerates were found on the surfaces of these ball-milled composite powders (Fig. 7. 2). This demonstrates that the MWNT was de-agglomerated and dispersed by ball milling into the aluminium powders. When 2.0 wt. % of MWNT was added, small MWNT cluster was found inside the ball-milled Al-2.0 wt. % MWNT composite powders. This indicates that 2.0 wt. % of MWNT is over the limit for homogenous dispersion of MWNT in aluminium powders using the ball milling method. It is possible to enhance the dispersion of high concentration of MWNT by increasing: (a) the ball to powder weight ratio (i. e. 15:1 and 20:1) (b) milling time; or (c) milling speed to increase the effectiveness of dispersion.

Due to the van der Waals force of attraction between the long and thin tube [244], carbon nanotube are prone to agglomerate together and form bundles as displayed in Fig. 3. 3. (A) and (B). The de-agglomeration and homogeneous dispersion of carbon nanotube is by far the most significant and critical challenge in the field of carbon nanotube reinforced composite [119]. Most researchers found the presence of CNT agglomerates in the ball-milled powders or bulk specimen produced using various methods including: hot-pressing [31, 33], hot-extrusion [31], mixer-shaking [28, 36], ball milling [28, 35], hot-rolling [28] and spark

plasma sintering [36]. This study has shown that composite particles with MWNT content up to 1.0 wt. % MWNT is found to be de-agglomerated and uniformly distributed in the aluminium matrix by ball milling. However, the MWNT agglomerates are formed in the ball-milled Al-MWNT composite powders with MWNT content of 2.0 wt. %. Thus, additional processing is needed in order to evenly disperse MWNT of higher content in aluminium powders.

7. 2. 2. 2. The evolution of MWNT in the ball-milled Al-MWNT composite powders

The I_D/I_G and the relative intensity of D band peak in the Raman spectra of 15 h ball-milled Al-MWNT composite powders increased with increasing concentration of MWNT (Fig. 7. 9 and Fig. 7. 8). This indicates that more defective structure of MWNT existed in the 15 h ball-milled Al-MWNT composite powders with higher concentration of MWNT. It can be seen from the Fig. 7. 2 that more MWNT of shorter length or smaller diameter were distributed on the surface of the 15 h ball-milled composite powders. This suggests more MWNT were damaged by the impact of milling balls. Also, the median particle size of the ball-milled Al-MWNT decreased with increasing concentration of MWNT. Thus, for the same weight of starting powders, the amount of composite particles is larger in the 15 h ball-milled Al-MWNT composite with higher content of MWNT. There more chances for the friction between MWNT and ball-milled aluminium particles to occur. Therefore, the degree of damage in the structure of MWNT was increased with increasing MWNT concentration.

7. 2. 2. 3. The effect of MWNT concentration on the ball-milled Al-MWNT composite powders

As can be seen from Fig. 7. 1 and Fig. 7. 5 that, with increasing MWNT concentration, the median particle size of the 15 h ball-milled Al-MWNT composite powders decreased while the particle size range became narrower. The median particles size for the ball-milled Al-0.5 wt. % MWNT composite powders was 58.84 ± 3.84 μm. Further increasing the MWNT concentration to 1.0 wt. % and 2.0 wt. %, the median particle size reduced to 46.59 ± 3.30 μm and 27.33 ± 4.52 μm, respectively. The reason for this behaviour is the existence of MWNT between the aluminium powders hindered the direct contact of the fresh fracture surface of aluminium particles during the ball milling process. This prevents the diffusion and cold-welding of aluminium particles. As the MWNT concentration increases, more MWNT are distributed on the surfaces of aluminium particles, resulting less cold welding process as compared to fracturing process during ball milling. Thus, the addition of MWNT concentration reduced the rate of welding but the rate of fracturing kept the same level. Subsequently, the particle size of the 15 h ball-milled Al-MWNT composite powders reduced with increasing MWNT concentration. This result is in agreement with the findings in the section 6. 2. 1 that the addition of 1.0 wt. % MWNT into aluminium powders leading to the reduction of particle size after ball milling.

7. 2. 3 Summary

The effect of the concentration of MWNT on the morphology, microstructure, hardness, as well as MWNT structure of the 15h ball-milled Al-MWNT composite powders was studied.

The results of the research can be summarized as follows:

1. The particle size of the 15 h ball-milled Al-MWNT composite powders decreased with increasing MWNT concentration due to the presence of a larger amount of MWNT acted as barriers and impeded the welding of Al particles.

2. 0.5 wt. % and 1.0 wt. % MWNT were successfully de-agglomerated and uniformly dispersed in the 15 h ball-milled Al-MWNT composite powders by ball milling.

3. The level of defects and structural damage in MWNT increased with increasing MWNT content due to repeat impact of milling balls on the exposed MWNTs during ball milling.

7. 3. The effect of multi-walled carbon nanotube concentration on the sintered Al-MWNT composite materials

7. 3. 1 Results

7. 3. 1. 1. *Cross section microstructure*

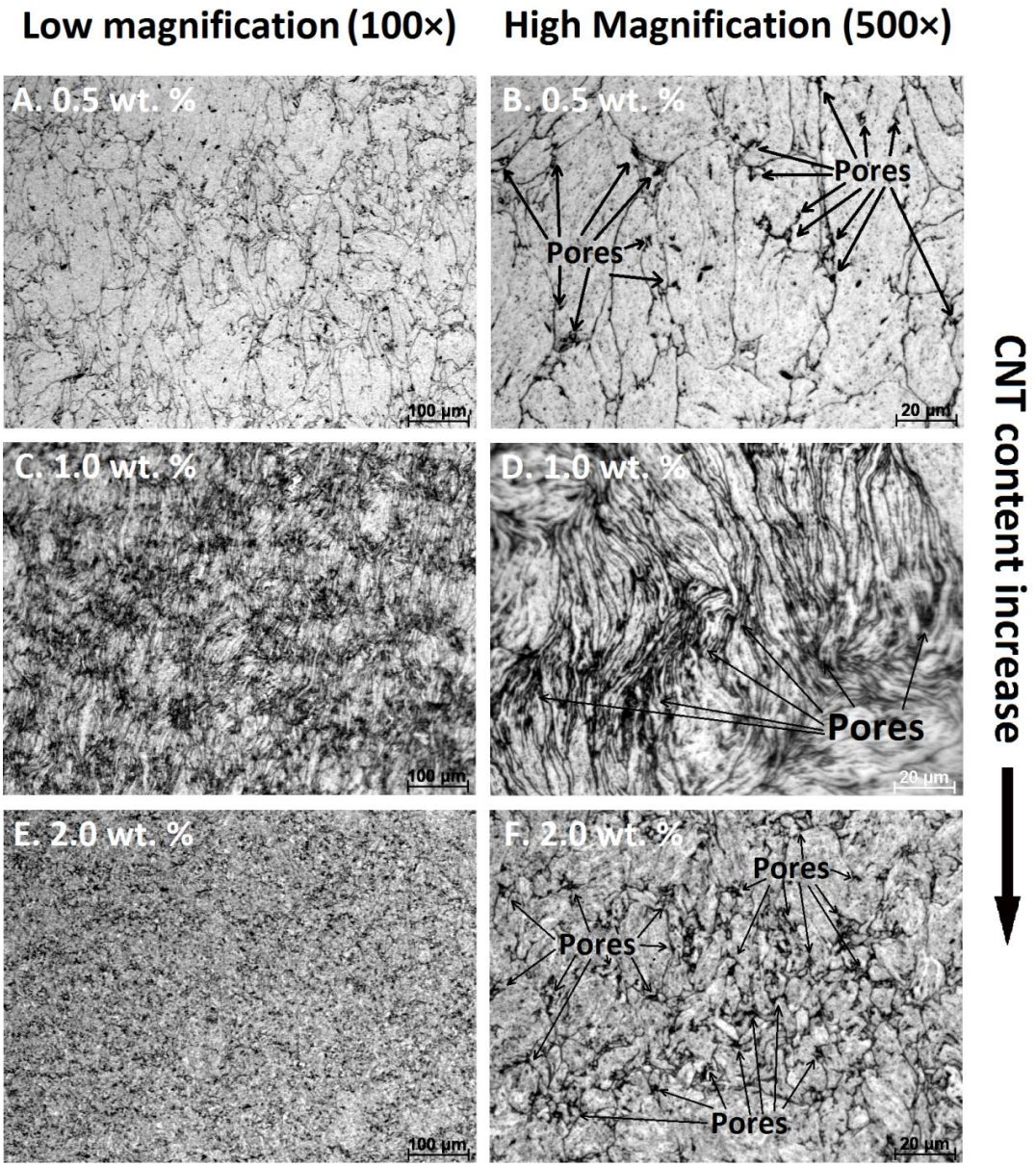


Fig. 7. 11 The optical micrographs showing the cross-section of the sintered specimens fabricated using 15 h ball-milled Al-MWNT composite powder containing: (A) and (B) for 0.5 wt. %, (C) and

(D)1.0 wt. % and (E) and (F) 2.0 wt. %. The micrographs in the left column (A, C, E) and right column (B, D, F) are taken at magnifications of 100× and 500×, respectively. The arrows in (B), (D) and (F) indicate the presence of pores.

Fig. 7. 11 shows micrographs of the cross-sectional microstructure of sintered Al-MWNT composites containing various amount of MWNT. It was found that, the amount of pores at the boundaries increased but the pore size was decreased with increasing MWNT content (as indicated by arrows in Fig. 7. 11 (B), (D) and (F)). According to Fig. 7. 10, the Al-MWNT composite powders containing more MWNT exhibit higher hardness and therefore possess poor compressibility. Subsequently, the green density of the Al-MWNT composite compact is expected to be lower with higher content of MWNT. Moreover, the addition of MWNT can obstruct the diffusion of aluminium atoms and impede the densification process since the wettability of aluminium on MWNT is relatively low [124, 152, 245]. Therefore, the sintered density of the Al-MWNT composite deteriorates with increasing MWNT content. Similar sintered density decreasing of Al-MWNT composite with increasing MWNT concentration was also observed by other researchers [35, 246].

7. 3. 1. 2. Sintered density

The density of the sintered Al-MWNT composite specimens as a function of MWNT content is shown in Fig. 7. 12. It can be seen in Fig. 7. 12 that the sintered density of the Al-0.5 wt. % MWNT composite reached to 2.51 ± 0.01 g/cm^3 (relative density: 93.16 ± 0.44 %). Increasing the concentration of MWNT to 1.0 wt. %, the sintered density of the composite materials slightly increased to 2.54 ± 0.02 g/cm^3 (relative density: 94.05 ± 0.59 %) before it

reduced to 2.47 ± 0.02 g/cm^3 (relative density: 91.61 ± 0.67 %) with the addition of 2.0 wt. % MWNT.

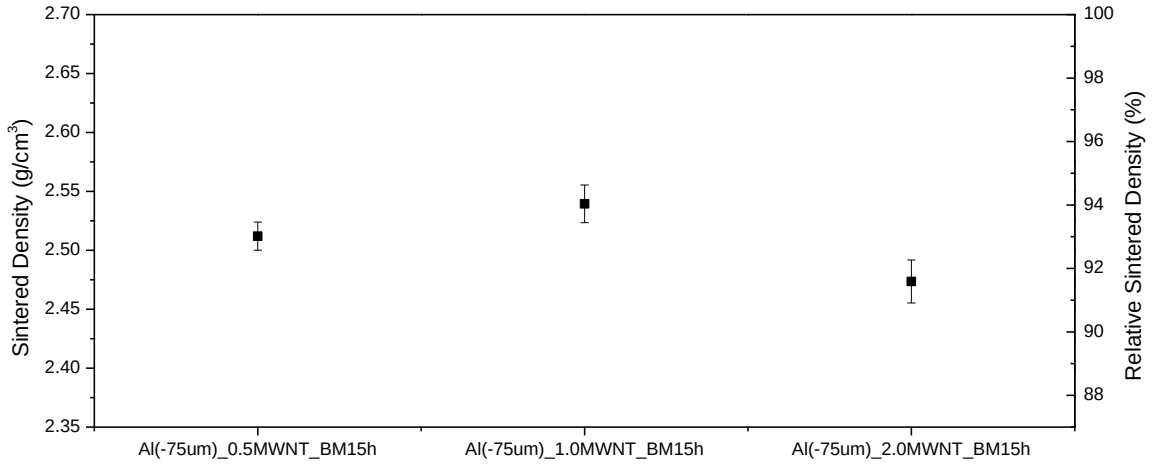


Fig. 7. 12 The sintered density of the Al-MWNT composite specimens fabricated using the 15 h ball-milled Al-MWNT composite powders.

7. 3. 1. 3. X-ray diffraction

The XRD patterns of sintered Al-MWNT specimens containing various MWNT content are plotted in Fig. 7. 13. All XRD spectra contained characteristic peaks corresponding to Al_3C_4 phase as well as aluminium. It is worth noticing that the intensity of the Al_3C_4 peaks increased with increasing MWNT concentration. This indicates the amount of Al_3C_4 in the sintered Al-MWNT composite increased with increasing content of MWNT.

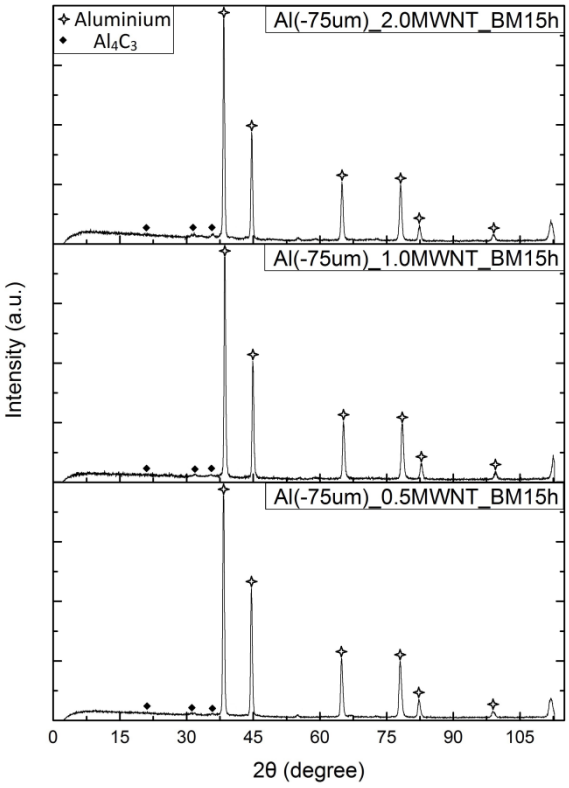


Fig. 7. 13 The XRD patterns of the sintered bulk composite specimens fabricated using the 15 h ball-milled Al-MWNT composite powders.

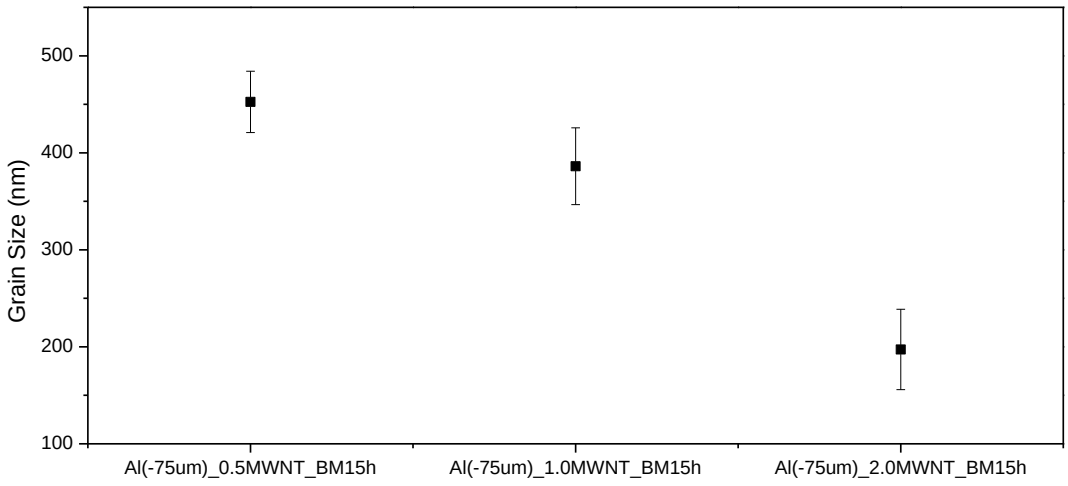


Fig. 7. 14 The grain size of the sintered Al-MWNT composite specimens calculated by the William-Hall method.

The width of the XRD peaks corresponding to Al phase increased with increasing MWNT

concentration as a result of the grain refinement and lattice strain [138, 169]. The grain size of the sintered composite materials was calculated according to the William-Hall method [138, 169] and the values of the grain size are shown in Fig. 7. 14. It can be seen that the grain size of the Al-MWNT composite decreased with increasing MWNT concentration. The calculated grain size of the sintered Al-0.5 wt. % MWNT composite materials was 492.55 ± 31.58 nm. When the content of MWNT increased to 1.0 wt. % and 2.0 wt. %, the calculated grain size was reduced to 386.19 ±39.54 nm and 177.23 ±41.43 nm respectively.

7. 3. 1. 4. Tensile strength

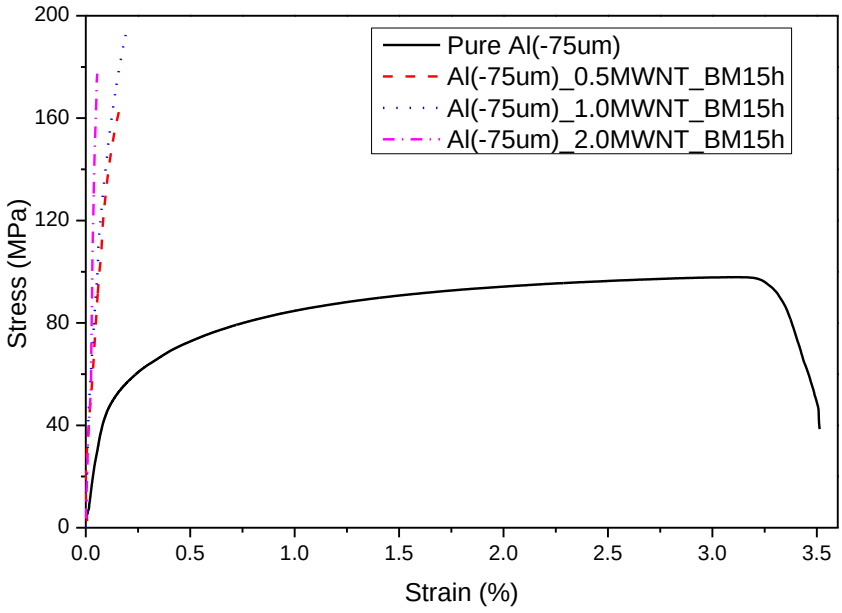


Fig. 7. 15 The stress-strain curves of the bulk composite specimens fabricated by the 15 h ball-milled Al-MWNT composite powders.

The stress-strain curves and detailed mechanical properties of sintered elemental Al and Al-MWNT composite specimen with different MWNT concentration are shown in Fig. 7. 15 and Table 7. 1. As can be seen that both the strength and the maximum fracture strain of the

Al-MWNT are affected by the amount of MWNT. The ultimate tensile strength of the Al-0.5 wt. % MWNT composite materials was found to be 164.54 ± 8.23 MPa. For higher MWNT content of 1.0 wt. %, the UTS increased further to 195.84 ± 9.79 MPa. However, when the concentration of MWNT increased to 2.0 wt. %, the UTS of the composite dropped to 177.46 ± 8.87 MPa.

Table 7. 1 The mechanical properties of the sintered elemental Al and Al-MWNT composite specimens fabricated using the 15 h ball-milled Al-MWNT composite powders.

Materials	**Yield strength (MPa)**	**Ultimate tensile strength (MPa)**	**Maximum strain before failure (%)**
Pure Al(-75um)	52.62 ± 1.74	97.87 ± 4.89	3.51 ± 0.08
Al(-75um)_0.5MWNT_BM15h	119.92 ± 7.56	164.54 ± 8.23	0.166 ± 0.008
Al(-75um)_1.0MWNT_BM15h	124.76 ± 8.35	195.84 ± 9.79	0.200 ± 0.010
Al(-75um)_2.0MWNT_BM15h	121.32 ± 8.42	177.46 ± 8.87	0.055 ± 0.002

However, the maximum fracture strain of the sintered Al-MWNT composite decreased with increasing concentration of MWNT. The sintered elemental aluminium shows a maximum failure strain of 3.51 ± 0.08 %. When 0.5 wt. % of MWNT was applied, the maximum failure strain reduced significantly to 0.166 ± 0.008 %. Further increasing the content of MWNT to 1.0 and 2.0 wt. %, the maximum failure strain of the sintered Al-MWNT composite specimens further reduced to 0.200 ± 0.010 % and 0.055 ± 0.002 %, respectively.

7. 3. 2 Discussion

7. 3. 2. 1. The strengthening mechanism of the sintered Al-MWNT composite materials

Table 7. 2 Comparison of the estimated and experimentally measured yield strength of the sintered Al-MWNT composite materials

Sintered materials	Estimated yield strength by Hall-Petch equation (MPa)	Estimated yield strength by Kelly-Tyson equation (MPa)	Experimentally measured yield strength (MPa)
Al(-75um)_0.5MERCNT_BM15h	118.09	154.93	119.92
Al(-75um)_1.0MERCNT_BM15h	124.45	161.44	124.76
Al(-75um)_2.0MERCNT_BM15h	164.01	-[2]	121.65

The yield strength of the sintered Al-MWNT composite materials with different content of MWNT was calculated according to the Hall-Petch equation (grain refinement strengthening, section 2. 4. 3. 1) and Kelly-Tyson equation (load transfer strengthening, section 2. 4. 3. 5). The estimated and experimentally measured yield strengths of the Al-MWNT composites are presented in Table 7. 2. As can be seen from Table 7. 2 that the experimentally measured yield strength of the sintered Al-0.5 wt. % MWNT composite is 119.92 MPa. Increasing the concentration of MWNT to 1.0 wt. % and 2.0 wt. %, the experimentally measured yield strengths of the sintered Al-1.0 wt. % MWNT and Al-2.0 wt. % MWNT composite increased to 124.76 MPa and 121.65 MPa respectively.

On the other hand, the estimated yield strength of the sintered Al-MWNT composite calculated by both the Hall-Petch equation and Kelly-Tyson equation are found to increase with increasing MWNT content. However, it can be seen from Table 7. 2 the difference between the experimentally measured and estimated yield strengths are more pronounced when shear lag model (Kelly-Tyson equation) was employed. Especially, the experimentally

[2] No reference yield strength of matrix available

measured yield strength of the sintered Al-0.5 wt. % MWNT and Al-1.0 wt. % MWNT composite almost coincided with the yield strength of the same composites calculated by the Hall-Petch equation. This indicates that the strengthening in the Al-MWNT composite fabricated using 15 h ball-milled Al-MWNT composite powders is mainly attributed to grain refinement.

Also, it is noteworthy that the Hall-Petch equation assumes materials that are 100% dense. However, it can be seen from Fig. 7. 12 that the as-sintered Al-MWNT composite is not fully dense. Theoretically the experimentally measured yield strength of the Al-MWNT composite with relative density below 100 % would below the estimated values calculated by the Hall-Petch equation. Nevertheless, the sintered Al-0.5 wt. % MWNT and Al-1.0 wt. % MWNT composites with relative densities of 93.16 % and 94.05 % (Fig. 7. 12) showed experimentally measured yield strengths of 119.92 MPa and 124.76 MPa respectively, which are higher than the values estimated by the Hall-Petch equation (118.09 MPa and 124.45 MPa). Hence, it is considered that MWNT in the composite matrix also enhanced the mechanical properties of the composite by load sharing through the interface between matrix and MWNT. As can be seen from the Fig. 7. 16 MWNTs (as indicated by arrows) were found in the fracture surface of the sintered Al-1.0 wt. % MWNT composite materials. Both ends of the MWNTs are in the matrix and they bridged the separated section on the fracture surface. This is a typical load sharing behaviour in the fibre reinforced composite [247-249].

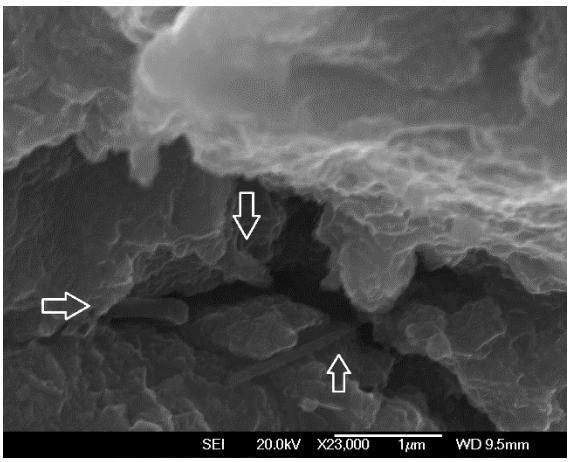


Fig. 7. 16 The MWNTs found in the fracture surface of the sintered Al-1.0 wt. % MWNT composite materials showing the bridging of MWNT over cracks. The arrow indicates the presence of MWNT.

Further increasing the MWNT concentration to 2.0 wt. %, the difference between the experimentally measured yield strength (121.65MPa) and the estimated yield strength (164.01MPa) calculated by Hall-Petch equation increased significantly (Table 7. 2). This can be explained by a combination of the reduction of relative sintered density (91%) of the sintered Al-2.0 wt. % MWNT composite and the formation of Al_4C_3. Firstly, the increased porosity led to the stress concentration in certain regions in the composite material which resulted in the failure of composite materials at lower stress level. Also, the mismatch of thermal expansion coefficient and elastic modulus between Al_4C_3 and aluminium matrix may lead to the stress and strain increase at the interface between Al_4C_3 and Al. This may result in the crack initiate at the interface.

Moreover, it is obvious that there are significant differences between the experimentally measured and estimated yield strength by the Kelly-Tyson equation (Table 7. 2). This is because that Kelly-Tyson equation assumes the properties of the reinforcements are isotropic,

the dispersion of reinforcements in the composite is homogeneous, the structure of reinforcements is unchangeable and the interface between reinforcement and matrix is very strong that the stress transfers directly at the interface without any loss. However, in the real sintered Al-MWNT composite, the strength of the MWNT is anisotropic that the tensile strength of the MWNT is significantly stronger than its shear strength. Secondly, the dispersion of MWNT in the composite matrix is not uniform as CNT agglomerates were observed in the sintered Al-2.0 wt. % MWNT composite (Fig. 7. 17). Thirdly, the MWNT structure was damaged during the ball milling process (Fig. 7. 8) and the length and diameter of the MWNT is found to reduce after ball milling (Fig. 7. 2). Moreover, the load on the composite cannot transfer freely from the matrix to reinforcements without any loss. All these factors deteriorate the load transfer strengthening of MWNT in the sintered Al-MWNT composite. Thus the experimentally measured yield strengths of the sintered Al-MWNT composite are noticeably lower than the yield strength estimated according to the shear lag model.

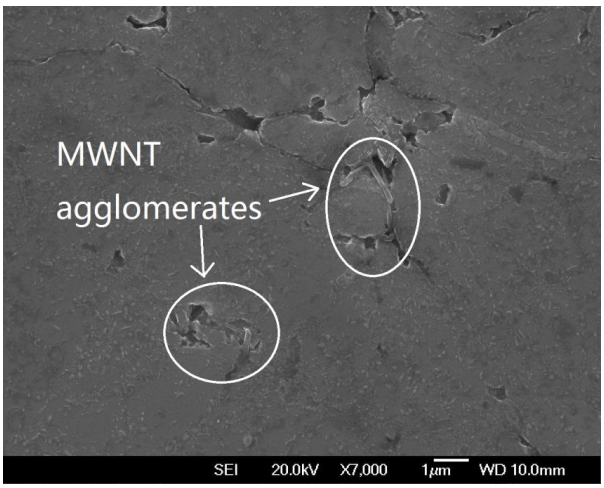


Fig. 7. 17 The MWNT agglomerates found at the cross-section of the sintered Al-2.0 wt. % MWNT composite materials.

T. Noguch [124] and J. Yuuki et al. [250] fabricated Al-1.6 vol. % (≈ 2.0 wt. %) MWNT composite materials by a combination of sintering (800 ℃) and hot extrusion (400 ℃， 2 mm/min) and achieved a density of 99.5 % and a yield strength of 210 MPa. The current author produced Al-2.0 wt. % MWNT composite with a density of 91 % and a yield strength of 121.65 MPa. Obviously, the density of the Al-MWNT composite materials is very critical in achieving better mechanical properties A. Agarwal et al. [233] reported that the good density of the Al-MWNT composite led to high load transfer efficiency and demonstrated that the good density of the Al-MWNT is critical for the load transfer strengthening of MWNT in the Al-MWNT composite.

7. 3. 3 Summary

The microstructure and properties of the as-sintered Al-MWNT composite containing various amount of MWNT were studied. Several findings are summarised as follows:

1. The sintered density of Al-MWNT composite increased up to 1.0 wt. % MWNT and then decreased with increasing MWNT content due to the increased hardness of particles lowered their compressibility and the increased amount of MWNT impedes the diffusion during the sintering and led to lower sintered density.

2. Al_3C_4 was formed in the Al-MWNT composite after sintering. The amount of Al_3C_4 increased with increasing CNT content.

3. The ultimate tensile strength of the sintered Al-MWNT composite reached to maximum value of 195.84 ± 9.79 MPa at 1.0 wt. % MWNT.

4. The strengthening in the Al-MWNT composite is mainly due to grain refinement. The load transfer of MWNT also contributes to the enhancement of the Al-MWNT composite.

Chapter 8. Conclusion and future work

8. 1. Conclusion

1. The use of process control agent such as stearic acid and ethanol are needed to prevent excessive welding of aluminium powders during the ball milling process. By using same amount (i.e. 1. 0 wt. %) of stearic acid and ethanol in the ball milling of Al-1.0 wt. % MWNT, finer particle size (i.e. 2.43 μm) was achieved but more defects were introduced into MWNT (i.e. I_D/I_G: 1.11) when 1.0 wt. % of ethanol was employed.

2. The grain size was refined during the ball milling of elemental aluminium. The grain size of the "as-milled" elemental aluminium powders was reduced with the increasing of milling time. Consequently, the hardness and the tensile strength of the as-sintered bulk materials fabricated using "as-milled" elemental aluminium powders were improved with the increasing of milling time. However, the ductility of the as-sintered Al-1.0 wt. % MWNT composite was reduced with the increasing of milling time due to increased hardness of "as-milled" elemental aluminium particles. This deteriorates the compactability and lowered the achieved green density of compact. Also, the increase of the thickness of alumina on the surfaces of the "as-milled" elemental aluminium particles impeded the densification process and reduced the sintered density.

3. Ball milling has been demonstrated to be an effective method to uniformly disperse up to 1.0 wt. % of multi-walled carbon nanotube into aluminium matrix.

4. The addition of 1.0 wt. % multi-walled carbon nanotube to aluminium powders reduced both particle size and grain size of the "as-milled" Al-1.0 wt. % composite powders. This along with the load-sharing contribution of 1.0 wt. % MWNT and hard phases (i.e. Al_3C_4 and Al_2O_3) improved the hardness and tensile strength of the Al-1.0 wt. % composite.

5. The structure of MWNT was damaged during the ball milling process which produced amorphous carbon and allowed the formation of Al_3C_4 during the sintering process. Also, the degree of damage increased with increasing milling time. Thus, the amount of Al_3C_4 formed in the sintered composite matrix is proportional to the milling time.

6. Both the particle size and grain size of the "as-milled" Al-MWNT composite powders and sintered Al-MWNT composite decreased with the increasing of milling time and the concentration of MWNT. This led to the enhancement of the hardness and tensile strength of the Al-MWNT composite materials. Nevertheless, the ductility of the Al-MWNT composite materials was found to reduce due to the lowered compactability of the "as-milled" composite powders, leading to reduced green density. Moreover, the formation of Al_3C_4 and Al_2O_3 increased the brittleness

of the Al - 1.0 wt. % composite materials.

7. MWNT agglomerates were found in the sintered Al-2.0 wt. % MWNT composite. It lowered the sintered density and degraded the tensile strength of the Al-MWNT composite as a result of increased porosity. Also, the Al_3C_4 formed in the composite is proportional to the MWNT content. However, the sintered density of the sintered Al-MWNT composite is inversely proportional to the concentration of MWNT. Therefore, the increased porosity and the amount of Al_3C_4 resulted in the reduction of the ductility of the Al-MWNT composite.

8. 2. Future work

1. Novel techniques like the wet mixing and surface treatment of carbon nanotube need to be explored and developed to homogeneously disperse multi-walled carbon nanotube into metal matrix while keeping the structure of multi-walled carbon nanotube intact so that the full potential of multi-walled carbon nanotube can be utilized.

2. The interface between multi-walled carbon nanotube and aluminium needs to be enhanced so that higher sintered density and better enhancement can be achieved.

3. The sintering aids such as: Sn and Mg can be added into the Al-MWNT composite

to form liquid phase to enhance the densification process during powder consolidation process to achieve higher sintered density and better load transfer efficiency.

4. Consolidation techniques such as: spark plasma sintering (SPS) can be attempted to shorten the sintering period to reduce the formation of Al_3C_4 and impede the excessive grain growth in the sintering process.

5. Post-sintering processing such as: forging, hot-rolling, hot-extrusion, equal channel angular pressing (ECAP), hot isostatic pressing (HIP) can be applied on the as-sintered bulk composite materials to further reduce the porosity and improve the overall properties of the composite.

6. Since the properties of the MWNT are anisotropic, the uniform alignment of MWNT in the composite matrix is of great interest to produce composites with anisotropic properties. This is supposed to be achievable through severe plastic deformation such as equal channel angular pressing (ECAP) and hot rolling. Also, the grain size of the composite is expected to be reduced and better mechanical properties are expected to obtain in the composite.

Reference

[1] T. Peng, I. Chang, Uniformly dispersion of carbon nanotube in aluminum powders by wet shake-mixing approach, Powder Technol, 284 (2015) 32-39.

[2] T. Peng, I. Chang, Mechanical alloying of multi-walled carbon nanotubes reinforced aluminum composite powder, Powder Technol, 266 (2014) 7-15.

[3] T. Peng, I. Chang, A Novel Method to Homogenously Disperse Carbon Nanotubes in Aluminum Powders, in: Euro Powder Metallurgy 2014 Congress & Exhibition, Salzburg, Austria, 2014.

[4] D. Uzunsoy, T. Peng, I. Chang, I. Istif, Investigation of Wear Behavior of Aluminum Alloy Reinforced with Carbon Nanotubes, SAE International Journal of Materials and Manufacturing, 7 (2014) 596-601.

[5] I. Istif, O. Isın, D. Uzunsoy, T. Peng, I. Chang, Prediction of Wear Behavior of Aluminum Alloy Reinforced with Carbon Nanotubes Using Nonlinear Identification, in, SAE Technical Paper, 2014.

[6] T. Peng, I. Chang, Mechanical Alloying of Multi-wall Carbon Nanotube and Aluminium Composite Powder, in: National Student Conference in Metallic Materials Manchester, UK, 2012.

[7] Electrical Conductivity of the elements, in, Mathematica's ElementData.

[8] A.A. Yaroshevsky, Abundances of chemical elements in the Earth's crust, Geochem Int+, 44 (2006) 48-55.

[9] A.A.S.M. Inc., Characteristics of Aluminum 7075-T6, in.

[10] E. Sansoucy, P. Marcoux, L. Ajdelsztajn, B. Jodoin, Properties of SiC-reinforced aluminum alloy coatings produced by the cold gas dynamic spraying process, Surf Coat Tech, 202 (2008) 3988-3996.

[11] S.G. Qu, H.S. Lou, X.Q. Li, Properties of SiCp/6061-Al metal matrix composites prepared by infiltrating molten aluminum into ternary packing of SiC preforms, J Compos Mater, (2015) 0021998314568166.

[12] M. Mujahid, L. Friska, Influence of mechanical milling on the SiC particulate size in an Al-SiC composite, J Mater Eng Perform, 14 (2005) 69-74.

[13] C. Carreno-Gallardo, H. Barriga-Calvillo, E. Lozano-Rodriguez, I. Estrada-Guel, M.A. Neri-Flores, C. Lopez-Melendez, R. Martinez-Sanchez, Effect of Mechanical Milling on the Microstructure and Morphology of Al2024/SiC Nanocomposite, Microscopy and Microanalysis, 19 (2013) 1566-1567.

[14] M. Kok, Production and mechanical properties of Al2O3 particle-reinforced 2024 aluminium alloy composites, J Mater Process Tech, 161 (2005) 381-387.

[15] Z.R. Hesabi, A. Simchi, S.M.S. Reihani, Structural evolution during mechanical milling of nanometric and micrometric Al 2 O 3 reinforced Al matrix composites, Materials Science and Engineering: A, 428 (2006) 159-168.

[16] L. Vázquez, E. Hernández, A. Altamirano, V. Cortés, E. Garfias, E. Refugio, M. Vite, Effect of Composition of B4C-Aluminum Composites on Mechanical Properties and Resistance Corrosion, in: Advanced Composites for Aerospace, Marine, and Land Applications, John Wiley & Sons, Inc., 2014, pp. 23-33.

[17] T. Thiyagarajan, R. Subramanian, S. Dharmalingam, N. Radika, A. Gowrisankar, Wear Behaviour Of B4c Reinforced Hybrid Aluminum-Matrix Composites, Mater Tehnol, 49 (2015) 9-13.

[18] P. Sharma, S. Sharma, D. Khanduja, Production and some properties of Si3N4 reinforced aluminium alloy composites, Journal of Asian Ceramic Societies, 3 (2015) 352-359.

[19] Y. Iwai, T. Honda, T. Miyajima, Y. Iwasaki, M.K. Surappa, J.F. Xu, Dry sliding wear behavior of Al2O3 fiber reinforced aluminum composites, Compos Sci Technol, 60 (2000) 1781-1789.

[20] S.S. L. Sinian, Y. Tianqin, C. Huimin, Z. Youshou and C. Hong: 2005, , Mater. Sci. Forum, , 488.

[21] M.F. Yu, O. Lourie, M.J. Dyer, K. Moloni, T.F. Kelly, R.S. Ruoff, Strength and breaking mechanism of multiwalled carbon nanotubes under tensile load, Science, 287 (2000) 637-640.

[22] X. Lu, Z.F. Chen, Curved Pi-conjugation, aromaticity, and the related chemistry of small fullerenes (< C-60) and single-walled carbon nanotubes, Chem Rev, 105 (2005) 3643-3696.

[23] J.W. Che, T. Cagin, W.A. Goddard, Thermal conductivity of carbon nanotubes, Nanotechnology, 11 (2000) 65-69.

[24] E. Pop, D. Mann, Q. Wang, K.E. Goodson, H.J. Dai, Thermal conductance of an individual single-wall carbon nanotube above room temperature, Nano Lett, 6 (2006) 96-100.

[25] D. Zheng, J.S. Ye, W.D. Zhang, Some properties of sodium dodecyl sulfate functionalized multiwalled carbon nanotubes electrode and its application on detection of dopamine in the presence of ascorbic acid, Electroanal, 20 (2008) 1811-1818.

[26] R.S. Ruoff, D. Qian, W.K. Liu, Mechanical properties of carbon nanotubes: theoretical predictions and experimental measurements, Cr Phys, 4 (2003) 993-1008.

[27] M.F.L. De Volder, S.H. Tawfick, R.H. Baughman, A.J. Hart, Carbon Nanotubes: Present and Future Commercial Applications, Science, 339 (2013) 535-539.

[28] A.M.K. Esawi, M.A. El Borady, Carbon nanotube-reinforced aluminium strips, Compos Sci Technol, 68 (2008) 486-492.

[29] A.H. Javadi, S. Mirdamadi, M.A. Faghihisani, S. Shakhesi, R. Soltani, Fabrication of well-dispersed, multiwalled carbon nanotubes-reinforced aluminum matrix composites, New Carbon Mater, 27 (2012) 161-165.

[30] X.D. Yang, E.Z. Liu, C.S. Shi, C.N. He, J.J. Li, N.Q. Zhao, K. Kondoh, Fabrication of carbon nanotube reinforced Al composites with well-balanced strength and ductility, J Alloy Compd, 563 (2013) 216-220.

[31] T. Kuzumaki, K. Miyazawa, H. Ichinose, K. Ito, Processing of carbon nanotube reinforced aluminum composite, J Mater Res, 13 (1998) 2445-2449.

[32] J.Z. Liao, M.J. Tan, Mixing of carbon nanotubes (CNTs) and aluminum powder for powder metallurgy use, Powder Technol, 208 (2011) 42-48.

[33] C.L. Xu, B.Q. Wei, R.Z. Ma, J. Liang, X.K. Ma, D.H. Wu, Fabrication of aluminum-carbon nanotube composites and their electrical properties, Carbon, 37 (1999) 855-858.

[34] A.S. Khan, B. Farrokh, L. Takacs, Effect of grain refinement on mechanical properties of ball-milled bulk aluminum, Mat Sci Eng a-Struct, 489 (2008) 77-84.

[35] M. Jafari, M.H. Abbasi, M.H. Enayati, F. Karimzadeh, Mechanical properties of nanostructured Al2024-MWCNT composite prepared by optimized mechanical milling and hot pressing methods, Adv Powder Technol, 23 (2012) 205-210.

[36] J.Z. Liao, M.J. Tan, I. Sridhar, Spark plasma sintered multi-wall carbon nanotube reinforced aluminum matrix composites, Mater Design, 31 (2010) S96-S100.

[37] http://www.geologycafe.com/class/chapter2.html, Chapter 2 - Basic Geologic Principles in: Introduction to Geology

[38] http://www.alu-support.com/newsdisp.php?ID=129.

[39] H. Kroto, H. Terrones, Carbon nanotubes and related structures - new materials for the twenty-first century, Interdiscipl Sci Rev, 25 (2000) 78-80.

[40] E. Burstein, A major milestone in nanoscale material science: the 2002 Benjamin Franklin Medal in physics presented to Sumio lijima, J Franklin I, 340 (2003) 221-242.

[41] S. Iijima, Helical Microtubules of Graphitic Carbon, Nature, 354 (1991) 56-58.

[42] W. Kratschmer, L.D. Lamb, K. Fostiropoulos, D.R. Huffman, Solid C-60 - a New Form Of Carbon, Nature, 347 (1990) 354-358.

[43] P.J.F. Harris, Carbon Nanotubes and Related Structures, Cambridge University Press, (1999).

[44] M. Paradise, T. Goswami, Carbon nanotubes - Production and industrial applications, Mater Design, 28 (2007) 1477-1489.

[45] C.N.R. Rao, R. Voggu, A. Govindaraj, Selective generation of single-walled carbon nanotubes with metallic, semiconducting and other unique electronic properties, Nanoscale,

1 (2009) 96-105.

[46] A.G. C N Ram Rao, Nanotubes and Nanowires, Royal Society of Chemistry, 2011.

[47] S. Iijima, Carbon nanotubes: past, present, and future, Physica B, 323 (2002) 1-5.

[48] A. Hirsch, Funktionalisierung von einwandigen Kohlenstoffnanorohern, Angew Chem., 114 (2002) 1933–1939.

[49] R.F. Zhang, Y.Y. Zhang, Q. Zhang, H.H. Xie, W.Z. Qian, F. Wei, Growth of Half-Meter Long Carbon Nanotubes Based on Schulz-Flory Distribution, Acs Nano, 7 (2013) 6156-6161.

[50] A.M.K. Esawi, K. Morsi, A. Sayed, M. Taher, S. Lanka, The influence of carbon nanotube (CNT) morphology and diameter on the processing and properties of CNT-reinforced aluminium composites, Compos Part a-Appl S, 42 (2011) 234-243.

[51] L. Wang, H. Choi, J.M. Myoung, W. Lee, Mechanical alloying of multi-walled carbon nanotubes and aluminium powders for the preparation of carbon/metal composites, Carbon, 47 (2009) 3427-3433.

[52] T.W. Ebbesen, P.M. Ajayan, Large-Scale Synthesis of Carbon Nanotubes, Nature, 358 (1992) 220-222.

[53] D.S. Bethune, C.H. Kiang, M.S. Devries, G. Gorman, R. Savoy, J. Vazquez, R. Beyers, Cobalt-Catalyzed Growth of Carbon Nanotubes with Single-Atomic-Layerwalls, Nature, 363 (1993) 605-607.

[54] S. Iijima, T. Ichihashi, Single-Shell Carbon Nanotubes of 1-Nm Diameter, Nature, 363 (1993) 603-605.

[55] T. Guo, P. Nikolaev, A. Thess, D.T. Colbert, R.E. Smalley, Catalytic Growth of Single-Walled Nanotubes by Laser Vaporization, Chem Phys Lett, 243 (1995) 49-54.

[56] B.I. Yakobson, R.E. Smalley, Fullerene nanotubes: C-1000000 and beyond, Am Sci, 85 (1997) 324-337.

[57] Y.H.Z.J. Li Qingwen, Liu Zhongfan, Dependence of the formation of carbon nanotubes on the chemical structures of hydrocarbons, Presented at the 8th International Conference on Electronic Materials (IUMRS-ICEM 2002, Xi'an, China, 10–14 June 2002), (2002).

[58] A.M.K. Esawi, M.M. Farag, Carbon nanotube reinforced composites: Potential and current challenges, Mater Design, 28 (2007) 2394-2401.

[59] P.G. Collins, P. Avouris, Nanotubes for electronics, Sci Am, 283 (2000) 62-+.

[60] J. Hone, B. Batlogg, Z. Benes, A.T. Johnson, J.E. Fischer, Quantized phonon spectrum of single-wall carbon nanotubes, Science, 289 (2000) 1730-1733.

[61] E.T. Thostenson, C.Y. Li, T.W. Chou, Nanocomposites in context, Compos Sci Technol, 65 (2005) 491-516.

[62] J.M. Planeix, N. Coustel, B. Coq, V. Brotons, P.S. Kumbhar, R. Dutartre, P. Geneste, P.

Bernier, P.M. Ajayan, Application of Carbon Nanotubes as Supports in Heterogeneous Catalysis, J Am Chem Soc, 116 (1994) 7935-7936.

[63] J. Kong, N.R. Franklin, C.W. Zhou, M.G. Chapline, S. Peng, K.J. Cho, H.J. Dai, Nanotube molecular wires as chemical sensors, Science, 287 (2000) 622-625.

[64] S.J. Tans, A.R.M. Verschueren, C. Dekker, Room-temperature transistor based on a single carbon nanotube, Nature, 393 (1998) 49-52.

[65] W.A. Curtin, B.W. Sheldon, CNT-reinforced ceramics and metals, Mater Today, 7 (2004) 44-49.

[66] Z.Y. Liu, B.L. Xiao, W.G. Wang, Z.Y. Ma, Tensile Strength and Electrical Conductivity of Carbon Nanotube Reinforced Aluminum Matrix Composites Fabricated by Powder Metallurgy Combined with Friction Stir Processing, J Mater Sci Technol, 30 (2014) 649-655.

[67] T. Laha, Y. Chen, D. Lahiri, A. Agarwal, Tensile properties of carbon nanotube reinforced aluminum nanocomposite fabricated by plasma spray forming, Compos Part a-Appl S, 40 (2009) 589-594.

[68] T. Manzur, N. Yazdani, M.A.B. Emon, Effect of Carbon Nanotube Size on Compressive Strengths of Nanotube Reinforced Cementitious Composites, Journal of Materials, 2014 (2014).

[69] K.T. Kim, S. Cha, S.H. Hong, Hardness and wear resistance of carbon nanotube reinforced Cu matrix nanocomposites, Mat Sci Eng a-Struct, 449 (2007) 46-50.

[70] C.R. Bradbury, J.K. Gomon, L. Kollo, H. Kwon, M. Leparoux, Hardness of Multi Wall Carbon Nanotubes reinforced aluminium matrix composites, J Alloy Compd, 585 (2014) 362-367.

[71] W. Wang, P. Ciselli, E. Kuznetsov, T. Peijs, A.H. Barber, Effective reinforcement in carbon nanotube - polymer composites, Philos T R Soc A, 366 (2008) 1613-1626.

[72] I. Brodie, C. Spindt, Vacuum microelectronics, Adv Electron El Phys, 83 (1992) 1-106.

[73] A.G. Rinzler, J.H. Hafner, P. Nikolaev, L. Lou, S.G. Kim, D. Tomanek, P. Nordlander, D.T. Colbert, R.E. Smalley, Unraveling Nanotubes - Field-Emission from an Atomic Wire, Science, 269 (1995) 1550-1553.

[74] H.J. Dai, J.H. Hafner, A.G. Rinzler, D.T. Colbert, R.E. Smalley, Nanotubes as nanoprobes in scanning probe microscopy, Nature, 384 (1996) 147-150.

[75] S.S. Wong, J.D. Harper, P.T. Lansbury, C.M. Lieber, Carbon nanotube tips: High-resolution probes for imaging biological systems, J Am Chem Soc, 120 (1998) 603-604.

[76] D.L.a.A.A. S. R. Bakshi, Carbon nanotube reinforced metal matrix composites – a review, International Materials Reviews, 55 (2010) 41-64.

[77] M. Moniruzzaman, K.I. Winey, Polymer nanocomposites containing carbon nanotubes,

Macromolecules, 39 (2006) 5194-5205.

[78] D.E. Hill, Y. Lin, A.M. Rao, L.F. Allard, Y.P. Sun, Functionalization of carbon nanotubes with polystyrene, Macromolecules, 35 (2002) 9466-9471.

[79] P.C. Ma, N.A. Siddiqui, G. Marom, J.K. Kim, Dispersion and functionalization of carbon nanotubes for polymer-based nanocomposites: A review, Compos Part a-Appl S, 41 (2010) 1345-1367.

[80] M.S.P. Shaffer, A.H. Windle, Fabrication and characterization of carbon nanotube/poly(vinyl alcohol) composites, Adv Mater, 11 (1999) 937-941.

[81] V.N. Khabashesku, J.L. Margrave, E.V. Barrera, Functionalized carbon nanotubes and nanodiamonds for engineering and biomedical applications, Diam Relat Mater, 14 (2005) 859-866.

[82] D. Qian, E.C. Dickey, R. Andrews, T. Rantell, Load transfer and deformation mechanisms in carbon nanotube-polystyrene composites, Appl Phys Lett, 76 (2000) 2868-2870.

[83] R. Andrews, D. Jacques, D.L. Qian, T. Rantell, Multiwall carbon nanotubes: Synthesis and application, Accounts Chem Res, 35 (2002) 1008-1017.

[84] J.G. Smith, D.M. Delozier, J.W. Connell, K.A. Watson, Carbon nanotube-conductive additive-space durable polymer nanocomposite films for electrostatic charge dissipation, Polymer, 45 (2004) 6133-6142.

[85] M.N. Tchoul, W.T. Ford, M.L. Ha, I. Chavez-Sumarriva, B.P. Grady, G. Lolli, D.E. Resasco, S. Arepalli, Composites of single-walled carbon nanotubes and polystyrene: preparation and electrical conductivity, Chem Mater, 20 (2008) 3120-3126.

[86] S. Rawal, Metal-matrix composites for space applications, Jom-J Min Met Mat S, 53 (2001) 14-17.

[87] P.R. Soni, Mechanical alloying: fundamentals and applications, Cambridge Int Science Publishing, 1998.

[88] M. Adamiak, Mechanical alloying for fabrication of aluminium matrix composite powders with Ti-Al intermetallics reinforcement, Journal of Achievements in Materials and Manufacturing Engineering, 31 (2008) 191-196.

[89] C.C. Koch, R.O. Scattergood, K.M. Youssef, E.H. Chan, Y.T.T. Zhu, Nanostructured materials by mechanical alloying: new results on property enhancement, J Mater Sci, 45 (2010) 4725-4732.

[90] K. Morsi, A. Esawi, Effect of mechanical alloying time and carbon nanotube (CNT) content on the evolution of aluminum (Al)-CNT composite powders, J Mater Sci, 42 (2007) 4954-4959.

[91] A. Esawi, K. Morsi, Dispersion of carbon nanotubes (CNTs) in aluminum powder, Compos Part a-Appl S, 38 (2007) 646-650.

[92] A. Javadi, S. Mirdamadi, M. Faghisani, S. Shakhesi, Investigation of new method to achieve well dispersed multiwall carbon nanotubes reinforced Al matrix composites, World Acad. Sci. Eng. Technol, 59 (2011) 16-22.

[93] Z.Y. Liu, S.J. Xu, B.L. Xiao, P. Xue, W.G. Wang, Z.Y. Ma, Effect of ball-milling time on mechanical properties of carbon nanotubes reinforced aluminum matrix composites, Compos Part a-Appl S, 43 (2012) 2161-2168.

[94] T. Laha, A. Agarwal, T. McKechnie, S. Seal, Synthesis and characterization of plasma spray formed carbon nanotube reinforced aluminum composite, Mat Sci Eng a-Struct, 381 (2004) 249-258.

[95] S.M. Zhou, X.B. Zhang, Z.P. Ding, C.Y. Min, G.L. Xu, W.M. Zhu, Fabrication and tribological properties of carbon nanotubes reinforced Al composites prepared by pressureless infiltration technique, Compos Part a-Appl S, 38 (2007) 301-306.

[96] B. Abbasipour, B. Niroumand, S.M. Monirvaghefi, Mechanical Properties of A356-Cnt Cast Nano Composite Produced by a Special Compocasting Route, Tms 2012 141st Annual Meeting & Exhibition - Supplemental Proceedings, Vol 1: Materials Processing And Interfaces, (2012) 733-740.

[97] B. Abbasipour, B. Niroumand, S.M.M. Vaghefi, Compocasting of A356-CNT composite, Transactions of Nonferrous Metals Society of China, 20 (2010) 1561-1566.

[98] T. Zhang, L. Kumari, G.H. Du, W.Z. Li, Q.W. Wang, K. Balani, A. Agarwal, Mechanical properties of carbon nanotube-alumina nanocomposites synthesized by chemical vapor deposition and spark plasma sintering, Compos Part a-Appl S, 40 (2009) 86-93.

[99] J. Tan, T. Yu, B. Xu, Q. Yao, Microstructure and wear resistance of nickel-carbon nanotube composite coating from brush plating technique, Tribol Lett, 21 (2006) 107-111.

[100] X.H. Chen, C.S. Chen, H.N. Xiao, F.Q. Cheng, G. Zhan, G.J. Yi, Corrosion behavior of carbon nanotubes - Ni composite coating, Surf Coat Tech, 191 (2005) 351-356.

[101] C. Guo, Y. Zuo, X.H. Zhao, J.M. Zhao, J.P. Xiong, The effects of electrodeposition current density on properties of Ni-CNTs composite coatings, Surf Coat Tech, 202 (2008) 3246-3250.

[102] S.I. Cha, K.T. Kim, S.N. Arshad, C.B. Mo, S.H. Hong, Extraordinary strengthening effect of carbon nanotubes in metal-matrix nanocomposites processed by molecular-level mixing, Adv Mater, 17 (2005) 1377-+.

[103] S.I. Cha, K.T. Kim, K.H. Lee, C.B. Mo, S.H. Hong, Strengthening and toughening of carbon nanotube reinforced alumina nanocomposite fabricated by molecular level mixing process, Scripta Mater, 53 (2005) 793-797.

[104] C.N. He, N.Q. Zhao, C.S. Shi, X.W. Du, J.J. Li, H.P. Li, Q.R. Cui, An approach to obtaining homogeneously dispersed carbon nanotubes in Al powders for preparing reinforced Al-matrix composites, Adv Mater, 19 (2007) 1128-1132.

[105] P. Quang, Y.G. Jeong, S.C. Yoon, S.H. Hong, H.S. Kim, Consolidation of 1 vol. %

carbon nanotube reinforced metal matrix nanocomposites via equal channel angular pressing, J Mater Process Tech, 187 (2007) 318-320.

[106] P. Quang, Y.G. Jeong, S.C. Yoon, S.I. Hong, S.H. Hong, H.S. Kim, Carbon nanotube reinforced metal matrix nanocomposites via equal channel angular pressing, Progress in Powder Metallurgy, Pts 1 and 2, 534-536 (2007) 245-248.

[107] P. Quang, Y.G. Jeong, S.H. Hong, H.S. Kim, Equal channel angular pressing of carbon nanotube reinforced metal matrix nanocomposites, Key Eng Mat, 326-328 (2006) 325-328.

[108] R.M. German, A - Z of Powder Metallurgy, Elsevier, 2006.

[109] A.K. Shukla, N. Nayan, S.V.S.N. Murty, S.C. Sharma, P. Chandran, S.R. Bakshi, K.M. George, Processing of copper-carbon nanotube composites by vacuum hot pressing technique, Mat Sci Eng a-Struct, 560 (2013) 365-371.

[110] A.I. Rudskoy, T.S. Koltsova, F.M. Shakhov, O.V. Tolochko, V.G. Mikhailov, Effect of Hot Pressing Modes on the Structure and Properties of an 'Aluminum - Carbon Nanofibers' Composite Material, Met Sci Heat Treat+, 56 (2015) 525-530.

[111] A.M.K. Esawi, K. Morsi, A. Sayed, A.A. Gawad, P. Borah, Fabrication and properties of dispersed carbon nanotube-aluminum composites, Mat Sci Eng a-Struct, 508 (2009) 167-173.

[112] S.F. Bartolucci, J. Paras, M.A. Rafiee, J. Rafiee, S. Lee, D. Kapoor, N. Koratkar, Graphene-aluminum nanocomposites, Mat Sci Eng a-Struct, 528 (2011) 7933-7937.

[113] J. Stein, B. Lenczowski, N. Fréty, E. Anglaret, High-performance Metal Matrix Composites Reinforced by Carbon Nanotubes, 18th International Conference on Composite Materials, (2011).

[114] C.S. Goh, J. Wei, L.C. Lee, M. Gupta, Simultaneous enhancement in strength and ductility by reinforcing magnesium with carbon nanotubes, Materials Science and Engineering: A, 423 (2006) 153-156.

[115] C.S. Goh, J. Wei, L.C. Lee, M. Gupta, Ductility improvement and fatigue studies in Mg-CNT nanocomposites, Compos Sci Technol, 68 (2008) 1432-1439.

[116] K.K. Chawla, Composite materials: Science and engineering, 2nd ed., Springer, 2001.

[117] S. Ray, Synthesis of Cast Metal-Matrix Particulate Composites, J Mater Sci, 28 (1993) 5397-5413.

[118] I.A. Ibrahim, F.A. Mohamed, E.J. Lavernia, Particulate Reinforced Metal Matrix Composites - a Review, J Mater Sci, 26 (1991) 1137-1156.

[119] A. Agarwal, S.R. Bakshi, D. Lahiri, Carbon nanotube reinforced metal matrix composites, CRC Press, 2010.

[120] B. Boesl, D. Lahiri, S. Behdad, A. Agarwal, Direct observation of carbon nanotube induced strengthening in aluminum composite via in situ tensile tests, Carbon, 69 (2014) 79-85.

[121] A.M.K. Esawi, K. Morsi, A. Sayed, M. Tahera, S. Lanka, Effect of carbon nanotube (CNT) content on the mechanical properties of CNT-reinforced aluminium composites, Compos Sci Technol, 70 (2010) 2237-2241.

[122] R. Perez-Bustamante, C.D. Gomez-Esparz, I. Estrada-Guel, M. Miki-Yoshida, L. Licea-Jimenez, S.A. Perez-Garcia, R. Martinez-Sanchez, Microstructural and mechanical characterization of Al-MWCNT composites produced by mechanical milling, Mat Sci Eng a-Struct, 502 (2009) 159-163.

[123] H. Kwon, M. Estili, K. Takagi, T. Miyazaki, A. Kawasaki, Combination of hot extrusion and spark plasma sintering for producing carbon nanotube reinforced aluminum matrix composites, Carbon, 47 (2009) 570-577.

[124] T. Noguchi, A. Magario, S. Fukazawa, S. Shimizu, J. Beppu, M. Seki, Carbon nanotube/aluminium composites with uniform dispersion, Mater Trans, 45 (2004) 602-604.

[125] Y. Feng, H.L. Yuan, M. Zhang, Fabrication and properties of silver-matrix composites reinforced by carbon nanotubes, Mater Charact, 55 (2005) 211-218.

[126] S.M. Uddin, T. Mahmud, C. Wolf, C. Glanz, I. Kolaric, C. Volkmer, H. Holler, U. Wienecke, S. Roth, H.J. Fecht, Effect of size and shape of metal particles to improve hardness and electrical properties of carbon nanotube reinforced copper and copper alloy composites, Compos Sci Technol, 70 (2010) 2253-2257.

[127] W.M. Daoush, B.K. Lim, C.B. Mo, D.H. Nam, S.H. Hong, Electrical and mechanical properties of carbon nanotube reinforced copper nanocomposites fabricated by electroless deposition process, Mat Sci Eng a-Struct, 513-14 (2009) 247-253.

[128] J.H. Wu, H.L. Zhang, Y. Zhang, X.T. Wang, Mechanical and thermal properties of carbon nanotube/aluminum composites consolidated by spark plasma sintering, Mater Design, 41 (2012) 344-348.

[129] S. Yamanaka, H. Kadokura, A. Kawasaki, H. Sakamoto, Y. Mekuchi, M. Kuno, T. Tsukada, Fabrication and thermal evaluation of carbon nanotube/aluminium composite by spark plasma sintering method, J Jpn Soc Powder Powder Metall, 53 (2006) 965-970.

[130] S. Cho, K. Kikuchi, T. Miyazaki, K. Takagi, A. Kawasaki, T. Tsukada, Multiwalled carbon nanotubes as a contributing reinforcement phase for the improvement of thermal conductivity in copper matrix composites, Scripta Mater, 63 (2010) 375-378.

[131] K. Chu, H. Guo, C.C. Jia, F.Z. Yin, X.M. Zhang, X.B. Liang, H. Chen, Thermal Properties of Carbon Nanotube-Copper Composites for Thermal Management Applications, Nanoscale Res Lett, 5 (2010) 868-874.

[132] H.L. Zhang, J.F. Li, K.F. Yao, L.D. Chen, Spark plasma sintering and thermal conductivity of carbon nanotube bulk materials, J Appl Phys, 97 (2005).

[133] R. George, K.T. Kashyap, R. Raw, S. Yamdagni, Strengthening in carbon nanotube/aluminium (CNT/Al) composites, Scripta Mater, 53 (2005) 1159-1163.

[134] C.F. Deng, X.X. Zhang, D.Z. Wang, Q. Lin, A.B. Li, Preparation and characterization

of carbon nanotubes/aluminum matrix composites, Mater Lett, 61 (2007) 1725-1728.

[135] W.D. Callister, Fundamentals of Materials Science and Engineering, 2nd ed., Wiley & Sons.

[136] N. Hansen, Hall-Petch relation and boundary strengthening, Scripta Mater, 51 (2004) 801-806.

[137] D. Poirier, R. Gauvin, R.A.L. Drew, Structural characterization of a mechanically milled carbon nanotube/aluminum mixture, Compos Part a-Appl S, 40 (2009) 1482-1489.

[138] S. Vives, E. Gaffet, C. Meunier, X-ray diffraction line profile analysis of iron ball milled powders, Mat Sci Eng a-Struct, 366 (2004) 229-238.

[139] C.S. Goh, J. Wei, L.C. Lee, M. Gupta, Development of novel carbon nanotube reinforced magnesium nanocomposites using the powder metallurgy technique, Nanotechnology, 17 (2006) 7-12.

[140] C.S. Goh, J. Wei, L.C. Lee, A. Gupta, Simultaneous enhancement in strength and ductility by reinforcing magnesium with carbon nanotubes, Mat Sci Eng a-Struct, 423 (2006) 153-156.

[141] S.K. Thakur, G.T. Kwee, M. Gupta, Development and characterization of magnesium composites containing nano-sized silicon carbide and carbon nanotubes as hybrid reinforcements, J Mater Sci, 42 (2007) 10040-10046.

[142] S.M.L. Nai, J. Wei, M. Gupta, Improving the performance of lead-free solder reinforced with multi-walled carbon narlotubes, Mat Sci Eng a-Struct, 423 (2006) 166-169.

[143] R.J. Arsenault, The Strengthening of Aluminum Alloy-6061 by Fiber and Platelet Silicon-Carbide, Mater Sci Eng, 64 (1984) 171-181.

[144] D. Lahiri, S.R. Bakshi, A.K. Keshri, Y. Liu, A. Agarwal, Dual strengthening mechanisms induced by carbon nanotubes in roll bonded aluminum composites, Mat Sci Eng a-Struct, 523 (2009) 263-270.

[145] B. Chen, S.F. Li, H. Imai, L. Jia, J. Umeda, M. Takahashi, K. Kondoh, Load transfer strengthening in carbon nanotubes reinforced metal matrix composites via in-situ tensile tests, Compos Sci Technol, 113 (2015) 1-8.

[146] Z. Xia, L. Riester, W.A. Curtin, H. Li, B.W. Sheldon, J. Liang, B. Chang, J.M. Xu, Direct observation of toughening mechanisms in carbon nanotube ceramic matrix composites, Acta Mater, 52 (2004) 931-944.

[147] K.T. Lau, Interfacial bonding characteristics of nanotube/polymer composites, Chem Phys Lett, 370 (2003) 399-405.

[148] H.L. Cox, The Elasticity and Strength of Paper and Other Fibrous Materials, Brit J Appl Phys, 3 (1952) 72-79.

[149] H.J. Choi, G.B. Kwon, G.Y. Lee, D.H. Bae, Reinforcement with carbon nanotubes in aluminum matrix composites, Scripta Mater, 59 (2008) 360-363.

[150] R. Mitra, Y.R. Mahajan, Interfaces in Discontinuously Reinforced Metal-Matrix Composites - an Overview, B Mater Sci, 18 (1995) 405-434.

[151] T. Laha, S. Kuchibhatla, S. Seal, W. Li, A. Agarwal, Interfacial phenomena in thermally sprayed multiwalled carbon nanotube reinforced aluminum nanocomposite, Acta Mater, 55 (2007) 1059-1066.

[152] K.P. So, I.H. Lee, D.L. Duong, T.H. Kim, S.C. Lim, K.H. An, Y.H. Lee, Improving the wettability of aluminum on carbon nanotubes, Acta Mater, 59 (2011) 3313-3320.

[153] K.P. So, I.H. Lee, D.L. Duong, T.H. Kim, S.C. Lim, K.H. An, Y.H. Lee, Improving the wettablity of aluminium on carbon nanotubes, in: 18th International Conference on Composite Materials, 2009.

[154] J.M. Molina, R. Voytovych, E. Louis, N. Eustathopoulos, The surface tension of liquid aluminium in high vacuum: The role of surface condition, Int J Adhes Adhes, 27 (2007) 394-401.

[155] S. Nuriel, L. Liu, A.H. Barber, H.D. Wagner, Direct measurement of multiwall nanotube surface tension, Chem Phys Lett, 404 (2005) 263-266.

[156] T.J.P. Dong S.R , Zhang X.B., An investigation of the sliding wear behavior of Cu2matrix composite reinfored by carbon nanotubes, Materials Science and Engineering: A, 313 (2001) 83.

[157] W.X. Chen, J.P. Tu, L.Y. Wang, H.Y. Gan, Z.D. Xu, X.B. Zhang, Tribological application of carbon nanotubes in a metal-based composite coating and composites, Carbon, 41 (2003) 215-222.

[158] T. Kuzumaki, O. Ujiie, H. Ichinose, K. Ito, Mechanical characteristics and preparation of carbon nanotube fiber-reinforced Ti composite, Adv Eng Mater, 2 (2000) 416-418.

[159] M.T.Z. Hassan, A.M.K. Esawi, S. Metwalli, Effect of carbon nanotube damage on the mechanical properties of aluminium-carbon nanotube composites, J Alloy Compd, 607 (2014) 215-222.

[160] New 'Met for the Non-Metallurgist' book makes metallurgy easy to understand, Adv Mater Process, 153 (1998) 69-69.

[161] M.R. Pickus, Tips for Fountain Pens - a Case History on Adaptability Of Powder Metallurgy Process, Int J Powder Metall, 5 (1969) 7-&.

[162] A. Upadhyaya, G.S. Upadhyaya, Powder Metallurgy: Science, Technology and Materials, Universities Press, 2011.

[163] T. Tsutsui, Recent technology of powder metallurgy and applications, Hitachi Chemical Technical Report, (2012) 12.

[164] R. Morales, R.E. Aune, S. Seetharaman, O. Grinder, The powder metallurgy processing of refractory metals and alloys, JOM, 55 (2003) 20-23.

[165] C.L. Hsieh, W.H. Tuan, Elastic properties of ceramic-metal particulate composites,

Mat Sci Eng a-Struct, 393 (2005) 133-139.

[166] Conventional PM Process, in.

[167] A.M.K. Esawi, K. Morsi, A. Sayed, M. Taher, S. Lanka, The influence of carbon nanotube (CNT) morphology and diameter on the processing and properties of CNT-reinforced aluminium composites, Composites Part A: Applied Science and Manufacturing, 42 (2011) 234-243.

[168] E.o.N. Materials. Committee, Definitions, Compilation of ASTM standard definitions, in, American Society for Testing and Materials.

[169] A.K. Zak, W.H.A. Majid, M.E. Abrishami, R. Yousefi, X-ray analysis of ZnO nanoparticles by Williamson-Hall and size-strain plot methods, Solid State Sci, 13 (2011) 251-256.

[170] P.V. Ananthapadmanabhan, K.P. Sreekumar, N. Venkatramani, R. Kameswaran, C.C. Dias, S.C. Mishra, Particle morphology and size distribution of plasma processed aluminium powder, B Mater Sci, 19 (1996) 559-564.

[171] L. Wang, H. Choi, J.-M. Myoung, W. Lee, Mechanical alloying of multi-walled carbon nanotubes and aluminium powders for the preparation of carbon/metal composites, Carbon, 47 (2009) 3427-3433.

[172] P.S. Gilman, W.D. Nix, The structure and properties of aluminum alloys produced by mechanical alloying: Powder processing and resultant powder structures, Metallurgical Transactions A, 12 (1981) 813-824.

[173] M. Ramezani, T. Neitzert, Mechanical milling of aluminum powder using planetary ball milling process, JAMME, 55 (2012) 790-798.

[174] P.R. Soni, Mechanical Alloying: Fundamentals and Applications, 2000.

[175] W. Lee, S.I. Kwun, The effects of process control agents on mechanical alloying mechanisms in the Ti Al system, Journal of Alloys and Compounds, 240 (1996) 193-199.

[176] Y.F. Ternovoi, A.G. Tsipunov, S.B. Kuratchenko, O.M. Kuimova, K.V. Kondakova, Pore formation in atomized powders, Soviet Powder Metallurgy and Metal Ceramics, 24 (1985) 10-13.

[177] Y.S. Kwon, K.B. Gerasimov, S.K. Yoon, Ball temperatures during mechanical alloying in planetary mills, J Alloy Compd, 346 (2002) 276-281.

[178] J.B. Fogagnolo, E.M. Ruiz-Navas, M.H. Robert, J.M. Torralba, The effects of mechanical alloying on the compressibility of aluminium matrix composite powder, Materials Science and Engineering: A, 355 (2003) 50-55.

[179] P. Scherrer, Bestimmung der Grösse und der inneren Struktur von Kolloidteilchen mittels Röntgenstrahlen, Nachrichten von der Gesellschaft der Wissenschaften zu Göttingen, Mathematisch-Physikalische Klasse, 26 (1918).

[180] K. Ada, M. Goekgoez, M. Oenal, Y. Sankaya, Preparation and characterization of a

ZnO powder with the hexagonal plate particles, Powder Technol, 181 (2008) 285-291.

[181] T. Balakrishna Bhat, V.S. Arunachalam, Strengthening mechanisms in alloys, Proc. Indian Acad. Sci. (Engg. Sci.), 3 (1980) 275-296.

[182] X. Zhang, N. Hansen, Y. Gao, X. Huang, Hall–Petch and dislocation strengthening in graded nanostructured steel, Acta Mater, 60 (2012) 5933-5943.

[183] A. Nouri, P.D. Hodgson, C. Wen, Effect of ball-milling time on the structural characteristics of biomedical porous Ti–Sn–Nb alloy, Materials Science and Engineering: C, 31 (2011) 921-928.

[184] S.S. Razavi-Tousi, J.A. Szpunar, Microstructural evolution and grain subdivision mechanisms during severe plastic deformation of aluminum particles by ball milling, Philosophical Magazine, 95 (2015) 1425-1447.

[185] A. Gökçe, F. Fındık, Mechanical and physical properties of sintered aluminum powders, Journal of achievements in materials and manufacturing engineering, 30 (2008) 157-164.

[186] I.A. MacAskill, R.L. Hexemer Jr, I.W. Donaldson, D.P. Bishop, Effects of magnesium, tin and nitrogen on the sintering response of aluminum powder, J Mater Process Tech, 210 (2010) 2252-2260.

[187] G.B. Schaffer, T.B. Sercombe, R.N. Lumley, Liquid phase sintering of aluminium alloys, Mater Chem Phys, 67 (2001) 85-91.

[188] T. Laha, Y. Chen, D. Lahiri, A. Agarwal, Tensile properties of carbon nanotube reinforced aluminum nanocomposite fabricated by plasma spray forming, Composites Part A: Applied Science and Manufacturing, 40 (2009) 589-594.

[189] C.S. Goh, J. Wei, L.C. Lee, M. Gupta, Development of novel carbon nanotube reinforced magnesium nanocomposites using the powder metallurgy technique, Nanotechnology, 17 (2006) 7.

[190] A. Sanaty-Zadeh, Comparison between current models for the strength of particulate-reinforced metal matrix nanocomposites with emphasis on consideration of Hall-Petch effect, Mat Sci Eng a-Struct, 531 (2012) 112-118.

[191] R. Casati, M. Vedani, Metal Matrix Composites Reinforced by Nano-Particles-A Review, Metals-Basel, 4 (2014) 65-83.

[192] Z.B. Lei, K. Zhao, Y.G. Wang, L.N. An, Thermal Expansion of Al Matrix Composites Reinforced with Hybrid Micro-/nano-sized Al2O3 Particles, J Mater Sci Technol, 30 (2014) 61-64.

[193] A. Mazahery, M. Ostadshabani, Investigation on mechanical properties of nano-Al2O3-reinforced aluminum matrix composites, J Compos Mater, 45 (2011) 2579-2586.

[194] M. Habibnejad-Korayem, R. Mahmudi, W.J. Poole, Enhanced properties of Mg-based

nano-composites reinforced with Al2O3 nano-particles, Mat Sci Eng a-Struct, 519 (2009) 198-203.

[195] G.B. Schaffer, S.H. Huo, J. Drennan, G.J. Auchterlonie, The effect of trace elements on the sintering of an Al–Zn–Mg–Cu ALLOY, Acta Mater, 49 (2001) 2671-2678.

[196] G.B. Schaffer, T.B. Sercombe, R.N. Lumley, Liquid phase sintering of aluminium alloys, Mater Chem Phys, 67 (2001) 85-91.

[197] K. Kondoh, A. Kimura, R. Watanabe, Effect of Mg on sintering phenomenon of aluminium alloy powder particle, Powder Metall, 44 (2001) 161-164.

[198] D. Bozic, J. Stasic, B. Dimcic, M. Vilotijevic, V. Rajkovic, Multiple strengthening mechanisms in nanoparticle-reinforced copper matrix composites, B Mater Sci, 34 (2011) 217-226.

[199] Z.Y. Liu, B.L. Xiao, W.G. Wang, Z.Y. Ma, Analysis of carbon nanotube shortening and composite strengthening in carbon nanotube/aluminum composites fabricated by multi-pass friction stir processing, Carbon, 69 (2014) 264-274.

[200] J.R. Groza, J.C. Gibeling, Principles of Particle Selection for Dispersion-Strengthened Copper, Mat Sci Eng a-Struct, 171 (1993) 115-125.

[201] E.A. Bloch, Dispersion-strengthened aluminium alloys, Metallurgical Reviews, 6 (1961) 193-240.

[202] S. Queyreau, G. Monnet, B. Devincre, Orowan strengthening and forest hardening superposition examined by dislocation dynamics simulations, Acta Mater, 58 (2010) 5586-5595.

[203] B. Verlinden, Severe plastic deformation of metals, MJoM, 11 (2005) 165-182.

[204] L. Kurmanaeva, Y. Ivanisenko, J. Markmann, C. Kübel, A. Chuvilin, S. Doyle, R.Z. Valiev, H.J. Fecht, Grain refinement and mechanical properties in ultrafine grained Pd and Pd–Ag alloys produced by HPT, Materials Science and Engineering: A, 527 (2010) 1776-1783.

[205] S.S. Razavi-Tousi, J.A. Szpunar, Effect of structural evolution of aluminum powder during ball milling on hydrogen generation in aluminum-water reaction, Int J Hydrogen Energ, 38 (2013) 795-806.

[206] H. Abdoli, M. Ghanbari, S. Baghshahi, Thermal stability of nanostructured aluminum powder synthesized by high-energy milling, Mat Sci Eng a-Struct, 528 (2011) 6702-6707.

[207] M.S. Dresselhaus, A. Jorio, A.G. Souza Filho, R. Saito, Defect characterization in graphene and carbon nanotubes using Raman spectroscopy, Philosophical Transactions of the Royal Society of London A: Mathematical, Physical and Engineering Sciences, 368 (2010) 5355-5377.

[208] M. Ahmad, J.V. Anguita, V. Stolojan, T. Corless, J.S. Chen, J.D. Carey, S.R.P. Silva, High Quality Carbon Nanotubes on Conductive Substrates Grown at Low Temperatures,

Advanced Functional Materials, 25 (2015) 4419-4429.

[209] H. Murphy, P. Papakonstantinou, T.T. Okpalugo, Raman study of multiwalled carbon nanotubes functionalized with oxygen groups, J Vac Sci Technol B, 24 (2006) 715-720.

[210] V.C.S. Chandrasekaran, S.G. Advani, M.H. Santare, Role of processing on interlaminar shear strength enhancement of epoxy/glass fiber/multi-walled carbon nanotube hybrid composites, Carbon, 48 (2010) 3692-3699.

[211] M.F. Yu, B.I. Yakobson, R.S. Ruoff, Controlled sliding and pullout of nested shells in individual multiwalled carbon nanotubes, J Phys Chem B, 104 (2000) 8764-8767.

[212] A.H. Barber, S.R. Cohen, H.D. Wagner, Measurement of carbon nanotube-polymer interfacial strength, Appl Phys Lett, 82 (2003) 4140-4142.

[213] C.A. Cooper, S.R. Cohen, A.H. Barber, H.D. Wagner, Detachment of nanotubes from a polymer matrix, Appl Phys Lett, 81 (2002) 3873-3875.

[214] B. Peng, M. Locascio, P. Zapol, S.Y. Li, S.L. Mielke, G.C. Schatz, H.D. Espinosa, Measurements of near-ultimate strength for multiwalled carbon nanotubes and irradiation-induced crosslinking improvements, Nat Nanotechnol, 3 (2008) 626-631.

[215] M.S. Dresselhaus, G. Dresselhaus, J.-C. Charlier, E. Hernandez, Electronic, thermal and mechanical properties of carbon nanotubes, Philosophical Transactions of the Royal Society of London A: Mathematical, Physical and Engineering Sciences, 362 (2004) 2065-2098.

[216] P.R. Bandaru, Electrical properties and applications of carbon nanotube structures, J Nanosci Nanotechno, 7 (2007) 1239-1267.

[217] A. Eatemadi, H. Daraee, H. Karimkhanloo, M. Kouhi, N. Zarghami, A. Akbarzadeh, M. Abasi, Y. Hanifehpour, S.W. Joo, Carbon nanotubes: properties, synthesis, purification, and medical applications, Nanoscale Res Lett, 9 (2014) 1-13.

[218] J. Zhang, J.M. Zuo, Structure and diameter-dependent bond lengths of a multi-walled carbon nanotube revealed by electron diffraction, Carbon, 47 (2009) 3515-3528.

[219] J.W.G. Wilder, L.C. Venema, A.G. Rinzler, R.E. Smalley, C. Dekker, Electronic structure of atomically resolved carbon nanotubes, Nature, 391 (1998) 59-62.

[220] Z. Konya, J. Zhu, K. Niesz, D. Mehn, I. Kiricsi, End morphology of ball milled carbon nanotubes, Carbon, 42 (2004) 2001-2008.

[221] M.S. Sidhu, C.M. Bishop, M.V. Kral, Formation of aluminium carbide by cast iron and liquid aluminium interaction, Int J Cast Metal Res, 27 (2014) 321-328.

[222] G. Zhang, S.R. Feng, Q. Li, J.T. Blucher, J.A. Cornie, Control of Interface Reactions between P-55 Fibers and Aluminum Alloy Matrices during Pressure Infiltration Processing, in: H. Ishida (Ed.) Controlled Interphases in Composite Materials, Springer Netherlands, 1990, pp. 343-357.

[223] M. Lancin, C. Marhic, TEM study of carbon fibre reinforced aluminium matrix

composites: influence of brittle phases and interface on mechanical properties, J Eur Ceram Soc, 20 (2000) 1493-1503.

[224] E. Pippel, J. Woltersdorf, M. Doktor, J. Blucher, H.P. Degischer, Interlayer structure of carbon fibre reinforced aluminium wires, J Mater Sci, 35 (2000) 2279-2289.

[225] W. Zhou, S. Bang, H. Kurita, T. Miyazaki, Y. Fan, A. Kawasaki, Interface and interfacial reactions in multi-walled carbon nanotube-reinforced aluminum matrix composites, Carbon, 96 (2016) 919-928.

[226] L.J. Ci, Z.Y. Ryu, N.Y. Jin-Phillipp, M. Ruhle, Investigation of the interfacial reaction between multi-walled carbon nanotubes and aluminum, Acta Mater, 54 (2006) 5367-5375.

[227] H. Kurita, H. Kwon, M. Estili, A. Kawasaki, Multi-walled carbon nanotube-aluminum matrix composites prepared by combination of hetero-agglomeration method, spark plasma sintering and hot extrusion, Mater Trans, 52 (2011) 1960-1965.

[228] L. Ci, Z. Ryu, N.Y. Jin-Phillipp, M. Rühle, Investigation of the interfacial reaction between multi-walled carbon nanotubes and aluminum, Acta Mater, 54 (2006) 5367-5375.

[229] T. Ungár, Microstructural parameters from X-ray diffraction peak broadening, Scripta Mater, 51 (2004) 777-781.

[230] J.B. Rao, G.J. Catherin, I.N. Murthy, D.V. Rao, B.N. Raju, Production of nano structured silicon carbide by high energy ball milling, International Journal of Engineering, Science and Technology, 3 (2011).

[231] S.R. Bakshi, D. Lahiri, A. Agarwal, Carbon nanotube reinforced metal matrix composites - a review, Int Mater Rev, 55 (2010) 41-64.

[232] C. Suryanarayana, Non-equilibrium processing of materials, Elsevier, 1999.

[233] A. Agarwal, S.R. Bakshi, D. Lahiri, Carbon nanotubes: reinforced metal matrix composites, CRC press, 2010.

[234] C.F. Deng, P. Zhang, Y.X. Ma, X.X. Zhang, D.Z. Wang, Dispersion of multiwalled carbon nanotubes in aluminum powders, Rare Metals, 28 (2009) 175-180.

[235] T. Borkar, J. Hwang, J.Y. Hwang, T.W. Scharf, J. Tiley, S.H. Hong, R. Banerjee, Strength versus ductility in carbon nanotube reinforced nickel matrix nanocomposites, J Mater Res, 29 (2014) 761-769.

[236] P. Chandran, T. Sirimuvva, N. Nayan, A.K. Shukla, S.V.S.N. Murty, S.L. Pramod, S.C. Sharma, S.R. Bakshi, Effect of Carbon Nanotube Dispersion on Mechanical Properties of Aluminum-Silicon Alloy Matrix Composites, J Mater Eng Perform, 23 (2014) 1028-1037.

[237] E. Castillejos, B. Bachiller-Baeza, M. Perez-Cadenas, E. Gallegos-Suarez, I. Rodriguez-Ramos, A. Guerrero-Ruiz, K. Tamargo-Martinez, A. Martinez-Alonso, J.M.D. Tascon, Structural and surface modifications of carbon nanotubes when submitted to high temperature annealing treatments, J Alloy Compd, 536 (2012) S460-S463.

[238] X.L. Gao, K. Li, A shear-lag model for carbon nanotube-reinforced polymer

composites, Int J Solids Struct, 42 (2005) 1649-1667.

[239] K.K. Ang, K.S. Ahmed, An improved shear-lag model for carbon nanotube reinforced polymer composites, Compos Part B-Eng, 50 (2013) 7-14.

[240] J. Zhang, C. He, A three-phase cylindrical shear-lag model for carbon nanotube composites, Acta Mech, 196 (2008) 33-54.

[241] S.E. Shin, D.H. Bae, Strengthening behavior of chopped multi-walled carbon nanotube reinforced aluminum matrix composites, Mater Charact, 83 (2013) 170-177.

[242] H. Kwon, D.H. Park, J.F. Silvain, A. Kawasaki, Investigation of carbon nanotube reinforced aluminum matrix composite materials, Compos Sci Technol, 70 (2010) 546-550.

[243] A.A. Moosa, K.K. Al-Khazraji, O.S. Muhammed, Tensile Strength of Squeeze Cast Carbon Fibers Reinforced Al-Si Matrix Composites, Journal of Minerals and Materials Characterization and Engineering, 10 (2011) 127.

[244] F. Inam, T. Peijs, Re-agglomeration of carbon nanotubes in two-part epoxy system; influence of the concentration, (2007).

[245] T.-H. Kim, M.-H. Park, K.-W. Song, J.-H. Bae, J.-W. Lee, C.D. Lee, C.-W. Yang, Density Control and Wettability Enhancement by Functionalizing Carbon Nanotubes with Nickel Oxide in Aluminum-Carbon Nanotube System, J Nanosci Nanotechno, 13 (2013) 7685-7688.

[246] R. Pérez-Bustamante, F. Pérez-Bustamante, I. Estrada-Guel, L. Licea-Jiménez, M. Miki-Yoshida, R. Martínez-Sánchez, Effect of milling time and CNT concentration on hardness of CNT/Al 2024 composites produced by mechanical alloying, Mater Charact, 75 (2013) 13-19.

[247] I. Ahmad, B. Yazdani, Y.Q. Zhu, Recent Advances on Carbon Nanotubes and Graphene Reinforced Ceramics Nanocomposites, Nanomaterials-Basel, 5 (2015) 90-114.

[248] J. Macutkevic, P.P. Kuzhir, A.G. Paddubskaya, J. Banys, S.A. Maksimenko, E. Stefanutti, F. Micciulla, S. Bellucci, Broadband dielectric/electric properties of epoxy thin films filled with multiwalled carbon nanotubes, J Nanophotonics, 7 (2013).

[249] T.J. Kang, J.W. Yoon, D.I. Kim, S.S. Kum, Y.H. Huh, J.H. Hahn, S.H. Moon, H.Y. Lee, Y.H. Kim, Sandwich-type laminated nanocomposites developed by selective dip-coating of carbon nanotubes, Adv Mater, 19 (2007) 427-+.

[250] J. Yuuki, H. Kwon, A. Kawasaki, A. Magario, T. Noguchi, J. Beppu, M. Seki, Fabrication of carbon nanotube reinforced aluminum composite by powder extrusion process, in, Trans Tech Publ, pp. 889-892.